SCIENTIFIC SOCIETY FOR MECHANICAL ENGINEERING (SSME/GTE)

PROCEEDINGS

OF THE

12TH INTERNATIONAL CONFERENCE ON

RAILWAY BOGIES AND RUNNING GEARS

Budapest, Hungary

5 - 8 September, 2022

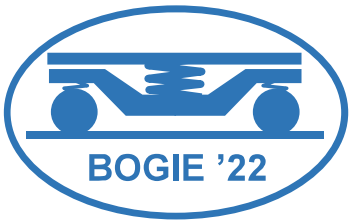

Edited by

Prof. András Szabó

Department of Rolling Stock, SSME/GTE

SCIENTIFIC SOCIETY FOR
MECHANICAL ENGINEERING
(SSME/GTE)

PROCEEDINGS

OF THE

12TH INTERNATIONAL CONFERENCE ON

RAILWAY BOGIES AND RUNNING GEARS

Budapest, Hungary

5 - 8 September, 2022

Edited by

Prof. András Szabó

Department of Rolling Stock, SSME/GTE

The Conference Organising Committee gratefully acknowledges the generosity of the following *Major Sponsors* and Sponsors:

STADLER MAGYARORSZÁG Kft. (H)

KNORR-BREMSE VASÚTI JÁRMŰ RENDSZEREK HUNGÁRIA Kft. (H)

NIPPON STEEL CORPORATION (J),

GANZ MOTOR Kft. (H)

GYSEV GYŐR-SOPRON-EBENFURTI VASÚT Zrt. (H)

MÁV VAGON Kft (H).

SIEMENS MOBILITY Kft. (H),

Issued by the *Department of Rolling Stock* of the SSME, Budapest, 2022
Printed form (book): ISBN 978-963-9058-45-3; Electronic form (pdf): ISBN 978-963-9058-46-0

The 11 Countries interested in BOGIE ’22

Editor in Chief:
Prof. András Szabó

This volume was prepared using MS Word files submitted by the authors.
No scientific or linguistic revisions were provided by the Organising Committee.

CONTENTS

PREFACE

Today, we are living in an era of efforts to reduce energy consumption and environmental impact. In such an environment, railway transport, freight and passenger carrying comes to the fore due to its favorable characteristics in terms of the set goals. Due to its priority importance, it is needed to develop the railway transport, and within the railway vehicles that carry out railway transport. Thus, progress is also necessary in the area of railway bogies and running gears, which are one of the main elements of vehicles. It is necessary to continue the research activity in order to gain a deeper understanding of the structural operation and to apply new technologies and methods in the production, repair and maintenance processes.

The aim of the international conference, which focuses on railway bogies and running gears, is for researchers and specialists in the field to familiarize themselves with the results, opportunities and experiences achieved in the fields indicated above in the last three years. This publication includes the presentations at the 12th International Conference on Railway Bogies and Running Gears to be held in Budapest between September 5-8, 2022. In addition, our publication also contains a short, personal commemoration of Prof. Dr. István Zobory, who organized the conference series for more than twenty years and recently passed away.

Prof. András Szabó
editor in chief

ISTVÁN ZOBORY - SCIENTIST AND ORGANIZER OF SCIENCE

Sergey V. MYAMLIN

JSC "Ukrainian Railways"
Svyatoshinska str. 13, Kyiv, Ukraine

Received: September 5-8, 2022

ABSTRACT

At the beginning of this year, an outstanding mechanical scientist and organizer of international scientific conferences in the field of railway transport, honorary professor of the Budapest University of Technology and Economics, member of the international editorial board of the scientific and practical journal "Railway Transport of Ukraine", Doctor of Technical Sciences, Professor István Zobory, passed away. Starting his career at the Budapest University of Technology and Economics in 1976, István Zobory remained faithful to the traditions of university science to the end. In 1981 he defended the thesis of a candidate of technical sciences, and in 1993 he defended his thesis of a doctor of technical sciences. During his work at the university, he went from a teacher of the department to the head of the department and the dean of the faculty. During its history, the department and faculty have changed their name, but have always been associated with railway transport and engineering. Professor István Zobory has always been distinguished by high decency, intelligence and humanity in relations with students, teachers and colleagues.

Keywords: Dr. Zobory István, mechanical scientist, longitudinal train dynamics, rolling stock dynamics, interaction between rolling stock and track

At the beginning of this year, an outstanding mechanical scientist and organizer of international scientific conferences in the field of railway transport, honorary professor of the Budapest University of Technology and Economics, member of the international editorial board of the scientific and practical journal "Railway Transport of Ukraine", Doctor of Technical Sciences, Professor István Zobory, passed away.

Starting his career at the Budapest University of Technology and Economics in 1976, István Zobory remained faithful to the traditions of university science to the end. In 1981 he defended the thesis of a candidate of technical sciences, and in 1993 he defended his thesis of a doctor of technical sciences. During his work at the university, he went from a teacher of the department to the head of the department and the dean of the faculty. During its history, the department and faculty have changed their name, but have always been associated with railway transport and engineering.

The main scientific interests of Professor István Zobory were related to railway transport, namely: stochastic dynamic modeling, longitudinal dynamics of trains, fatigue and reliability of transport structures, analysis of the causes of rolling stock accidents, dynamics and safety of rail vehicles, measurement of railway track parameters, interaction of rolling stock railways and tracks, wear of wheels and rails, creation of new designs of bogies and wagons.

Professor István Zobory is the author of more than 200 scientific publications in national and international publications, some of them are given in the reference bibliography, and some scientific publications of scientists from Ukraine at conferences organized by Professor István Zobory are cited in the literature [1-10]. He also supervised the training of 15 candidates and doctors of technical sciences.

Our first acquaintance with Professor István Zobory took place in November 1994, when the delegation of the Dnipropetrovsk State Technical University of Railway Transport (DIIT, now the Dnipro University of Science and Technology) consisting of: Professor Kablukov V.A. (Rector of the University), Professor Blokhin E.P. (First Vice-Rector of the University), Professor Danovich V.D. (Professor of the Department of Structural Mechanics), Senior Researcher Myamlin S.V. (Head of the Branch Research Laboratory of Rolling Stock Dynamics and Strength - ONIL DPPS DIIT), researcher Litvin V.A. (an employee of ONIL DPPS DIIT) was invited with scientific reports to a conference on traffic safety at the Budapest University of Technology and Economics. For me, then a young scientist, it was the first trip abroad and the first participation in an international scientific conference. Of course, we were very prepared to show the results of the research of our scientific school - the Scientific School of Transport Mechanics, which was created by Academician of the Academy of Sciences of Ukraine Vsevolod Arutyunovich Lazaryan. Our reports were devoted to the dynamics of rail vehicles, the peculiarities of investigating cases of derailment, the longitudinal dynamics of trains, the spatial dynamics of rail vehicles and the creation of simulators for locomotive drivers to teach safe and energy-saving train driving technologies. It was not without curiosities, it was planned that Litvin V.A. will voice all the reports as a person who has completed an internship at the University of Delft and speaks English well, but just before the speech he caught a cold and lost his voice, so I had to do all the reports. It was a serious test.

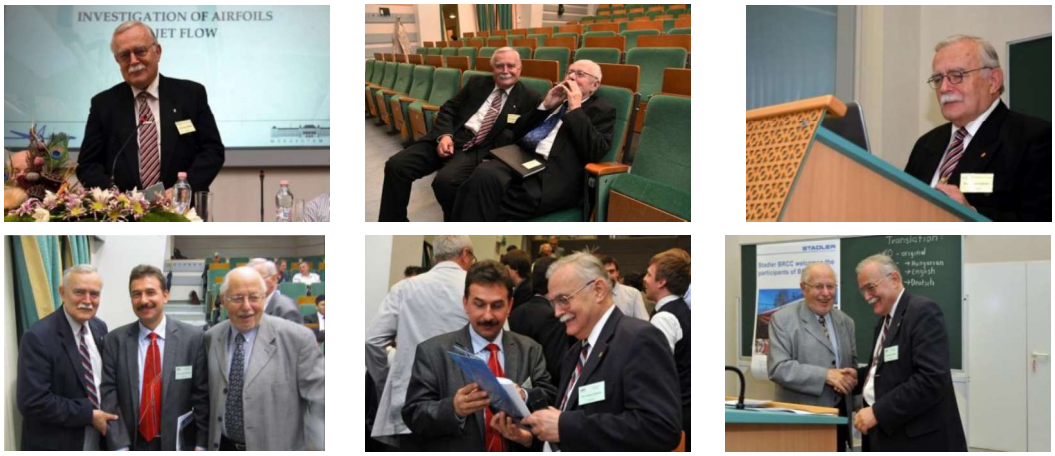

But, thanks to the professionalism and experience of Professor István Zobory, our presentations and answers to questions went quite smoothly and well. Then, representatives of our university and other scientific organizations of Ukraine many times visited various scientific forums, which were organized on the basis of the Budapest University of Technology and Economics and were the president of these conferences, Professor István Zobory, and for about 15 years I was lucky to be a member of the scientific committees of some international conferences such as the world-class Symposium on Railway Bogies and Running Gear. Professor István Zobory has also collaborated for many years with our journal, "Railway Transport of Ukraine", as a member of the international editorial board.

Professor István Zobory has always been distinguished by high decency, intelligence and humanity in relations with students, teachers and colleagues.

Bibliography of Prof. István Zobory.

Zobory I., Békefi E. On real-time simulation of the longitudinal dynamics of trains on a specified railway line // Periodica Polytechnica Transportation Engineering. 1995. Vol. 23 (1-2). P. 3-17.

Zobory I. Prediction of Wheel/Rail Profile Wear // Vehicle System Dynamics. – 1997. – Vol. 28, Iss. 2-3. – P. – 221-259. Doi 10.1080/00423119708969355

Zobory I. On stochastic field model of the wheel/rail rolling/sliding contact force transfer // Proceedings of the 10th Mini Conference on Vehicle System Dynamics, Identification, and Anomalies VSDIA 2006 (2006, Budapest, Hungary). Budapest: Budapest University of Technology and Economics, 2008. P. 95-116.

Zobory I. Irregular Brake Disc Wear Caused by Dynamically Unstable Running // Proceedings of the 15th Mini Conference on vehicle system dynamics, identification and anomalies (Budapest, Hungary, 7-9 November, 2016). Budapest: Budapest University of Technology and Economics, 2017. P. 55-64.

Zobory I., Nagy D. Dynamical Analysis of a Special Anti-Skid-System for Railway Cars and Traction Units // Proceedings of the 15th Mini Conference on vehicle system dynamics, identification and anomalies (Budapest, Hungary, 7-9 November, 2016). Budapest: Budapest University of Technology and Economics, 2017. P. 149-162.

Sábitz L., Zobory I. Sliding Friction Coefficient and Wear Multiplier as Functions of the Tribological State-Vector // Proceedings of the 15th Mini Conference on vehicle system dynamics, identification and anomalies (Budapest, Hungary, 7-9 November, 2016). Budapest: Budapest University of Technology and Economics, 2017. P. 311-320.

Sábitz L., Zobory I. Finite element modelling of the thermo-elastic processes in tread-braked wheels // Proceedings of the 8th International Conference on Railway Bogies and Running Gears - BOGIE ’10. Budapest: BME, Department of Railway Vehicles and Vehicle System Analysis, 2010, P.103-113.

Sábitz L., Zobory I. Simulation of local heat processes on the tread of a blockbraked railway wheel // Proceedings of the 13th Mini Conference on Vehicle System Dynamics, Identification and Anomalies - VSDIA 2012. Budapest: BME, Department of Railway Vehicles and Vehicle System Analysis, 2014. P. 245-252.

Sábitz L., Zobory I. On Simulating the Thermal Conditions of Martensite Formation on Railway Wheel Treads // Proceedings of the Second International Conference on Railway Technology. Civil-Comp Press, paper 105. DOI: 10.4203/ccp.104.105

Sábitz L., Zobory I. Combined Thermal and Stress Finite Element Analysis of Tread-Braked Wheels // Proceedings of the 12th MINI Conference on Vehicle System Dynamics, Identification and Anomalies - VSDIA 2010. Budapest: BME, Department of Railway Vehicles and Vehicle System Analysis, 2011. P. 203-213.

Szőke D., Zobory I. Dynamical Characteristics of Crank Mechanisms // Proceedings of the 15th Mini Conference on vehicle system dynamics, identification and anomalies (Budapest, Hungary, 7-9 November, 2016). Budapest: Budapest University of Technology and Economics, 2017. P. 321-330.

Zobory I. Vehicle Dynamics. Lecture notes. Budapest: BME, Department of Railway Vehicles, 1999.

Zobory I., Győri J., Kolonits F., Békefi E. On Reliability Analysis of Bogies and Running Gears // Proceedings of the 7th International Conference on Railway Bogies and Running Gears. Budapest: BME Department of Railway Vehicles, 2007. P. 367-383.

Szabó A., Zobory I. On Deterministic and Stochastic Simulation of Wheel and Rail Profile Wear Process // Periodica Polytechnica - Transportation Engineering. 1998. Vol. 26 (1-2). P. 3-17.

Zoller V., Zobory I. On dynamics of the track/vehicle system in presence of inhomogeneous rail supporting parameters // Periodica Polytechnica - Transportation Engineering. 2011. Vol.39 (2). P. 83-85.

Zoller V., Zobory I. Railway track dynamics with periodically varying stiffness and damping in the Winkler foundation // Periodica Polytechnica - Transportation Engineering. 2011. Vol. 39 (2). P. 87-90.

Zobory I., Békefi E. Control Strategies of Brake Dynamics for Railway Vehicles Equipped with Anti-Slip-Device // Proceedings of the 9th MINI Conference on Vehicle System Dynamics, Identification and Anomalies (VSDIA 2004). Budapest: BME, 2004. P. 227-236.

Zobory I., Zoller V., Zibolen E. Theoretical investigations into the dynamical properties of railway tracks using a continuous beam model on elastic foundation // Periodica Polytechnica, Ser. Transp. Eng. 1994. Vol. 22, No.1. P. 35-54.

Zoller V., Zobory I. Relations between the motion-responses caused by fixed and moving loads acting on discretely supported strings and beams // Progress in Industrial Mathematics at ECMI 2000, Mathematics in Industry 1. Berlin: Springer, 2002. P. 657-661.

REFERENCES

[1] Myamlin, S. - Blokhin, E. - Danovich, V. - Litvin, V. Influence of railway vehicle models of detail on the results of wheel wear prediction. Proc. of the 2nd Mini Conference on "Contact Mechanics and Wear of Rail/Wheel Systems", Budapest, 1994.

[2] Blokhin, E. - Evdomakha, G. - Zheleznov, K. - Myamlin, S. Automational complex for studying train movement as a system and its utilization for drivers training in safe and economic method of movement. Proc. of the 1996 5th Mini Conference on Vehicle System Dynamics, Identification and Anomalies, Budapest, Hung., 11–13 Nov. 1996, p. 251–253.

[3] Blokhin, E. - Danovich, V. - Myamlin, S. Influence of railway vehicles models degree of detail on the results of wheel wear prediction. Proc. of the 2nd Mini Conference on Contact Mechanics and Wear of Rail/Wheel Systems, Budapest, 29–31 July 1996, Techn. Univ. of Budapest, p. 297–303.

[4] Myamlin, S. Mathematical modelling of body connections in railway vehicles. 6th Mini Conference on Vehicle System Dynamics, Identification and Anomalies, 9–11 November 1998, Budapest, Hungary, Budapest Faculty of Transportation Engineering, 1998.

[5] Pshin'ko, O. - Blokhin, Y. - Myamlin, S. Effect of the lengths of rail line horizontal and vertical irregularities on dynamic loading of open wagon. Abstracts of the 7th Mini Conference on Vehicle System Dynamics, Identification and Anomalies, Budapest Univ. of Technology and Econ., 2000, p. 14.

[6] Pshin'ko, O. - Blokhin, Y. - Myamlin, S. The influence of the length of horizontal and vertical irregularities of railway track on dynamic loading of an open wagon. Proc. of the 7th Mini Conference on Vehicle System Dynamics, Identification and Anomalies, Budapest Univ. of Technology and Econ., 2000, p. 247–254.

[7] Blokhin, Y. - Pshin'ko, O. - Myamlin, S. Optimization of parameters of spring suspension of the freight car three-piece bogie. Proc. 5th International Conference on Railway Bogies and Running Gears, Budapest, 2001, p. 263–271.

[8] Blokhin, Y. - Pshin'ko, O. - Myamlin, S. Peculiarities of dynamics of empty freight wagon. Proc. of the 8th Mini Conference on Vehicle System Dynamics, Identification and Anomalies, 11–13 November 2002, Budapest, Hungary, Budapest Univ. of Technology and Econ., 2002, p. 167–174.

[9] Pshin'ko, O. - Myamlin, S. - Yalovoy, A. - Rasporskiy, V. Modernization of three-piece bogies. Proc. 6th International Conference on Railway Bogies and Running Gears, Budapest, 13–16 September, 2004, p. 175–180.

[10] Pshin'ko, O. - Manashkin, L. - Myamlin, S. - Bodnar, B. - Pys'mennyy, Y. On measuring vertical forces in freight car bogies. Proc. 9th Mini Conference on Vehicle System Dynamics, Identification and Anomalies, Budapest, 8–10 Nov, 2004, Budapest Univ. of Technology and Econ., p. 195–200.

DEVELOPMENT OF A BOGIE FRAME MONITORING SYSTEM USING A STRESS ESTIMATION METHOD

Shota ITO(*1), Takahiro FUJIMOTO(*1), Daisuke SHINAGAWA(*2), Yoshiyuki SHIMOKAWA(*2), Hideki MINAMI(*2), Osamu KONDO(*3), Gaku IOKIBE(*3) and Junichi NAKAGAWA(*4)

*2:Quality Management Div., Nippon Steel Corporation
*3: Nipponsteel Technology Co. Ltd.
*4: The University of TOKYO
6-1,Marunouchi 2-chome, Chiyoda-ku, Tokyo, 100-8071 Japan,
itoh.mr2.shohta@jp.nipponsteel.com

Received: August 5. 2022

ABSTRACT

A bogie frame monitoring system based on a new concept stress estimation method has been developed. The system is based on the equations of motion of the bogie frame obtained by modal analysis using commercially available finite element method (FEM) software. This system does not use devices such as strain gauges because it estimates bogie stress based on FEM using axle box acceleration as input. Stress calculations by FEM for complex structures such as bogie frames are computationally expensive, but this method can reduce the computational cost to a realistic level by using affine transformation group theory. It was confirmed that the system can accurately predict the displacement and stress of bogie frames during train operation. It was also confirmed that the fatigue life calculated using the predicted stresses agreed precisely with the fatigue life calculated using the stresses measured by strain gauges.

Keywords: finite element method, bogie frame stress, fatigue life

1 INTRODUCTION

The bogie frame of a rolling stock supports not only the car body, but also the drive and braking systems, etc., and complex loads are transmitted to the bogie frame during running. In particular, the stresses occurs when components such as the traction motor and end beam are vibrated due to track irregularity are high and difficult to predict. The strength design procedure of bogie frames against these external forces is specified in the JIS standard[1] in Japan, but there are cases where external forces exceed the expected level To improve the reliability of bogie frames, it is necessary to know the stresses on the bogie frame caused by these external forces during running. Generally, strain gauges are used to measure stresses in bogie frames. However, strain gauges can only measure narrow areas to which they are attached, and the number of gauges is enormous when measuring stresses in multiple points. In addition, they are not suitable for long-term measurement. As a solution to this problem, a stress estimation method1) using FEM dynamic analysis was developed. To estimate the stress without using strain gauges, this system uses the vibration characteristics of the bogie frame obtained by FEM analysis to solve the equation of motion with the axle box acceleration, which represents the effect of track irregularity. In order to evaluate the cumulative fatigue damage of bogie frames due to stress, it is necessary to calculate the stress in overall running. However, the conventional method using FEM dynamic analysis requires a great deal of time to analyze a complex structure like a bogie frame, and analysis period was limited to about 10 seconds. Therefore, we developed a faster calculation method.

2 CONCEPT

The concept of the developed stress estimation system is presented below. As shown in Figure 1, first, this system measures axle box acceleration on-track running. Then, the measured acceleration is converted to external force loading on the bogie frame and input into a dynamic analysis model based on FEM. The dynamic analysis model determines the displacement and stress distribution at each node of the bogie frame. Since the dynamic analysis model is based on FEM, stresses at all nodes meshed by FEM can be calculated. In addition, this method can be used acceleration sensors that are suitable for long-term use, unlike strain gauges. Furthermore, since the axle box acceleration is mainly due to track irregularities and is not affected by sprung mass, the axle box acceleration data measured with one monitoring bogie can be used for other bogies running the same track, as shown in Figure 2. This reduces the number of monitoring bogies, and it leads to reduce the cost of measurement.

1. Fig. Calculation flow of the bogie frame monitoring system

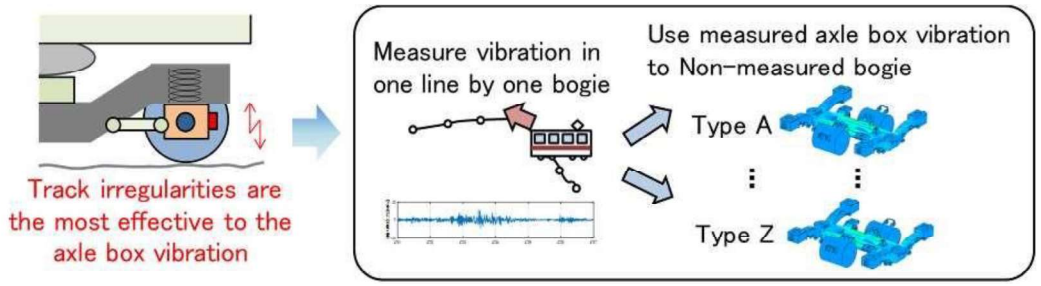

2. Fig. Overview of Cost Reduction by bogie frame monitoring System

3 BOGIE FRAME STRESS CALCULATION METHOD

3.1 Overview of Calculation Method

The flow of the stress calculation method using this system is shown below. First, FEM eigenvalue analysis of the bogie frame is performed to calculate the vibration characteristics (modal stiffness, modal mass, modal damping, modal vector, etc.). Next, equations of motion in the modal coordinate of the bogie frame are constructed using the modal characteristics. Furthermore, the external force loading on the bogie frame is obtained from the axle box acceleration measured during on-track running. The obtained external force is input into the equation of motion in the modal coordinate, and the vibration

displacement of the bogie frame is calculated. Finally, stresses are obtained from the displacements of each element of the bogie frame. The fatigue life is estimated from the frequency of these stresses.

3.2 Details of Calculation Method

The stress estimation method in this system is based on the bellow. First, the equation of motion of the bogie frame is expressed by the following equation (1).

$$[M]\{\ddot{u}\} + [C]\{\dot{u}\} + [K]\{u\} = \{f\} \tag{1}$$

M is the mass matrix, C is the viscosity matrix, and K is the stiffness matrix. If □ is the mode matrix obtained by eigenvalue analysis of the equations of motion, then the mass matrix M, the viscosity matrix C, and the stiffness matrix K can be expressed as the modal mass matrix M_ξ, the modal viscosity matrix C_ξ, and the modal stiffness matrix K_ξ as in equation (2)~(4).

$$[\phi]^T[M][\phi] = [M_\xi] \tag{2}$$

$$[\phi]^T[C][\phi] = [C_\xi] \tag{3}$$

$$[\phi]^T[K][\phi] = [K_\xi] \tag{4}$$

Furthermore, the displacement u in physical coordinates can be transformed into a displacement ξ in modal coordinates using a modal matrix, and the external force f can also be transformed into a modalized external force f_ξ.

$$\{u\} = [\phi]\{\xi\} \tag{5}$$

$$[\phi]^T\{f\} = [f_\xi] \tag{6}$$

Using these transformations, the equations of motion in equation (1) are transformed into the equations of motion in modal coordinates shown in equation (7).

$$[M_\xi]\{\ddot{\xi}\} + [C_\xi]\{\dot{\xi}\} + [K_\xi]\{\xi\} = \{f_\xi\} \tag{7}$$

In this equation of motion in modal coordinates, the state variable is defined as equation (8), and the equation of state can be expressed as equation (9).

$$\chi = [\ \dot{\xi}^{(1)}, \xi^{(1)}, \ldots, \dot{\xi}^{(n)}, \xi^{(n)}\ ] \tag{8}$$

$$\chi = \mathrm{A}\chi + \mathrm{GF} \tag{9}$$

The state transition matrix A in the equation(9) is expressed by equation (10).

$$A = \begin{bmatrix} -\frac{c_\xi^{(1)}}{m_\xi^{(1)}} & -\frac{k_\xi^{(1)}}{m_\xi^{(1)}} & 0 & 0 & \cdots & 0 & 0 \\ 1 & 0 & 0 & 0 & \cdots & 0 & 0 \\ 0 & 0 & -\frac{c_\xi^{(2)}}{m_\xi^{(2)}} & -\frac{k_\xi^{(2)}}{m_\xi^{(2)}} & \cdots & 0 & 0 \\ 0 & 0 & 1 & 0 & \cdots & 0 & 0 \\ \cdots & \cdots & \cdots & \cdots & \cdots & \cdots & \cdots \\ 0 & 0 & 0 & 0 & \cdots & -\frac{c_\xi^{(n)}}{m_\xi^{(n)}} & -\frac{k_\xi^{(n)}}{m_\xi^{(n)}} \\ 0 & 0 & 0 & 0 & \cdots & 1 & 0 \end{bmatrix} \tag{10}$$

The modalized external force vector F in the equation (9) is expressed by equation (11).

$$\mathrm{F} = [\ f_\xi^{(1)}\ f_\xi^{(2)}\ \ldots f_\xi^{(n)}] \tag{11}$$

The matrix G in the equation (9) is expressed by equation (12).

$$G = \begin{bmatrix} \frac{1}{m_\xi^{(1)}} & 0 & \cdots & 0 \\ 0 & 0 & \cdots & 0 \\ 0 & \frac{1}{m_\xi^{(2)}} & \cdots & 0 \\ 0 & 0 & \cdots & 0 \\ \cdots & \cdots & \cdots & \cdots \\ 0 & 0 & \cdots & \frac{1}{m_\xi^{(n)}} \\ 0 & 0 & \cdots & 0 \end{bmatrix} \quad (12)$$

For any node q, its displacement is expressed by equation (13).

$$u_{q,i} = \phi_{q,i}^{(1)} \xi^{(1)} + \phi_{q,i}^{(2)} \xi^{(2)} + \cdots + \phi_{q,i}^{(n)} \xi^{(n)} = \sum_{k=1}^{n} \phi_{q,i}^{(k)} \xi^{(k)} \quad (13)$$

By solving this equation, the displacement of each node of the bogie frame can be obtained. To obtain the stress tensor of an element surrounded by a certain node, the conventional procedure is calculating principal stress using the spatial gradient of displacement. And it would have been computationally expensive. We solve this problem by using a mathematical method called affine transformation[2]. We have developed a method to obtain the principal stress directly from the information on the 3-axis displacement of 4 or more nodes by factorizing the deformation to "rigid body motion," "rotation of deformation axis," "strain deformation on the deformation axis (principal strain)"and "rotation on coordinates of deformation axis ".

4 VERIFICATION OF ACCURACY

4.1 Running Test

The running test was conducted by using bolster bogies (distance between axles: 2100 mm, gauge: 1435 mm, maximum width: 2640 mm) on an actual track (running distance 8.5 km) . The running speed during the test was about 40 km/h.

4.2 Overview of the FEM model

Fig. 3 shows an overview of the FEM model of the bogie. The model includes the spring system including the bogie frame, bolster, traction motor and yaw damper, and the model is considered follows:

- the effect of traction motor to the natural vibration mode of the bogie frame,
- the effect of spring system to the response characteristic,
- the characteristics of the bogie.

The bogie frame and traction motor are solid models with tetrahedral quadratic elements. The spring system is modelled using spring elements and damping elements. The air spring is a linear model, and the spring constant and damping coefficient are assumed that it corresponds to the internal pressure. The axle spring was assumed to have a spring constant corresponding to a coil spring and a damping coefficient corresponding to a damping rubber, and the same assumptions were made for the plate spring. The bolster and bogie frame were assumed to have rotational stiffness and damping coefficient corresponding to a center pin. The side bearing was assumed to have contact stiffness and damping coefficient.

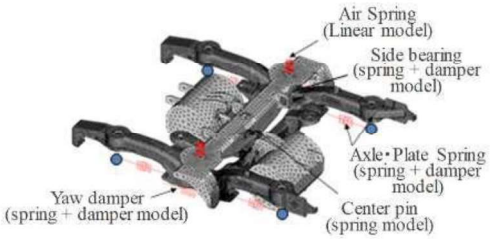

3. Fig. Analysis model

4.3 Verification of Accuracy

A comparison of the vertical displacement of the axle box converted from the acceleration measured in running test and the displacement obtained by this system is shown in Fig. 4. A comparison of their frequency characteristics is shown in Fig. 5. As shown in these figures, the results calculated by the system match well with the measured results, including the overall displacement and the time which the amplitude increases. Furthermore, frequency characteristics are also in good agreement with the test results.

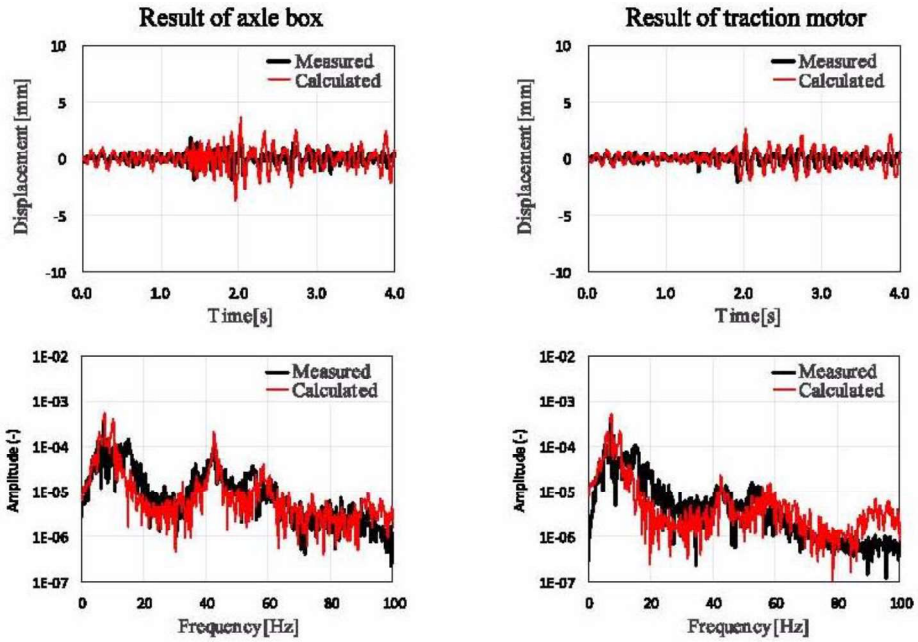

4. Fig. Comparison of calculated result and measurement result

The accuracy of the stresses was also compared. The stress at the joint between the cross beam and the center plate, where the highest stress was observed in the on-track running, was evaluated. The test and calculated results are shown in Fig. 5 and Fig. 6. The time history characteristics of the stresses are in very good agreement between the measured and analytical results.

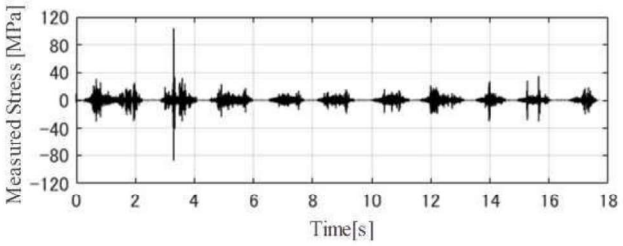

5. Fig. Measured stress

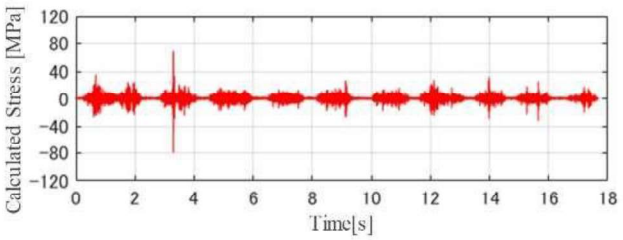

6. Fig. Calculated stress

Using the above stresses, we performed a fatigue life calculation using the cumulative fatigue damage law. This is obtained by summing in each stress range the ratio n_i/N_i of the observed stress frequency to the limit number of crack initiation in the stress range $\Delta\sigma_i$. The cracking is considered to occur when the sum of the cumulative fatigue damage exceeds 1. The results of the fatigue life calculation are shown in Table 1. The results show that the estimated cumulative fatigue damage is about 70% of the measured value. and the prediction is slightly on the risky side. It is confirmed that the system can predict the life with sufficient accuracy.

Table 1 Comparison of fatigue life

	Measurement	Calculated
cumulative fatigue damage	3.77×10^{-6}	2.49×10^{-6}
life distance	225million km	341 million km

5 REFERENCE TO STATIC LOAD TEST CONDITIONS

5.1 Identification of dominant vibration modes on-track running

Using the stress estimation method, the dominant motion modes that occur during running were examined. We focused on the vertical motion of the traction motor, which is a representative component in strength design. First, the main deformation modes were calculated by eigenvalue analysis using FEM. The calculated modes are shown in Fig. 7. The modes in Fig. 7 (a) and (b) are deformation modes which the left and right side beam are in opposite phases and the bogie frame twists. The mode in Fig. 7 (c) is a deformation mode which the left and right side beam and the traction motor swing in opposite phases. In the case of (a) and (b), the two traction motors are in phase, and in

the case of (c), the traction motors are in opposite phase. In this paper, the modes (a) and (b) are referred to as the motor in-phase mode and the mode (c) as the motor opposite phase mode, and these three natural vibration modes are collectively referred to as the vertical vibration modes of the traction motor.

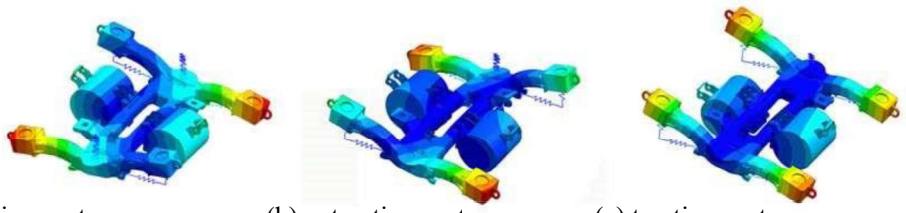

(a) traction motor in-phase vibrate + torsion of bogie frame (in-phese to tractuin motor)

(b) traction motor in-phase vibrate + torsion of bogie frame (opposite phese to traction motor)

(c) traction motor opposite phase vibrate + pitching of bogie frame

7. Fig. The main deformation modes calculated by eigenvalue analysis

Next, to identify the key vibration modes, the acceraration calculated by using overall natural vibration modes was compared with the acceraration for each of the above modes In Fig. 8, mode (a) and (b) were found to be dominant, and in Fig. 9, mode(c) was found to be dominant during in this time period.

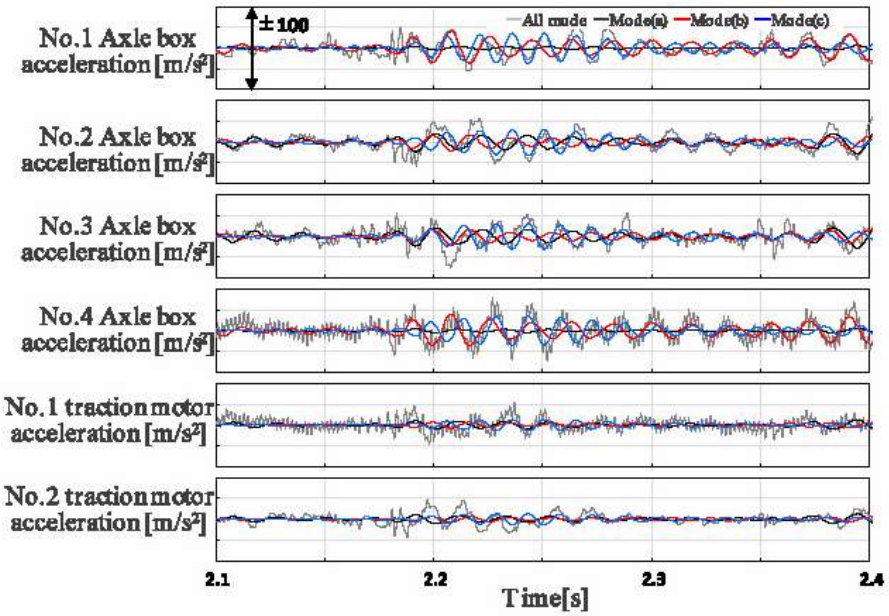

8. Fig. Comparison of acceraration in overall modes and acceraration in each modes.(mode (a) and (b) is dominant)

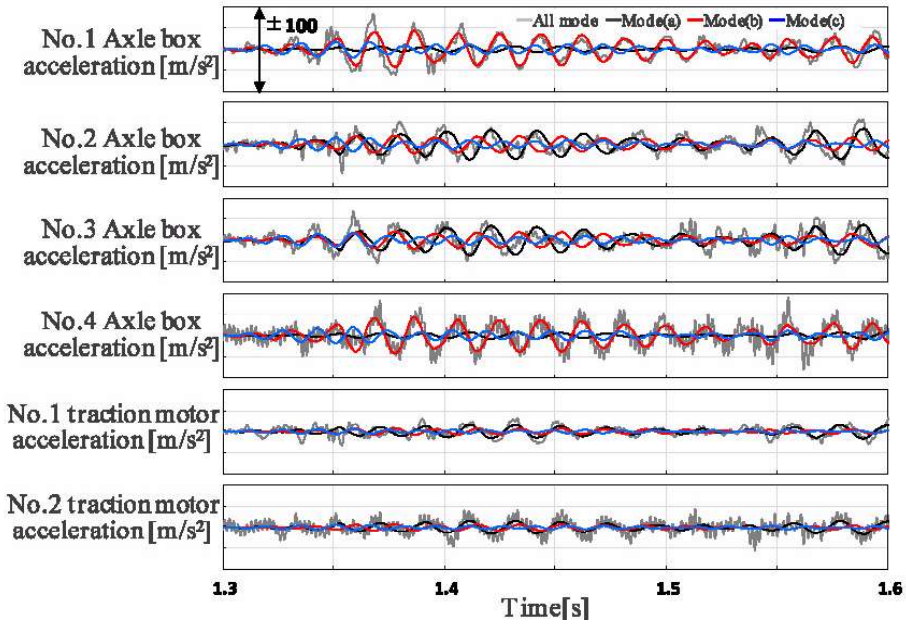

9. Fig. Comparison of acceraration in overall modes and acceraration in each modes.(mode (a) and (b) is dominant)

5.2 Occurrence of loads due to major vibration modes

We evaluated the correspondence between the vertical vibration modes of the traction motor and the typical load modes in static load tests [3]: (1) traction motor in-phase mode, (2) traction motor opposite phase mode, and (3) bogie frame torsion mode. The vibration mode (c) was not included because it exhibited side-beam pitching which is different from the deformation caused by the three loading modes described above. Comparison of the vertical vibration modes of the traction motor with the typical loading modes of the static load test was performed as follows.

First, the displacements of two air spring seats at the time when the displacement of the traction motor reached a minimum value were obtained, and the 4 points of rotation angles on cross beam generated by loading were calculated. Next, a static analysis equivalent to the JIS static load test was conducted to determine the rotation angles at the four points on the cross beam. Using these displacements and rotation angles, the ratio of the loading modes of the static load test were calculated to represent the vertical vibration modes of the traction motor was obtained using equation (14) and (15).

$$\{y_i^j\} = a\{x_i^1\} + b\{x_i^1\} + c\{x_i^1\} + d \tag{14}$$

$$a, b, c \geq 0 \tag{15}$$

y represent the rotation angle obtained from dynamic analyses and x represent from static analyses, and the subscript i represents the position of the evaluation point and j represents the vibration mode (mode 7 or 8). x_1 represent displacements corresponding to traction motor in-phase mode in the static load test, and x_2 represent traction motor opposite phase mode, and x_3 represent bogie frame torsion mode.

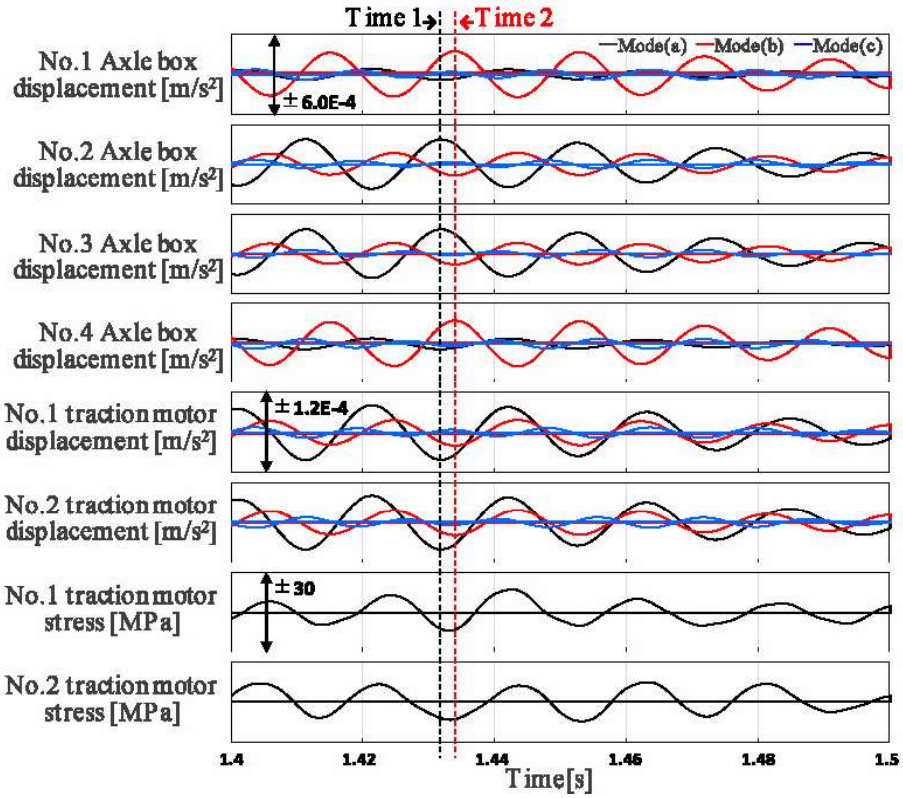

10. Fig. Comparison of acceraration in on-track running and acceraration in each modes.(mode (c) is dominant)

The results obtained in equation (14) can be a combination of static load mode multiplied by sign of rotation angle in the dynamic analysis, and among these combinations, the one with the largest coefficient of determination (R2) for a, b, c ≥ 0 was selected. From these regression coefficients, the ratio of the coefficients for each static load mode(a, b, c) was calculated as the contribution ratio of each load mode. The regression coefficients and contribution ratios are shown in Table2. The strain energy distribution for each vibration mode is shown in Fig. 11, and the Mises stress distribution during static load analysis is shown in Fig. 12, along with the deformation diagrams. From these tables, it is confirmed that mode (a) has a large contribution from the bogie frame torsion mode, and mode (b) has a large contribution from the traction motor opposite phase mode.

Table2 Regression coefficients and distribution ratios

Modes of dynamic analisys \ Modes of static load		Traction motor in-phase mode	Traction motor opposite phase mode	Bogie frame torsion mode
Mode (a)	Degression coefficient	0.359	0.000	2.707
	distribution ratio	0.12	0.00	0.88
Mode(b)	Regression coefficient	0.968	0.000	0.176
	Distribution ratio	0.85	0.00	0.15

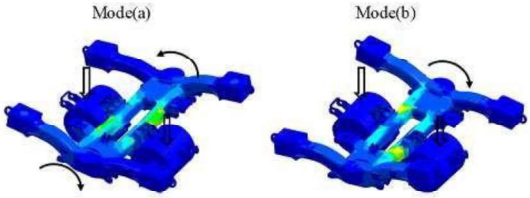

11. Fig. Strain energy distribution for each vibration mode

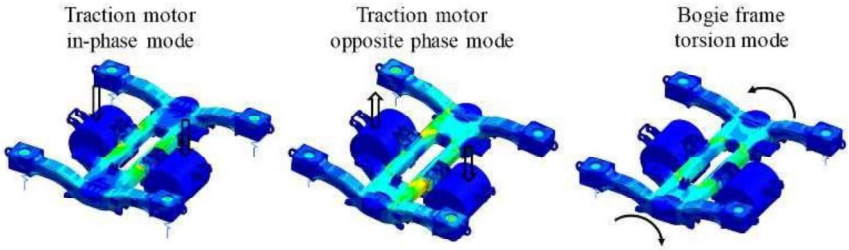

12. Fig. Mises stress distribution during static load analysis

6 CONCLUDING REMARKS

Improving the reliability of bogie frames needs measurement of stress for a long time, but usual method could not measure it for a long time. Therefore, a new stress estimation method using the vibration characteristics of the bogie frame has been constructed. It was confirmed that the displacement and stress of the bogie frame calculated by this system coincided with the measured values. Moreover, the cumulative fatigue damage and the life distance predicted by the system were about 70% of those by using the measured values. Next, the possibility to extract the contribution ratios of each vibration mode during running by using this system was shown. Furthermore, as a result of evaluating the correspondence between the vertical vibration modes of the traction motor and the deformation modes in static load tests, the possibility to decompose the vibration modes into static load modes was shown.

7 REFERENCES

[1] Osamu Kondo, Yoshiyuki Shimokawa, Takahiro Fujimoto, A study on transient dynamic analysis for railway bogie frame stress in consideration of axle box vibration acceleration as the input, Proceedings of J-Rail2011, S1-2-1, PP.147-150, 2011

[2] Ken Anjo, Hiroyuki Ochiai, Mathematical Basics of Motion and Deformation in Computer Graphics, Morgan & Claypool Publishers

[3] Rolling stock - Bogie - Strength test - Part 1: Methods for static load testing, JIS E 4208-1:2021

DEVELOPMENT OF UNIVERSAL RAILWAY BOGIES FOR AUTONOMOUS TRACTION MODULES

Sergey V. MYAMLIN and Frantishek BURES

JSC "Ukrainian Railways"
Svyatoshinska str. 13, Kyiv, Ukraine

Received: September 5-8, 2022

ABSTRACT

The development of advanced vehicles, as well know, requires the use of innovative technical solutions for the design. Autonomous traction modules are already being actively used on some railway lines and continue to be used in both passenger and freight transportation on the railways.

The authors have developed conceptual technical solutions for the designs of bogies for autonomous traction modules, which can be used to transport trains in the intercontinental traffic Europe - Asia - the Far East. The main features of the proposed bogies include the following advantages: the possibility of using different gauge standards on railways, improved dynamic qualities, an individual braking system, and an increased resource. The main structural elements are designed taking into account the shortcomings of standard designs, which can significantly improve both the technical characteristics and the economic efficiency of their use in interstate traffic.

The report presents a mathematical model of the dynamics of a rail vehicle with the new type of bogies and the results of theoretical studies of the dynamic qualities of autonomous traction modules with universal bogies.

Analysis of the research results indicates the correctness of the chosen technical solutions.

Thus, the authors proposed technical solutions and the results of theoretical studies of the dynamics of universal bogies for railway autonomous traction modules, which take into account promising operating conditions and interoperability requirements for various railways.

Keywords: bogie, railway rolling stock, autonomous traction module, dynamic model

1 INTRODUCTION

The development of promising vehicles for railway transport, as you know, requires the use of innovative technical solutions for the design. This applies to both the design of cars and the design of railway traction rolling stock. Autonomous traction modules are already being actively used on some railway lines and continue to be used in both passenger and freight transport on the railways. Although autonomous traction modules are most widely used on passenger rail lines (monorail transport, railway lines or subways), which are used, as a rule, at airports or on urban railway lines. But the development of freight traffic in domestic and international traffic imposes new technical requirements on the design of the rolling stock. And, as you know, the formation of the dynamic qualities of the entire vehicle depends on the characteristics of the chassis, in this case, the bogies of the autonomous traction module.

The authors have developed conceptual technical solutions for the design of bogies for autonomous traction modules, which can be used to transport trains in the intercontinental traffic Europe - Asia - the Far East. Previously, the authors considered the solution of scientific and technical problems for the creation and improvement of rolling stock of railways [1-3], including problems related to the creation of autonomous traction modules [4-7]. In this study, the authors focus on the consideration of the dynamic qualities of autonomous traction modules with two-axle bogies of the original design.

The main features of the proposed bogies include the following advantages: the possibility of operating on railways of various gauge standards, improved dynamic qualities, an individual braking system, and an increased resource. The main structural elements have been developed taking into account the shortcomings of standard structures, which can significantly improve both the technical characteristics and the economic efficiency of their use in interstate traffic.

Next, we give a brief description of the mathematical model of the dynamics of a rail vehicle in the form of an autonomous traction module with an original design of bogies.

2 THE MAIN PART OF RESEARCHES

The mechanical scheme of a four-axis autonomous traction module can be represented as a system of the following elements: a body, bogies and wheelsets. The body of the autonomous traction module is mounted on 2 two-axial bogies. The connections of the body with the frame of the bogie provide the possibility of turning the bogies relative to the body in a horizontal plane, which creates a moment of friction necessary to dampen the oscillations of the wobbling of the bogies (center connection). To limit the vibrations of the body relative to the bogies in the vertical plane, sliders are installed on the frames of the bogies [1-3].

The main elements of a two-axle bogie are wheelsets and a frame. The two-axle bogie is equipped with an individual traction drive for each axle with a support-axial suspension of the engine. The design of the bogie has axle box (first stage) and central (second stage) spring suspension using elastic elements and vibration dampers. Axle spring suspension provides support for the bogie frame on each axle box through two packages of coil springs. To dampen vertical vibrations, a hydraulic vibration damper is installed parallel to the springs between the axle boxes and the bogie frame, one per axle box assembly. The body rests on the side parts of the bogie frame through sets of double-row coil springs. Deviations of the bogies relative to the body in the transverse direction are limited by elastic side stops located in the middle of the side-frame on the outside of the bogies, that is, the characteristic of the transverse connection of the body with the bogies is essentially non-linear.

The movement of an autonomous traction module along an elastic-viscous-inertial railway track is considered, which is modeled by a mass reduced to each wheel (eight reduced masses), which has only vertical and transverse horizontal displacements and rests in these directions on springs and viscous friction dampers, modeling elastically - dissipative properties of rails and rail base.

The calculation scheme of an autonomous traction module is built as a mechanical system, which consists of nineteen solid bodies: a body, two frames, four engines, four wheelsets and eight reduced track masses, having only vertical and transverse horizontal displacements. Thus, in general, the system has $11\times6+8\times2=82$ degrees of freedom.

When describing the movement of the autonomous traction module under consideration along sections of the path of an arbitrary shape, we choose a fixed coordinate sys-

tem $\widetilde{O}\xi\eta\zeta$, and for each rigid body – two moving coordinate systems: natural $Oxyz$ and associated with a rigid body $Cx'y'z'$ (Cx', Cy', Cz' – are the main central axes of inertia). We will accept all coordinate systems as right, and we will assume that the axes $\widetilde{O}\xi$, Ox, Cx' – are directed from left to right, and the axes $\widetilde{O}\zeta$, Oz, Cz' – are directed downwards (Fig.1).

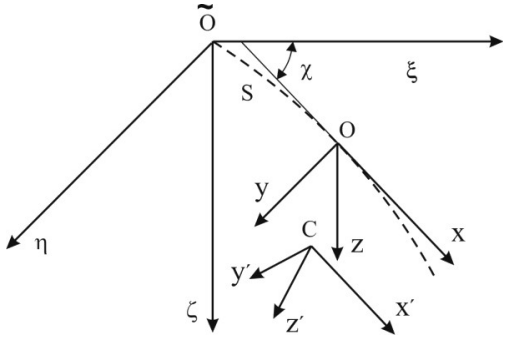

Fig.1. Mathematical model coordinate system:
$\widetilde{O}\xi\eta\zeta$ – fixed coordinate system;
$Oxyz$ – moving natural coordinate system;
$Cx'y'z'$ – moving coordinate system associated with a rigid body;
S – trajectory of autonomous traction module;
χ – angle between axles $\widetilde{O}\zeta$ and Ox.

The axes of the natural coordinate system are directed respectively along the tangent, normal and binormal to the axis of the path. The origin of coordinates O for each rigid body is located at a distance from its position at the initial moment of time (here, s – the distance traveled). The position of the natural coordinate system relative to the fixed one is characterized by an arc coordinate along the track axis s, the angle χ between the axes Ox and $\widetilde{O}\xi$ in the plan, as well as the angles φ_h and θ_h between these axes in vertical planes, which are determined by the elevation of the outer rail. The rail parameters χ, h_r are given functions of the coordinate s, for a circular curve $\dot{\chi}$ and h_r are constant, for a straight line they are equal to zero [4].

When deriving the equations of motion, the generally accepted notation for the displacements of individual bodies of the system was used – $x, y, z, \psi, \varphi, \theta$ [5]. Translational movements x, y, z and angles of rotation ψ, φ, θ describe, respectively, twitching, lateral drift, bouncing and wobbling, galloping, and side rolling of a solid body.

When designating the coordinates of the rigid bodies of the system, the following indices were introduced: body – f, bogie frame – sl (l =1,2), engines – b ($b=\overline{1,4}$), wheelset – i ($i=\overline{1,4}$ – number of the wheelset in the motion direction of the vehicle), wheel – ij (j =1 – left side of the autonomous traction module, j=2 – right side), rails at the points of contact – rij.

When compiling the equations of locomotive motion, the following design features are taken into account:

- the action of dry friction forces arising from the mutual movements of the body and the bogie in the plan;

- elastic-viscous connection of the body with the bogie frame;

- nonlinear characteristic of the force in the center plate knot;

- elastic-viscous connection of the bogie frame with wheelsets;

- the presence of an additional connection between the bogie frame and the axle of the wheelset, caused by the presence of engines with support-frame suspension;

- curvilinearity of the profiles of the rolling surfaces of the wheel and rail, as well as the nonlinearity of the forces of interaction between them.

To determine the number of degrees of freedom of the considered mechanical system, the restrictions imposed on the movements of bodies due to generally accepted assumptions and design features of the running gears of an autonomous traction module are taken into account [6].

Vertical movements and lateral rolling of wheelsets are expressed through vertical movements of the wheels:

$$z_i = \frac{z_{i1} + z_{i2}}{2}; \quad \theta_i = \frac{z_{i2} - z_{i1}}{2d_1}; \ (i = \overline{1,4}), \tag{1}$$

where $2d_1$ – the distance between the average wheelset rolling circles.

It is assumed that the radii r of the rolling circles of all wheels are equal to each other. Then, if the longitudinal planes of symmetry of the track and the bogie coincide, when the car moves along the axis of the track, all the wheels will turn by the same angle:

$$\varphi_i = -\frac{x_i + s}{r}, \ (i = \overline{1,4}). \tag{2}$$

Engines in all directions, except galloping, move together with the bogie frame:

$$\begin{aligned} x_{sl} &= x_b; \\ y_{sl} &= y_b; \\ z_{sl} &= z_b; \\ \theta_{sl} &= \theta_b; \\ \psi_{sl} &= \psi_b \quad (b = \overline{1,4}). \end{aligned} \tag{3}$$

Taking into account relations (1) – (3), the system "autonomous traction module - rail track" has 82–32=50 degrees of freedom.

The generalized coordinates describing the configuration of the considered mechanical system are chosen as follows:

$$q_1 = y_f; \quad q_2 = y_{s1}; \quad q_3 = y_{s2}; \quad q_4 = y_1; \quad q_5 = y_2;$$
$$q_6 = y_3; \quad q_7 = y_4; \quad q_8 = \psi_f; \quad q_9 = \psi_{s1}; \quad q_{10} = \psi_{s2};$$
$$q_{11} = \psi_1; \quad q_{12} = \psi_2; \quad q_{13} = \psi_3; \quad q_{14} = \psi_4; \quad q_{15} = \theta_f;$$
$$q_{16} = \theta_{s1}; \quad q_{17} = \theta_{s2}; \quad q_{18} = z_f; \quad q_{19} = z_{s1}; \quad q_{20} = z_{s2};$$
$$q_{21} = \varphi_f; \quad q_{22} = \varphi_{s1}; \quad q_{23} = \varphi_{s2}; \quad q_{24} = x_f; \quad q_{25} = x_{s1};$$
$$q_{26} = x_{s2}; \quad q_{27} = x_1; \quad q_{28} = x_2; \quad q_{29} = x_3; \quad q_{30} = x_4;$$
$$q_{31} = \varphi_{b1}; \quad q_{32} = \varphi_{b2}; \quad q_{33} = \varphi_{b3}; \quad q_{34} = \varphi_{b4};$$

$$q_{35} = y_{r11}; \quad q_{36} = y_{r12}; \quad q_{37} = y_{r21}; \quad q_{38} = y_{r22}; \quad q_{39} = y_{r31};$$
$$q_{40} = y_{r32}; \quad q_{41} = y_{r41}; \quad q_{42} = y_{r42}; \quad q_{43} = z_{r11}; \quad q_{44} = z_{r12};$$
$$q_{45} = z_{r21}; \quad q_{46} = z_{r22}; \quad q_{47} = z_{r31}; \quad q_{48} = z_{r32}; \quad q_{49} = z_{r41};$$
$$q_{50} = z_{r42}.$$

The differential equations of motion of a four-axis autonomous traction module as a complex mechanical system are composed in the form of Lagrange equations of the second kind [7-9]:

$$\frac{d}{dt}\left(\frac{\partial T}{\partial \dot{q}_i}\right) - \frac{\partial T}{\partial q_i} + \frac{\partial \Pi}{\partial q_i} + \frac{\partial \Phi}{\partial \dot{q}_i} = Q_i + S_i^*, \quad (i = \overline{1,50})$$

where T and Π – kinetic and potential energies of the system;

Φ – scattering function;

$q_i, \dot{q}_i$ – generalized coordinates and their velocities;

Q_i – the corresponding generalized forces that do not have the potential;

S_i^* – applied external forces.

The external forces S_i^* acting on the autonomous traction module are the traction force F_T developed by the autonomous traction module, the braking force B_T that occurs when the brakes are applied, and the movement resistance forces W, which include all other external forces.

In the general case, external forces acting on an autonomous traction module can be represented as

$$S_i^* = W_i + B_i + F_T,$$

where W_i – force of resistance to translational motion applied to the i-th rigid body;

B_i – braking force applied to the i-th rigid body;

F_T – traction force of an autonomous traction module.

After substituting the expressions for kinetic and potential energies, scattering functions and generalized forces into the Lagrange equations, a system of nonlinear differential equations was obtained that describes the movement of a four-axle autonomous traction module along straight and curvilinear sections of the track and is a system of ordinary nonlinear differential equations 100-order [10].

To conduct theoretical studies using this mathematical model, the authors developed a special computer program for calculations, on which the necessary calculations were performed. As a result of the calculations, the parameters of the spring suspension of the bogies were determined from the conditions for ensuring the maximum speed of movement and the minimum indicators of dynamics. This made it possible to develop recommendations on the choice of parameters for autonomous traction module bogies for further practical implementation and commissioning.

3 CONCLUDING REMARKS

Thus, the authors have developed conceptual technical solutions for the designs of bogies for autonomous traction modules, which can be used to transport trains in intercontinental traffic.

This study describes a mathematical model of the dynamics of a rail vehicle with two-axle bogies for subsequent theoretical studies of the dynamic qualities of autonomous traction modules with universal bogies of the original design.

The authors also proposed technical solutions and a mathematical model for theoretical studies of the dynamics of universal bogies for railway autonomous traction modules, which take into account promising operating conditions and interoperability requirements for various railways. The proposed technical solutions and a mathematical model of the dynamics of an autonomous traction module can be used to create new designs of railway rolling stock and modernize existing structures.

4 REFERENCES

[1] Myamlin, S. V. - Neduzha, L. O. Design improvement of the locomotive running gears. Science and Transport Progress, 2013, vol. 5 (47), p. 124-136. doi: 10.15802/stp2013/17977

[2] Myamlin, S. V. - Lunys, O. - Neduzha, L. O. Peculiarities of running gear construction of rolling stock. Science and Transport Progress, 2017, vol. 3 (69), p. 130–146. doi: 10.15802/stp2017/104824

[3] Spiryagin, M. - Wolfs, P. - Cole, C. - Spiryagin, V. - Sun, Y. Q. - McSweeney, T. Design of Mechanical Systems of Locomotives from: Design and Simulation of Heavy Haul Locomotives and Trains. CRC Press, 2016, 477 p.

[4] Radchenko, N. A. Krivolineynoye dvizheniye relsovykh transportnykh sredstv [Curvilinear motion of railway vehicles]. Kyiv: Naukova dumka, 1988, 212 p.

[5] Lazaryan, V. A. Dinamika transportnykh sredstv [The dynamics of vehicles]. Kyiv: Naukova dumka, 1985, 528 p.

[6] Garg, V. - Dukkipati, R. Dynamics of Railway Vehicle Systems. Toronto : Academic press, 1984, 407 p.

[7] Domin, Y. V. - Dlugach, L. A. - Korotenko, M. L. - Markova, O. M. Auto oscillations and motion stability of rail vehicles. Kyiv: Naukova dumka, 1984, 160 c.

[8] Myamlin, S. V. Modeling of the railway vehicle dynamics. Dnipropetrovsk: Novaya ideologiya, 2002, 240 p.

[9] Myamlin, S. - Dailidka, S. - Neduzha, L. Mathematical Modeling of a Cargo Locomotive. Proceedings of 16th International Conference - Transport Means, Kaunas, 2012, p. 310-312.

[10] Bures, F. Mathematical model of spatial oscillations of a railway four axle autonomous traction module. Collection of scientific works of the Ukrainian state university of railway transport, 2020, vol. 194, p. 52-65. https://doi.org/10.18664/1994-7852.194.2020.230168

SUSPENSION FAILURE DETECTION IN RAILWAY BOGIES USING ARTIFICIAL NEURAL NETWORK

[1]Ravi Kumar, [1]Om Prakash Yadav, [2]Manish Pandey, [1]Nalinaksh S. Vyas

[1]Dynamics & Vibration Laboratory, Department of Mechanical Engineering
Indian Institute of Technology Kanpur
Kanpur (U.P.), India
[2]Rolling Stock Workshop, Government of India, Ministry of Railways
Charbagh, Lucknow (U.P.), India

Received: August 5. 2022

ABSTRACT

With an increasing demand for economical and faster transportation, there have been continuous efforts by the railway sector to increase the speed of trains. Adoption of LHB coaches equipped with FIAT bogies, capable of running up to 120 kmph, for mainline passenger trains by the Indian Railway is no exception. Increased speed however leads to large dynamic forces and non-reliability of track and train elements. Frequent failures of primary and secondary suspension are recently reported in FIAT bogies used in the coaches of passenger trains of Indian Railway. Early prediction of such failures or unacceptable degradation of components using condition-based monitoring is the best approach to avoid interruption and downtime. This study attempts to diagnose the suspension faults present in the FIAT bogie using an artificial neural network approach. A detailed multi-body dynamic model of complete LHB coach is modelled in SIMPACK software. Transient simulations are performed for the train running at a speed of 120 kmph for 30 seconds. Track irregularities for 0.3 kms sections obtained from field test data are incorporated to simulate real-time dynamic forces. Numbers of virtual accelerometer sensors are incorporated on the coach floor and at the axle box to capture the transient vertical vibration response of the coach. Simulations are carried out for the cases with and without suspension faults on bogie. Different faults such as, primary spring failure, damper failure, secondary spring failure and combination of them, are included. Simulated vibration responses are used to train and validate a Feed Forward Artificial Neural Network (ANN) architecture. It correlates the acceleration features with type of suspension faults. The proposed approach satisfactorily predicted the faults and can be used to diagnose the suspension faults of LHB coaches.

Keywords: LHB Coaches, Rail-wheel contact (FASTSIM), Suspension system failure, Artificial Neural Network architecture, Residual error estimation

1 INTRODUCTION

A previous report published by Indian Railway on accidents over five years shows that 75%-85% of the total accidents [1] occurred due to human errors during manual inspection. Higher operational speed of the trains induces large dynamic forces, causing degradation of track and vehicle elements [2]. Preventive maintenance strategies used for periodic inspections of components [4], irrespective of the components condition, costs huge financial burden and downtime. Again, faults induction between two consecutive periods of inspection are not identifiable with such strategies. Therefore, real time condition monitoring of components is important for fault identification and to take necessary actions to avoid any catastrophic failure [5].

Bogies of a railway train being the intermediate equipment, transmitting and managing rail-wheel contact forces, inertial forces, coupler forces, etc., their components are subjected to large dynamic forces [6]. These continuous dynamic forces lead to repetitive loading and unloading of bogie components and cause fatigue failures [7]. Frequent failures of primary and secondary suspension elements of FIAT bogies, used in the passenger coaches, are recently reported by Indian Railway [8]. An example of a failed primary spring assembly, consisting of an outer and an inner spring is shown in Figure 1. these

failures lead to the progressive failure of other suspension elements and eventually causing suspended operation of the trains to avoid the catastrophic failure, if identified earlier.

Figure 1 (a) Broken inner and outer spring of primary suspension, (b) Exploded view of outer spring failure

Various reasons of suspension elements failure; especially spring failures can be identified as degraded stiffness and damping parameters, manufacturing defects, inadequate force management, etc. [9]. As an effort to reduce suspension failures and to improve ride comfort, Bideleh [10] and Johnsson et al. [11] performed studies on optimization of design parameters of suspension elements. Kumar et al. [8] recently proposed few geometrical modifications in existing primary suspension spring to improve the fatigue life. Fully flexible finite element model of bogie was developed for improved accuracy in estimation of dynamic behaviour. Minimal changes in spring geometry are proposed, requiring no changes in the designs of associated assembly components and in manufacturing set-up. Dimitriu [12] analysed vertical dynamics of a railway bogie under asymmetric damping. Interference of various vibration modes and their effects on vertical vibrations are discussed in detail. A recent study by Qazizadeh et al. [13] proposed a replacement of vertical dampers with actuators and used skyhook method to calculate reference forces. Proposed modifications resulted in better ride comfort and vertical displacements.

Hamed et al. [14] analysed the effects of spring degradation behaviour on suspension performance on a road vehicle. Also, they have used frequency response function (FRF) approach to detect these degradation faults and stated that FRF can effectively detect such faults. Hayashi et al. [15] demonstrated the possibility of detecting suspension failure using a multiple model approach. Mode probabilities and suspension system states are estimated using Kalman filter. The bogie system was modelled mathematically, and the study was basically focused on lateral damper failure.

Mei et al. [16] analysed a railway bogie suspension system under damper degradation conditions, using a nine degree of freedom dynamic model. Proposed dynamic model is effective in assessing dynamic response variations with the variations in primary dampers. However, it does not consider coupled effects of lateral and yaw damper, as needed to accurately estimate the response due to the secondary suspension system. Thus, Mathias

et al. [17] extended this model by incorporating lateral and yaw dampers to analyze dynamic response and to detect the faults in secondary suspension system. A Kalman filter was used to detect and isolate the faults present in the suspension systems. Ye et al. [18] developed a vehicle simulation model using commercial MBD software to identify the suspension faults by applying combination of MPE-LLTSA and validated the simulation results with test results. They showed that the proposed data-driven approach, MPE-LLTSA can accurately identify the suspension faults. Wu et al. [19] proposed a group convolutional network to assign group of signals with similar patterns to different channels. These individual channels are characterized by different specific groups of neurons to improve the accuracy in fault classification than normal convolution techniques.

Various fault detection approaches ranging from linear mapping-based filtering techniques such as Kalman filter to non-linear mapping based artificial neural networks are popularly used for identification of bogie suspension faults [20]. However, the behaviour of rolling stock components is highly non-linear and complex. Artificial neural networks can closely map the nonlinearities [23]. Therefore, artificial neural network-based approaches are more accurate in predictions of such faults.

Because of essence and interest of worldwide railway community to adopt real time condition monitoring of such crucial components, this study aims to develop a condition monitoring methodology to predict suspension failures of a railway bogie. This paper proposes a methodology of measuring vibration signatures and mapping its characteristic features using artificial neural networks (ANN) for accurate prediction of suspension faults. A proposed ANN model is trained without and with faults in suspension elements by varying stiffness and damping coefficients of primary and secondary suspension elements.

2 MULTI-BODY DYNAMIC MODEL

To study the dynamic response of a railway bogie in the presence of different faults in bogie suspension elements, a SIMPACK model is built. The car body and various bogie structures are treated as a rigid body. Kinematic and dynamic parameters (e.g. inertia, mass) are estimated from the CAD models of LHB coach and FIAT bogie, used in Indian passenger trains. The multi-body dynamic model consists of all important bodies, appropriate joints and constraints, suspension elements, rail-wheel interaction and track excitations. Simulations are carried out at vehicle speed of 120 km/h. Developed model is used to generate the vertical acceleration signals without and with faults in primary and secondary suspensions. SIMPACK model of vehicle and sensors' locations are presented in Figure 2.

As seen in Figure 2, four acceleration probes are mounted on the bogie frame (SA1, SA2, SA3, SA4); just above the axle-boxes [24], two acceleration probes (SB1, SB2) are mounted on the bolster beam; above the secondary suspension. Eight additional sensors; four sensors on the coach floor at the extreme ends (SE1, SE2, SE3, SE4) of the coach and four sensors are mounted around the centre (SM1, SM2, SM3, SM4) of the coach.

Figure 2 Simpack MBD model and sensors locations

2.1 Bogie model

To represent the close characteristics of a FIAT bogie, MBD model of bogie consists of a bogie frame, a bolster, two wheelsets, four primary spring-damper elements, two secondary spring-damper elements, a lateral damper and two yaw dampers. Spring and damping coefficients of primary suspension are 1.22×106 N/m and 6×105 N.s/m respectively. Spring and damping coefficients of secondary suspension are 4.3×105 N/m and 2.5×104 N.s/m respectively.

2.2 Rail track model

UIC 60E1 rail profiles and S1002 wheel profiles are considered in accordance with Indian railway's wheel-track designs. The measured rail irregularities shown in Figure 3 spanning 0.3 kms of straight track are repeated to form a total track length of 1 km.

2.3 Rail-wheel contact

FASTSIM algorithm is chosen to accurately model the rail-wheel contact forces. To validate the model, analytical kinematic frequency of wheelset is compared against the kinematic frequency of wheelset estimated from SIMPACK model.

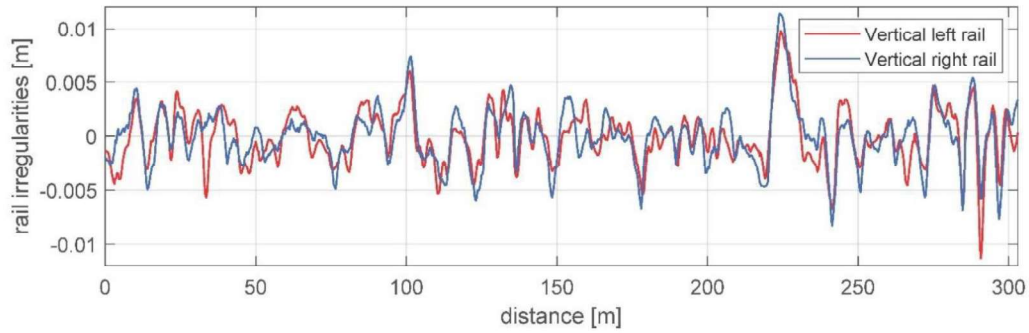

Figure 3 Measured rail-track irregularities over 304 meters

2.4 Modelling Suspension Faults

Over the time, spring, damper, and connection elements of suspension system lose their effectiveness due to degradation of structural properties such as, degradation of spring stiffness, connections loosening, leakage of damper fluid, etc., under fatigue loading [14]. A fault in the suspension system is defined such as the equivalent parameters fall outside the acceptable values. In this study, equivalent damping and stiffening parameters are considered as the indicators of the concerned element condition. Multi-body dynamic simulations for a total of eight such combinations of the stiffness and damping parameters are chosen (presented in Table 1). Where, degraded value is assumed as degraded value = Normal value × 10^{-10}.

Table 1 Fault combinations

Fault ID	Primary Suspension fault			Secondary Suspension fault		
	Equivalent stiffness	Equivalent damping	Fault presence	Equivalent stiffness	Equivalent damping	Fault presence
Fault0	Normal	Normal	No	Normal	Normal	No
Fault1	Normal	Degraded	Yes	Normal	Normal	No
Fault2	Degraded	Normal	Yes	Normal	Normal	No
Fault3	Degraded	Degraded	Yes	Normal	Normal	No
Fault4	Degraded	Degraded	Yes	Degraded	Degraded	Yes
Fault5	Normal	Normal	No	Degraded	Degraded	Yes
Fault6	Normal	Normal	No	Degraded	Normal	Yes
Fault7	Normal	Normal	No	Normal	Degraded	Yes

3 ARTIFICIAL NEURAL NETWORK FOR FAULT DETECTION

To capture the nonlinear effects, neural networks are used which can map the nonlinear effects precisely. Generally, convolution based deep neural networks are used for the prediction and classification of faults which is a complex network and requires large computational time. This study therefore uses a simple feed-forward back propagation neural network approach. The ANN model in this study comprises a series of two networks. Where, the first stage network is used for estimation of parameters and errors, in second stage, these estimates were fed into the neural network for identifying and classifying the faults. Figure 4, represents the flow diagram of various steps followed in identification and classification of the faults using proposed scheme.

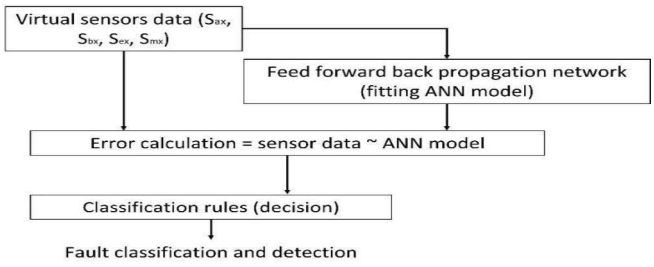

Figure 4 Flow diagram of the proposed approach

3.1 Fitting model (ANN1)

To accommodate the time shift, three different set of simulations with random time delay for all the sensors and for each fault category were carried out. The sensors responses were pre-processed to discard the higher frequency (over 100 Hz) content present in the data. The data is then normalized about mean and standard deviation, Eqn. (1).

$$x_i = \frac{x_i - x_{mean}}{x_{std.dev}} \tag{1}$$

After the pre-processing of time series data, it was then fed into a tri-layered ANN network, with 35-20-18 neurons sequence, to fit a non-linear input-output model. The Bayesian regularization propagation algorithm is to optimize the training performance as it can efficiently preserve the model generality.

3.2 Categorical Classification strategy (ANN2)

The presence of faults corresponding to the parameter's degradation over the time, usually results in terms of slight deviation in the dynamic behaviours. This deviation in form of rms residual error [25] between fitted ANN response of each of the fault category and fitted ANN response of healthy suspension are calculated by moving rms method, shown in Eqn. (2).

$$\left.{}^{F_j}_{F_0}E_{avg}(i)\right]_{S_x} = \frac{1}{N_s}\sum_{k}^{N_s-1}\frac{\left\{y_{nn}^{F_0}(i-k) - y_{nn}^{F_j}(i-k)\right\}^2}{\left(y_{nn}^{F_0}(i-k)\right)^2} \tag{2}$$

Where, y_{nn} is the model response of the ANN, F_c is the fault condition, N_s is the number of samples considered for the moving window L and S_x is the number of sensors.

The approach adopted in this study, assumes that a fault can be detected when the computed residual for each set falls over a threshold value $T_{\%}$, occurring more than a threshold number n, during sliding window of length L. The predicted classification variable $C_{T\%}$ from Eq. (3) is used to decide the condition of the suspension components.

$$C_{T_{\%},L,n} = \begin{cases} 1\ (fault) & if\ E_{avg,L}(j) > T_{\%} \quad \forall j \in [i; i - n \times L_s] \\ 0\ (no\ fault) & otherwise \end{cases} \tag{3}$$

Where, x is integer penalty value corresponds to fault condition, varies from 1 to 7

The second stage network uses these residual error signals as input for each of the fault case (8 × 14). Output layer carries 14 neurons and uses the 'SoftMax' activation function, and all hidden layers use ReLU activation function. Proposed architecture in Figure 5 comprises two stages: (1) Sensor data estimation with ANN and (2) Classification of condition based on active residual deviation from the normal condition.

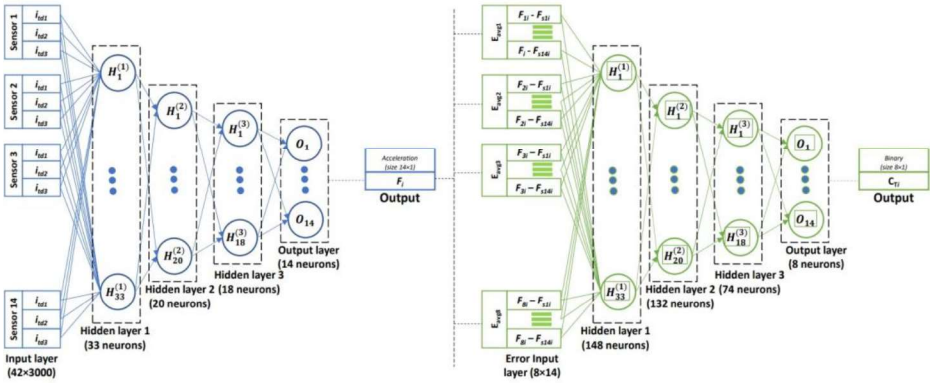

Figure 5 Proposed ANN architecture

4 RESULTS

In Figure 6, the developed ANN model results and the Simpack model results were compared. It can be seen that the developed model provides a close agreement between simulated acceleration response obtained from sensor and estimated acceleration response from ANN model. For the classification decision variables, emphasis was given to the residual deviation of response during the presence of faults, compared to the response of healthy components.

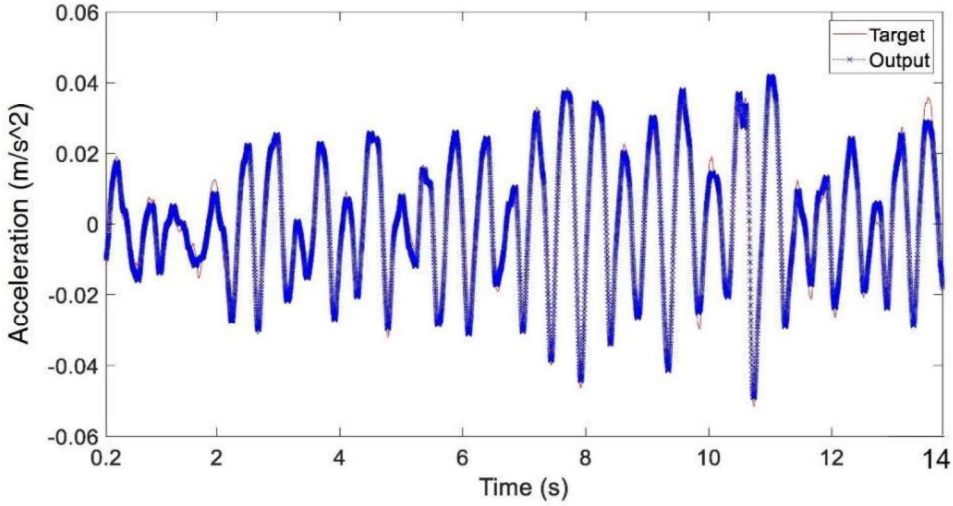

Figure 6 Comparison of estimated acceleration response from ANN model and of measured signal from axle box sensor

$N_{faults} = 3000$ samples were taken for each case of the fault validation, followed by testing. Hyperparameters were varied (with 30 max iterations) to estimate the optimum architecture for classification. The point marked in Figure 7, corresponds to the relatively optimized performance point over the considered range of parameters.

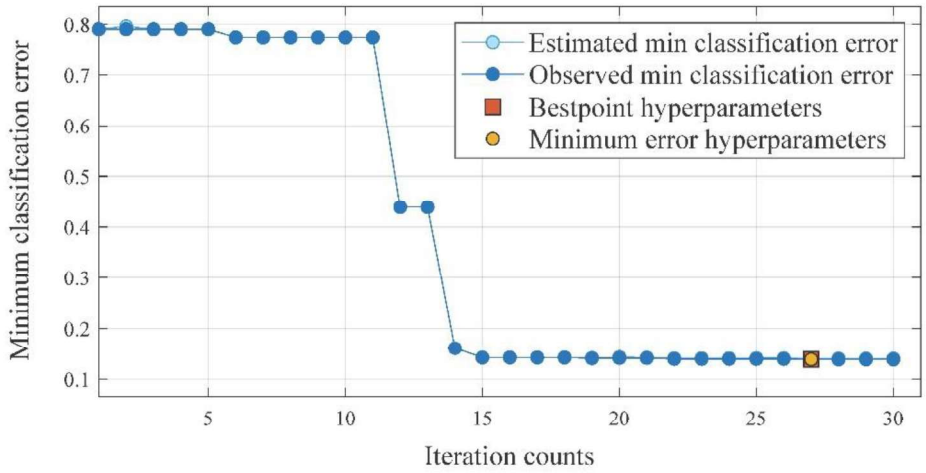

Figure 7 Hyperparameters optimization

Several manual tests with different numbers of neurons were performed to get a significantly high prediction rate. Figure 8-10 present the confusion matrix with prediction accuracy to show the effectiveness of the numbers of neurons. In test 1, presented in Figure 8, it can be seen that individual false negative/discovery rate, are high for fault nos 5 and 6. Similarly for test 2, presented in Figure 9, it can be seen that false negative/discovery rate is not satisfactory. However, in both the cases, overall fault detection accuracies are 81.9% and 91.1% and can provide a decent assessment of the condition of the suspensive system. Moreover, test 3 (Figure 10) with 354 neurons gives the best results as overall detection and classification accuracy is above 97%, with very low rate of false detection (below 5%).

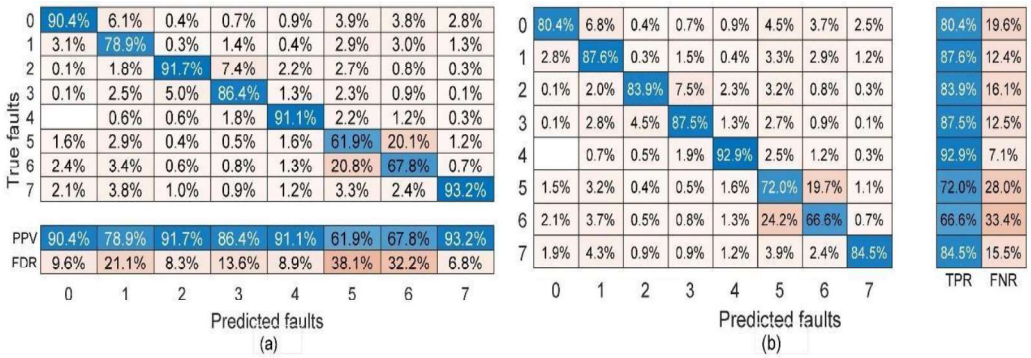

Figure 8 (a) False detection and (b) false negative results of test1 using tri-layer neural network with 190 neurons (81.9% detection rate)

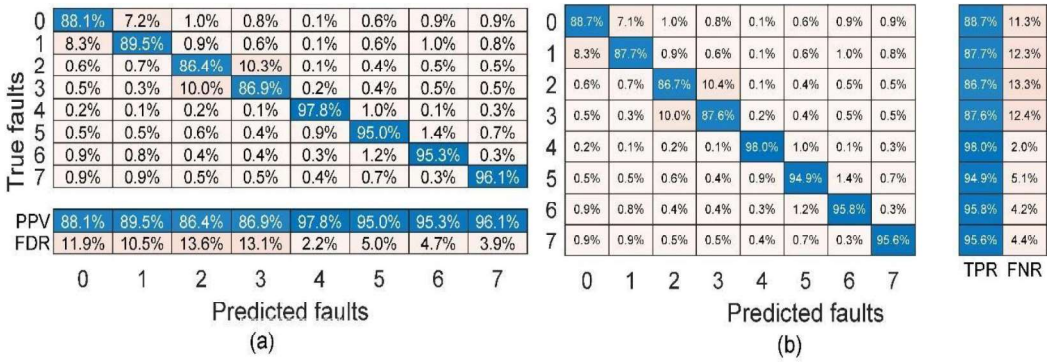

Figure 9 (a) False detection and (b) false negative results of test2 using tri-layer neural network with 295 neurons (91.1% detection rate)

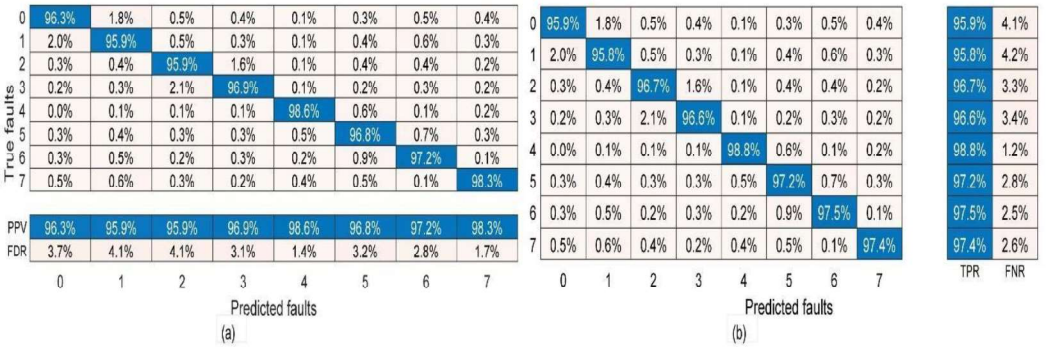

Figure 10 (a) False detection and (b) false negative results of test3 using tri-layer neural net-work with 354 neurons (97% detection rate)

5 CONCLUDING REMARKS

The study demonstrates the use of artificial neural network scheme for detection and classification of faults in a railway bogie suspension system. A classification approach using a decision maker (combination of binary and SoftMax) strategy, based on the residual error between measured data and the ANN modelled data is proposed. Feasibility of the condition monitoring and fault detection has been presented using multi-body dynamic model. Modelling and operational parameters of the multi-body model are tried to keep as realistic as possible, for accurate estimation of dynamic response of a railway bogie. Proposed ANN model is first optimized for hyperparameters and then the test results are presented for various numbers of neurons. For the designed ANN model, a prediction accuracy of 97% is achieved.

6 REFERENCES

[1] Debroy, B. Desai, K.: Fund Deployment Framework for Rashtriya Rail Sanraksha Kosh: Indian Railways, 2018.

[2] Jin, Xue-song. "Key problems faced in high-speed train operation." In China's High-Speed Rail Technology, pp. 27-45. Springer, Singapore, 2018.

[3] Li, Y. D., C. B. Liu, N. Xu, X. F. Wu, W. M. Guo, and J. B. Shi. "A failure study of the railway rail serviced for heavy cargo trains." Case Studies in Engineering Failure Analysis 1, no. 4 (2013): 243-248.

[4] Naveen, S., C. P. Kiran, and M. Prabhu. "Study on bogie and suspension system of an electric locomotive (Wap-4)." IJMER 4 (2014): 1-14.

[5] Tsunashima, Hitoshi. Railway condition monitoring, present and application for regional railways. Vol. 102. Tokyo, Japan: Nihon University, 2018.

[6] Ralev, Vanio, and Dobrinka Atmadzhova. "Failure Analysis in Passenger Bogies from the Railway System of the Republic of Bulgaria."

[7] Seo, Jung-Won, Hyun-Moo Hur, Hyun-Kyu Jun, Seok-Jin Kwon, and DongHyeong Lee. "Fatigue design evaluation of railway bogie with full-scale fatigue test." Advances in Materials Science and Engineering 2017 (2017).

[8] Kumar R., Sharma T., Shekhar A., Vyas N.S.: Primary suspension failure analysis in FIAT type LHB bogies and life estimation: Engineering Failure Analysis, vol 138, Aug 2022.

[9] Li, Yong-Hua, Yue-Dong Wang, and Wen-Zhong Zhao. "Bogie failure mode analysis for railway freight car based on FMECA." In 2009 8th International Conference on Reliability, Maintainability and Safety, pp. 5-8. IEEE, 2009.

[10] Mousavi Bideleh, Seyed Milad. "Robustness analysis of bogie suspension components Pareto optimised values." Vehicle System Dynamics 55, no. 8 (2017): 11891205.

[11] Johnsson, Albin, Viktor Berbyuk, and Mikael Enelund. "Pareto optimisation of railway bogie suspension damping to enhance safety and comfort." Vehicle system dynamics 50, no. 9 (2012): 1379-1407.

[12] Dumitriu, Mădălina. "Study on the effect of damping asymmetry of the vertical suspension on the railway bogie vibrations." Symmetry 14, no. 2 (2022): 327.

[13] Qazizadeh, Alireza, Rickard Persson, and Sebastian Stichel. "On-track tests of active vertical suspension on a passenger train." Vehicle System Dynamics 53, no. 6 (2015): 798-811.

[14] Hamed, M., and M. Elrawemi. "Effects of Spring Stiffness on Suspension Performances Using Full Vehicle Models." (2018).

[15] Hayashi, Yusuke, Hitoshi Tsunashima, and Yoshitaka Marumo. "Fault detection of railway vehicle suspension systems using multiple-model approach." Journal of Mechanical Systems for Transportation and Logistics 1, no. 1 (2008): 88-99.

[16] Mei, T. X. – Ding, X. J.: Condition monitoring of rail vehicle suspensions based on changes in system dynamic interactions: Vehicle System Dynamics, Vol 47:9, 2009, p. 1167-1181, DOI: 10.1080/00423110802553087.

[17] Mathias J. - Katrin E.: Fault detection and isolation for a railway vehicle by evaluating estimation residuals. Procedia IUTAM 13, 2015, p. 14 – 23.

[18] Ye, Y., Zhang, Y., Wang, Q., Wang, Z., Teng, Z., & Zhang, H.: Fault diagnosis of high-speed train suspension systems using multiscale permutation entropy and

linear local tangent space alignment: Mechanical Systems and Signal Processing, 138, 2020, https://doi.org/10.1016/j.ymssp.2019.106565.

[19] Wu, Yunpu, Weidong Jin, Junxiao Ren, and Zhang Sun. "Fault diagnosis of high-speed train bogie based on synchrony group convolutions." Shock and Vibration 2019 (2019).

[20] Zoljic-Beglerovic, Selma, Georg Stettinger, Bernd Luber, and Martin Horn. "Railway suspension system fault diagnosis using cubature Kalman filter techniques." IFAC-PapersOnLine 51, no. 24 (2018): 1330-1335.

[21] Ward, Christopher P., Roger M. Goodall, Roger Dixon, and Guy Charles. "Condition monitoring of rail vehicle bogies." In UKACC International Conference on Control 2010, pp. 1-6. IET, 2010.

[22] Yang, Yang, Na Qin, Deqing Huang, and Yuanzhe Fu. "Fault diagnosis of high-speed railway Bogies based on LSTM." In 2018 5th International Conference on Information, Cybernetics, and Computational Social Systems (ICCSS), pp. 393398. IEEE, 2018.

[23] Ye, Yunguang, Ping Huang, and Yongxiang Zhang. "Deep learning-based fault diagnostic network of high-speed train secondary suspension systems for immunity to track irregularities and wheel wear." Railway Engineering Science 30, no. 1 (2022): 96-116.

[24] Gadhave, R. and Vyas, N.S., Rail-wheel contact forces and track irregularity estimation from on-board accelerometer data. Vehicle System Dynamics, 60(6), pp.2145-2166.

[25] Capriglione D, Carratù M, Pietrosanto A, Sommella P. NARX ANN-based instrument fault detection in motorcycle. Measurement. 2018 Mar 1;117:304-11.

PARTIAL SAFETY FACTOR-BASED ESTIMATION METHOD OF FATIGUE LIFE AND FAILURE PROBABILITY OF WELDS IN RAILWAY BOGIE FRAMES

Taizo MAKINO*, Takanori KATO*, Shoichi HASEGAWA, Yosuke YAMAZAKI*, Satoshi KIKKO** and Yoshiyuki SHIMOKAWA****

*Research & Development, Nippon Steel Corporation
1-8 Fuso-cho, Amagasaki-shi, Hyogo 660-0891, Japan
**Kansai Steel Works, Nippon Steel Corporation
5-1-109 Shimaya, Konohana-ku, Osaka-shi, Osaka 554-0024, Japan

Received: August 5, 2022

ABSTRACT

The present study aimed to clarify the relationship between the fatigue life under in-service conditions and the failure probability of welded joints in a railway bogie frame. Considering the effects of the stress ratio and weld toe radius, the authors determined the *P–S–N* curves by applying the fatigue data of cruciform as-welded joints to the Smith Watson Topper method. The *P-S-N* curves were classified into two types according to weld toe radius. An estimation method for the probability of fatigue failure was proposed based on the partial safety factor method (JIS B 9955, JSME S 018). Subsequently, the following two concepts were introduced to the fatigue failure issue: one employed the accumulated fatigue damage and its criterion as an evaluation parameter, and the other employed the interval estimation of the scatter of the aforementioned damages based on the t-distribution. Therefore, the proposed method allows the variability of in-service cyclic stress to be considered. The method is applied to a vehicle in commercial operation that is designed in accordance with JIS E 4207 and JIS E 4208 using the modified Miner's rule and the aforementioned *P–S–N* curves. Consequently, the failure probability increased with an increase in the mileage of the vehicle, and the relationship between the failure probability and the mileage varied because of the variability of the in-service stress. Therefore, the proposed method enables the estimation of the fatigue life and failure probability of welded joints in railway bogie frames.

Keywords: fatigue life, failure probability, welded joint, railway bogie frame, partial safety factor method

1 INTRODUCTION

Because railway bogie frames are subjected to complex loads through attached components while they are operating, their strength reliability must be ensured to enable their long-term use. The reliability of our designs is ensured since we adhered to Japanese industrial standards (JIS E 4207 [1], JIS E 4208 [2]); furthermore, the designs are based our experience from many years of actual use. However, only a few cases of failed welded components have been reported [3]. To reduce such failure cases, the authors improved the stress assessment method for welds [4],[5],[6]. In a previous study, the authors proposed a strain gauge attachment method, in which the base edge of the gauge is aligned with the weld toe, referred to as "gauge edge type," as the stress assessment method, and indicated that the method significantly reduced the variability of assessed stresses due to strain measurements.

Because the stress amplitude and ratio vary under in-service conditions, even if the reversed stress is lower than the fatigue limit, fatigue damage may occur on the bogie frames. Therefore, in addition to the fatigue limit design described above, the fatigue life must be estimated to ensure the fatigue reliability of bogie frames. Some researchers have attempted life estimation, but the estimations did not support the gauge-edge-type stress [3], [7], [8], [9], [10], [11].

Not only the variability of the strength side, but also that of the load side should be considered when evaluating failure probability. The partial safety factor method was proposed for evaluating failure probability. The general principles of the method are defined in JIS B 9955[12], and the guidelines for applying the method to specific targets are explained in JSME S 018[13]. The present study is performed to clarify the relationship between fatigue life under in-service conditions and the failure probability of welded joints in a railway bogie frame. We determine the *S*–*N* curves for fatigue life evaluation and develop a partial factor-based estimation method to estimate the fatigue life and failure probability while considering the variability of in-service stresses. Moreover, we apply an in-service stress spectrum to the aforementioned method and discuss its applicability. Please note that the present paper is a shortened English version of another Japanese paper by the authors [14],[15].

2 DETERMINATION OF *S*–*N* CURVES FOR FATIGUE LIFE ASSESSMENT

We reorganized the fatigue test data of load-carrying fillet as-welded cruciform joint specimens obtained by the authors [4],[16]. The specimens were fabricated using steel sheets that confirmed to JIS SM400B and SM490YB, and a weld metal that conformed to JIS YGW-19. They were classified into "small-ρ" and "large-ρ" based on the weld toe radius. The weld toe radii were 0.2–1.5 mm (average = 0.6 mm) and 1.6–3.3 mm (average = 2.6 mm) for the small-ρ and large-ρ specimens, respectively. The test stress was set as the gauge-edge-type stress, as schematically illustrated in Fig. 1. Two load types were employed: tension–compression and bending. The stress ratios *R* were 0.05 and 0.5 in tension–compression, and -1 in bending. The small-ρ and large-ρ specimens were fatigue tested at $R = 0.05$, 0.5 and $R = 0.05$, -1, respectively.

The fatigue test data were organized based on the Smith Watson Topper (SWT) method [17] using the equivalent stress amplitude σ_{SWT}, referred to as the "SWT stress," which is defined in Eq. 1.

$$\sigma_{SWT} = \sqrt{\sigma_a \cdot \sigma_{max}} = \sqrt{\sigma_a(\sigma_a + \sigma_m)} = \sqrt{\frac{2}{1-R}}\sigma_a \tag{1}$$

Figure 2 shows the *S*–*N* diagram modified using the SWT method. The *S*–*N* curves of small-ρ and large-ρ were approximated using Eq. 2.

$$N = A \cdot {\sigma_{SWT}}^{-4.375}$$
$$A = 2.080 \times 10^{15}\ (\text{small-}\rho), \qquad 7.656 \times 10^{15}\ (\text{large-}\rho) \tag{2}$$

Because we confirmed that the variability of the fatigue life reflects a lognormal distribution, we obtained 0.4113 as the standard deviation for the natural logarithm of the fatigue life S_{lnN}. Subsequently, using the value of S_{lnN}, the *P*–*S*–*N* curves were expressed as shown in Eq. 3.

$$
\begin{aligned}
&N = A' \cdot \sigma_{\mathrm{SWT}}{}^{-4.375} \\
&A' = \exp(\ln A - B \cdot S_{\ln N}),\ B = 2.0\ (P_{\mathrm{f}} = 2.3\%), 3.0\ (P_{\mathrm{f}} = 0.1\%) \\
&A'(\text{small-}\rho) = 9.137 \times 10^{14}\ (P_{\mathrm{f}} = 2.3\%), 6.056 \times 10^{14}\ (P_{\mathrm{f}} = 0.1\%) \\
&A'(\text{large-}\rho) = 3.363 \times 10^{15} (P_{\mathrm{f}} = 2.3\%), 2.229 \times 10^{15}\ (P_{\mathrm{f}} = 0.1\%)
\end{aligned}
\tag{3}
$$

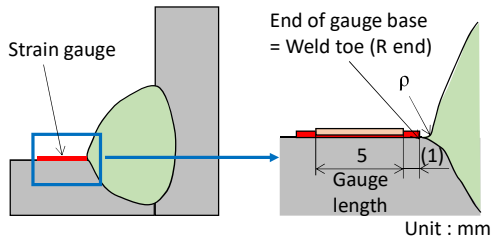

Fig. 1 Strain gauge attachment position in the edge type method

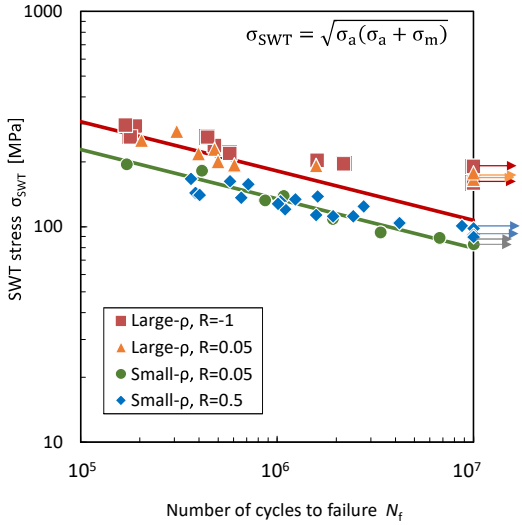

Fig. 2 *S–N* diagram modified using the SWT method

3 METHOD CONSIDERING VARIABILITY IN IN-SERVICE STRESS BASED ON PARTIAL SAFETY FACTOR METHOD

The partial safety factor method determines the partial safety factors for load and strength and evaluates the reliability, i.e., the fracture probability is calculated using a reference formula based on these factors [12], [13]. This method enables a deterministic reliability evaluation without requiring complicated probability calculations. Figure 3 shows the concept of reliability evaluation using the partial safety factor method [13]. First, we assume that the load and strength exhibit a probability distribution that reflects a normal distribution. As shown in Fig. 3(a), the contour of the probability density function obtained from the synthesis of the load and strength distributions is drawn in two-dimensional axes, where the load and strength are represented in the vertical and horizontal axes, respectively. Here, the top of the mountain by the contour lines corresponds to the mean load and strength. Next, we consider an expression for the fracture threshold, which is known as the limit state function G

$$G = R - L = 0 \tag{4}$$

where R is the strength, and L is the load. In Fig. 3(a), the upper-left region of line G represent $R < L$, i.e., the failure region, and the lower-right region of line G represents $R > L$, i.e., the non-failure region. The upper-left hem of the probability distribution,

represented by the contour lines, overlaps partially with the failure region. The failure probability was calculated by integrating the overlapping areas.

To simplify the calculation, the standard normalized coordinates with mean transformed to zero, and the standard deviation transformed to unity, as shown in Fig. 3(b), were used. Here, U is the standard normalized coordinate, μ the mean, and S the standard deviation. The strength and load are expressed as follows with the subscripts of "R" and "L" representing strength and load, respectively.

$$R = S_{\mathrm{R}} U_{\mathrm{R}} + \mu_{\mathrm{R}} \tag{5}$$

$$L = S_{\mathrm{L}} U_{\mathrm{L}} + \mu_{\mathrm{L}} \tag{6}$$

Because the mean of the load and strength expressed in standard normalized coordinates are both zero, the probability density function combining both is a concentric distribution centered at the origin. The limit state function G is transformed into the following equation by substituting Eqs. 5 and 6 into Eq. 4:

$$G = (S_{\mathrm{R}} U_{\mathrm{R}} + \mu_{\mathrm{R}}) - (S_{\mathrm{L}} U_{\mathrm{L}} + \mu_{\mathrm{L}}) = 0 \tag{7}$$

G was drawn as a line from the origin in Fig. 3(b). The failure region in Fig. 3(b) is to the upper left of line G. The upper-left hem of the contour lines overlaps partially with the failure region in Fig. 3(b), similar to Fig. 3(a). The integral of the overlapping area can be obtained from the distance β from the origin to line G. β corresponds to the reliability index. Applying this to the cumulative distribution function Φ of the standard normal distribution, as shown in the following equation, allows the failure probability P_{f} to be calculated.

$$P_f = 1 - \Phi(\beta) \tag{8}$$

The closest point on line G from the origin is referred to as the "design point."

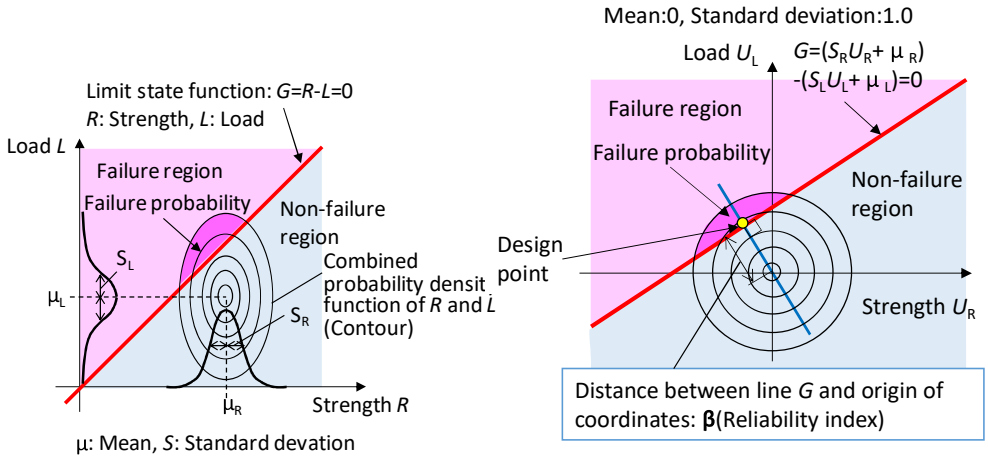

(a) Load vs. strength (b) Conversion to standard normalized coordinates

Fig. 3 Concept of reliability evaluation using the partial safety factor method [14]

To apply the partial safety factor method to fatigue life evaluation, JIS B 9955 [12] indicates that the cumulative damage rule should be used; however, JSME S 018[13] does not describe a specific method. In this regard, only a few related studies have been performed, e.g., those by Takanashi et al. [18] and Hasegawa et al. [19]. In this study, we considered a new approach, as shown in Fig. 4. Using the cumulative damage rule approach, the evaluation parameter on the load side is the accumulated damage value D, and the evaluation parameter on the strength side is the critical damage value D_{cr}. The accumulated damage value D is obtained via the following procedure: First, the damage value D' is calculated by applying the in-service stress spectrum measured in the actual vehicle operating test to the following equation:

$$D' = \sum_i \frac{n_i}{N_i} \tag{9}$$

where n_i is the number of cycles of the ith stress level, and N_i is the lifetime of the ith stress level derived from Eq. 2. Subsequently, D'/L is determined as the division of D' by the operating distance L. The calculation is executed on several sections, preferably 10 or more sections of approximately equal distance, and the sample data of D'/L are obtained. Subsequently, a statistical analysis of D'/L is conducted, and its mean and standard deviation are obtained. The accumulated damage value D for the vehicle operating on all the sections is expressed as follows:

$$D = \sum_j \left\{ \left(\frac{D'}{L} \right)_j L_j \right\} \tag{10}$$

where $(D'/L)_j$ is the D'/L of the jth section, and L_j is the distance of the jth section.

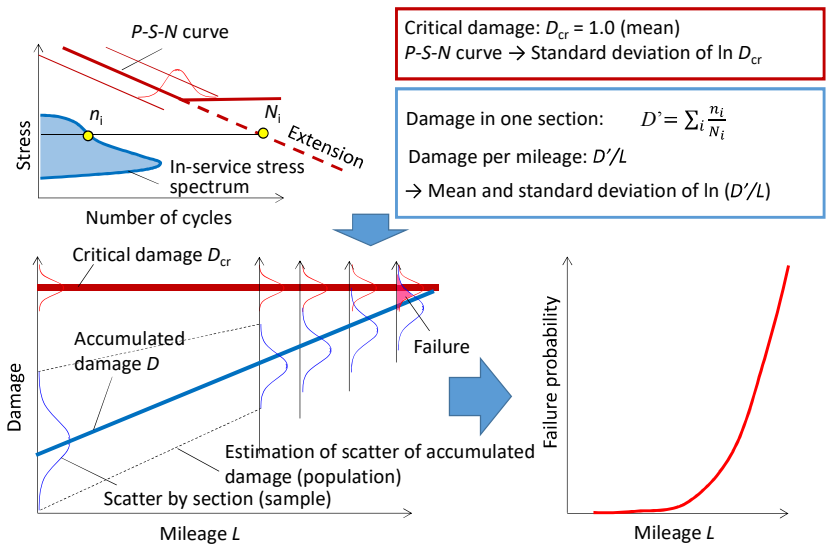

Fig. 4 Application of the partial safety factor method to the fatigue failure issue

As shown in Fig. 4, the critical damage D_{cr} is constant regardless of the mileage. Meanwhile, the accumulated damage value, D, increases with the mileage. The overlapping region between the lower and upper sections of both deviations widens, and the failure probability increases. Because D is defined as the accumulated value at all stress levels and sections, as expressed in Eqs. 9 and 10, the deviation of D should be considered after the mileage increases. Because the deviations are different in D'/L and D, the standard deviation of D was derived as follows: A sample in the statistics and population were assumed to be D'/L and D, respectively. An interval estimation of the population mean based on the t-distribution was performed; the interval containing the population mean with a probability of 68.26%, i.e., the 68.26% confidence interval, corresponds to the range by mean ±1 times the standard deviation of D, because the probability of the range by ±1 times the standard deviation in a normal distribution is ±34.13%. The relationship between the population mean μ and sample mean μ' expressed using the t-value in the t-distribution t is as follows:

$$-t \leq \frac{\mu - \mu'}{S/\sqrt{n_s}} \leq +t \tag{11}$$

where n_s is the number of samples. Expanding the equation above yields

$$|\mu - \mu'| \leq t\frac{S}{\sqrt{n_s}} \tag{12}$$

By substituting $t_{0.1587}$, i.e., a t-value equivalent to 34.13% on one side, into t in Eq. 12, the right side of the equation above corresponds to the standard deviation of the natural logarithm of D $S_{\ln D}$. $t_{0.1587}$ is listed as a value that depends on the degree of freedom m_s (= n_s - 1) in the t-distribution table. Therefore, $S_{\ln D}$ is expressed as follows, using the standard deviation of the natural logarithm of the sample damage value $S_{\ln D'}$:

$$S_{\ln D} = t_{0.1587}\frac{S_{\ln D'}}{\sqrt{n_s}} = t_{0.1587}\frac{S_{\ln(D'/L)}}{\sqrt{n_s}} \tag{13}$$

If L is constant in a log-normal distribution, then $S_{\ln D'}$ is equal to $S_{\ln (D'/L)}$. To apply $S_{\ln D}$ to the partial safety factor method, the limit state function G is redefined as follows:

$$G = D_{cr} - D = 0 \tag{14}$$

D_{cr} and D are expressed under the assumption that both reflect log-normal distributions, as follows:

$$D_{cr} = \exp(S_{\ln Dcr}U_{\ln Dcr} + \mu_{\ln Dcr}) \tag{15}$$

$$D = \exp(S_{\ln D}U_{\ln D} + \mu_{\ln D}) \tag{16}$$

where U is the standard normalized coordinates; μ is the mean; S is the standard deviation; subscripts "ln Dcr" and "ln D" are added to the parameters of strength and load, respectively. Here, $\mu_{\ln Dcr}$ is zero because the mean of D_{cr} is unity. $S_{\ln Dcr}$ is the same as

$S_{\ln N}$, based on the definition of a lognormal distribution, and its value is determined to be 0.4113 (see Section 2). $\mu_{\ln D}$ and $S_{\ln D}$ are discussed in Section 4. Substituting Eqs. 15 and 16 into Eq. 14, and establishing the relationship between $U_{\ln Dcr}$ and $U_{\ln D}$, we obtain the following equation:

$$U_{\ln D} = \frac{S_{\ln Dcr}}{S_{\ln D}} U_{\ln Dcr} + \frac{\mu_{\ln Dcr} - \mu_{\ln D}}{S_{\ln D}} \tag{17}$$

This equation corresponds to G in the standard normalized coordinates shown in Fig. 3(b). Finally, the distances from the origin to line G in the various mileages are derived and assumed to be the reliability index β. Using β and Eq. 8, the failure probability can be estimated.

4 TRIAL APPLICATION TO ACTUAL BOGIE FRAME

4.1 Analysis of stress data measured in actual vehicle operating test

Aided by a railway operator A, the authors conducted an actual vehicle operating test for four months. Two sets of round-trip data from one set of round-trip data measured continuously each day were extracted from the data of Day-1, immediately after the start of the test, and from Day-2, i.e., before termination for a period of four months. The two-round trip data were analyzed for each section divided by 16 sections per one-way trip, with one section being the distance between adjacent stations. One section measured 0.52–1.75 km long for one round trip, i.e., the total long for 32 sections was 34.5 km. The stress measurement point was an as-welded component on the supporting member of the rail guard in the bogie frame.

Two-dimensional rainflow counting was performed on stress history data. Combinations of the stress amplitude, mean stress, and cycle counts were obtained. They were converted into SWT stresses using Eq. 1. Subsequently, 5 MPa of SWT stress was set as the cut-off stress, and cycle counts equal to or less than 5 MPa were excluded in the following evaluation. This is because we confirmed in advance that the accumulated damage value and the life estimated using the modified Miner's rule between two cases, i.e., where cycle counts equal to or less than 5 MPa were excluded and included, did not differ significantly.

The SWT stress spectrum was applied to the modified Miner's rule, and the damage values D' for each section and their divisions based on operating distance D'/L were derived. Figure 5 shows the analysis result of D'/L. Data for D'/L in the figure were calculated using the S–N curve of large-ρ. The D'/L for different sections varied significantly. Figure 5(a) shows that the D'/L of the same section varies between the inbound and outbound lines. Figure 5(b) indicates that D'/L changes slightly during the four months in the same section and in the same travel direction.

Statistical analysis was conducted using a sample comprising 32 sections (n_s = 32) for one round trip for the D'/L of each section. The distribution reflected a lognormal distribution, and the standard deviation of the natural logarithm of D'/L, i.e., $S_{\ln(D'/L)}$, was calculated to be 3.155. This is the higher value obtained via the statistical analysis of one round trip each for Day-1 and Day-2. The standard deviation of the natural logarithm of D, i.e., $S_{\ln D}$, was 0.5669, as calculated using Eq. 13, which is used to estimate the interval

based on the t-distribution. For $t_{0.1587}$ in Eq. 13, we used 1.016 as the value corresponding to 31 degrees of freedom m_s (= n_s - 1) in the t-distribution table. The mean of D'/L should be obtained from the accumulated damage values over the longest possible mileage. Therefore, we obtained 9.887×10^{-7} /km (small-ρ) and 2.686×10^{-7} /km (large-ρ) as the means of D'/L from data corresponding to a mileage of 4103 km.

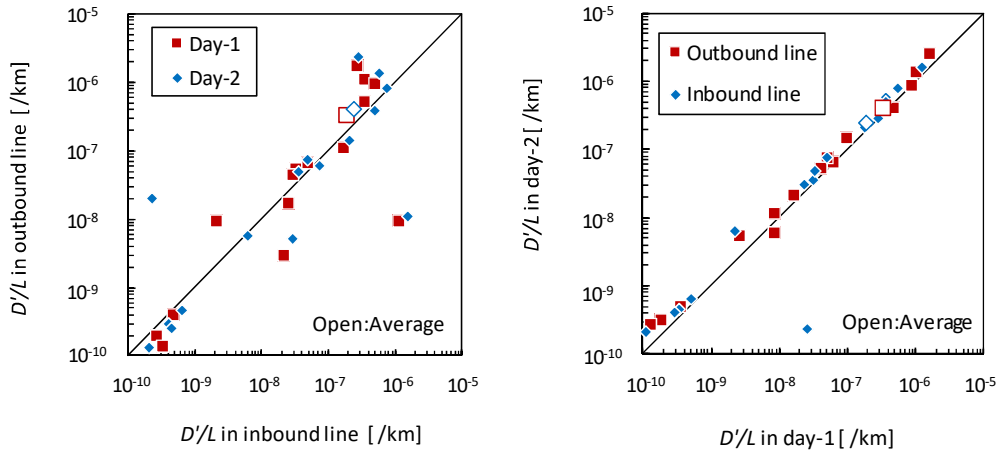

(a) Comparison between the inbound and outbound lines (b) Comparison by the measurement date

Fig. 5 Damage per unit mileage in each section (large-ρ)

4.2 Fatigue life evaluation considering variabilities in both strength and load using partial safety factor method

We performed fatigue life evaluation by applying data from the actual vehicle operating test (see Section 4.1) using the method proposed in Section 3. The values of the parameters used for life evaluation are listed in Table 1. The evaluation parameters on the strength and load sides are D_{cr} and D, respectively. Notably, for the sample data on the load side, the damage value per unit mileage D'/L was used. The mean and logarithmic standard deviation values of these parameters are listed in the table. By substituting these values into Eq. 17 shown in Section 3 yields the following equations for the limit state function:

$$U_{\ln D}(\text{small-}\rho) = 0.7255 \cdot U_{\ln Dcr} + \frac{13.83 - \ln L}{0.5669}$$
$$U_{\ln D}(\text{large-}\rho) = 0.7255 \cdot U_{\ln Dcr} + \frac{15.13 - \ln L}{0.5669} \quad (28)$$

Drawing lines depicting the equations above on the standard normalized coordinates of Fig. 3(b) allowed us to obtain the distance from the origin to the drawn line β. Subsequently, we derived the failure probability by substituting β into Eq. 8. By executing such calculations for various mileages, we obtained the relationship between the mileage

and failure probability, as shown in Fig. 6. Table 2 lists the predicted lifetimes for each failure probability obtained from the life evaluations. Based on Fig. 6 and Table 2, compared with the case where only the strength-side variability is considered, the estimated life is shorter for failure probabilities lower than 50% when both strength and load variabilities are considered, and the lower the failure probability, the greater is the difference between the two. For example, at a failure probability of 0.1%, the estimated life when both the strength and load variabilities are considered is 0.42 times greater than the estimated life when only the strength variability is considered.

Hence, it can be concluded that the life evaluation based on the in-service stress spectrum, which considers the variability of both the strength and load, is more conservative than the evaluation that considers only the variability of the strength for a failure probability lower than 50%. The evaluated bogie frame is designed according to JIS E 4207 [1] and satisfies the same standard. By contrast, the evaluation results using the partial safety factor method, as summarized in Table 2, shows that the mileage until crack initiation is approximately 1.24×10^5–4.55×10^5 km.

Table 1 Values of parameters used for life evaluation

	Strength side parameter		Load side parameter (sample)		Load side parameter (population)	
	Critical damage D_{cr}		Damage per unit mileage D'/L		Accumulated damage D	
Antilogarithmic mean	μ_{Dcr}	1.0	$\mu_{D'/L}$ [/km]	(Small-ρ) 9.887×10^{-7}	μ_D	(Small-ρ) $9.887\times10^{-7}L$
				(Large-ρ) 2.686×10^{-7}		(Large-ρ) $2.686\times10^{-7}L$
Logarithmic mean	$\mu_{\ln Dcr}$	0	$\mu_{\ln (D'/L)}$	(Small-ρ) -13.83	$\mu_{\ln}$	(Small-ρ) -13.83+ln L
				(Large-ρ) -15.13		(Large-ρ) -15.13+ln L
Logarithmic standard deviation	$S_{\ln Dcr}$	0.4113	$S_{\ln (D'/L)}$	3.155	S	0.5669

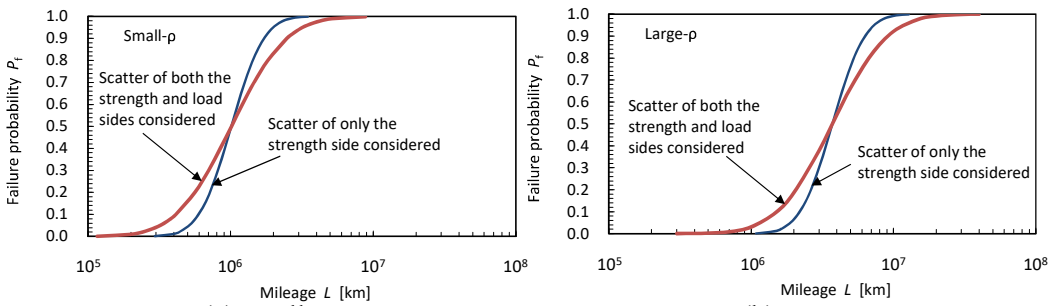

(a)Small-ρ (b) Large-ρ

Fig. 6 Relationship between mileage and failure probability

Table 2 Predicted lifetime (mileage [km]) for each failure probability

Failure probability P_f	Scatter of only the strength side considered		Scatter of both the strength and load sides considered		Ratio of predicted life (both sides / only strength side)
	Small-ρ	Large-ρ	Small-ρ	Large-ρ	
0.5	1.01×10^{6}	3.72×10^{6}	1.01×10^{6}	3.72×10^{6}	1.00
0.023	4.44×10^{5}	1.64×10^{6}	2.49×10^{5}	9.17×10^{5}	0.56
0.001	2.95×10^{5}	1.08×10^{6}	1.24×10^{5}	4.55×10^{5}	0.42
10^{-4}	2.19×10^{5}	8.07×10^{5}	7.48×10^{4}	2.75×10^{5}	0.34
10^{-5}	1.75×10^{5}	6.44×10^{5}	5.10×10^{4}	1.88×10^{5}	0.29
10^{-6}	1.43×10^{5}	5.27×10^{5}	3.62×10^{4}	1.33×10^{5}	0.25

5 CONCLUDING REMARKS

- *P*–*S*–*N* curves, classified based on the weld toe radius and the effects of the stress ratio, were determined by applying the fatigue data of cruciform as-welded joints to the SWT method.
- A method for estimating the probability of fatigue failure was developed using the partial safety factor method. In the method, the accumulated fatigue damage and its criteria were used as evaluation parameters for the load and strength, respectively.
- In the case where the section and direction of travel were the same and no changes occurred in the track, the damage value per unit distance was similar for vehicle travel. The damage values per unit distance were different for different track sections or different vehicle travel directions, even when the track maintenance controls were the same.
- Applying stress data measured in actual vehicle operating tests to the proposed estimation method showed that the failure probability increased with the vehicle mileage; additionally, the relationship between the failure probability and mileage varied because of the variability in the in-service stress.
- The railway bogie frames evaluated in this study were designed in accordance with JIS E 4207 and JIS E 4208 standards. It was confirmed that the proposed method enables the estimation of the fatigue life and failure probability of welded joints in railway bogie frames.

6 REFERENCES

[1] JIS E 4207, Rolling stock – Bogie – General rules for design of bogie frame strength, Japanese standards association, 2019 (in Japanese).

[2] JIS E 4208-1, Rolling stock – Bogie – Strength test – Part 1: Methods for static load testing, Japanese standards association, 2021 (in Japanese).

[3] Nagase, T.: Strength and maintenance of bogie frame, Kenyusya, 1999, p.7–12, 51–114, 179–185 (in Japanese).

[4] Makino, T., Yamamoto, M., Kondo, O., Kusumoto, F., Sato, Y. and Shimokawa, Y.: Evaluation of fatigue properties on welded joints and application to fatigue

design standard of railway bogie frame, Proceedings of the 14th JSME Transportation and Logistics Conference (Translog'05), No.2306, 2005, p.355–358 (in Japanese).

[5] Makino, T. and Ishiduka, H.: Fundamentals of fatigue and recent trends on fatigue design in mechanical structures, Ⅴ: Railway vehicles, Journal of the Society of Materials Science, Japan, Vol. 59, No. 5, 2010, p.398–405 (in Japanese).

[6] Kato, T., Kikko, S., Tanimine, T., Yamamoto, M., Shimokawa, Y., Makino, T., Kondo, O. and Wada, K.: Stress assessment of welded joints in railway bogie frame, Transactions of the JSME (in Japanese), Vol. 86, No.889, 2020, DOI:10.1299/transjsme.20-00089.

[7] Oda, Y., Yagi, T., Okino, T. and Ishiduka, H.: Fatigue life estimation for welds of truck frames for rolling stock using stress frequency in service load, Transactions of the Japan Society of Mechanical Engineers, Series A, Vol.73, No.734, 2007, p.1171–1176 (in Japanese).

[8] Nagase, T.: Fatigue strength of welded steel bogie frame, Kenyusya, 2010, p.102–110 (in Japanese).

[9] Yagi, T., Yamamoto, M., Kato, Y. and Takagaki, M.: Fatigue strength evaluation method for the welded joint structure of the truck frame by cumulative damage, RTRI Report, Vol.29, No.9, 2015, p.35–40 (in Japanese).

[10] Guo, F., Wu, S. C., Liu, J. X., Zhang, W., Qin, Q. B. and Yao, Y.: Fatigue life assessment of bogie frames in high-speed railway vehicles considering gear meshing, International Journal of Fatigue, Vol. 132, 2020, DOI:10.1016/j.ijfatigue.2019.105353.

[11] Ji, C., Sun, S., Li, Q., Ren, Z. and Yang, G.: Realistic fatigue damage assessment of a high-speed train bogie frame by damage consistency load spectra based on measured field load, Measurement, Vol.166, 2020, DOI:10.1016/j.measurement.2020.108164.

[12] JIS B 9955, General principles on reliability for mechanical products, Japanese standards association, 2017 (in Japanese).

[13] JSME S 002, Standard method of statistical fatigue testing (2nd Edition), The Japan Society of Mechanical Engineers, 1994 (in Japanese).

[14] Makino, T., Kato, T., Hasegawa, S., Yamazaki, Y., Kikko, S., Shimokawa, Y.: Estimation of the fatigue life and failure probability of welded joints in the bogie frames using the partial safety factor method (JIS B 9955-2017). Transactions of JSME (in Japanese), 88, 915, 2020, DOI:10.1299/transjsme.22-00102.

[15] Makino, T., Kato, T., Hasegawa, S., Yamazaki, Y., Kikko, S., Shimokawa, Y.: Estimation of the fatigue life and failure probability of welded joints in the Bogie frames using the partial safety factor method (JIS B9955-2017), Proceedings of the 30th JSME Transportation and Logistics Conference (TRANSLOG 2021), 2021, TL-10-4 (in Japanese).

[16] Kato, T., Makino, T., Tominaga, T., Shimanuki, H., Yamazaki, Y., Yokozeki, K., Shimokawa, Y. and Kikko, S.: Improvement of fatigue strength of welded joints

in railway bogie frames through ultrasonic impact, 28th Jointed Railway Technology Symposium (J- Rail 2021), 2021, SS6-1-2 (in Japanese).

[17] Smith, K. N., Watson, P. and Topper, T. H.: A stress–strain function for the fatigue of metals, Journal of Materials, Vol. 5, No.4, 1970, p.767–778.

[18] Takanashi, M., Higuchi, M., Maeda, J. and Sakai, S.: Fatigue design margin evaluation for carbon and low-alloy steels by reliability-based load and resistance factor method, Proceedings of ASME 2011 Pressure Vessels & Piping Division Conference, PVP2011-57421, 2011, p.1–9.

[19] Hasegawa, K., Hirayama, H., Izumi, S. and Sakai, S.: Application of probabilistic reliability method for piping affected by a seismic load, JSME Materials & Mechanics Division Conference (M&M 2010), 2010, p.208–210 (in Japanese).

APPENDIX

The procedure for the proposed partial safety factor-based estimation method for fatigue life and failure probability is summarized in Fig. A

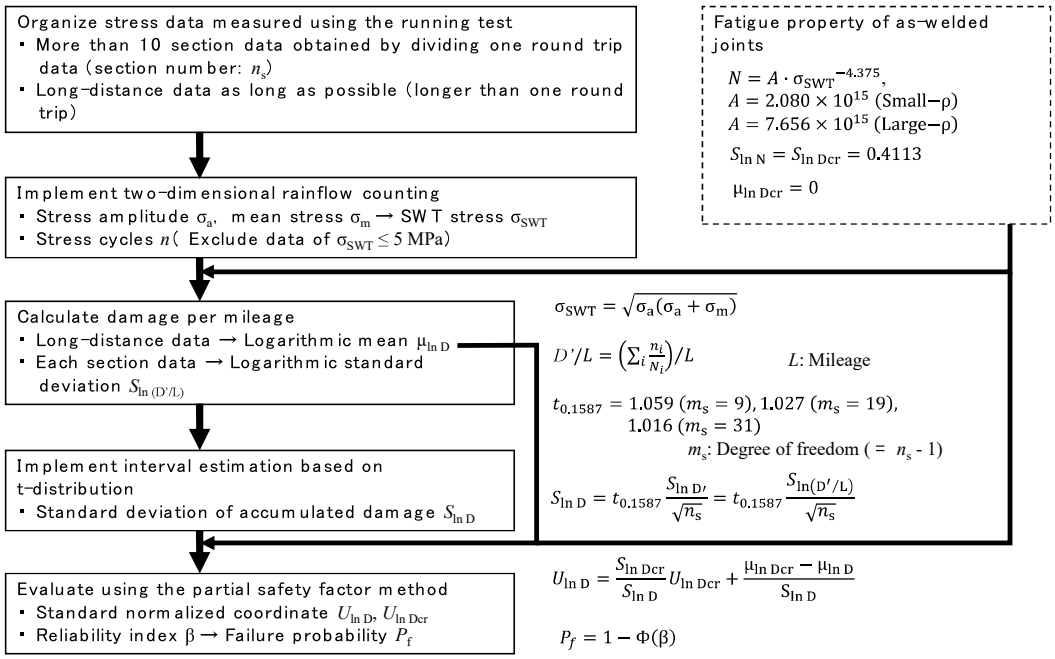

Fig. A Flow diagram of proposed method for estimating fatigue life and failure probability by considering variability of in-service stress using partial safety factor method

DEVELOPMENT OF THE DESIGN OF FREIGHT CAR BOGIES FOR DIFFERENT TRACKS

Sergey V. MYAMLIN and Nikolay MANKEVICH

Branch "Center for diagnostics of railway infrastructure"
JSC "Ukrainian Railways",
Svyatoshinska str. 13, Kyiv, Ukraine

Received: September 5-8, 2022

ABSTRACT

The development of innovative designs of bogies for railway rolling stock is an important area of scientific research. The authors propose the results of research on the design of a two-axle bogie for a 1520 mm gauge freight car with the possibility of switching to a 1435 mm gauge and back. For this, an original design of a wheel set with sliding wheels is proposed. A design feature of the proposed freight car bogie is also the fact that it allows not only to provide the necessary indicators of the dynamics and strength of the structure, but also allows the generation of energy for autonomous power supply of refrigerated cars or refrigerated containers during their transportation on flat cars.

Preliminary studies of the proposed design of the freight car bogie allow us to conclude that this technical solution is promising when used for freight cars for the transportation of perishable goods or goods requiring special temperature conditions for railway transportation.

When choosing the parameters of the bogie structural elements, proven software systems were used to calculate the strength parameters of the main elements and dynamic qualities for various types of cars, taking into account the movement along straight and curved sections of railways.

The authors propose a model range and a variation of the configuration of freight car bogies for different types of cars and for various operating conditions, including taking into account the possibility of increasing speeds while ensuring traffic safety indicators.

Keywords: bogie, innovative design, railway rolling stock, dynamics, strength.

1 INTRODUCTION

The improvement of the designs of the rolling stock of railways is mainly associated with the improvement of the dynamic and strength qualities of rail vehicles. A significant improvement in the dynamic qualities of, for example, freight cars depends on the design features of the bogies. At the same time, a cardinal improvement can only be achieved through the development of innovative bogie designs, taking into account current trends in the needs for the transportation of goods. Therefore, the development of innovative designs of bogies for rolling stock of railways is an important area of scientific research. This is especially relevant for the rolling stock, which ensures the transportation of perishable goods or goods that require special temperature conditions for transportation and, accordingly, additional energy supply.

2 MAIN PART OF INVESTIGATIONS

The authors propose the results of research on the creation of a two-axle bogie design for a four-axle freight car with a 1520 mm gauge with the possibility of switching to a 1435 mm gauge and back. For this, an original design of a wheelset with sliding wheels is proposed. A feature of the design of the proposed freight car bogie is also the fact that it allows not only to provide the necessary indicators of the dynamics and

strength of the structure, but also allows the generation of energy for autonomous power supply of refrigerated cars or refrigerated containers during their transportation on specialized platform cars.

Previously, the authors studied the designs of freight car bogies for different railway gauges, and these studies were associated with the development and introduction into production and further operation on railways of cars with bogies with an axle load of 23.5 tons and 25.0 tons [1-5]. But, taking into account the requirements of the operator companies, the authors have developed a conceptual innovative design of a two-axle freight car bogie, which has a number of design features. The main design features of the proposed bogie include the fact that the bogie has improved spring suspension parameters and has a generator on the axle, which allows generating electricity starting from low speeds. These design solutions make it possible to achieve the desired result for the rolling stock of railways, which is operated on railways with a gauge of 1520 and 1435 mm in various climatic zones. And the design principles underlying the design of this bogie can be used for other types of rolling stock, which allows you to create a whole range of bogies. It is proposed to form a model range of bogies in the main functional areas: heavy, high-speed, increased durability, improved dynamics, cargo-passenger and refrigerated, as well as bogies for specialized rolling stock (tank cars with heating or cooling cargo, and other types of specialized rolling stock).

Preliminary studies of the proposed design of a freight car bogie allow us to conclude that this technical solution is promising when used for freight cars for the transportation of perishable goods or goods that require special temperature conditions for transportation by rail.

When choosing the parameters of the bogie structural elements, proven software systems were used to calculate the strength parameters of the main elements and dynamic qualities for various types of cars, taking into account the movement along straight and curved sections of railways.

The authors also propose a model range and a variation in the configuration of freight car bogies for different types of cars and for various operating conditions, including taking into account the possibility of increasing speeds while ensuring traffic safety indicators and reducing the impact forces of the rolling stock on the railway track. The authors prepared the relevant patents for inventions and copyright protection documents for the main structural elements and bogies in general, and also carried out the necessary set of studies to assess the dynamic and strength qualities of freight cars with bogies of the proposed design.

3 CONCLUDING REMARKS

Thus, the authors of this paper have developed and propose innovative designs of bogies for freight cars for use in transport engineering and railways, which are designed to transport perishable goods and goods requiring special temperature conditions for transportation. The features of these bogie designs include their improved dynamic qualities and increased reliability of the main parts and assemblies due to the use of original engineering solutions, as well as the possibility of using on railways with different gauges – 1520 mm and 1435 mm.

The results of theoretical studies of the dynamic and strength qualities of the bogies developed by the authors testify to the correctness of the chosen parameters of the spring suspension. These designs of bogies have good prospects for use on the railways of different countries.

4 ADDITIONAL COMMENTS

The authors express their sincere gratitude and deep respect to the memory of **Professor Istvan Zobori**, who was the organizer and active participant in numerous international scientific conferences dedicated to the exchange of research results in the field of railway rolling stock mechanics.

5 REFERENCES

[1] Myamlin, S. - Neduzha, L. - Lunys, O. Estimation of dynamic qualities of freight wagons on bogies of a perspective model. Transport problems 2017 : Proc. IX International Scientific conf., 26-30 June 2017, Katowice, Silesian University of Technology, 2017, P. 459–469.

[2] Bubnov, V. M. - Mankevich, N. B. - Myamlin, S. V. Ways to improve the strength characteristics of the running gears of freight cars. Vagonnyy park [Rolling stock], 2012, No. 2, p. 4–6.

[3] Bubnov, V. - Myamlin, S. - Mankevych, N. Theoretical and experimental investigations of strength properties of cast parts for freight cars bogie with axle load of 245 kN. Proc. 8th intern. scient. conf. Transbaltica-2013, Vilnius, 2013, p. 9–12.

[4] Myamlin, S. - Lingaitis, L. P. - Dailydka, S. - Vaiciunas, G. - Bogdevicius, M. - Bureika, G. Determination of the dynamic characteristics of freight wagons with various bogie. Transport, 2015, vol. 30, iss. 1, p. 88–92, doi: 10.3846/16484142.2015.1020565

[5] Bubnov, V. M. - Myamlin, S. V. - Mankevych, N. B. Dynamic performance of freight cars on bogies model 18-1711. Science and Transport Progress, 2013, vol. 4 (46), p. 118–126. https://doi.org/10.15802/stp2013/16616

SIMPLE MODEL AND COMPUTATION PROCEDURE OF THE STARTING AND STOPPING OF THE RAILWAY WHEEL

András SZABÓ

Department of Railway Vehicles and Vehicle System Analysis
Faculty of Transportation Engineering and Vehicle Engineering
Budapest University of Technology and Economics
H-1111 Budapest, Stoczek József utca 6, Hungary
szabo.andras@kjk.bme.hu

Received: August 5. 2022

ABSTRACT

Both the dynamical simulation of the main-motion of a railway vehicle, and of the longitudinal vibration of a railway vehicle or vehicle-system, generally the creep-depended tangential force used in the rail-wheel contact. During the starting or stopping of the wheel there are moments, when the wheel velocity equal to zero, thus the creep cannot be calculated. In this paper a simple model and computation procedure is presented, which takes into the account also the flexible property of the contact. In the framework a simple dynamical model the effect of the elaborated procedure is presented for three different runoff of the traction-torque.

Keywords: Railway wheel-rail contact, dynamical simulation, creep-force, non-linear creep force

1 INTRODUCTION

Both the dynamical simulation of the main-motion of a railway vehicle, and of the longitudinal vibration of a railway vehicle or vehicle-system, generally the creep-depended tangential force used in the rail-wheel contact. The creep is the seeming relative velocity-difference between the wheel and rail in the wheel-rail connection. To calculate this creep it is necessary to divide the mentioned seeming velocity-difference by the velocity of the wheel. However at the moment of the starting or the stopping of the wheel-rolling, this divider velocity has zero value, so the division cannot be executed, and the creep also is cannot be computed.

This problem is seldom in the focus of the researches, but sometimes can be very interesting or important, for example in the analysis of the transmission system vibrations or brake system vibration, as latter is in the paper [1]. Formerly a procedure is elaborated for this problem in paper [2] which is similar, but that is more complicated.

In this paper the deformation procedures playing role in the wheel-rail contact are analysed in the framework of a simple model. First of all, the deformation relations of the "belt-drive" are analysed, because the deformations of the belt in this drive are similar to the deformation of wheel and rail in the wheel-rail contact. Based on the experiences of the belt-drive a simple deformation model is elaborated for the wheel-rail contact. The model takes into the account that while the driving moment already active on the wheel, but the rolling of the wheel yet does not start or already stopped, the wheel is fixed to the rail, and moves realising the flexible and damped torsion swing. Due to different deformation state of the wheel and rail caused by the tangential force in the wheel-rail contact during the wheel rolling distance covered by the wheel and the rolled down arc length on the wheel will be different. In this paper a complex formula is elaborated which takes into account also the wheel flexible deformation and the deformation

difference realised during the wheel-rolling mentioned above. In the framework of some dynamic simulation the effect of the computation method is presented.

2 ANALYZING THE DEFORMATION CONDITIONS OF A BELT-DRIVE

The deformation conditions of the longitudinal wheel-rail contact and the belt-drive illustrated in Fig. 1. are similar.

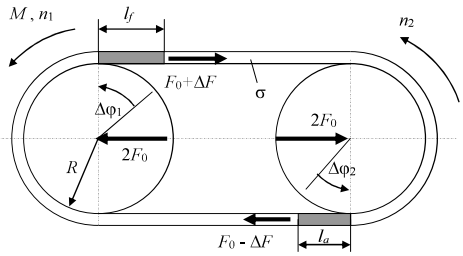

Fig. 1 Deformation conditions of a belt-drive

Due to M torque acting to the disks the belt-forces in the upper and lower part of the belt are different, and that causes differentia also between the deformation of these belt-parts. These ΔF force and Δl deformation-changing of the two parts are equal but converse, so $\Delta l = (l_f - l_a)/2$. If s means the stiffness of the l long belt, then we can write that

$$\Delta F = \Delta l \; s = (l_f - l_a) \; s \; / \; 2 = (l_f - l_a) \; s_e \tag{1}$$

where $s_e = s/2$ is the resulting stiffness of the two part of the belt as an in-line spring system. Because the stiffness of the belt is inversely proportional to its length, it is necessary to define a specific-stiffness σ ($[\sigma]$=N) by the formula below

$$\sigma = s_e \; l_a \; . \tag{2}$$

Using this in formula (2), after some conversion from (1) occurs that

$$l_f \; / \; l_a = 1 + \Delta F \; / \; \sigma = 1 + \varepsilon \; , \tag{3}$$

where the

$$\varepsilon = \Delta F \; / \; \sigma = l_f \; / \; l_a - 1 = (l_f - l_a) \; / \; l_a \tag{4}$$

is defined as a relative length change. During Δt time l_f respectively l_a bend-lengths roll-up to the driver respectively drove disks so the ratio of the angular rotation of disks is

$$l_f \; / \; l_a = R \; \Delta\varphi_1 \; / \; R \; \Delta\varphi_2 = \Delta\varphi_1 \; / \; \Delta\varphi_2 = \; 1 + \; \varepsilon \; . \tag{5}$$

By the way if this formula is divided by Δt time, than gives the ratio between the peripheral velocities, and taking into account formula (3), after some conversion the s slip of the belt-drive is

$$s = \frac{v_1 - v_2}{v_1} = 1 - \frac{v_2}{v_1} = 1 - \frac{1}{1+\varepsilon} = \frac{\varepsilon}{1+\varepsilon} = \frac{\Delta F/\sigma}{1+ \Delta F/\sigma} = \frac{\Delta F}{\sigma + \Delta F} \; . \tag{6}$$

3 SIMPLE MODEL OF THE DEFORMATIONS IN THE WHEEL-RAIL CONTACT

The model of the deformations of the wheel-rail longitudinal connection is sown in Fig. 2. Similar to belt-drive, the deformations of the wheel-surface and the rail-surface are proportional to the transmitted force. If during Δt time there is $\Delta x_o = R \; \Delta\varphi_o$ common length, which come to contact, and $\Delta\varphi_g$ is the angular rotation of the wheel, Δx is the

distance covered, and s_W and s_R are the local stiffness of the wheel surface and rail surface, then the force transmitted by the flexible connection is

$$F = s_W \left(R\,\Delta\varphi_g - R\,\Delta\varphi_o \right) = s_R \left(\Delta x_o - \Delta x \right) . \tag{7}$$

Taking into account that $\Delta x_o = R\,\Delta\varphi_o$, after some conversion

$$F\,(1/s_W + 1/s_R) = F / s = R\,\Delta\varphi_g - \Delta x , \tag{8}$$

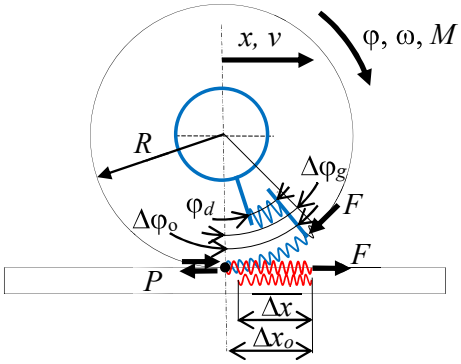

Fig. 2 Model of the deformations of the wheel-rail longitudinal connection

Where the s resultant stiffness is defined as the resultant of the in-line spring system of the s_W wheel surface stiffness and the s_R rail surface stiffness, by formula: $1/s = 1/s_W + 1/s_R$. Similar to belt-drive, this resultant stiffness is also inversely proportional to length of the surfaces, so similar to formula (2), it is necessary to define a specific-stiffness σ ([σ]=N) by the formula below

$$\sigma = s\,\Delta x . \tag{9}$$

Similar to formula (4), the relationship between the F force end ε relative deformation is now

$$\varepsilon = F/\sigma \tag{10}$$

In formula (8) taking into account both this (10) and previous (9) formulas, after conversions

$$R\,\Delta\varphi_g = \Delta x + F\,\Delta x / \sigma = \Delta x \left(1 + F / \sigma \right) = \Delta x \left(1 + \varepsilon \right) \tag{11}$$

is the relationship between the $\Delta\varphi_g$ angular rotation of the wheel and the Δx distance covered. If this formula is divided by Δt rolling time, then the relationship between the angular velocity and the velocity of wheel motion can be given as

$$\left(R\,\omega_g - v \right) / v = \varepsilon , \tag{12}$$

so we can state, that this ε relative deformation is equivalent to the creep, which is used general in railway dynamics. Further, from the formula (13) of the ε relative deformation we can write, that

$$F = \sigma\,\varepsilon , \tag{13}$$

so this method means, that the linear creep-depended traction force is used.

In the procedure we want to take into account the flexibility of the contact as well. So it is supposed, that the s_l is the local stiffness, and d_l is the local damping of the contact, so for the F contact force the next formula has to be valid:

$$F = s_l\,R\,\varphi_d + d_l\,R\,\dot{\varphi}_d , \tag{14}$$

where φ_d is the necessary deformation-angular-rotation, and $\dot{\varphi}_d$ its derivative.

In the following the increments are in the focus of the investigation. So at the given moment there is F_o force in the contact, and during next Δt time the next increments are taken into account: Δx longitudinal moving; $\Delta\varphi$ angular rotation of the wheel, $\Delta\varphi_g$ angular rotation due to rolling and $\Delta\varphi_d$ angular rotation due to the deformation. The $\Delta\varphi$ increment of the angular rotation of the wheel is the summa of the two latter, and using the formula (11)

$$R\,\Delta\varphi = R\,\Delta\varphi_g + R\,\Delta\varphi_d = \Delta x\,(1+\varepsilon) + R\,\Delta\varphi_d\,, \tag{15}$$

This relationship is valid between the velocities as well, so

$$R\,\Delta\dot{\varphi} = R\,\Delta\dot{\varphi}_g + R\,\Delta\dot{\varphi}_d = R\,\omega = v\,(1+\varepsilon) + R\,\Delta\dot{\varphi}_d\,, \tag{16}$$

because $\Delta\dot{\varphi} = \omega$ is the angular velocity of the wheel, and $\Delta\dot{x} = \dot{x} = v$ is the motion velocity of the wheel. The formula (14) is valid for the ΔF increment of the force, so

$$F = F_o + \Delta F = F_o + s_l\,R\,\Delta\varphi_d + d_l\,R\,\Delta\dot{\varphi}_d\,. \tag{17}$$

Taking into account the relationships (15) and (16), using the formulas (13), after conversions finally

$$F = \frac{F_o + s_l\,(R\,\Delta\varphi - \Delta x) + d_l\,(R\,\omega - v)}{1 + s_l\,\Delta x / \sigma + d_l\,v / \sigma}\,. \tag{18}$$

In this formula there is the flexibility feature and the linear creep-force feature as well, and it can also be used if Δx and/or v is equivalent to zero. This relationship is valid during that Δt time, while the F force can be considered as constant.

3.1 The non-linear creep-force

A typical non-linear creep-depended longitudinal wheel-rail contact force is shown in Fig. 3. In this case the linearization of this function gives the solution.

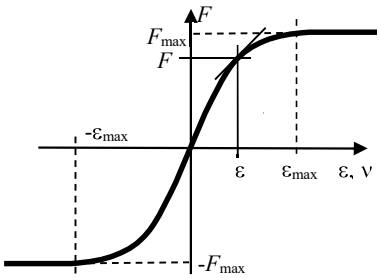

Fig. 3 Typical nonlinear creep-depended longitudinal wheel-rail contact force

At given moment there is F_o force near ν_o creep respectively ε_o relative deformation, and at this point the tangent of the function is σ, so the linearized F force is

$$F = F_o + \sigma\,(\nu - \nu_o) = F_o + \sigma\,(\varepsilon - \varepsilon_o)\,. \tag{19}$$

From this the relative deformation is

$$\varepsilon = (F - F_o)\,/\sigma + \varepsilon_o = \Delta F/\sigma + \varepsilon_o\,. \tag{20}$$

Taking into account this relationship when formula (16) and (17) are combined, after conversions

$$F = F_o + \Delta F = F_o + \frac{s_l\,(R\,\Delta\varphi - \Delta x\,(\,1 + \varepsilon_o\,)) + d_l\,(R\,\omega - v\,(\,1 + \varepsilon_o\,))}{1 + s_l\,\Delta x\,/\,\sigma + d_l\,v\,/\,\sigma}\,. \qquad (21)$$

As it is seen in Fig. 3, the tangent of the creep-diagram can be zero, when the formula above cannot be computed, respectively results zero ΔF. However $\Delta F/\sigma$ can be non-zero, and from formula (21)

$$\Delta F/\sigma = \frac{s_l\,(R\,\Delta\varphi - \Delta x\,(\,1 + \varepsilon_o\,)) + d_l\,(R\,\omega - v\,(\,1 + \varepsilon_o\,))}{\sigma + s_l\,\Delta x + d_l\,v}\,. \qquad (22)$$

It is already can be computed in a first step, and in second step by formula (20) ε relative deformation is known, and consequently from the $F(\varepsilon)$ non-linear function F force can be determined.

3.2 Slipping of the wheel rotation

In case the wheel-slipping the F force has constant $+/-F_{max}$ value, the deformation velocity is zero, so the deformation is "freezed" at $+/-\varepsilon_{max}$ value. The formula (16) loses its validity, and will be again valid, when gives $|\varepsilon|<\varepsilon_{max}$ relative deformation value.

3.3 Stopping of the wheel

The using of the elaborated formula important when the wheel velocity is low, but can be used for the long time simulation as well. In this case there is nothing necessary have to do, when the wheel velocity is decreasing, and the motion of wheel stops.

If during a long-term simulation using of the elaborated formula is ignored, but necessary to stop the wheel, it is necessary to take-up a deformation position. At given moment of the simulation the F_o force and ε_o relative deformation can be considered as known, and formula (21) or (22) can be used during the wheel stopping.

4 DYNAMICAL MODEL FOR THE TESTING OF THE METHOD

For testing the elaborated formulas and method a very simple dynamical model is used. In this model there are two free coordinates: the φ wheel angular rotation and the x longitudinal motion of the wheel. The equations of the motions by Newton's second law are

$$M(t) - R\,F = \Theta\,\ddot{\varphi} \quad \text{and} \quad F - F_r = m\,\ddot{x}\,. \qquad (23)$$

In this equations: $M(t)$ is the traction torque acting on the wheel, as the excitation; R (0.5 m) the radius of the wheel; F is the longitudinal force in the wheel-rail contact, computed by formulas above; F_r is the rolling-resistance force; Θ (187.5 kgm^2) is the moment of inertia of the wheel; and m (10 t) is the moving mass. The non-linear differential equation system is solved numerically, using Euler's method, and non-constant time step. In the simulation the non-linear creep-force is used seen in Fig. 3.

The F_r rolling-resistance force is constant if there is any motion, and computed by the next formula:

$$F_r = \begin{cases} \text{sign}(F)\,\min(\,|F|,\,F_{rmax}\,); & \text{ha } v = 0; \\ \text{sign}(v)\,F_{rmax} & \text{ha } v \neq 0 \end{cases} \qquad (24)$$

In the simulation actually F_{rmax} = 5 kN.

5 RESULTS OF THE TEST

The excitation of the dynamical model described above is the traction-torque explained to the wheel. In the test procedure there are three kinds of traction-torque excitation:

- M1: that means, the torque increases, then has constant level for a short time and after decreases to zero, but the constant level is lower (95 %) than the rolling resistance, so the longitudinal motion of the wheel does not start.
- M2: that means, the torque increases, then has constant level for a short time and after decreases to the level of the rolling resistance. The longitudinal motion of the wheel starts and becomes permanent.
- M3: that means, the torque increases, then has constant level for a short time and after decreases to the negative constant level also for a short time and finally increases to zero level. The longitudinal motion of the wheel starts forward and then turns around, finally stops.

The dynamical simulations are executed taken into account a nonlinear wheel-rail contact (as it is seen in Fig. 3) and two maximum value of the force-coefficient in the wheel-rail contact. In figures mark “mu4” means that the maximum value is 0.4, and mark “mu2” means that the maximum value is 0.2. Because the wheel load is 100 kN, the maximum tangential force in the wheel-rail contact is in first case 40 kN, while in second case 20 kN.

The results are shown in Fig. 4 - Fig. 6, where the forces, accelerations and velocities are presented. In all figures parallel seen the results case of higher force-coefficient on left side, and case of lower force-coefficient on right side. In upper part-figures there are the forces,” F_M” marks the tangential force from the torque, “F_C” marks the force realized in the wheel-rail contact, while the “F_R” marks the rolling-resistance force. In the middle and in the third part-figures the “R fi_pp” respectively “R fi_p” mean the angular acceleration respectively angular velocity of the wheel both of them converted to wheel circumference, and “X_pp” respectively “X_p” mean the longitudinal acceleration respectively velocity of the wheel. In figures the bottom six part-figures show some highlights of the figures above. In figures above the highlighted parts of the diagram are marked by windows.

In Fig. 4 results of excitation torque type M1 presented. As seen, the force from the traction torque is not enough to start the longitudinal motion of the wheel, but due to the torque, the wheel makes damped torsion swing. This swing every time restarts, when there is any change in the trend of the torque. In this case of excitation there is no big difference depending on the force-coefficient, but interesting, that the amplitude of the swing or the force alteration are little bit bigger in case of lower force-coefficient.

The results of the simulations when the excitation type M1 realized seen in Fig. 5. In this excitation case there is relevant difference depending on the force coefficient. In case of higher force coefficient only the restarted torsion swing is seen every time, when the torque trend changed as it was seen in case of previous excitation. Furthermore, there is seen, that the longitudinal motion starts only after that the traction force from the torque reaches the level of the rolling-resistance.

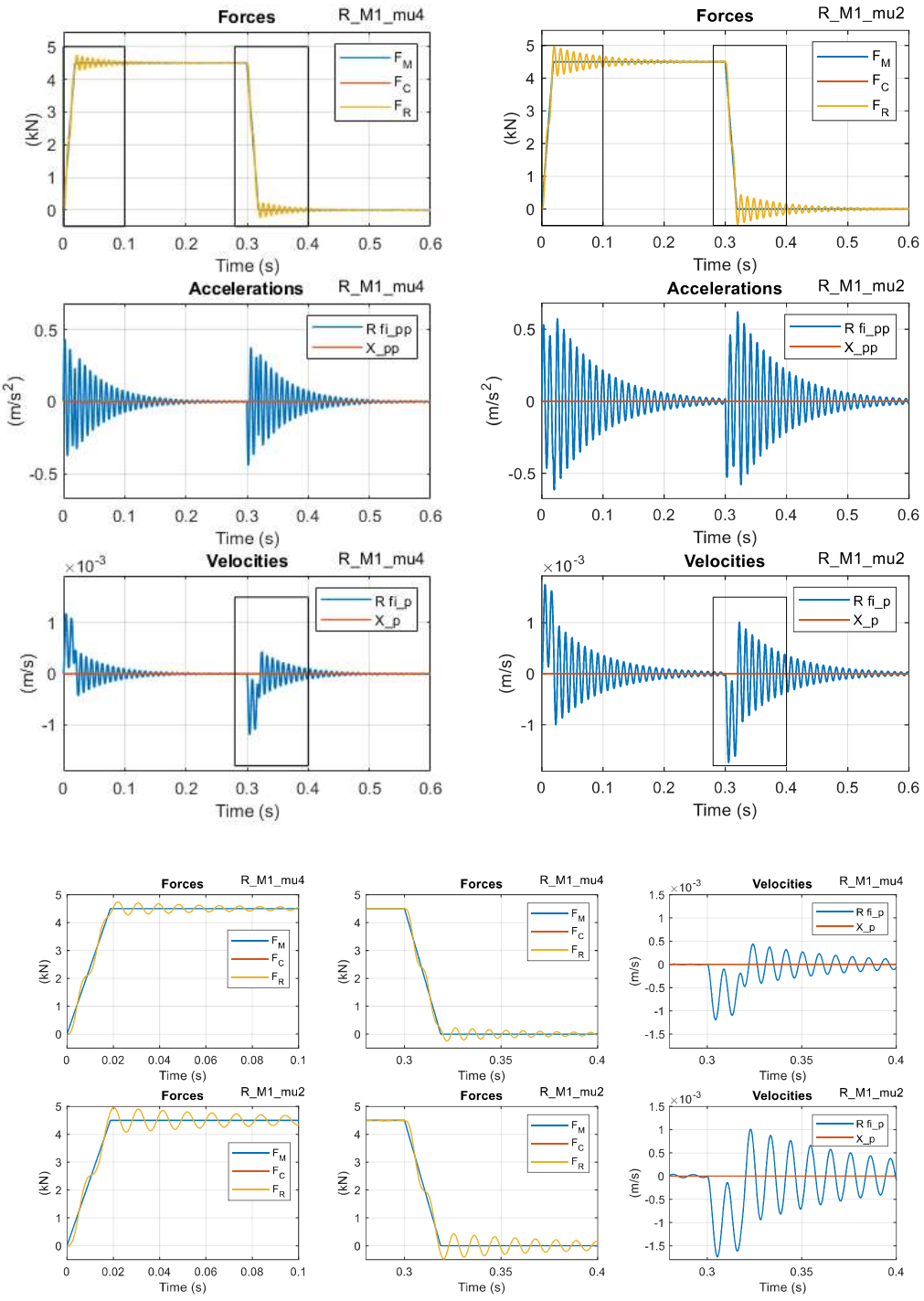

Fig. 4 The simulation result in case of torque-type M1

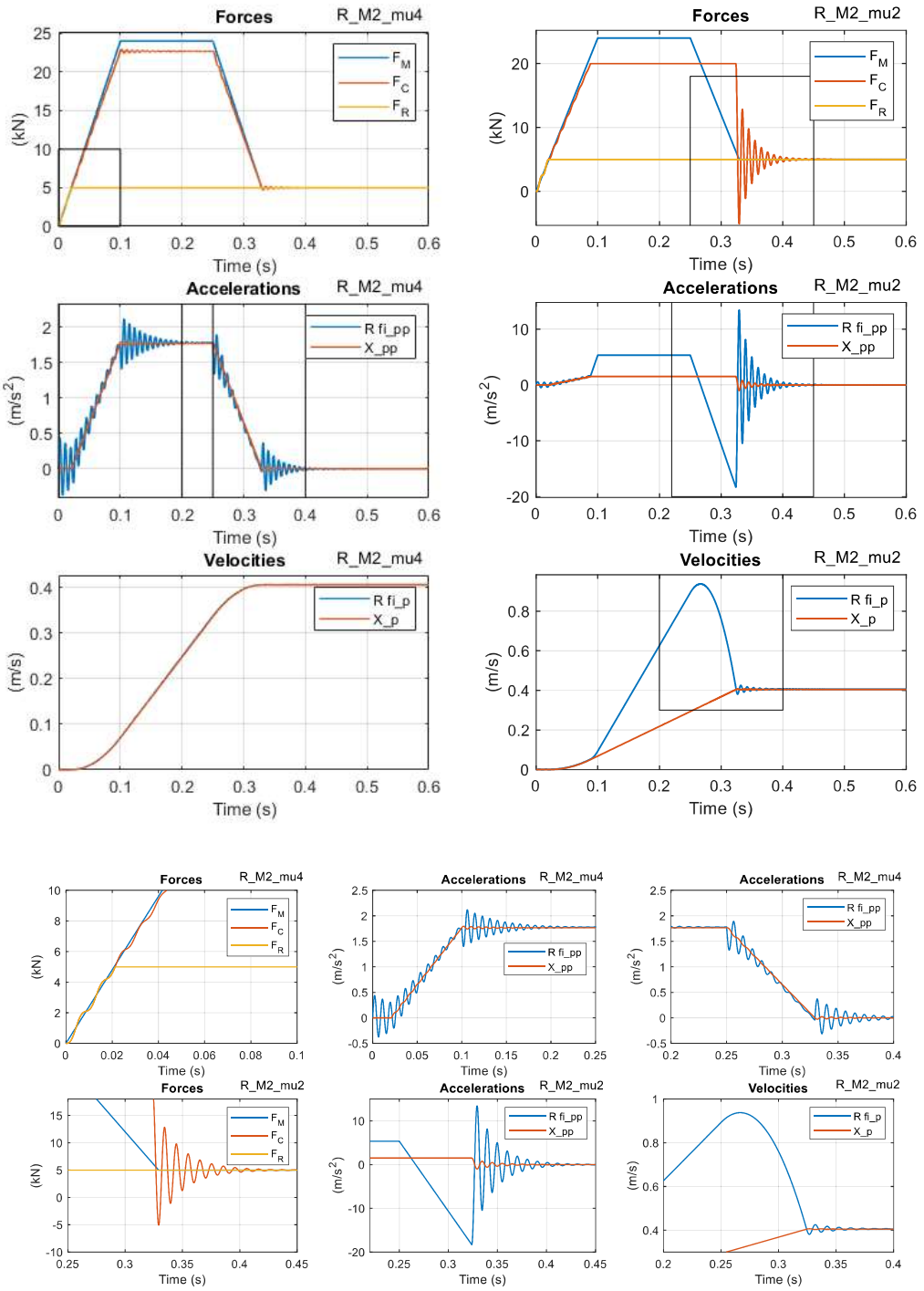

Fig. 5 The simulation result in case of torque-type M2

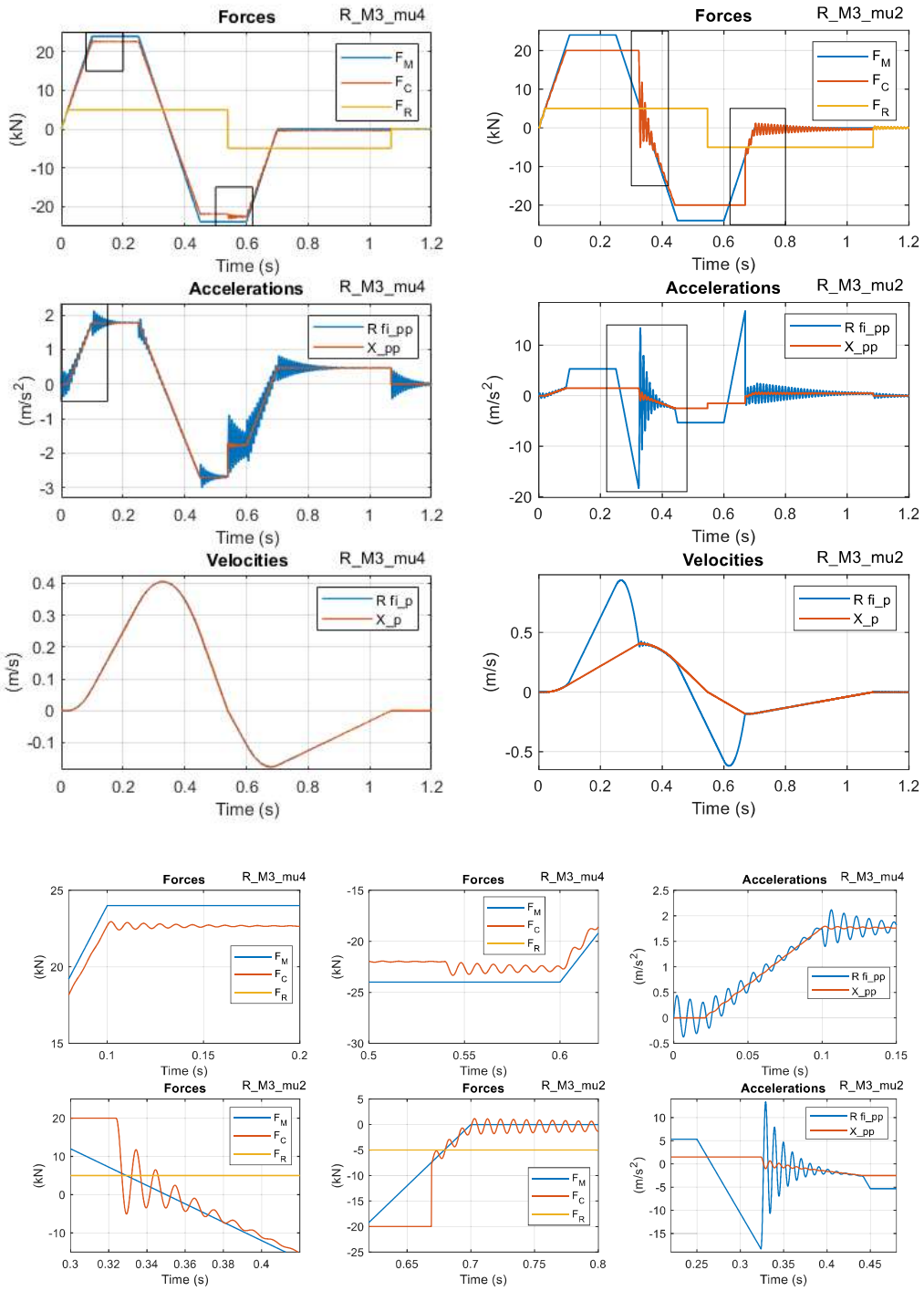

Fig. 6 The simulation result in case of torque-type M3

In case of the lower force-coefficient the traction force from the torque exceeds the maximum value possible in the wheel-rail contact, so the wheel slip occurs, and the wheel rolling by macro-sliding. This macro-sliding ceases very suddenly and long after that the decreasing of the traction force coming from the torque reaches the maximum level of the wheel-rail contact force.

In Fig. 6 the simulation results of the third, M3 type torque excitation are presented. In this case there is a change in the sign of the torque. The wheel longitudinal motion is realized both direction toward and forward, so the zero velocity in this motion occurs as well between these two motions.

When the longitudinal motion stops for a moment, then the sign of the rolling-resistance force also changes, and this causes little swing as well, as it is seen in the case of higher force-coefficient.

In case of the lower force-coefficient the wheel slip occurs both during the forward and backward longitudinal motion of the wheel. As it is seen in diagrams, the wheel is just slipping to backward direction when the change of direction in the longitudinal motion is just occurred.

6 CONCLUDING REMARKS

In this paper a simple computation formula is elaborated to determine the longitudinal force in the wheel-rail contact taking into account the flexible properties of this contact. On the basis of the simulation results can be established:

- In the force computed by the elaborated formula both the flexible and creep-dependent features are prevailed.
- The elaborated formula is applicable to compute realistic longitudinal force in the wheel-rail contact.
- The formula gives an opportunity to compute longitudinal force in case of the zero longitudinal velocity as well.
- The simulation results show that a damped torsion swing every time occurs when there is a change in the trend of the forces affected to the wheel.
- The procedure elaborated can correctly handle the starting and the stopping of the wheel macro-slide as well.

7 REFERENCES

[1] Zobory, I.: How does the friction braked vehicle stop? In: Zobory, István (ed.) Proceedings of the 13th MINI Conference on Vehicle System Dynamics, Identification and Anomalies : VSDIA 2012, Budapest, Hungary: BUTE (2012) 623 p. pp. 101-111. , 11 p.

[2] Szabó, A,: Flexible rolling-connection in the moment of starting and stopping. In: Sábitz, L.(ed.) Studies from subject area of the railway vehicles and vehicle system dynamics : Memory book on occasion of the 70th birthday of Prof.Dr. István Zobory; Budapest, Hungary : Öt évszak Kft. (2014) 317 p. pp. 216-233. (in Hungarian)

ANALYSIS OF TRAM RAIL-WHEEL CONTACT GEOMETRY IN HUNGARIAN COUNTRY-SIDE

Róbert CSÉPKE

infrastructure civil engineer, freelancer
H-2030 Érd, Ürmös u. 19., csepke.robert@gmail.com

Received: August 2022

ABSTRACT

At the Budapest Transport Company (BKV) in Budapest, there have been new rules for rail-wheel contact geometry of tramways in force since November 2019. It was introduced in Proceedings of Bogie'19. These are rules for running characteristic of wheelsets in sharp curves and in a strait track. In this new work it has been analysed, how the regulations of tramways and the newly implemented tram-train system can be fulfilled (between Szeged and Hódmezővásárhely, where new Stadler vehicles use MÁV tracks as well) in the country-side in Hungary. I investigated the local rail types and the geometry of the tread profiles of the Hungarian tram systems. For the simple comparison, I analysed and showed the data in a small table using + and - marks in compliance with the new rules. The findings were, that the features of the popular "Budapest type", so-called "wear out" profile and its "clones" are not adequate. In practice, where this geometry of tread profiles are in use, short-wavy corrugations developed on the rail heads rapidly. Unfortunately, the operators are not always aware of the cause of this phenomenon and how to prevent it. In the beginning of the test operation of the new tram-train line, hunting problem of the vehicle occurred on the MÁV track section, despite there is standardised S1002 profile in use. The speed of the vehicles has to be limited to 80 km/h instead of 100 km/h. As a consequence, it can be seen, that there are lot of necessary improvement needed in this area in the practice. We have to improve the geometry of tram wheel profiles in Hungary, where there are mixed traffic on various track types an rail types. In my opinion the presented rules are able to show this conformity and able to develop new, universally usable tread profile with the lowest unfavourable impact on rails.

Keywords: wheel profile, tram-train, sharp curves, universal tread profile, mixed traffic, RRD

1 INTRODUCTION

At the BOGIE'19 conference [1], a specification system based on the geometrical conformity of rail-wheel contact, which existed only as a proposal at that time, was presented and was "introduced" in November 2019 in the P.1.II. volume [2], which is valid for road railways operated by BKV Zrt. However, it still does not - legally - apply to domestic rural road rail operations. The question arises as to whether, even if they were not covered by the regulation, they would be able to comply with it. Would these smaller operational units be harmonised with these parameters of the track-to-train system, especially in the new tram-train system?

2 THE NEW REGULATION

The rail/wheel contact geometry (hereinafter referred to as RWCG) specifications mentioned in the introduction can be found in the approved instructions [2]. It is not necessary to go into the details here, only the more important parts and points covered here and included in the general introduction are recalled. (Points V, IX, XII-XIV are therefore not included here.)

The new parameters to be introduced for domestic use

Specifications of applicable wheel profile:

I. A min. 120mm of wheel width should be avoided as much as possible.

II. The possibility to use 130mm wheel width, which can be a target of 135mm.

III. In sharp curves, with 1450mm track gauge and asymmetric rail inclination, the possibility of rolling radius difference, of Δr min.=5,5mm.

IV. In the case of 59R2 grooved rail (at 1:∞ rail inclination) and MÁV 48 vignol rail, taking into account 1:40 rail inclination, to fully comply with the parameters below (VI, VII, VIII and X).

V. In the case of other rail profiles and rail inclination combinations, to fully comply with points VI, VII. and VIII. at 1432-1450mm track gauge.

Specifications for rail/wheel contact geometry:

VI. Equivalent conicity ($\tan\gamma_e$, at ±3 mm y diversion and 1435 mm track gauge)

a. max 0,4 and min 0,05 design value (new wheel and rail)

b. max 0,5 and min 0,05 maintenance value (rails and wheel within the wear limit).

VII. Running $\tan\gamma_e$ function can only increase monotonically in the direction of the increase of $\hat{y}$ lateral deflection (in the case of 1432-1450 track gauges).

VIII. In the Δr function, a "jump" greater than 2 mm is not allowed in the interval y = ± 6 mm (except in the range of ± 2 mm of the maximum side deflection).

IX. Less than 1432 mm track gauge in the track is not tolerable.

X. The upper limit of equivalent conicity (max $\tan\gamma_e$) is max 0.6 within the total y lateral displacement range.

The introduction of the lower limit of $\tan\gamma_e$ during hunting oscillation is necessary to ensure the return force of the wheelset to the centre.

However, a "large contact surface" is not good in itself, a conforming, "matching", "messed up" contact is particularly harmful! See [3].

The aim of the regulation is to ensure that the rail-wheel parameters are so harmonised that the result is the least possible material wear, such as rail wear and wheel wear, per unit operating time, as this is in the fundamental technical/economic interest of the operator (and of course the users and those providing the operator's resources).

The railway wheel runs along the track with a lateral oscillation. This is determined by the geometry of the wheel profile, the track gauge, the geometry of the rail head profile and the inclination of the rails. This is the track-wheel contact geometry, which is based on the Klingel formula. [4;5;6]

What is this "favourable" alignment? A system can be harmonised if the following conditions are met:

The properties of the run on *strait* track

- The least favourable $\tan\gamma_e$ equivalent conicity value is sought.
- On tramway tracks, this is not a safety issue, but the aim is to significantly reduce rail and wheel wear by using low “snaking” frequency (high wavelength).
- In the P.1. volume II. published by BKV Zrt. in 2019 [2] the limits are: at a standard y=±3 mm $\tan\gamma_e$ max. 0.4, minimum 0.05 (for "new" rails and wheels).

The properties of the run in *curves with small radii*

- We are looking for the rolling radius difference Δr corresponding to the radius of the curve (in smaller radius curves, the largest possible rolling radius difference on a wheelset, Δr_{wheel} or Rolling Radii Difference; RRD).
- To maximise this, an asymmetric rail inclination (outer rail: 1:∞, inner rail: 1:20) and the maximum possible gauge (e.g. 1450 mm) are used in the track (below R=100-120m).
- In such a curve, the wheelset can run with a free roll and radial axial alignment up to the Δr_w limit above. Below about R=50-70 m, this constellation is exhausted, at which point the outer wheel flange running on the rail head can only fulfil the requirement of free rolling. (And that is the goal!)

Between these properties can be found a *contradiction*! The same wheelset should solve these conflicting requirements.

3 METHODOLOGY FOR THE ANALYSIS OF DOMESTIC RAIL-VEHICLE SYSTEMS IN THE COUNTRY-SIDE

In a previous analysis [7], the current track-to-vehicle systems of Hungarian non-Budapest road railways (trams) are compared, with local specificities identified. As a refreshing new feature, the theoretical analysis of the mixed track parameters and the wheel profile designed for mixed traffic used by the first tram-train in Hungary is also a current task.

On this basis, the following cases were analysed:

- Miskolc - MVK, type Skoda 26THU3 tram,
- Debrecen -DKV, types CAF Urbos 3 and GANZ KCSV-6 trams,
- Szeged - SZKT, types Tatra KT4D és PESA 120Nb trams,
- Szeged-Hódmezővásárhely tram-train – MÁV, Stadler CityLink

A summary of the possible vehicle/wheel/track/track profile variations worth investigating is shown in Table 1.

Table 1. The investigated vehicle/wheel/track/track profile variations

Nr.	Operator	Type od vechicle	Wheel profile	Nominal gauge [mm]	Rail pro-files
1.	MVK	Skoda 26THU3	Skoda 26THU3 (*Combino* „clone")	1435	MÁV48, 59R2
2.	MVK	Skoda 26THU3	Skoda 26THU3 (*Combino* „clone")	1432	60R2
3.	DKV	Ganz KCSV-6	Ganz	1435	MÁV48, 59R2, 60R2
4.	DKV	CAF Urbos 3	CAF "*Debrecen A*"	1435	MÁV48, 59R2, (60R2), B3
5.	DKV	CAF Urbos 3	CAF "*Debrecen C*" (similar as BKV *Siemens Combino* wheel)	1435	MÁV48, 59R2, B3
6.	DKV	CAF Urbos 3	CAF "*Debrecen C*" (Similrar as BKV *Siemens Combino* wheel)	1432	60R2
7.	SZKT	Tatra KT4D	SZKT	1435	MÁV48, 49E1, 59R2,
8.	SZKT	PESA „Swing" 120Nb	SZKT	1435	MÁV48, 49E1, 59R2,
9.	SZKT	Stadler CityLink	„tram-train"	1435	MÁV48, 49E1, 59R2, 54E5
10.	SZKT	Stadler CityLink	„tram-train"	1432	60R2

Space limitations do not allow for a detailed description of all constellations in text form. Those RWCG cases will be highlighted which bring the most anomalies in relation to the limit system, i.e. the most unfavourable ones, or the comparison with each other will provide more information worth mentioning.

The individual results are presented in a summary table. To help you analyse the tabulated data, a description of a general RWCG analysis is presented below as a sample. Let's consider, for example, the specific theoretical properties of a tram wheelset run (rail-wheel contact geometry) in Vignol rail turnout in deflective direction.

„Sample case”

After 2013 produced, type 48 100/100 system turnout, rail profile: MÁV48, track gauge: 1435 mm, rail inclination 1:∞, wheel profile: *Siemens Combino Budapest* "wear out" profile.

Running in curve

Here, the compliance with limit values I to IV (see Chapter 2) is the subject of the assessment.

- There is a ~2x1.5 mm "jump", a total of 3 mm, in the radius-difference diagram at y=~0.0, with a maximum Δr of ~4.2 mm, which occurs at the maximum lateral displacement of ~±7.5 mm (see Figure 1).
- This would theoretically correspond to a radius of about R = 120 m (R=t*r0/Δr; for a Tatra tram with *Combino* wheel profile this takes 1500*335/4.2=119642 mm, which is appr. R=120 m [4;5;8]), so it *is not sufficient* for a radius of 100 m.

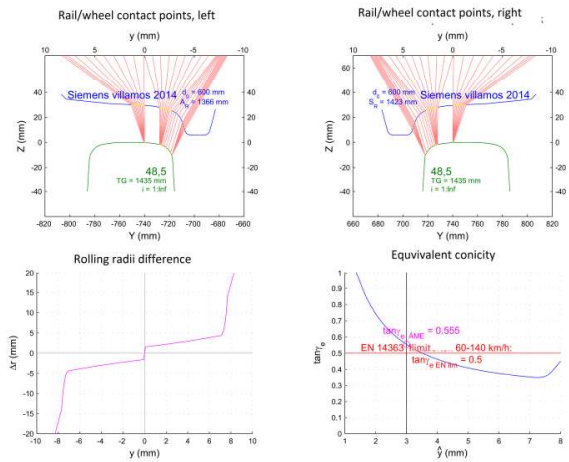

Figure 1 Properties of a *Siemens Combino* wheelset in a turnout type 48 100/100

Running on strait track

In this case, the wheel-rail system contacting is examined in accordance with points VI,VIII, X-XI of Chapter 2.

- From the equivalent conicity diagram in Figure 1, this value is also 0.555 for the y±3 mm comparison value. This does *not satisfy* the rule (max. 0.4)!
- The function is not monotonically increasing (y±~7.5mm strictly mon. decreasing), this is *not satisfying* either!

- There is a jump in it, which occurs when it is already out of the theoretical centre position and thus, given 2x~1.5 mm, it is about 3 mm, *not satisfying*.
- The contact points on the rail head (assuming a rigid material model) are distributed in a small strip(s) of 1-2 mm. The same can be said for the HC fault-generating contact in the gauge corner: this is *unfavourable*.

Unfortunately, the mentioned analysis of all domestic tramway wheels has shown that *none of them comply* with the set of rules that have been introduced. This means that they are detrimental to track wear patterns. This can also be seen in the very large corrugation phenomena on domestic tramways.

4 ANALYSIS OF THE TRAM-TRAIN TRACK/VEHICLE SYSTEM

The wheel profile of the first Hungarian tram-train system for mixed traffic is designed by the Budapest University of Technology [9]. The ORE S1002 profile is designed and manufactured for the running surface. See Figure 2.

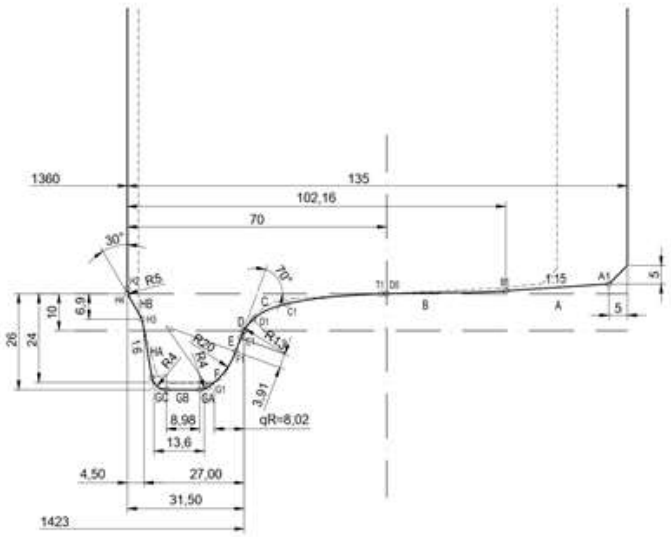

Figure 2 The Hungarian tram-train wheel profile

Based on the analysis presented in Chapter 3, I thought it worthwhile to tabulate the final results of the tram-train wheel analysis shown in Figure 2 for even easier comparison. The rail profile is the 54E5 installed on the MÁV line Nr. 135 (between Szeged-Rókus and Hódmezővásárhely-Népkert), which was installed with a rail inclination of 1:20. I have replaced the results in the table with simple symbols (See Table 2). This makes the compliance or non-compliance of the combination with the set of rules mentioned in chapter 2 even more obvious.

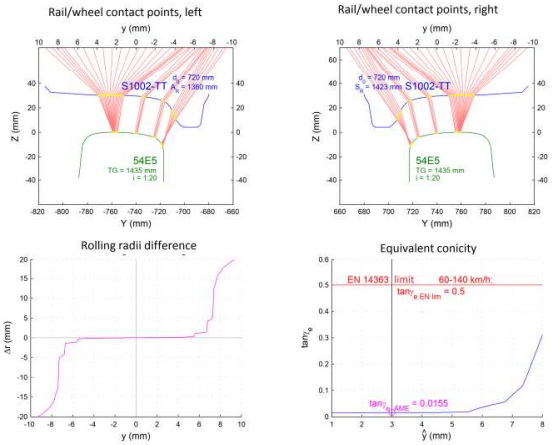

Figure 3 The properties of the Hungarian tram-train wheel

Table 2 Results of the analysis of the Hungarian tram-train wheel profile with symbols

Nr. of rule	Limit(s)	properties of *S1002 Tram-train* wheel	Symbol of result
I.	min. 120 mm	135 mm	+
II.	130 mm	135 mm	+
III.	min. 5,5 mm	4,8 mm	−
IV.	∑ VI.a-X.	− − + − +	−
VI.a.	max. 0,4 min. 0,05	0,0155	− −
VII.	monotonically increa-sing	*OK*	+
VIII.	max. 2 mm	~*y*=±5,5mm=~1,6 ~y=±6,8mm=~3,0	−
X.	max. 0,6 in the whole *y* displacement	~0,32	+
	∑∑	Gen. summary	−

The story is interesting because during the test run, the tram-train vehicle started to "shake" very unpleasantly at speeds of 77-78 km/h on some sections of track. This was so severe that passenger complaints were received (I tried it myself, it was very unpleasant for passengers). This made it impossible to implement the planned timetable. Stadler experimented with a wheel profile insertion designed for a similar vehicle at Sheffield in England [10], which had already shown similarly unpleasant phenomena on other MÁV lines back home. Eventually, the vehicle manufacturer was able to eliminate the unpleasant running phenomenon by changing the characteristics of the shock absorbers between the carriage cabinets. This has now solved the problem, only covered it.

5 CONCLUDING REMARKS

Regardless of that result above (or not), this new tram-train wheel profile is not favourable on tram track sections (in Hódmezővásárhely and Szeged) also [7].

- These results mean that an improved wheel profile that complies with the introduced set of rules is very likely to give good running and wear properties on both tram tracks and normal railway sections, and the same wheelset should solve these conflicting requirements of strait and curved track sections.
- The mentioned rules content the necessary design of the tracks also. These together could ensure the necessary and sufficient cooperation (RWCG) of the rail and wheel and optimised, limited the costs of the wear and corrugation.
- There would be helpful to develop of the rule of "conformity".

This development is ongoing and several versions have been tested and simulated. I have a version called BKV V1 (V1.5) which complies with most of the rules, see Figure 4 for the properties on the 59R2 rail type. Of course, a lot of testing is still needed before the desired result is achieved, but I think this existing regulation would be helpful at the further developments.

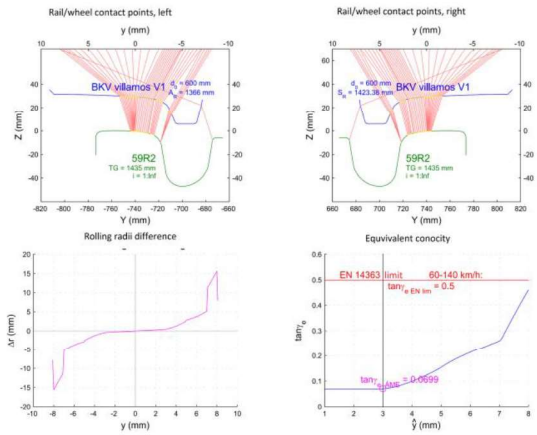

Figure 4 The proposed version of the tram wheel on 59R2 rail type

6 REFERENCES

[1] Csépke, R.: New Regulations of the Rail/Wheel Contact Mechanism for Hungarian Tramways / Proceedings of XI. International Railway Bogie and Running Gear Conference, (BOGIE'19), (aud.. Prof. István Zobory), Department of Railway Vehicles, Aircraft and Ships Faculty of Transportation Engineering and Vehicle Engineering, Budapest University of Technology and Economics, Budapest, 12-15 September

[2] P.1.II. kötet KÖZÚTI VASÚTI PÁLYAÉPÍTÉSI ÉS FENNTARTÁSI MŰSZAKI UTASÍTÁS (V01.02), Chapter 2.13., Budapest, 2019

[3] Brandau J.: Einsatz unsymmetrischer Schienenkopfprofile im Nahverkehr. Hannover: Universität Hannover, Diss. 1999. P. 35–41. DOI: https://doi.org/10.15488/9537

[4] Csépke, R.: Vasúti sín/kerék kapcsolat elemzése a kis sugarú ívekben (2. rész) Javaslat futástechnikai előírások bevezetésére, Sínek Világa, 2019. 2. szám, (11-20. o.).

[5] Zobory, I., Gáti, B., Kádár, L., Hadházi, D.: Járművek és mobil gépek I. Egyetemi tananyag, Budapesti Műszaki és Gazdaságtudományi Egyetem Közlekedésmérnöki és Járműmérnöki Kar, (2012)

[6] Zobory, I.: Prediction of Wheel/Rail Profile Wear: Vehicle System Dynamics, Vol. 28, (1997), ps. 221-259., Swets and Zeitlinger

[7] Csépke, R.: Vasúti sín/kerék kapcsolat elemzése a kis sugarú ívekben (3. rész) Hazai, vidéki villamosüzemek, Sínek Világa, 2021.1. szám, (9-18. o.).

[8] Csépke R.: Wheel-Rail Interface in narrow curves. Proceedings of the X. International Conference on Railway Bogies and Running Gears – Department of Rolling Stock of the Scientific Society of Mechanical Engineers : Conference Paper (Budapest, 12–15 September 2016). Budapest, 2016. ps. 297–305.

[9] Kisgyörgy, L., Bocz, P.: Tram-Train kerékprofil vizsgálata Szeged – Hódmezővásárhely Tram-Train járművekkel kapcsolatban, Budapesti Műszaki Egyetem, 2016. március (Második, javított változat)

[10] Crosbee, D., Allen, P. and Carroll, R.: Analysis of design and performance of tram-train profiles for dual-operation running. Proceedings of the Institution of Mechanical Engineers, Part F: Journal of Rail and Rapid Transit, 231 (5). pp. 578-597. (2017) ISSN 0954-4097

SAFETY AGAINST DERAILMENT OF COG RAILWAY VEHICLES WITH SPECIAL CONSIDERATION OF HELIX TWIST OF TRACK

Dipl.-Ing. Karl Tillmetz and Prof. Dr.-Ing. Martin Cichon

STADLER Bussnang AG (CH)
Narrow gauge, Rack railway and Special vehicles
Ernst-Stadler-Strasse 4, CH-9565 Bussnang, Switzerland

Nuremberg Institute of Technology
Institute for Vehicle Engineering (IFZN)
Keßlerplatz 12, D-90489 Nuremberg, Germany

Received: August 26, 2022

ABSTRACT

For the proof of *Safety against Derailment of Cog railway vehicles* (SaD-C), the technical rules AB-EBV, AB 54 given by the Swiss Federal Office of Transport (FOT) and the method of BORGEAUD have been standard for safety evaluation.

In difference to investigations of adhesion vehicles, the objective is to provide evidence of safety mainly in the worst-case scenario of simultaneous activation of both mandatory cogwheel brake systems in downhill sloped curves with crosswind – as a realistic overlay of the critical track situations with the critical conditions of the vehicle.

Based on the approved method of BORGEAUD introduced in the 1970s realized as Fortran / C++ code, STADLER has developed the modern simulation method BOR@SIM using the powerful MBS software SIMPACK© for vehicle dynamics

- to model the physical conditions more precisely,
- to describe the geometric boundary conditions of track layout, vehicle topology, the rail-wheel contact and the cograil-cogwheel contact more precisely and more complete,
- to improve the identified deficits of the previous method and
- to use all the possibilities of a current and approved simulation technology.

Beside other improvements the significant, but previously neglected effect of helix twist of track g_H was identified and re-derived analytically – being relevant in small curve radii R_{min} with large slope gradients N_{max}. On canted track of cog railways the helix twist can occur additionally to the twist of the cant ramp g_U.

In consequence, the evaluation criteria for safety against derailment had to be reviewed and further developed.

For the method BOR@SIM an approval was obtained from Swiss FOT introducing new criteria for safety against derailment of cog railways in the revised FOT guideline FV-MSZ: *Proof of running behaviour of meter gauge, special gauge and cog railways* – replacing the previous method of BORGEAUD and the associated safety criteria of AB-EBV, AB 54.1, which is no longer state-of-the-art.

Keywords: rack railway, cog railway, proof of safety against derailment, cograil-cogwheel contact, helix twist of track

1 INTRODUCTION

This presentation and paper are dedicated to Prof. Otmar KRETTEK who was for long time honorary president of the BOGIE-Conferences. In 1997 Prof. KRETTEK initiated and supervised a diploma thesis [14] on development and design of a cog railway [1] bogie with calculation of *longitudinal stability* and *safety against derailment* based on BORGEAUD's method [11]. Two decades later, the classical calculus was extended to

[1] cog railway: also known as rack-and-pinion railway, rack railway or cogwheel railway

state-of-the-art simulation techniques and a more realistic modelling is introduced: BOR@SIM.

Railway vehicle running gear is designed to high riding comfort in all specified velocity ranges and track qualities, low wear behaviour of all components and rail-wheel contact, low guiding forces and safety against derailment. Safety relevant requirements and corresponding demonstration of conformity for railway vehicles in European Union are described in commission regulation (EU) No 1302/2014 known as technical specifications for interoperability relating to the 'rolling stock – locomotives and passenger rolling stock' subsystem of the rail system in the European Union. For *safety against derailment on twisted track* the regulation refers to EN 14363 [1], Chapters 4, 5 and 6.1, valid for normal gauge adhesion railway vehicles, adapted to narrow gauge in the Swiss Federal Office of Transport (FOT) guideline FV-MSZ [4], Chapter 3.1 *Safety against Derailment of Adhesion railway vehicles* (SaD-A).

Wheel load changes due to tractive or brake forces are neglected. For cog railways these forces [2] are not limited by adhesion coefficients between wheel and rail but by mechanical resistance of the cog and in addition the wheel load decreases by vertical force components in the cog contact [8]. In cooperation with the vertical position of the center of gravity, coupler and buffer this may lead to complete unloading or even lifting of wheels [9]. BORGEAUD added HEUMANN's theory of minimum principle [10] to DOLEZALEK's [8] and PETER's [9] force calculations in [11]. A second method, based on the classical track guiding mechanics was established by PRIBNOW [12]. Meanwhile KALKER's theory on rail-wheel contact [13] was implemented in multibody system (MBS) simulation programs used for adhesion railway vehicles.

As technical specifications for cog railways the technical rules AB-EBV [2], AB 54 and guideline FV-MSZ [4] given by the Swiss FOT are referenced also by international customers and authorities.

Simulation techniques allow modelling track geometries of complete railway lines and special vehicle concepts under consideration of specific situations, e.g. crosswind forces, track irregularities and the effect of helix twist of track at high slope gradients [15].

2 ANALYSIS OF EXISTING METHODS

The methods of BORGEAUD and PRIBNOW were analyzed beforehand and compared with regard to the track and vehicle topology, to the considered effects shown and to the limit criteria. In the analysis of the method developed in the 1970s, a number of simplifications but also neglects were found due to the possibilities at that time.

The technological development of MBS simulation meanwhile offers many powerful possibilities and is therefore far more flexible, more precise and also more controllable.

[2] simultaneous activation of 2 mandatory independent cogwheel brake systems

2.1 Simplifications and Neglects of the previous Method

In the following, only the method of BORGEAUD is considered and single significant simplifications and neglects are explained:

From today's perspective, the *fixed modelling* in a predefined quasi-static state depicts the track and the vehicle in a rather rudimentary manner.

The *track layout* is only defined as a single situation and in a simplified way. The calculations are only carried out at selected track points that are classified as most critical.

All *spring stiffnesses* are only used to predetermine distribution factors in the respective quasi-static state and all *relative vehicle reactions* (e.g. shifts in the center of gravity due to pitching and rolling, torsion of the car body or bogie frame) are neglected.

Consequently, the very important effect of *helix twist of track*, which is really relevant for small curve radii and large slope gradients, is also neglected (see Chapter 4.2).

The basis for calculating the *track guidance* is the method according to HEUMANN [10] from the 1950s, which is no longer state-of-the-art.

The *turning resistance* of the bogies can only be introduced in a simplified manner by a constant turning torque. Neither the *axle guide stiffnesses* nor the exact *wheel and rail profiles* are taken into account.

The vehicle topology is limited to a *car with 2 bogies*, each with a maximum of 3 axles. Articulated vehicles have to be reduced and calculated in single steps.

These inaccuracies in modelling are compensated by *safety margins* of 5 to 25 % ([2], [3]).

On the other hand, in the previous modelling, centers of gravity and coupling forces should be assumed to act on the 'less favorable side', which results in conservative assumptions and overlays. However, finding the 'unfavorable side' of articulated vehicles is not trivial.

2.2 Potential of Improvement for an extended Method

Flexibility: By using a commercial MBS simulation tool, e.g. SIMPACK©, parameterizable models with individual vehicle, bogie and gear topologies can be generated – with clear data management and possibilities for modularization and automation.

Precision: Track layouts (including cant twist and helix twist, real tracks from the track layout database in Figure 8 in Annex 8.3), wheel and rail profiles and the rail-wheel contact (multipoint contact) can be precisely defined and reliably calculated. The calculation methods are used globally and are validated.

Controllability: The calculation results (time step integration) can be verified in various ways. In addition to the standard output channels of the joint and force elements, sensors can also be freely defined, which can be clearly displayed in post-processing and exported for further analysis (e.g. PDF | CSV).

3 INTEGRATION OF BORGEAUD INTO SIMPACK© (BOR@SIM)

Significant parts of the program BORGEAUD were integrated into SIMPACK© by porting or corresponding modelling (BOR@SIM submodules and models in Figure 9 and Figure 10 in Annex 8.4).

Therefore, the following effects on wheel unloading ΔQ (Figure 1) can now be illustrated:

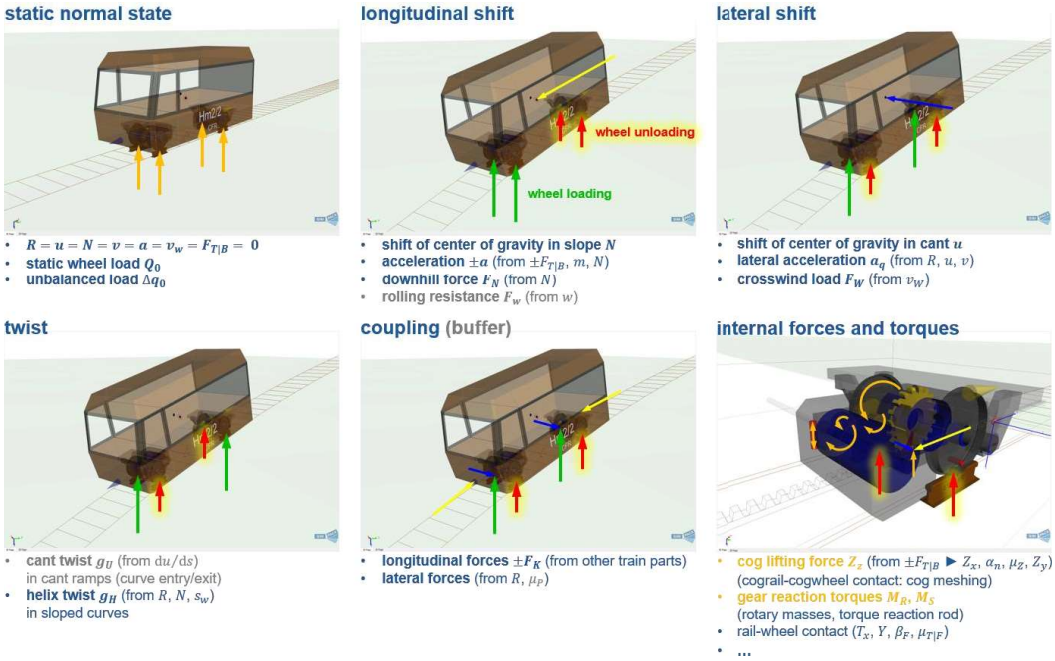

Figure 1: Effects on wheel unloading ΔQ

3.1 Cograil-Cogwheel Contact

The cograil-cogwheel contact (*cog meshing, 'quasi-static impulse'*) described in [11], Chapter 2.5f was ported directly as an algorithm from Fortran / C++ source code of BORGEAUD and modelled in the BOR@SIM submodules **WSG** (wheelset with gear/cogwheel) and **BG** (bogie with gear):

- longitudinal cog force (traction/brake)
- lateral cog force (guidance by friction)
- vertical cog force (lift due to cog meshing and friction)

The cog meshings, assumed to be constant in [11], are modelled variable in BOR@SIM and are therefore more conservative in case the wheelset is lifted or the cogwheel penetrates less the cograil.

3.2 Gear Reactions

The gear reactions (forces and torques from the rotatory masses and the torque reaction rod) described in [11], Chapter 4 were integrated in the BOR@SIM submodules **MG** (motor + gear) and **BG** (bogie with gear) by modelling the *complete drive train*.

The forces occurring during *quasi-static braking* [3] (traction and inertial forces) were verified by comparisons with the reactions from the corresponding dynamic braking.

3.3 Coupling Forces in the Train Set

The forces in the train set described in [11], Chapters 2.3 and 5 were modelled in the BOR@SIM submodule **VxT2** (train set with in front and rear wagons [4]). Herein the track layout **Trk**, the *train set including couplings* and the speed controller for the quasi-static braking are defined in single scenarios.

3.4 Crosswind Forces

The calculation method for the *quasi-static crosswind* in the BOR@SIM submodule **VxT2** was taken from the current simulation method for stability in crosswind based on DB guideline 807.04 [7] and corresponds to that of BORGEAUD. The conditions are defined within each scenario.

4 VERIFICATION OF BOR@SIM USING BORGEAUD

The verification was based on 7 real vehicle projects (Figure 2) of the 5 vehicle model families:

- **TL** MOB HGem 2/2 (2 traction cogwheels)
- **TW** BZB He 4/4 (4 traction cogwheels)
  MGB NZW (1 brake cogwheel)
- **GTW** MVR Beh 2/6 (2 traction + 2 brake cogwheels)
- **GTZ** BOB ABDeh 8/8 (8 traction cogwheels)
  WAB Bhe 4/8 (4 traction cogwheels)
- **FLIRT** GGB Bhe 4/6 (4 traction + 2 brake cogwheels)

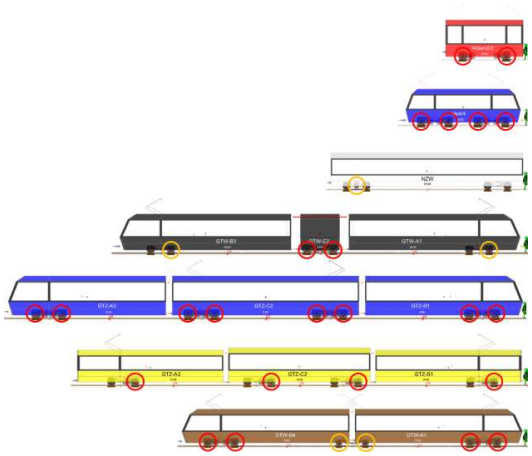

Figure 2: 7 real vehicle projects
with traction cogwheels (red) and brake cogwheels (orange)

[3] in the case of quasi-static braking, the inertial forces are artificially applied to the bodies.
[4] reduction of the adjacent train parts to each 2-axle cars (vehicle geometry and mass, virtual pivot base, coupling, traction/brake forces)

The simplifications and neglects of the previous method could be found and reproduced (Figure 6 in Annex 8.1):

- In BORGEAUD (flat track), the uphill-side wheel on the inner rail of the curve usually appears as the critical position – at 'fast' curving.
- With the effect of the helix twist, the uphill-side wheel on the outer rail of the curve will be unloaded so much, that this now becomes the real critical position – increasing when driving slowly through a (canted) curve.

This change in the position of the critical wheel unloading to the outside of the curve also means that the crosswind to inwards the curve and driving with the coupling tension forces becomes the most unfavorable load combination.

4.1 Results

For the analysis, comparison tables and charts were made of the following main results:

• Friction (cograil-cogwheel)	$\mu_{Z,y}$ und $\mu_{Z,z}$	identical
• Cog forces (cograil-cogwheel)	Z_x, Z_y und Z_z	identical
• Wheel forces (rail-wheel)	T_x, Y, Q	partially similar
• Safety against Derailment	Y/Q, $\Delta Q/\bar{Q}_0$, Δz_R	no comparison possible [5]
• Output values of BORGEAUD	R_0, S_Q, S_R	only unsharp comparison possible [6]

Both, the single vehicle and train sets, are considered, with or without crosswind. To find the most unfavorable basic scenario, right and left turns, slow and fast curving (lateral acceleration inside / outside) were evaluated.

In all verified cases, with the BOR@SIM method, the most unfavorable composition is the single vehicle driving slowly.

It turns out that the selected limit values are appropriate and that the previously approved vehicles can be evaluated in a similarly critical manner.

4.2 The Helix Twist of Track g_H

The common known track twist on cant ramps – cant twist g_U for short – which is being relevant for safety against derailment on adhesion railways ([1], [4]), can easily be calculated to

$$g_U = \frac{\mathrm{d}u}{\mathrm{d}s} = \frac{u}{l_U}$$

As a further track twist based on the examination results described above, the track twist in sloped curves – helix twist g_H for short – was found, re-derived analytically (Figure 3, see Schweizer Eisenbahn-Revue 12/2020 [15]) and verified. It depends on the slope gradient N, the curve radius R and the rail tapeline distance s_w.

[5] defined only in BOR@SIM (according to current standards, e.g. EN 14363 [1])
[6] unsharp comparison, due to split of the wheel forces (Figure 7 in Annex 8.2).

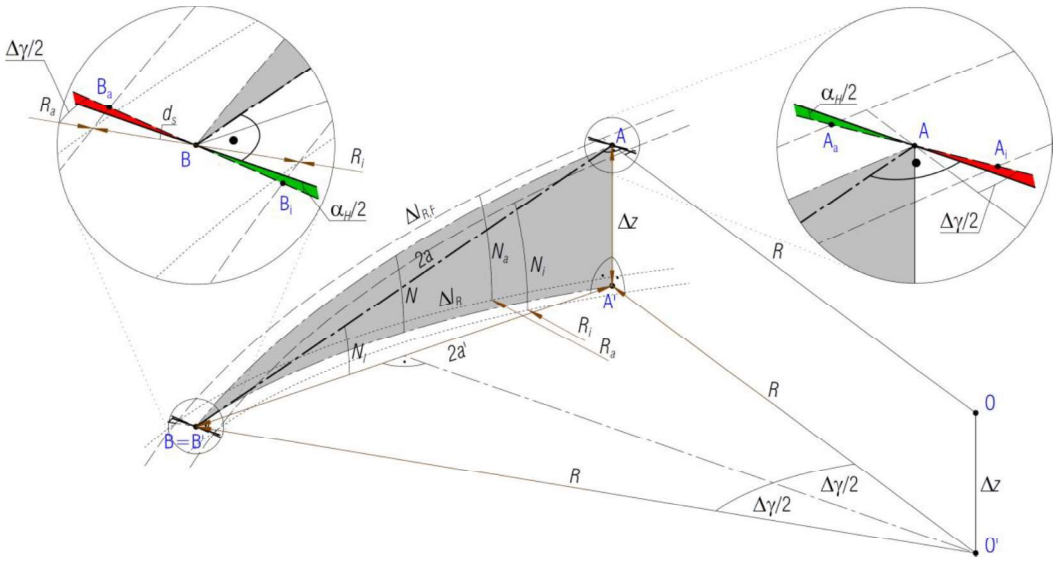

Figure 3: Derivation of the helix twist g_H

$$g_H = \frac{N_a - N_i}{1+N^2}\,\mathrm{sign}(R)$$

$$= \frac{-N}{1+N^2}\,\frac{R\,s_W}{R^2 - \left(\frac{s_W}{2}\right)^2}$$

$$\approx \frac{-N}{1+N^2}\,\frac{s_W}{R}$$

Some examples of maximum helix twists $g_{H,max}$ (combinations of $R_{k,min}$ und $N_{k,max}$) are given in Table 1 in Annex 8.1. This shows that the helix twists g_H, yet non-limited in cog railways, are of the same magnitude as the cant twists g_U limited according to AB-EBV [2] AB 17.

Both types of track twist can occur superimposed, giving the total track twist:

$$g^0 = g_U + g_H$$

As shown in Figure 4 and Figure 5, the most critical situation is the transition between the hillside ramp and the full curve, so it depends on the track position and not on the direction of travel:

- In the slope inclination ($N > 0$ ‰), the leading, curve outside wheel is unloaded shortly (Figure 4) – simultaneous with uphill start-up or static traction.
- In the slope declination ($N < 0$ ‰), the trailing, curve outside wheel is unloaded shortly (Figure 5) – simultaneous with downhill slow-down or static braking.
  A overlay with braking of both mandatory cogwheel brake systems is unlikely.

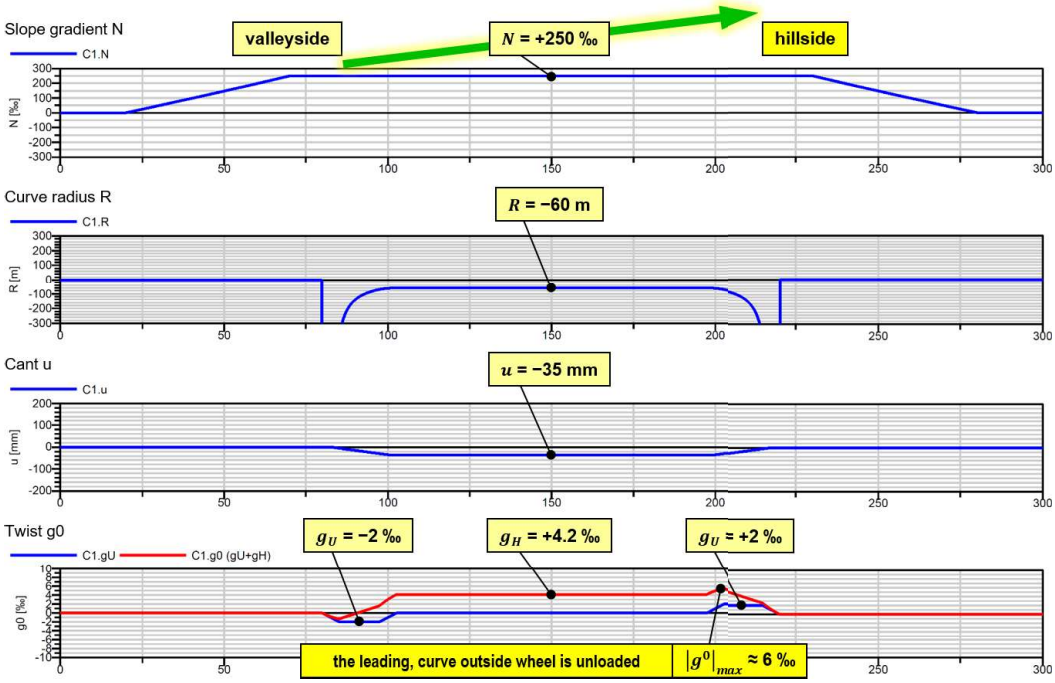

Figure 4: Total track twist g^0 in the slope inclination ($N > 0$ ‰)

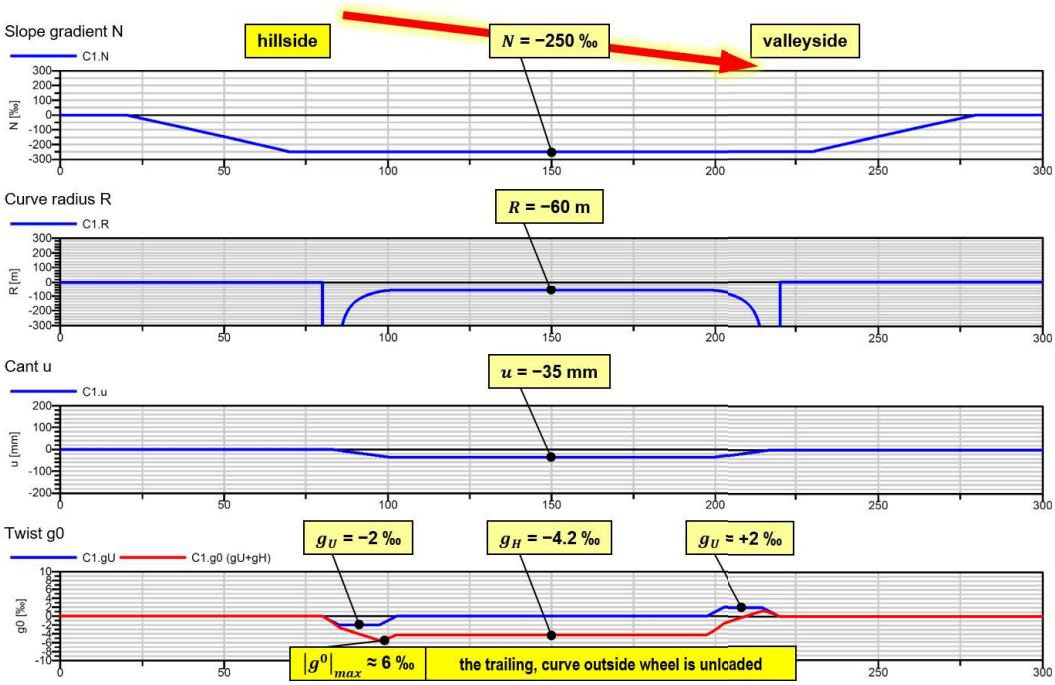

Figure 5: Total track twist g^0 in the slope declination ($N < 0$ ‰)

5 PROOF CONDITIONS

Corresponding to AB-EBV [2], AB 54.1 the following test conditions are applicable:

- Definition of specific track characteristics in agreement with responsible positions of infrastructure and authorities
  - curve radius $R \geq 60$ m (AB-EBV [2], AB 17, 5.2 / R RTE 22546 [5], 7.2)
  - cant $u \leq 35$ mm (AB-EBV [2], AB 17, 3.4 / R RTE 22546 [5], 5.5)
  - slope gradient $N \leq 250$ ‰ (AB-EBV [2], AB 17, 7.2 / R RTE 22546 [5], 9.2)
  - cant twist $g_U \leq 2.5$ ‰ (3.0 ‰) (AB-EBV [2], AB 17, 4.2 / R RTE 22546 [5], 6.2)
  - no track irregularities $\Delta g^+ = 0$ ‰ (common practice)
  - difference of wheel loads $\Delta q_0 \leq 5$ % (AB-EBV [2], AB 47.1, 2.2 / from measurements)
  - velocity (in track level) $v_F \leq 40$ km/h (AB-EBV [2], AB 76.1.a, 9+10)
  - velocity of crosswind $v_W \geq 50$ km/h (AB-EBV [2], AB 54.1, 5.3 / from measurements)
- friction coefficients
  - wheel flange $\mu_F = 0.3 \mid 0.15$ (AB-EBV [2], AB 54.1, 3.4)
  - wheel tread $\mu_T = 0.3$ (AB-EBV [2], AB 54.1, 3.4)
  - cograil $\mu_Z = 0.15$ (AB-EBV [2], AB 54.1, 3.4)
- brake force (from brake calculus) (AB-EBV [2], AB 54.2, 2.2) / from measurements
- vehicle condition
  - tare weight (if applicable gross weight) (composition like in operation)
  - nominal / air spring (no consideration of double faults, i.e. only double brake)
- Investigation with series-compliant wheel profiles and infrastructure network specific rail profiles (both in nominal condition) as well as with nominal track geometry (gauge, rail inclination).
- Further installation tolerances, wear and weather conditions are not taken into consideration.
- As additional safety margin, simulations with increased friction coefficient μ_Z for cograil-cogwheel contact are performed in specific scenarios (see Chapter 6.2).

6 EVALUATION CRITERIA

In 1929 the requirement of the Swiss FOT requested only longitudinal stability in straight track based on DOLEZALEK [8] and PETER [9] and the safety limit value was depending on the slope gradient, see comment No 8 in [3]. To overcome dependence on slope gradient, in the 1970s the safety factor for longitudinal stability S_Q was redefined and the safety factor for safety against derailment S_R [7] was introduced as follows:

$$S_Q = 1 + \frac{Q_{eff}}{Q_0}$$

longitudinal stability

(Q: load of wheelset vertical to track)

$$S_R = 1 + \frac{R_{eff}}{R_0}$$

safety against derailment

(R: wheel load vertical to track)

[7] the limit values S_R and $\Delta Q / \overline{Q}_0$ are compared in Annex 8.2.

The differentiation to the two cases *longitudinal stability* and *safety against derailment* is not motivated physically but historically. For longitudinal stability lateral forces due to rail-wheel contact or crosswind force are not considered. For evaluation of safety against derailment, vertical and lateral contact forces are investigated separately according to HEUMANN's calculus.

In addition, the helix twist in curved track with slope gradient was out of scope. Modern simulation methods enable to consider complete layout of the line with specific disturbance implementation. Thus, the evaluation criteria have to be reconsidered and an evaluation of specific limit values is required with respect to EN 14363 [1]. Based on these and the following considerations the FOT guideline FV-MSZ [4], Chapter 3.2 *Safety against Derailment of Cog railway vehicles* (SaD-C) was revised and introduced effectively.

6.1 Multilevel Security Criterion

According to EN 14363 [1] for normal gauge adhesion railway vehicles the following criteria are to be evaluated:

Wheel unloading factor $\Delta Q/\bar{Q}_0 \leq 60\ \%$ on twisted track is considered without brake or tractive forces. Because of high longitudinal deceleration and acceleration of cog railway vehicles, consecutive wheel load changes cannot be neglected and the limit value has to be adapted. Under consideration of quasi-static braking with both mandatory cogwheel brake systems for downhill run of the vehicle in sloped curves with crosswind the limit value of the relative wheel unloading $\Delta Q/\bar{Q}_0$ [7] evaluates *safety against derailment* with inherent *longitudinal stability* and additionally *stability against overturning for crosswind* [7] and is proposed as follows:

$$\left|\frac{\Delta Q}{\bar{Q}_0}\right| < \left|\frac{\Delta Q}{\bar{Q}_0}\right|_{lim} = 80\ \%$$

relative wheel unloading [1]

($\bar{Q}_0$: mean static wheel load of considered wheelset)

The bias against the limit value in EN 14363 considers brake and tractive forces of cog wheels. In case of exceeding this direct limit value, further investigations have to be performed. With respect to [4], Chapter 3.1, calculations have to comply with newly introduced indirect limit values for $\Delta Q/\bar{Q}_0|_{red}$, Y/Q and Δz:

$$\left|\frac{\Delta Q}{\bar{Q}_0}\right| < \left|\frac{\Delta Q}{\bar{Q}_0}\right|_{lim,red} = 95\ \%$$

relative wheel unloading

(stability against overturning for crosswind [7])

$$\frac{Y}{Q} < \left.\frac{Y}{Q}\right|_{lim} = \frac{2}{3} \cdot \frac{\tan\beta_F - \mu_F}{1 + \mu_F \cdot \tan\beta_F}$$

NADAL's Coefficient

(in full curves, safety against derailment [1])

$$\Delta z < \Delta z_{lim} = 5\ \text{mm}$$

wheel climbing

(safety against derailment [1])

6.2 Safety Margin

As described above, the classical method defined the most critical situations to be calculated. The proposed simulation method enables to simulate complete track line rides in order to find the most safety relevant scenarios. A vehicle run from straight track into a curved slope gradient should be investigated. For this safety case, in addition, calculations with increased friction coefficient μ_Z for cograil-cogwheel contact by 20 % for velocity series 2 (locomotives and locomotive-hauled trains) and by 25 % for velocity series 3 (electrical single or multiple units) should be performed as safety margin and it should be shown that a derailment, i.e. lifting of one wheel with the flange over the rail shoulder, will not appear even if the indirect limit values are exceeded.

7 REFERENCES

[1] EN 14363:2016 E: *Railway applications – Testing and Simulation for the acceptance of running characteristics of railway vehicles – Running behaviour and stationary tests*.
European Standardization Committee (CEN), 2016-03, Correction 2018-12

[2] AB-EBV:2020: *Ausführungsbestimmungen zur Eisenbahnverordnung*
- AB 54 *Zahnradbahnfahrzeuge*,
- AB 76.1.a, 9+10 *Höchstgeschwindigkeit in Abhängigkeit der massgebenden Neigung*.

Swiss Federal Office of Transport (FOT), 2020-07

[3] AB-EBV comments on cog railways:
- 5 *Abnützung der Zahnstangen von Zahnradbahnen*,
- 8 *Längsstabilität und Entgleisungssicherheit* (no longer needed),
- 9 *Mechanische Anhaltebremsen von Zahnradbahnen*,
- 10 *Höchstgeschwindigkeit in Funktion der Streckenneigung für Züge auf Zahnstangenstrecken*,
- 11 *Eingriffverhältnisse der Zahnräder in der Zahnstange – Gefahr des Aufkantens und Überrutschens bei ungenügender Eingriffsdauer*.

Swiss Federal Office of Transport (FOT), 1984-01

[4] BAV guideline FV-MSZ: *Nachweis sicheres Fahrverhalten Meterspur-, Spezialspur- und Zahnradbahnen*.
Swiss Federal Office of Transport (FOT), 2021-01 (V 1.3)

[5] Rules RTE 22546: *Geometrische Gestaltung der Fahrbahn, Meterspur*.
Swiss Union of Public Transport (VöV), 2012-01

[6] Documentation RTE 29700: *Systemtechnik Zahnradbahnen*.
Swiss Union of Public Transport (VöV), 2010-03

[7] DB guideline 807.04: *Richtlinie Aerodynamik / Seitenwind*, with
- Module 807.0439: *Standsicherheit von Fahrzeugen*.

Deutsche Bahn AG (DB), 2006-04

[8] DOLEZALEK, C.A.: *Die Zahnradbahn*.
Eisenbahntechnik der Gegenwart, Kreidels Verlag, 1905

[9] PETER, H.H.: (Part 5) *Spezialbahnen*.
SEEFEHLNER E.E.: Elektrische Zugförderung, Springer-Verlag, 1922

[10] HEUMANN, H.: *Grundzüge der Führung der Schienenfahrzeuge*.
Elektrische Bahnen (eb), 1950 – 1953, Oldenbourg-Verlag, 1954

[11] BORGEAUD, G.: *Stand- und Entgleisungssicherheit bei Zahnradbahnen*.
Schweizerische Bauzeitung (SBZ), 1969 + 1978

[12] PRIBNOW, H.-H.: *Ein Verfahren zur Berechnung der Entgleisungssicherheit von Schienenfahrzeugen*.
Schweizerische Bauzeitung (SBZ), 1972f and
Schweizer Ingenieur und Architekt (SIA), 1984

[13] KALKER, J.J.: *The computation of three-dimensional rolling contact with dry friction.*
International Journal for Numerical Methods in Engineering, 1979

[14] CICHON, M.: *Konzeptuntersuchung und konstruktive Lösungsfindung für ein Motordrehgestell mit Zahnradantrieb*.
FIAT-SIG Schienenfahrzeuge / RWTH Aachen, diploma thesis, 1997

[15] TILLMETZ, K. + BRAESS, P.: *Die Helixverwindung – ein kritischer Einflussfaktor bei der Trassierung und Auslegung von Bergbahnen*.
Schweizer Eisenbahn-Revue, 2020-12 + 2021-01

8 ANNEX

8.1 Verification

Figure 6 shows the comparison of the cogwheel and wheel forces by example of a 4-axle cogwheel locomotive. The middle column shows the results of an adapted SIMPACK model for simulating the neglected helix twist in combination with a simplified cylinder wheel profile (see Figure 7 in Annex 8.2).

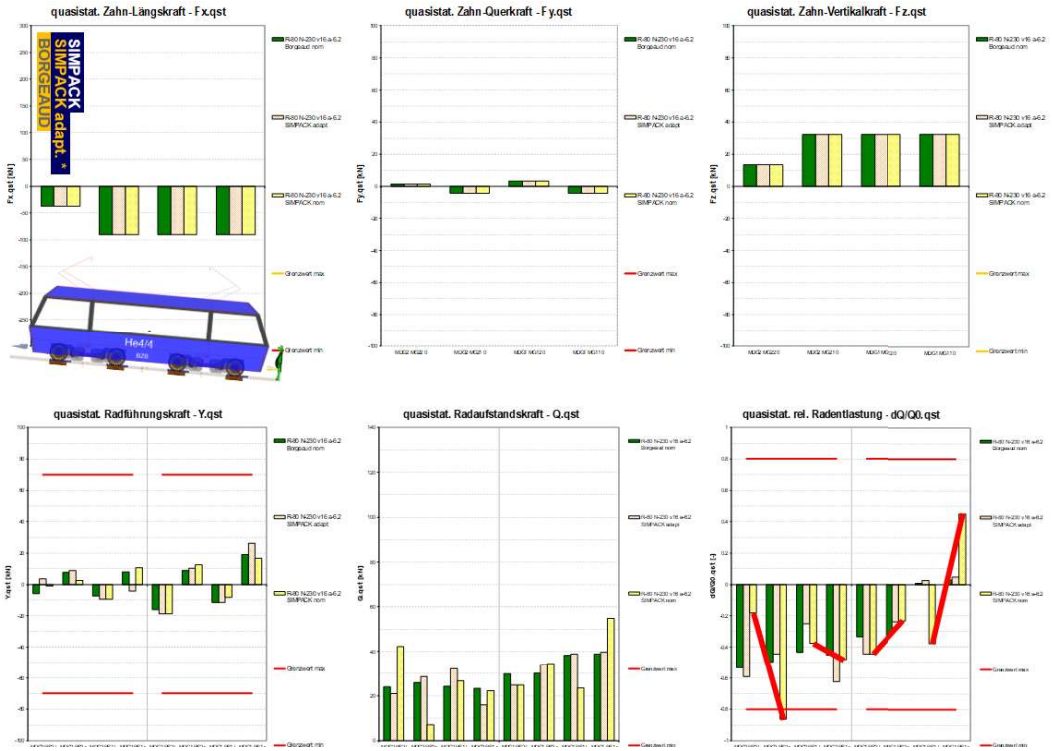

Figure 6: Comparison of the cogwheel and wheel forces
by example of a 4-axle cogwheel locomotive

Network / Line	System [8]	d_s [mm]	$R_{k,min}$ [m]	$N_{k,max}$ [‰]	$g_{H,max}$ [‰]	$2a^*$ [m]	$\alpha_{H,max}$ [°]	Remark
BLS: Bern – Schwarzenburg	-	1500	179	39	0.33	20.000	0.25	no cograil
BOB (Berner Oberland)	R	1050	103	117	1.19	12.290	0.79	
BZB (Zugspitze)	R	1054	80	230	**2.92**	11.240	1.76	DE (Bavaria)
GGB (Gornergrat)	A	1050	**60**	192	**3.28**	12.440	**2.20**	
JB (Jungfrau)	S	1050	73	246	**3.38**	12.390	**2.25**	
MGB: Schöllenen	A	1050	80	181	2.33	12.830	1.61	
MOB (Montreux)	-	1050	**60**	70	1.24	12.830	0.85	no cograil
MPPR (Manitou Pike's Peak)	S	1500	107	252	**3.34**	10.742	1.36	US (Colorado)
MVR: Vevey – Pléiades	S	1050	61	189	**3.18**	12.500	**2.14**	
PB (Pilatus)	L	850	**47**	**480**	**7.15**	7.420	**3.53**	no wheel climb possible (System L)
RB: Vitznau – Rigi Kulm	R	1500	120	233	**2.76**	13.470	1.42	
RhB: Bernina	-	1050	**43**	71	1.75	10.830	1.02	no cograil
SSB: Zacke	R	1050	120	178	1.53	13.320	1.10	DE (Stuttgart)
TdC: Corcovado	R	1050	111	**300**	**2.64**	7.390	1.05	BR (Rio de Janeiro)
TPC: Aigle – Leysin	A	1050	75	228	**3.07**	12.500	**2.07**	
WAB (Wengernalp)	R	850	**56**	**261**	**3.76**	9.750	**2.44**	
WB (Wendelstein)	S	1050	70	230	**3.32**	8.430	1.51	DE (Bavaria)
ZB: Brünig	R	1050	105	118	1.18	12.800	0.81	

Table 1: Examples of maximum helix twists

8.2 Comparison of limit values S_R and $\Delta Q/\bar{Q}_0$

The two expressions

$$S_R = 1 + \frac{R_{eff}}{R_0} = 1 + \frac{R_0+\Delta R}{R_0} = 2 + \frac{\Delta R}{R_0}$$

and

$$\frac{\Delta Q}{\bar{Q}_0} = \frac{Q-\bar{Q}_0}{\bar{Q}_0} = \frac{Q}{\bar{Q}_0} - 1$$

are both effective limit values for the relative wheel unloading.

In a first approximation they differ only by 2, if assumed that the static values

$$R_0 \approx \bar{Q}_0$$

(R_0: static wheel load, $\bar{Q}_0$: mean static wheel load of the wheelset)

and the values under evaluation conditions

$$R_{eff} \leq Q$$

(R_{eff}: in BORGEAUD only tread force $^*R$, Q: (complete) wheel load)

may be equivalent in special cases even if they are in general differently defined.

This is founded by different mechanical modelling of the physical real situation in former and current methods and standards (Figure 7):

[8] cograil systems: Riggenbach, Strub, Abt resp. Locher

BORGEAUD only used the tread force ${}^*R$ as wheel load and the vertical wheel flange force component was neglected as decreasing component.

Current methods do not differ between the two components but use the sum of vertical forces Q_i of all rail-wheel contacts referred to as wheel load Q, appearing equivalently in the resulting contact point.

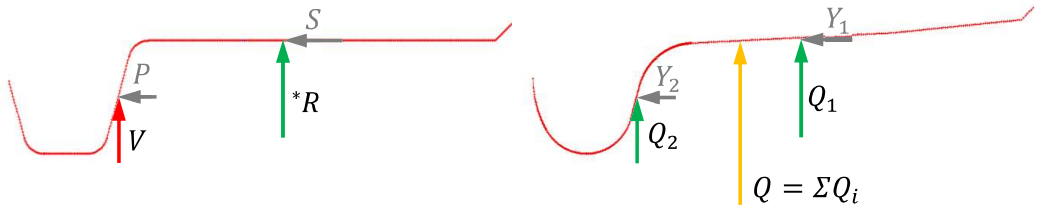

Figure 7: Wheel load in BORGEAUD (left) and in current practice, BOR@SIM (right)

8.3 Track Layout Database

The track layouts are defined as series of track elements (horizontal, cant and vertical) using the software TopoRail© (Figure 8), including also information of switches, cograil sections, engineering structures and stations.

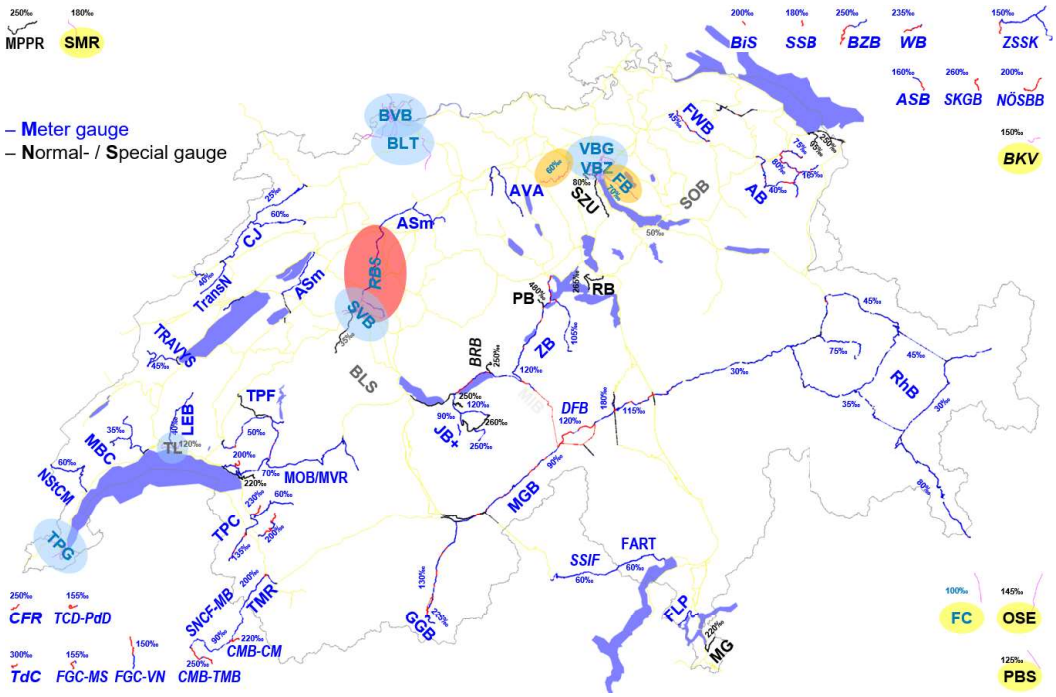

Figure 8: BOR@SIM track layout database (TopoRail©)

8.4 Submodule- and Model Database

The model database is defined like a building kit of submodules (Figure 9), each being runnable for testing. Optional asymmetries are introduced for individual topologies (Figure 10).

Figure 9: BOR@SIM submodule database (components, tracks)

Figure 10: BOR@SIM model database (5 families, basic/scenario)

MULTI BODY ANALYSIS OF A BRAKE RIGGING MECHANISM OF A FREIGHT TRAIN

Francesco Mazzeo, Matteo Santelia, Giorgio Confalonieri, Michele Vignati, Stefano Melzi

Dipartimento di Meccanica
Politecnico di Milano
Via La Masa, 1 I-20156 Milan, Italy

Received: 5 AUGUST 2022

ABSTRACT

This article investigates the dynamic characteristics of a brake rigging mechanism installed on an articulated freight train. Due to the increasing need to reduce rail wear caused by the wheel rail interaction especially during braking in slip conditions, the possibility of revamping existing train to equip them with wheel-slip-protection (WSP) system is considered. To do so, it is necessary to investigate the interaction between the brake rigging mechanism and the wheel-slip-prevention system (WSP) to evaluate the dynamic response of the mechanism in the working bandwidth of WSP. In this work, a multibody model of the rigging mechanism is developed and validated through experimental tests. Then a dynamic analysis of the system during a braking manoeuvre is performed to estimate the frequency response function (FRF) between the pressure in the braking cylinder and the contact force between the braking shoe and the wheel.

Keywords: rigging mechanism, wheel slip prevention, freight trains.

1 INTRODUCTION

Freight train transportation is regaining a central role in logistic system. This would reduce greenhouse gas emissions, truck-induced congestion, and noise pollution, while contributing to a more integrated logistics. As an example of this, the European Union plans on doubling freight rail's modal share by 2030 [1]. Hence the need to modernize and improve the vehicles currently available on the market both in terms of reliability and cost reduction. Among all the possibilities of improvement and the actions that can be taken with these aims, the need to reduce the wear caused by rail-wheel interaction during locking of the wheels is fundamental [2][3]. In fact, during high intensity braking manoeuvres, locking of the wheels could happen, causing an uneven wear of the wheels that results in a modification of the wheels profile [2][3]. This could reduce the stability and the safety of the vehicle and could induce high vibration to the convoy leading to the deterioration of the goods and damaging the vehicle itself [2][3]. At the moment, a preventative maintenance approach is adopted with the aim of changing the worn components before their use would become problematic. With the prospect of increasing the use of the freight transportation system, the scheduling of the maintenance will be more challenging, so it would be safer to avoid (or reduce) the uneven wear of the wheels. This could be achieved by avoiding the locking of the wheels, reducing thus their uneven wear, and increasing the lifetime of the components bringing also evident economic benefits.

The wheel slip prevention (WSP) system is an electro-mechanical system that detects the locking of the wheels and acts on the braking pressure in order to avoid the full sliding of the wheel on the rail. This system is installed especially on passenger high speed trains, where the locking of the wheels at very high speed could cause severe damages. At the moment, freight trains are not equipped with WSP systems, so, the

possibility of revamping existing freight bogies to equip them with wheel-slip-protection (WSP) system is considered. To accomplish this task, it is firstly necessary to investigate the interaction between the brake rigging mechanism and the system (WSP).

Brake rigging mechanisms studied in this paper are a fundamental subsystem composing standard brake framework of freight vehicles. Riggings are mechanical systems that connect, thanks to levers and other components, the pneumatic brake actuator with the brake blocks which act directly on the wheels. A dynamic analysis of these mechanical systems is a fundamental starting point for the design of WSP system for freight trains, since a poor integration of this subsystem can lead to a malfunction of the entire braking system, and a reduction of the braking performance. In this paper, the rigging system of the articulated freight vehicle T3000e is studied as it is one of the most common freight vehicles in Europe.

The study presented in this paper is organised in three main steps. Section 2 shows the multi-body model of the rigging mechanism. All the components of the linkage are modelled as three dimensional (3D) rigid bodies, applying the geometry and inertial characteristics described in the technical drawings. Then, the bodies are assembled in the model introducing joints, spring-damper elements, and force fields.

Section 3 reports the validation of the multi-body model through experimental tests: an experimental campaign was carried out to evaluate the kinematic of the rigging mechanism and compare the measurements with the results obtained with the model.

Finally, in section 4, the dynamic behaviour of the rigging mechanism is studied using numerical simulations: the Frequency-Response-Function (FRF) between the braking force and the input pressure is obtained to understand the interaction of the WSP system with the rigging mechanism.

2 MULTI-BODY MODEL

The vehicle analysed in this paper is the articulated freight wagon T3000e. The single wagon is composed by 2 frames, 3 bogies and 6 wheelsets. It is important to remark that two types of bogies are present in the vehicle: two extremity bogies and one middle bogie and they are equipped with two different types of brake rigging system. In this work, for sake of brevity, just the dynamics of rigging mechanism of the extremity bogies is studied. Fig. 1 shows the rigging mechanism mounted on the front bogie.

Fig. 1 picture of the brake rigging mechanism mounted on the front bogie.

The dynamics of the rigging mechanisms is studied using a multibody model built with Simscape Multibody, a dedicated multibody environment of the software Simulink-Matlab™. The model comprehends rigid bodies, linear spring-damper elements, actuators, nonlinear joints and constraints. Furthermore, the contact problem between the shoes and the wheel is included.

The first step consists in the modelling of the rigid bodies starting from technical drawings. The geometry of the components is modelled using a 3D CAD software and the details that are not important for dynamic simulations, such as threading and casting draft angles, are disregarded. The rigid bodies used for the simulation are shown in Fig. 2.

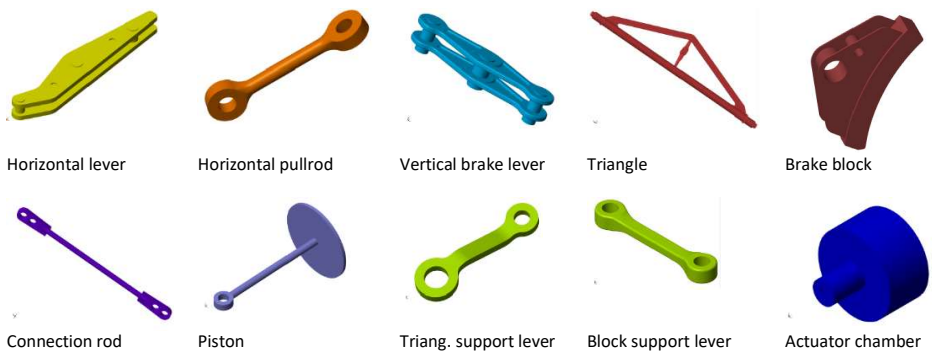

Fig. 2 3D CAD of the rigid bodies assembled in the model

At this point, the CAD models of the components are imported in the multibody environment. In this way, the software computes automatically the inertial characteristics of the pieces, using the geometry from the CAD and the density given by the user.

In order to set up the system correctly, each connection between bodies is created using joint connections, considering the absolute and relative degrees of freedom (d.o.f.) of the system. In addition, in order to simulate the dynamic behaviour of the mechanical system as close as possible to the real one, backlashes relative to joints are modelled. From a mathematical point of view, backlashes are introduced as nonlinear spring elements, that represents an additional d.o.f. with limitations. As it can be seen from Fig. 3, when the position of the d.o.f. exceeds a predefined value, called slack range, an increase of stiffness is introduced. Hence, a repulsion force occurs, in order to simulate the contact between different components. Moreover, a nonlinear damper element is added in parallel to the nonlinear spring to account for energy dissipation and improve numerical integration. The damper coefficient has the same behaviour of the stiffness, with a maximum value of 1e3 Ns/m.

As far as spring/damper element concerns, return spring inside the pneumatic actuators, which have the purpose to restore the brake blocks at the original position after the brakes are released, are modelled. The stiffness of the spring is taken by the technical data of the piston.

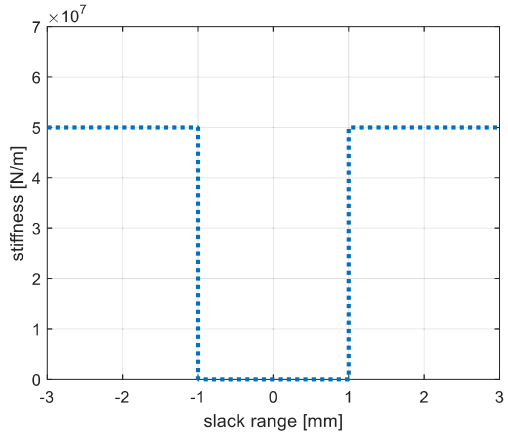

Fig. 3 stiffness coefficient of the backslashes vs slack range

Finally, since the final aim of this paper is to analyse the braking performance of the rigging system, the contact between the brake blocks and the wheel is introduced. A dedicated Simscape block has been used to detect when the bodies are in contact and consequently apply a repulsion force. The contact is automatically detected by the software computing, at each time instant, the distance between the two reference surfaces of the two bodies in contact: the brake pad and the wheel rolling table. The surfaces are discretised performing an interpolation of the geometry given by the CAD model. When the algorithm detects a contact in a certain point, it applies a repulsion force that depends on the local penetration of the two bodies. The force is computed using a nonlinear spring element. The stiffness is set to a value of 5e8 N/m in order to have a good trade-off between a real contact stiffness and avoidance of numerical integration problem. Furthermore, in order to avoid numerical problems, a nonlinear damper element is considered in parallel to the spring [5][6].

At this point, the multibody software can automatically define the non-linear equations of motion that describe the behaviour of the complete mechanical system. The equations of motion are integrated using a 5th order Runge-Kutta integrator, using a fixed step of 1e-5 s. Fig. 4 shows the assembly of the complete model of the system.

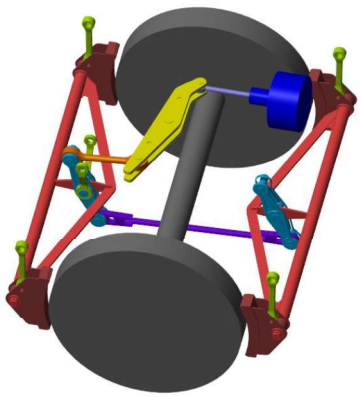

Fig. 4 multibody model of the complete mechanism

3 EXPERIMENTAL TEST AND MODEL VALIDATION

In this section, the multibody model is validated evaluating the braking performance targets required by technical specifications of the bogie for what concerns steady-state value. Regarding the dynamic response of the system, experimental data are used which were acquired in a dedicated experimental campaign.

3.1 Validation through datasheet

In the bogie specifications, the normal contact force between the brake blocks and the wheel is indicated. The values are related to a certain input pressure, and they are valid in steady state conditions. For the first step of the validation of the model, these values are compared with the results of the simulations, in order to achieve a dynamic analysis in steady state conditions. To perform these simulations, the pneumatic actuator is excited with a ramp pressure signal saturated at the steady state value reported in the datasheet and the normal contact force between the shoes and the wheel is measured. As an example, the time history of this kind of simulations in shown in Fig. 5 where a steady state pressure of 1.2 bar is considered.

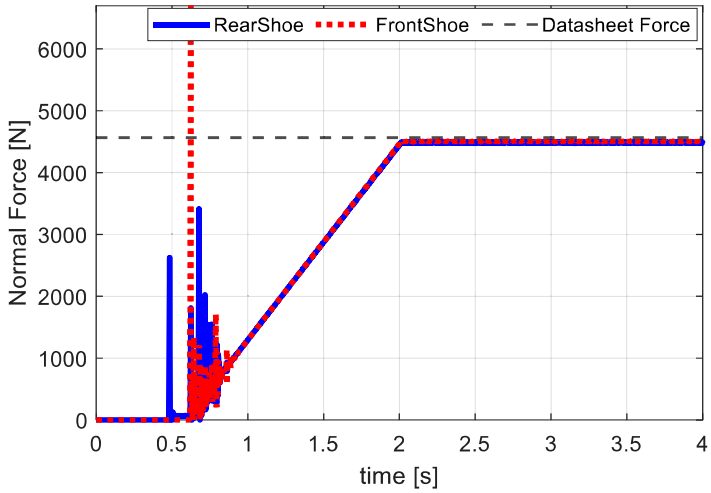

Fig. 5 comparison of the contact force given by the model and the value indicated in the datasheet

The comparison of the simulations results with the design value of the normal contact force is reported in the following table:

	Steady state pressure = 1.2 bar			Steady state pressure = 3.6 bar		
	Design force [kN]	Simulation force [kN]	Relative error [%]	Design force [kN]	Simulation force [kN]	Relative error [%]
Shoe external	4.57	4.49	1.75	16.19	17.11	5.6
Shoe internal	4.57	4.51	1.3	16.19	17.18	6.1

As it can be noticed, the multibody model simulates the contact force with a maximum error of 6 % with respect to the theoretical value. This means that the model can correctly reproduce the rigging ration of the real system.

3.2 Description of experimental tests

Experimental tests consists in free decay and forced motion of the riggin mechanism.

To measure the displacement of some interesting points of the system three laser displacements sensor M7L/200 are used. They were attached to the bogie frame pointing with the laser beam different moving parts of the systems as shown in Fig. 6.

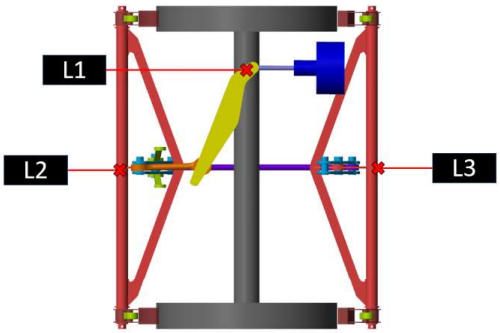

Fig. 6 position of the laser displacement sensors on extremity bogie

Considering Fig. 6, laser L1 points the upper part of the horizontal lever, which is rigidly connected to the piston. In this way, it was possible to measure the stroke of the piston, thus the input given to the system. Laser L2 and L3 measured, respectively, the horizontal displacement of the external triangle, and the internal one. This nomenclature was chosen considering the assembly of the entire bogie (see Fig. 1).

The measurement campaign was organised to perform two types of tests described in the following chapters

3.3 Comparison of the Forced motion

Fisrt test consists in applying a pressure in the brake cylinder and measuring the resulting displacement. This scenario represents a braking condition, and it has the aim of measuring the relation between the piston stroke (L1) and the displacements of the triangles (L2, L3).

The measurements acquired during this test are shown in Fig. 7. In this figure, it is also possible to see the result of the numerical simulation performed imposing the same initial conditions of the measured bogie and the input pressure that allows the same movement of the piston.

Considering Fig. 7 it can be notice that the steady state value obtained using the multibody model is similar to the measured one. These values are reported in in the following table where and the relative error is computed.

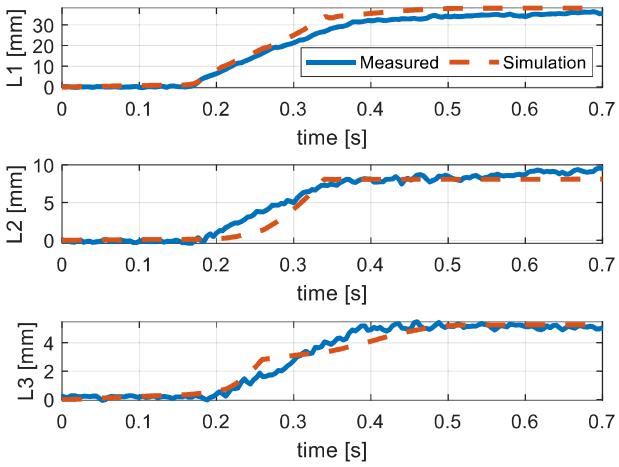

Fig. 7 movement of the triangles: experimental data vs simulation results

	Measure [mm]	Model [mm]	Relative error [%]
Piston stroke: L1	36	38	5.5
External triangle: L2	8.9	8.01	10
Internal triangle: L3	5.11	5.23	2.4

3.4 Comparison of the free decay motion

The second type of tests consisted in the measurement of the free motion of the system when no braking pressure is applied. In particular, the focus was the motion of the triangles (L2, L3) around the equilibrium position when the braking force is not present. To perform this test, the external triangles was pushed towards the wheelset up to obtain a complete contact of the brake blocks and the wheel. At this point, the system is suddenly released, becoming free to oscillate. This is possible since at the equilibrium position, the brake shoes are not in contact with the wheels, so there is a small clearance that allows the vibration of the triangles. This test was then replicated with the multibody model, applying the same initial conditions of the physical system. An important aspect that concerns this test is related to the dimension of the brake blocks. In fact, the experimental tests were performed on a bogie under maintenance, which means that the brake shoes were worn out. This condition strongly influences the behaviour of the system for two main reasons: firstly, because the inertial characteristics of the system change, then, because the gap between the brake shoes and the wheel increases and this will influence the dynamics of the nonlinear system. It must be noticed that the modelling of the components was done considering the technical drawings that represents the geometry of the new components, moreover, being the wear of the brake blocks not uniform, it was not possible to measure the exact geometry of the worn brake blocks mounted during the experimental campaign. For these reasons, a sensitivity analysis was performed, investigating the effect of the wear of the brake blocks on the free motion of the system. For this analysis, the thickness of the shoes is changed assuming a uniform reduction. The

result of this analysis is shown in Fig. 8. In particular, the experimental measurements are compared with three different level of worn shoes: 100% indicates a decrease of thickness of 40 mm, 50% means a decrease of thickness of 20 mm and new shoes are obtained with the dimensions given by the technical drawings.

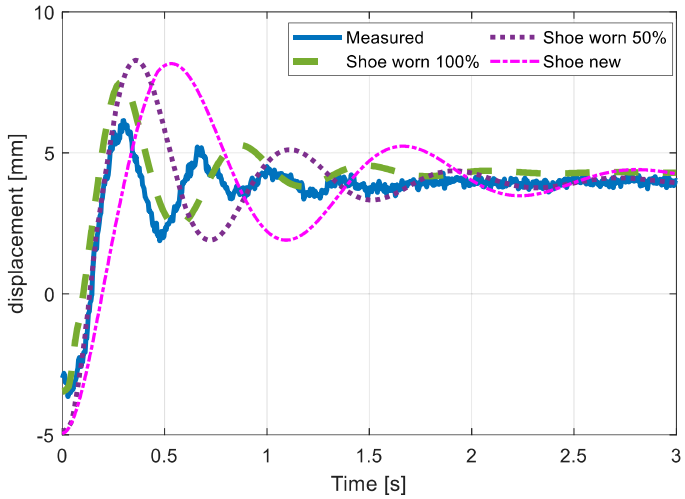

Fig. 8 sensitivity analysis considering different level of worn shoes

As it can be seen from Fig. 8, the free decay is strongly influenced by the wear of the shows. Furthermore, the 100% worn shoes are the ones that better reproduce he behaviour of the experimental data.

To conclude, since the numerical results are in accordance with the experimental tests, the multibody model will be used in order to infer the dynamic characteristics of the system when it is subjected to high frequency excitation.

4 DYNAMIC ANALYSIS

During the activation of the WSP valve, the pressure inside the cylinder varies with a frequency higher than common operative conditions [4]. This could lead to dynamic interaction that could interfere with the proper functioning of the WSP logic. In other words, if the excitation frequency caused by the modulation of the pressure due to the WSP valve is higher than the natural frequency of the rigging mechanism it means that the contact force is not responding properly degrading the WSP performance.

The frequency response function (FRF) is computed considering, as input, the pressure inside the cylinder, and, as output, the normal contact force at the shoe-wheel interface. Furthermore, since the system is not linear, the FRF will be computed considering different amplitude of the input pressure. Considering normal operating frequencies of WSP, a maximum frequency of 10 Hz is considered [4].

The system is excited with a sinusoidal pressure $p(t)$ acting on the cylinder. The force acting on the piston $F_{in}(t)$ can be computed multiplying the input pressure with the frontal surface of the piston A_p:

$$p(t) = P_0 + P_1 \sin(\omega t) \quad (1)$$

$$F_{in}(t) = p(t) A_p \quad (2)$$

Where: $\omega = 2\pi f$ is the circular frequency of the input pressure; f is the frequency of the excitation; P_0 is the bias value of the pressure and P_1 is the amplitude of the pressure variation. Furthermore, the relation $P_0 \geq P_1$ holds since, even if p is a relative pressure, only positive values are considered.

When the pressure is applied, the shoes start to move towards the wheel. In the first part of the cycle, since there is a small clearance between the shoes and the wheel, the normal contact force is null. Then, when the shoes touch the wheel, the normal forces at the contact interfaces start to increase, following the pressure trend. Fig. 9 shows the results of a simulation performed with the sinusoidal input pressure at 1 Hz.

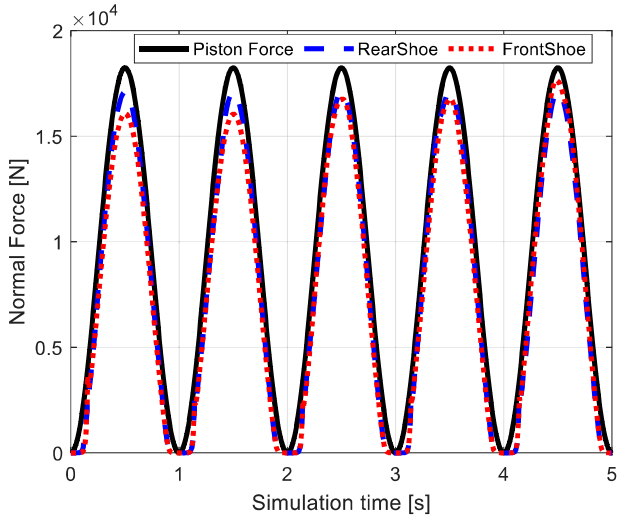

Fig. 9 contact forces considering an input pressure varying at 1 Hz, P0 = P1=1.8 bar.

Hence, the spectra of the normal force resulting at the shoe-wheel interface is computed performing a Fast Fourier Transform (FFT). Considering the frequency k, the frequency response function $H(f_k)$, between the input pressure and the normal force acting of the wheel, can be obtained performing the ratio output over input:

$$H(f_k) = \frac{Y(f_k)}{\mathrm{X}(f_k)} \quad (3)$$

$Y(f_k)$ and $\mathrm{X}(f_k)$ being the spectra of the output and input signal, respectively.

This procedure is performed for several input pressure at different frequencies, starting from 0.5 Hz up to 10 Hz. In this way it is possible to obtain the FRF between the input pressure and the normal contact force between the shoes and the wheel. For sake of semplicity, the FRF is normalized considering the input force, i.e. the force acting on the piston (see eq. 2).

Fig. 10, Fig. 11 and Fig. 12 show the FRF of the system obtained using different values for the amplitude of the input signal. As a matter of fact, being the system nonlinear, the output of the system could be influenced by both the frequency and the amplitude of the input. For this reason, since the operative condition given by the WSP control logic and the WSP valve could vary accordingly to external conditions, a sensitivity analysis is performed in order to study the response of the system at different amplitude of the input pressure.

Fig. 10 shows the FRF of the system obtained considering P0 =1.8 bar and P1 = 1.8 bar. This scenario represents a high intensity braking manoeuvre, when the pressure in the cylinder reaches the maximum value (3.6 bar, corresponding to the maximum available pressure in the general conduct) and it decreases up to a null value.

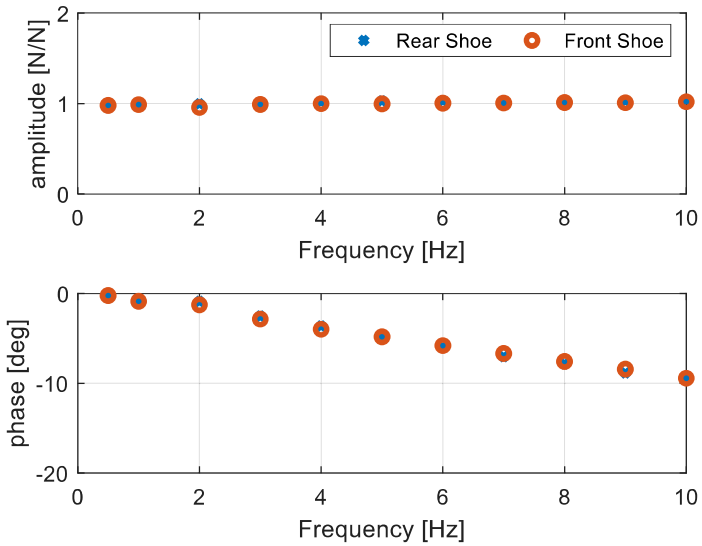

Fig. 10 Frequency Response Function of the system. P0 = P1 = 1.8 bar

It can be noticed that the amplitude of the FRF is mostly constant, and the phase remains near 0 especially in the first part of the plot. This means that the system works in the quasi-static region and the resonance is at frequency higher that 10 Hz.

Fig. 11 shows the FRF of the system obtained with a P0 = 2.7 bar and P1 = 0.9 bar, while the FRF shown in Fig. 12 is obtained considering P0 = 2.25 bar and P1 = 1.35 bar. These two cases represent a condition in which the pressure never reaches 0, so the shoes and the wheel are always in contact.

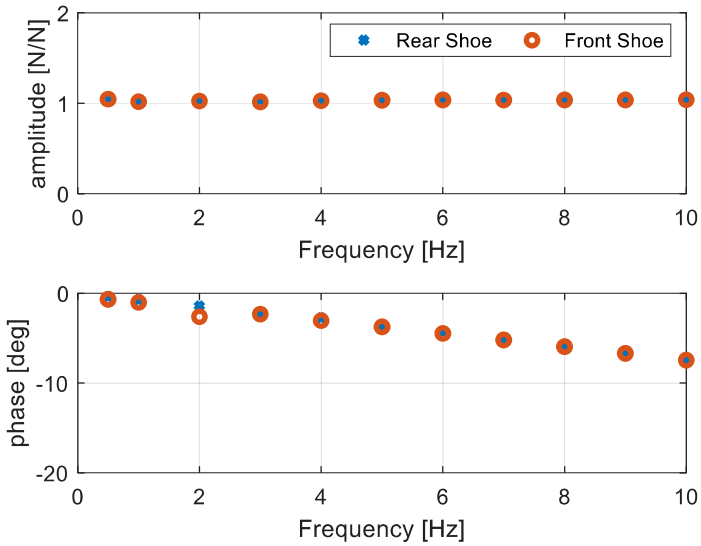

Fig. 11 Frequency Response Function of the system. P0 = 2.7 bar = 0.9 bar

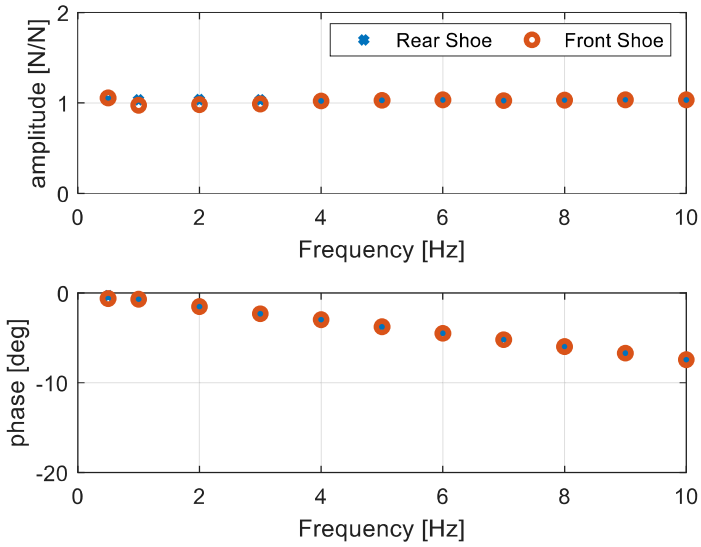

Fig. 12 Frequency Response Function of the system. P0 = 2.25 bar = 1.35 bar

From this analysis, it is evident that the rigging mechanism can work up to a frequency of 10 Hz, without causing a significant phase shift. For this reason, this analysis shows that the rigging mehcanism works in a quasi-static condition up to 10 Hz, so the dynamic of the rigging mechanism is much higher with respect to the dynamics of the WSP. This means that with this analysis it is possible to develop a WSP control logic considering a simplified model of the rigging system.

5 CONCLUSIONS

In this work, the dynamics of the rigging mechanism of the freight wagon T3000e has been analysed. The aim of the work is to verify the readiness of this mechanism in order to verify the feasibility of installing a Wheel-Slip-Prevention (WSP) system that avoids the complete locking of the wheels during high intensity braking manoeuvres. The main result of the work is the Frequency-Response-Function (FRF) between the braking pressure and the normal contact force at the shoe-wheel interface. Being the system nonlinear, a sensitivity analysis has been performed computing the FRF at different amplitude of the input pressure. In all the considered cases, the results show that the rigging mechanism has a higher dynamic than the WSP system. Consequently, to design a WSP control logic for this type of wagon, the dynamic of the rigging mechanism can be neglected.

Further developments of this work could be the study of the dynamic of the input pressure during the functioning of the WSP valve. Furthermore, future works could use this model to study the performance of a high intensity braking manoeuvre considering the rigging system and the wheel rail interaction.

6 REFERENCES

[1] 30 by 2030: Rail freight strategy to boost modal shift, Rail Freight Forward; European Commission, Mobility Strategy. https://www.railfreightforward.eu/sites/default/files/usercontent/white_paper-30by2030-150dpi6.pdf

[2] Soleimani, H., Moavenian, M. Tribological Aspects of Wheel–Rail Contact: A Review of Wear Mechanisms and Effective Factors on Rolling Contact Fatigue. Urban Rail Transit 3, 227–237 (2017). https://doi.org/10.1007/s40864-017-0072-2

[3] Zhu, Y., Wang, W., Lewis, R., Yan, W., Lewis, S. R., and Ding, H. (September 11, 2019). "A Review on Wear Between Railway Wheels and Rails Under Environmental Conditions." ASME. J. Tribol. December 2019; 141(12): 120801. https://doi.org/10.1115/1.4044464

[4] B. Allotta, R.Conti, E.Meli, L.Pugi, A.Ridolfi Development of a HIL railway roller rig model for the traction and braking testing activities under degraded adhesion conditions

[5] Qing Wu, et al. (2021) Freight train air brake models, International Journal of Rail Transportation, DOI: 10.1080/23248378.2021.2006808

[6] Shahab Teimourimanesh, Tore Vernersson e Rger Lundén. «Braking capacity of rail wheel-State of the art Survey.» In: Conference paper: 16th International Wheelset Congress (IWC16), Cape Town (RSA),(March 2010).

NEW BOGIE CONSTRUCTION REQUIREMENTS CONSIDERING ADVANCED BRAKE FUNCTIONS

Miklós KRÉMER

Knorr-Bremse Rail Systems Budapest
H-1238 Budapest, Hungary
Helsinki út 105

Department of Railway Vehicles and Vehicle System Analysis
Faculty of Transportation Engineering and Vehicle Engineering
Budapest University of Technology and Economics
H-1521 Budapest, Hungary

Received: September 05, 2022,

ABSTRACT

Not only the brake actuators and mechanism, but also the more advanced brake control has a demand on bogie construction. During wheel slide protection (wsp) actuation, the single wheelsets are braked and released rapidly one by one.
The ETCS train operation control system requires the so-called reliable deceleration to determine the actual braking curves. The medicine to overcoming uncertainties in our age is sad to be control and information. The onboard diagnostic system recognizes brake error on a vehicle or on bogie and control enters a brakeforce surplus to other wheelsets. The most difficult to handle factor is the wheel-rail adhesion. The eventual reduction of adhesion should detect as soon as possible.
Keywords: reliable deceleration, adhesion detection, adhesion information

1. INTRODUCTION

The European Train Control System (ETCS), Automatic Train Operation (ATO) and Driver Advisory (DAS) systems, need reliable deceleration and stopping distance on a high confidence level.

To cope with uncertainties constantly evolving advanced diagnostic systems are installed. The control systems nowadays can redistribute the braking forces if on some vehicles failure occurs and is detected.

There are significant tolerances in case of friction brakes. This is mainly due to variability in the coefficient of friction of the chosen brake pad and brake disc friction pairing.

The control systems can be open loop controls or closed loop ones. The open loop control can consider only a velocity dependence of the friction coefficient, or a more advanced method considers also friction surface temperature dependence with estimation of the surface temperature [1].

Most of closed loop controls considered the actuating force a to be controlled. The most advanced closed loop control is deceleration control (DCC), where the main feature, the train deceleration itself is measured onboard and controlled [2].

2. UNCERTAINTIES OF DECELERATION CAPABILITY ON VEHICLE SIDE AND TRACK/VEHICLE SIDE

The ETCS detaches the uncertainties of the vehicle side and the track/vehicle side. It can be considered that the first safety factor (considers uncertainties of the vehicle) can relevantly be reduced using onboard failure detection and/or advanced control system.

The basic assumption in case of novel systems is, that brake actuators can be controlled one by one. Of course, this can cause a special excitation on bogies. The second safety factor considers uncertainties of the track/vehicle, (the available adhesion) and can be reduced by different actions, in summary: the onboard adhesion management system. The aliments today are the sanding system, the magnetic track brakes, and the wheel slide protection (WSP)system. Generally, the WSP system recognises the "not adequate adhesion" and initialises the sanding system.

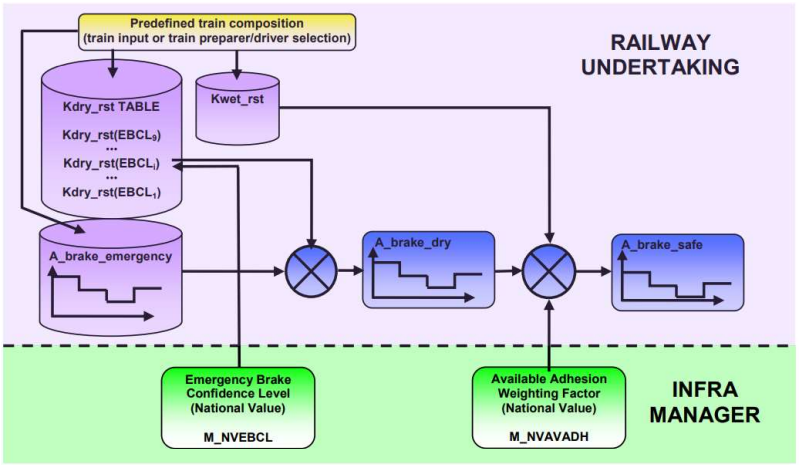

Fig. 1 Chart of "Safe deceleration" deduction of ETCS and the safety factor switches (green blocks) [3]

In Shift2Rail projects the representatives of the participating railways mentioned as unsolved question: the recognition of reduced adhesion, and so they use safety factors during onboard computation of the braking curves. Unnecessary safety factors limit the capacity of the infrastructure.

In case of train transport design (timetable creation), the designed braking power/demand shall be less then100% ("not the last brake stage" - UIC544-1 mentions: "Regular service brake ca.:2/3 of the maximum service brake deceleration") say 80%. So generally, trains do not use the designed adhesion (that shall be below 0,15 according to regulations). In normal train service it does not turn out that adhesion is getting slightly worse. The case of reduced adhesion turns out at first, when higher deceleration is needed (e.g.: Emergency brake demand) can cause dangerous situation. The safety can be increased if adhesion is measured/detected and communicated by the previous train. In this case the "safety factor is increased" and the ETCS or other system can compute the stopping distance according.

Another problematic question is that, when can the "safety factor increase" be withdrawn, after an event of "low adhesion was reported", The trains especially if reduced adhesion is reported not use high braking forces. The capacity of the track cannot be utilised until getting reliable information about the recovery of the normal adhesion.

3. ADHESION ESTIMATION USING SERVICE BRAKINGS [4]

Even if service braking is introduced (when there is traffic determined braking need (e.g.: before a signal)) it is advantageous of braking one of the wheelsets of the vehicle with its maximum designed braking torque (individual braking demand D%=100).

This suggestion comprises an upgraded BCU (brake control unit) or distributor valve or a separate unit behind normal BCU or distributor valve say „sampling redistributor" transforming the brake pressure demand (global D% or Pcv global) from equal values to nonequal (individual)ones, gaining the same deceleration (assuming no wheel slide) as demanded originally by BCU. On one of the wheelsets the braking demand must be 100% (so maximum designed). On other wheelsets the braking demand should be determined possibly unevenly as an example shown on Fig. 2.

Global Brak Demand (global D %) or (C_vglobal pressure%)	Redistribution (individual D %) of Cv_individual pressure % on the 4 wheelsets
100	100-100-100-100
90	100-90-90-80 or 80-90-90-100 or 90-100-80-90- in turn
80	100-90-80-50 or 80-50-90-100 or 80-50-100-90- in turn
…	

Fig. 2 Redistribution of braking demand to detect if adhesion is reduced

The „sampling redistributor" is part of the "adhesion estimator module" (Fig. 3). Also, without measurement, the estimation of adhesion between an upper and lower value is possible.

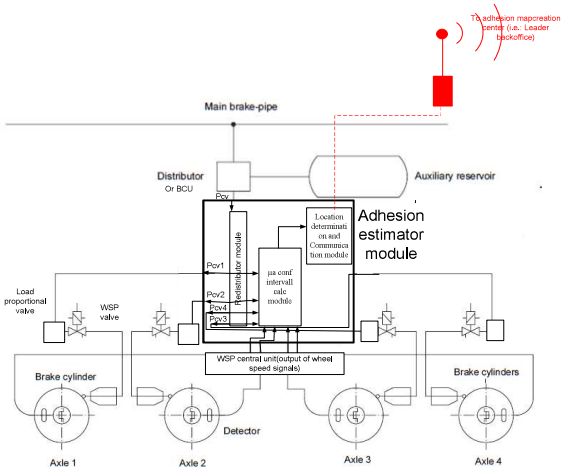

Fig. 3 Sketch of installation of the Adhesion estimator module (not shown on fig the Auxiliary reservoir connections)

If the vehicle is designed with separate load proportional valves at each wheelset, so all redistributed brake demands (individual D%) concerns to a single adhesion utilisation value independent of the actual loading conditions:

" brake demand level not causing wsp activity" itself can be a measure of the available adhesion.

" brake demand level causing wsp activity" itself can be a measure of reduction of adhesion.

3.1 Quasi calibrating" of the coach

To avoid measurements for available adhesion calculation preliminary "quasy calibration" of the vehicle is necessary (adhesion utilisation vs. Braking demand). A lookup table can be created "Quasi calibrating" of the coach, using the type test results or by performing (i.e.:braking the unhooking vehicle) test runs on dry track with the vehicle (planned to install with adhesion estimator module) and measure decelerations (Fig. 4).

- m: weighted mass of the vehicle
- a(global D %): average deceleration of the vehicle as a function of brake demand
- FB: average braking force between wheel and rail as a function of brake demand
- g: gravitational constant
- μa: adhesion utilisation

Speed dependence is neglected. On one hand the nature of wheel rail connection coefficient is that on higher speed its maximum value decreases. On the other hand, the wind resistance in higher speed participates in decelerating, reducing the detection failure. So, the chosen measure later in case of wheel slide will roughly characterize the track adhesion quality in large speed region. So μa value causing wheel macroslip will be a characteristic single value of track adhesion quality.

Braking demand Global D% equal at all wheelsets (before redistribution) [%]	Cv pressure [Bar] (or electric signal if relevant)	μa [-] (Adhesion utilisation) is a function of D%: μa(D%)
100	3,6	0,12
90	3,2	0,108
80	2,9	0,096
70	2,5	0,084
60	2,2	0,072
50	1,8	0,06
40	1,4	0,048
30	1,1	0,036
20	0,7	0,024
10	0,4	0,012

Fig. 4 Example with numbers to lookup table of "Quasi calibrating" process

3.2 Determination of adhesion intervals

Another lookup table can be used to determine actual adhesion value, so it is the essence of the "adhesion (μa) confidence interval calculation module"

axle1 WSP activity on axle1: D1%=100	axle2 WSP activity on axle 2: D2%=90	axle3 WSP activity on axle 3: D3%=80	axle4 WSP activity on axle 4: D4%=50	Adhesion estimation μa
no	no	no	no	higher than 0,12
yes	no	no	no	between (0,108…0,12)
yes	yes	no	no	between (0,096…0,108)
yes	yes	yes	no	between (0,06…0,096)
yes	yes	yes	yes	lower than 0,06

Fig. 5 Example for a Lookup table for adhesion adhesion (μa) confidence interval calculation if global brake demand is 80%

Example with numbers: i.e.: on a 80% global brake demand braking: redistributed among the local axles i.e.: 100-90-80-50% This moderate reduction of adhesion (above 0,096) were not detected when the braking torques were equally distributed on wheelsets, in case of an 80% braking demand (normal service braking).

The estimated adhesion characteristic value than can be transmitted to a central office that stores it with time and location data (like an adhesion map) and upgrades regularly. The adhesion data could be used i.e.: by driver advisory system or by train control system to compute the actual deceleration curves and safety distances: see Fig.6.

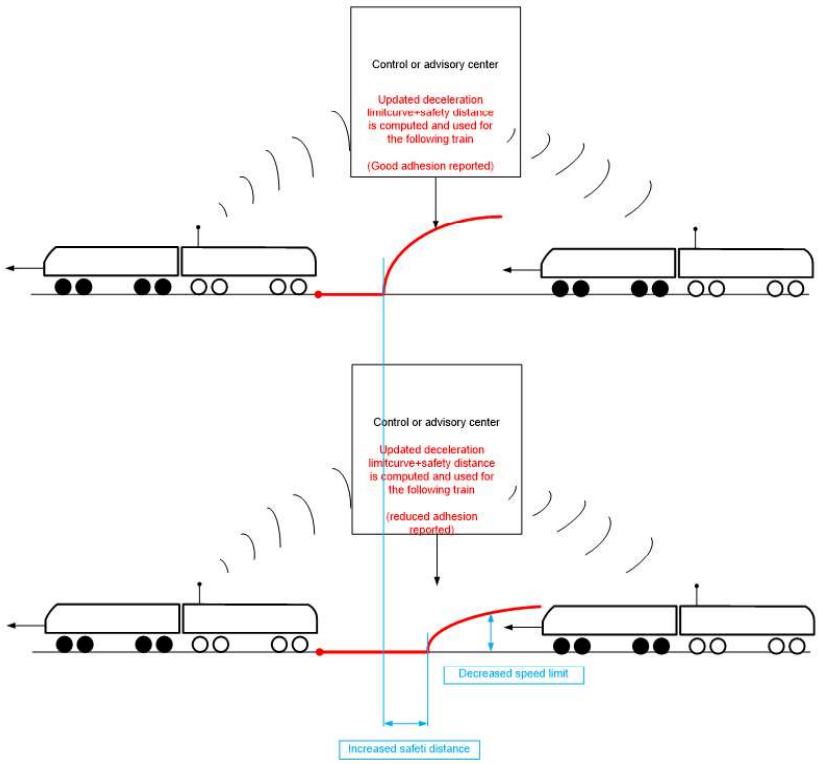

Fig. 6 Using the adhesion information in ETCS or DAS system, for computing the deceleration curve and/or safety distance.
In upper fig. normal adhesion was reported by front train
In lower fig reduced adhesion was reported by front train

4 QUICK DETECTION OF SUFFICIENCY OF ADHESION FOR AN INTRODUCED BRAKING

While introducing a braking on a section with an unknown reduced adhesion, considering the prescribed 3…5s brakeforce development time, 2…3 s can pass before the reduced adhesion is detected, and the adhesion management system is activated.

Example: If low adhesion is detected 2 seconds earlier by a travelling speed of 160km/h, the sanding system can be activated 2 seconds earlier, having 88m more pre-sanded section!

Keeping the present normative boundaries of action:

- The brakeforce development time, (or ramp or jerk) is limited 3…5s
- The brakeforce development time is prescribed on vehicle level .

Special braking rise technic can be proposed so that on one of the front wheelsets the braking force rises quicker, while the rest wheelsets brake with a controlled deadtime and rising ramp, so together the vehicle decelerating increase will be according to UIC, or TSI. The WSP system detects from the behaviour of the quickly braked wheelset the presence of reduced adhesion level, or appropriateness of adhesion.

The suggested control is feasible i.e., with systems: EP2002 or Hydraulically or electromechanically actuated brakes with integrated WSP function. In case of controlling the ED or blending brakes of traction units is the technic also feasible.

In case of a typical 4-wheel carriage, considering the UIC development time:

- On one axle the maximum braking torque develops in 1s
- The other 3 axles braking has 1s deadtime then the rise time on them is 3s
- So globally on the vehicle the break force development time is according to UIC 4s

If the adhesion is not adequate the WSP will detect it within 1 s, intervenes, and gives out the WSP active signal that can be used by adhesion management system, i.e.: by actuating automatic sanding, or tune the WSP strategy: see Fig.7.

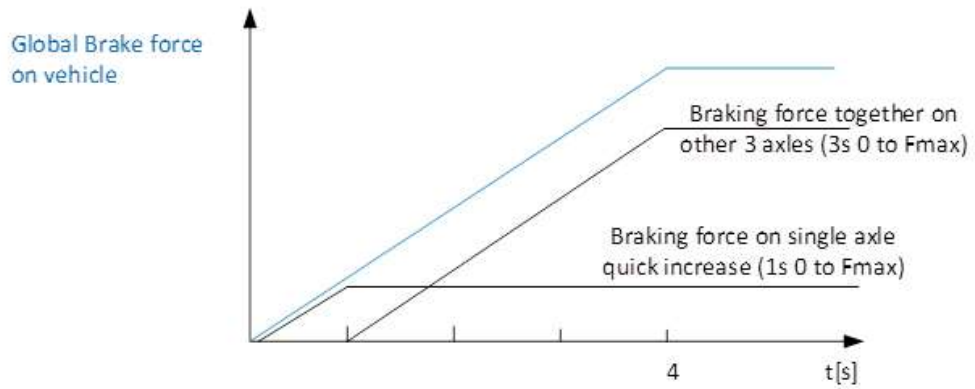

Fig. 7 Braking forces on different axles of a carriage for quick detection of sufficiency of adhesion

5 CONCLUDING REMARKS

It was general that the braking forces on bogies were equally distributed and jointly increased-decreased. The wheel slide protection system was one of the first embedded system that changed this principle. Spread of online diagnostic, and measurement systems created the opportunity of more reliable prediction of safe deceleration, and braking distance. Rarely occurring most critical factor to overcome is sudden uncertainty of adhesion. In some cases, adhesion problem probability can be noticed “by sight”, but generally during a braking “trial” only:

- Using, during service braking, on one alternating wheel the full braking force, the reduction of adhesion can be detected and communicated to central control office before a situation of a full power braking need were necessary.
- Using during all braking initiation on one alternating wheel a quick force increase, seconds can be won to overcome the dangerous situation e.g., by early introducing of magnetic track brakes, or sanding system.

6 REFERENCES

[1] Herden Marc-Oliver, Friesen Ulf, Schubert Michael; Krémer Miklós; Székely Ferenc: Bremseinrichtung und Verfahren zum gleichmäßigen Abbremsen: European Patent Register EP3221194B1 https://worldwide.espacenet.com/searchResults?ST=singleline&locale=en_EP&submitted=true&DB=&query=EP3221194B1

[2] Ulf Friesen, Ralf Furtwängler, Norman Kreisel, Jörg Braeseke, Dariusz Ciesielski: REPRODUCIBLE BRAKING DISTANCE: DECELERATION CONTROL. Repro-ducible Braking Distance, ZEVrail 2020 (Jahrgang 144) Ausgabe 01/02 Reproducible Braking Distance | Knorr-Bremse Systeme für Schienenfahrzeuge; Verzögerungsgeregeltes Fahrzeug ermöglicht ein stabileres Bremsverhalten in allen Geschwindigkeiten | ZEVrail.de

[3] INTRODUCTION TO ETCS BRAKING CURVES: ERA_ERTMS_040026 V1.5 https://www.era.europa.eu/sites/default/files/activities/docs/introduction_to_etcs_braking_curves_en.pdf

[4] Krémer Miklós: ADHESION ESTIMATING DEVICE FOR A BRAKE SYSTEM; European Patent Register EP3354524B1 https://worldwide.espacenet.com/searchResults?submitted=true&locale=en_EP&DB=EPODOC&ST=advanced&TI=&AB=&PN=EP3354524B1&AP=&PR=&PD=&PA=&IN=&CPC=&IC=

VIBRATION ATTENUATION OF DISC-BRAKE SYSTEMS

István NÉMETH

Department of Railway Vehicles and Vehicle System Analysis
Faculty of Transportation Engineering and Vehicle Engineering
Budapest University of Technology and Economics
H-1521 Budapest, Hungary

Received: August XX, 2022

ABSTRACT

This work aims to conceptionally investigate the applicability of tuned dynamic vibration absorbers to attenuate disturbing vibrations in disc brake systems of railway vehicles. The proposed simple two-degree of freedom model includes the equivalent mass of the brake unit with flexible suspension and an auxiliary mass coupled elastically to the brake unit. Furthermore, the model incorporates non-linear effects such as the friction pair brake pad and disc characteristics. The disc brake vibration generates structural vibrations and air-born noise which can be received by passengers and the surrounding areas but can have severe consequences on ride comfort and the service life of bogie components. From this follows an actual effort to develop measures to avoid or at least attenuate railway brake noise. Many publications demonstrate that the vibration of disc brake systems is basically a self-induced oscillation caused by the falling characteristic of the friction coefficient vs sliding velocity, which can be described as an unstable behaviour of the system at its equilibrium point. Experiments and everyday observations show that sometimes disc brake vibration of in-service vehicles appears and disappears seemingly in an unexpected way during operation, therefore the phenomenon must be more complex. A dynamic vibration absorber could be a valuable means of vibration attenuation in case of disc brakes, as well, however, in actual, operation the variability of the material parameters due to long-term aging and due to short-term environmental influence can tune out the system and widely degrade the effectiveness.

Keywords: disc-brake, vibration, dynamic vibration absorber

1 INTRODUCTION

Beyond rolling noise and aerodynamic noise, another, not a negligible source of vibration problems in case of railway vehicles is the friction-induced vibration of disk brakes, which is in the scope of this investigation. The vibration of disk brakes could be an important issue regarding passenger coaches: it lowers the vibration comfort of passengers and the dynamic fatigue effect give cause of concern, as well.

The most widely used technique for vibration attenuation is the application of vibration dampers, which can be viscous or frictional from the point of view of the operating mode, but their common feature is, that they couple *two* separate parts of the vehicle system, e.g. axle box and the bogie frame. Anti-drumming coatings and pasty dispersion materials are also widely used in the railway manufacturing industry in order to increase the own damping of some parts, e.g. sheet metals.

The application of an auxiliary mass system is another classical means of vibration attenuation. An auxiliary mass (rigid part) is attached to *one* part of the vibrating base system by springs and/or dampers. If the auxiliary mass is connected to the base system by using a spring element, then it is often called a *vibration neutraliser*. On the other hand, if only a damper or dashpot is used, then it is an *auxiliary mass damper*. In a general case when both springs and dampers are used to connect the auxiliary mass to the hosting primary system, then it is called a tuned *dynamic vibration absorber* (DVA). The term dynamic vibration absorber is often preceded by the adjectives “undamped”

or "damped" to emphasize the dominant property. Dynamic vibration absorbers are used for example in high buildings to combat the destroying effect of earthquakes, in the suspension of bridges to attenuate the vibration caused by the Kármán vortex street, but also in the steering wheel of cars to avoid the unpleasant vibration felt by the driver.

2 THE OBJECT OF THE INVESTIGATION

The object of the investigation is the typical two-axle bogie used under passenger carriages, see e.g. **Hiba! A hivatkozási forrás nem található.** and [2]. This kind of bogie has a two-level suspension including viscous dampers and is equipped with a disc-brake system containing two (to four) brake discs on each wheelset-axle. Details of the set-up of a one and a two degree of freedom (DOF) model are described in [3] together with the $\mu(v_s)$ friction coefficient vs. sliding velocity function fitted to data measured on a *Becorit 918* type brake pad. The friction coefficient characteristics has a negative slope in the range from $\mu'(v_s = 0) \approx -0.04\frac{s}{m}$ to $\lim_{v_s \to \infty} \mu'(v_s) = 0$.

3 METHOD OF INVESTIGATION

To introduce some nomenclature, it is advantageous to overview the major properties of DVAs, see Fig. 1. The differential equations of a vibration neutraliser are:

$$m\ddot{z} = -s \cdot z - s_1 \cdot (z - z_1) + F(t),$$
$$m_1\ddot{z}_1 = s_1(z - z_1).$$

The following simplifying terms are introduced as usual: $\alpha_0^2 = \frac{s}{m}$, $\alpha_1^2 = \frac{s_1}{m_1}$ and $k_1 = \frac{m_1}{m}$. Hence the differential equations take the form:

$$\ddot{z} + (\alpha_0^2 + k_1\alpha_1^2)z - k_1\alpha_1^2 z_1 = \frac{1}{m}F(t),$$
$$\ddot{z}_1 - \alpha_1^2 z + \alpha_1^2 z_1 = 0.$$

Assuming a sinusoidal $F(t) = F_0 \cos(\omega t)$ excitation, the amplification of the displacement amplitude of the base system relative to the static deflection due to a constant F_0 force:

$$U = \frac{\alpha_1^2 - \omega^2}{(\alpha_1^2 - \omega^2) \cdot (\alpha_0^2 - \omega^2) - k_1\alpha_1^2\omega^2},$$

while the amplification of the auxiliary mass is:

$$U_1 = \frac{\alpha_1^2}{(\alpha_1^2 - \omega^2) \cdot (\alpha_0^2 - \omega^2) - k_1\alpha_1^2\omega^2},$$

It can be seen, that if the vibration neutraliser is parameterized in such a way that its α_1 eigenfrequency is the same as the α_0 eigenfrequency of the standalone base system, then in the case of an excitation with $\omega = \alpha_0 = \alpha_1$ angular frequency, the mass of the base system remains perfectly at rest, while only the significantly smaller mass of the DVA vibrates. It can be seen, however, that an excitation with $\omega \neq \alpha_0$ angular frequency causes a nonzero vibration amplitude of the bases system as well. What more, two new resonance peaks arose at about the eigenfrequencies of the new 2 DOF system. By adding damping to the DVA the attenuation of the vibration at $\omega = \alpha_0$ may not be perfect,

i.e. the amplification is nonzero, but will be small even at the two new resonance peaks. The amount of damping of the DVA is a trade-off between the attenuation of the vibration and its effective bandwidth. Several strategies have been proposed to choose an "*optimal*" damping by considering additional constraints as well.

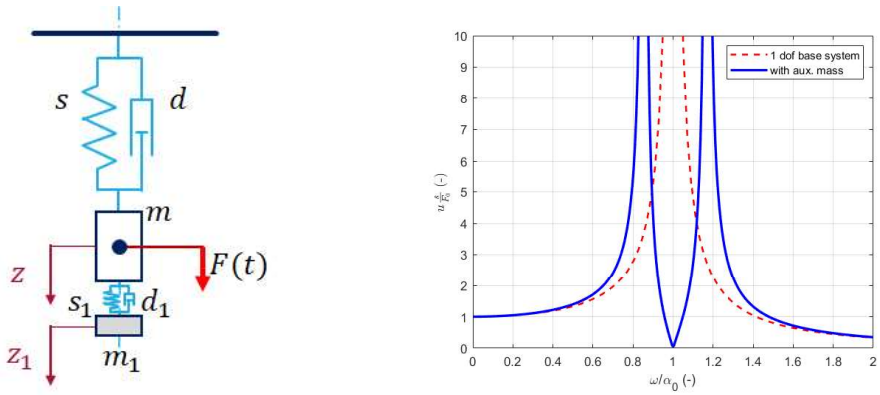

Fig. 1 Dynamic vibration absorber and its amplitude amplification characteristics

In the following, we investigate if a DVA can also be applied to attenuate the vibration of a disc brake system, when it is modelled according to Fig. 2. The principal difference compared to the model in Fig. 1 is the fact, that there is no $F(t)$ external excitation force with constant frequency, but the system is *self-excited* by the $F_f(v_s)$ friction force, which is assumed to be a function of $v_s = v_d - \dot{z}$ sliding velocity between brake pad and disc.

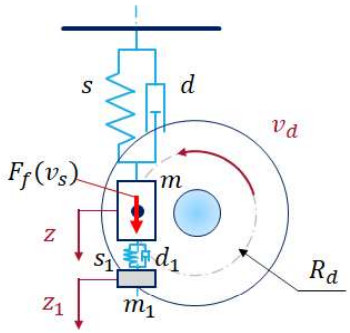

Fig. 2 Disc brake model with dynamic vibration absorber

In order to simplify the form of the differential equations of motions the following notations are applied: $\zeta = \frac{d}{2m\alpha_0}$, $\zeta_1 = \frac{d_1}{2m_1\alpha_1}$ are the damping ratios, $\beta = \frac{\alpha_1}{\alpha_0}$ is the ratio of the eigenfrequencies and $q = z - z_0$, $q_1 = z_1 - z_0$ are new variables introduced, where $z_0 = \frac{F_f(v_d)}{s}$ is the stationary position of the system, see [3]. Furthermore, the state vector is composed as $\boldsymbol{x} = [q, q_1, \dot{q}, \dot{q}_1]^T$. After linearising the friction force function at the stationary point [3], the differential equations can be written as $\dot{\boldsymbol{x}} = \boldsymbol{A} \cdot \boldsymbol{x}$, where the system matrix is

$$A = \begin{bmatrix} 0 & 0 & 1 & 0 \\ 0 & 0 & 0 & 1 \\ -\alpha_0^2 - k_1\alpha_1^2 & k_1\alpha_1^2 & -2\zeta\alpha_0 - 2k_1\zeta_1\alpha_1 - \tilde{F}_n\mu'(v_d) & 2k_1\zeta_1\alpha_1 \\ \alpha_1^2 & -\alpha_1^2 & 2\zeta_1\alpha_1 & -2\zeta_1\alpha_1 \end{bmatrix},$$

$\tilde{F}_n = \frac{F_n}{m}$ is the normal force acting on the brake pad scaled by the mass of the base system, and $\mu'(v_d) = \frac{\mathrm{d}\mu(v_s)}{\mathrm{d}v_s}\Big|_{v_s=v_d}$ is the slope of the friction coefficient characteristics at the stationary point. In the following, the independent variable of function $\mu'(v_d)$ is omitted if it does not impar the tangibility.

In case of the disc brake system the effectiveness of the DVA can by evaluated by analysing the stability of the entire system. To this aim, the characteristic polynomial equation of the system must be deduced and analysed. Firstly, by developing $\det(\boldsymbol{A} - \lambda\boldsymbol{I}) = 0$, we get the characteristic equation:

$$a_0\lambda^4 + a_1\lambda^3 + a_2\lambda^2 + a_3\lambda + a_4 = 0.$$

The specific polynomial coefficients are:

$$a_0 = 1, \tag{1.a}$$
$$a_1 = ((1 + k_1)\zeta_1\beta + \zeta)2\alpha_0 + \tilde{F}_n\,\mu', \tag{1.b}$$
$$a_2 = \big((1 + k_1)\beta^2 + 4\zeta\zeta_1\beta + 1\big)\alpha_0^2 + 2\zeta_1\alpha_0\beta\tilde{F}_n\mu', \tag{1.c}$$
$$a_3 = (2\zeta\beta^2 + 2\zeta_1\beta)\alpha_0^3 + \alpha_0^2\beta^2\tilde{F}_n\mu', \tag{1.d}$$
$$a_4 = \alpha_0^4\beta^2. \tag{1.e}$$

The system is stable if all the above polynomial coefficients are positive, i.e. $a_i > 0, i = 1, \dots, 4$ and all the *odd* indexed Hurwitz determinants are positive as well [4]. These are necessary and sufficient conditions. The Hurwitz determinants are defined by:

$$H_1 = a_1, \tag{2.a}$$
$$H_2 = a_1a_2 - a_0a_3, \tag{2.b}$$
$$H_3 = H_2\,a_3 - a_1^2a_4. \tag{2.c}$$

Although, the particular expressions of the Hurwitz determinants are rather cumbersome, they can be derived in a straightforward manner. It can be seen at first sight that a_0 and a_4 coefficients are always positive, and H_1 does not represent additional requirement as it is identical to a_1. Hence, only a_1, a_2, a_3 and H_3 need to be checked closer.

3.1 Application of an undamped dynamic vibration absorber

The slope of the friction coefficient is assumed to be eventually negative ($\mu' < 0$) and the sign of the normal force is of cause positive. If the damping ratios $\zeta = \zeta_1 = 0$, then $sign(a_1) = sign(\mu')$. It means that an undamped and unstable base system cannot be stabilised by an undamped DVA. Now let us assume that the base system has some $\zeta > 0$ damping and the undamped ($\zeta_1 = 0$) DVA is constructed – as usual – with $\beta = 1$, then there remains only one stability requirement, namely: $\mu' > \frac{2\zeta\alpha_0}{\tilde{F}_n}$. This is identical to the stability requirement which can be gained for the base system itself, see [3]. Hence, an unstable base system cannot be stabilised by an undamped DVA.

3.2 Application of a damped dynamic vibration absorber

In the following the necessary amount of damping of the DVA is searched for. It is still assumed that the value of the primary fitting parameter is $\beta = 1$. Solving the $a_1 > 0$ and $a_3 > 0$ inequalities for the damping factor of the DVA we get the two similar requirements respectively:

$$\zeta_1 > -\frac{1}{2} \cdot \frac{\tilde{F}_n \mu' + 2\zeta\alpha_0}{\alpha_0(k_1+1)}, \qquad \zeta_1 > -\frac{1}{2} \cdot \frac{\tilde{F}_n \mu' + 2\zeta\alpha_0}{\alpha_0}$$

from which the latter one is always stronger, see Fig. 3.b. The condition $a_2 > 0$ implies the requirement:

$$\zeta_1 < -\frac{1}{2} \cdot \frac{(k_1+2)\alpha_0}{\tilde{F}_n \mu' + 2\zeta\alpha_0},$$

which is an *upper limit*, however, in practical cases it is so high that it is far above the damping ratio of real materials, see Fig. 3.a below! The expression $H_3 > 0$ is a cumbersome 3rd order polynomial inequality in the variable ζ_1, therefore it is easier to analyse the results numerically, see Fig. 3. The applied parameter values are: $\alpha_0 = 2\pi \cdot 250 \ \frac{rad}{s}$, $\beta = 1$, $k_1 = 0.03$, $F_n = 15\ kN$, $m = 108.3\ kg$. Stability regions, i.e. regions of appropriate amount of ζ_1 damping are plotted in Fig. 3.c for undamped base system and in Fig. 3.d for slightly damped base system with $\zeta = 0.00168$ damping ratio.

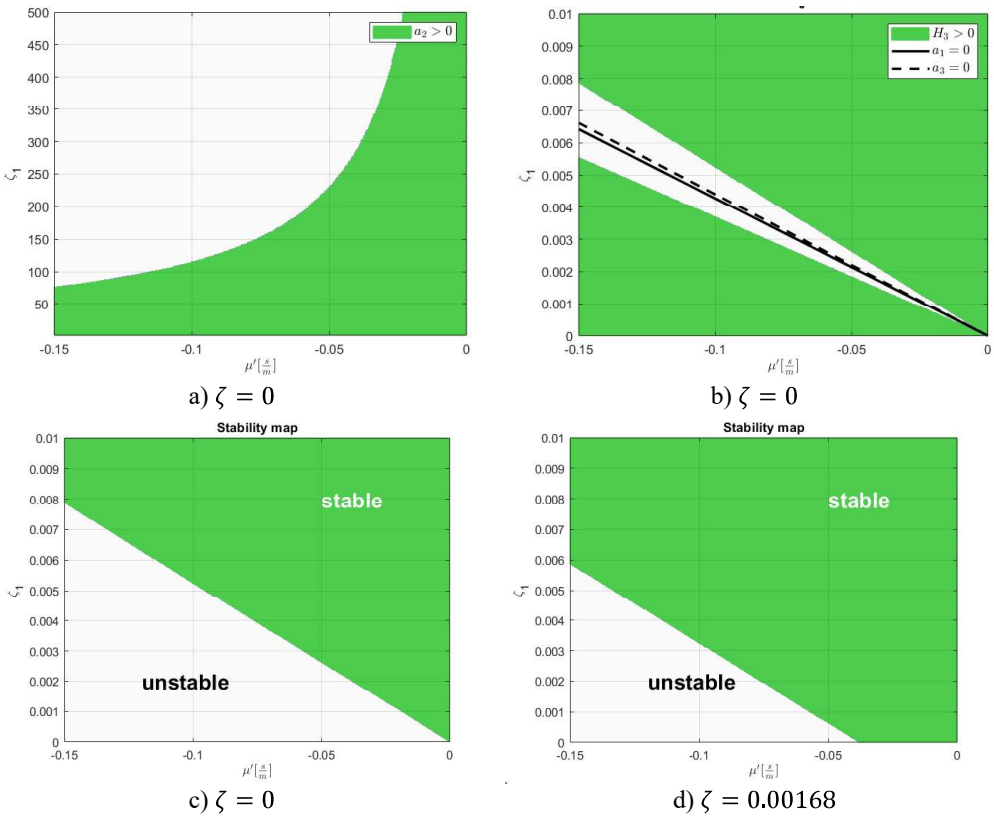

a) $\zeta = 0$ b) $\zeta = 0$

c) $\zeta = 0$ d) $\zeta = 0.00168$

Fig. 3 Requirements on the damping ratio of the dynamic vibration absorber

Although, setting the α_0 natural frequency of the dynamic vibration absorber equal to the α_0 natural frequency of the base system, i.e. using $\beta = 1$ parameter value seems to be reasonable, it can be difficult to adjust and keep this parameter exactly at the value of one in real operation.

In order to check the sensitivity of the system stability on parameter β, the positivity of the expressions in eqs. 1.b – d and 2.c must be evaluated. A numerical analysis is performed by varying parameter β in the range of 0 to 2, while the range of μ' is kept as above in the range of -0.15 $\frac{1}{m/s}$ to 0. Alongside the numerical analysis, analytical expressions can also easily be derived based on eqs. 1.b – d. for the stable domains of μ' vs. β (or vice versa) as follows:

$$a_1 > 0 \Rightarrow \mu' > -\frac{2\alpha_0(\zeta_1\beta(k_1+1)+\zeta)}{\tilde{F}_n},$$

$$a_2 > 0 \Rightarrow \mu' > -\frac{\alpha_0\big(4(\zeta\zeta_1\beta+\beta^2(k_1+1)+1)\big)}{2\tilde{F}_n\zeta_1\beta},$$

$$a_3 > 0 \Rightarrow \mu' > -\frac{2\alpha_0(\zeta\beta+\zeta_1)}{\beta\tilde{F}_n}$$

The second requirement (from $a_2 > 0$) is much weaker than the other two, therefore it is not represented in Fig. 4.a below. The closed form expressions based on eq. 2.c are too complex to write them out here, therefore they are only accounted for in the numerical analysis, see Fig. 4.b. The μ' slope of the friction characteristics of the considered *Becorit 918* brake pad material only varies from -0.04 to 0 $\frac{1}{m/s}$, hence a damping ratio of $\zeta_1 = 0.003$ seems to be more than enough.

The results of the numerical analysis are plotted in Fig. 4. The final stability map can be seen in Fig. 4.c for an undamped base system and in Fig. 4.d for a damped base system. It can be seen that the stability area is getting narrower as the friction coefficient characteristics with negative μ' slope is getting steeper. With other words, the chance that a small deviation from $\beta = 1$ causes the loss of stability is higher at larger negative slope of the friction coefficient. It is to be noted that the intersection point of the curves with conditions $a_1 = 0$ and $a_3 = 0$ marks the peak point of the stable area on its left end but it is slightly below the $\beta = 1$ level, see Fig. 4.c – d. Therefore, the stability at $\beta = 1$ level ends up a little bit right from this peak point.

The coordinates of the $a_1 = a_3$ intersection point can be given as well:

$$\mu' = -\frac{2\alpha_0\big(\zeta_1\sqrt{k_1+1}+\zeta\big)}{\tilde{F}_n} \quad \text{and} \quad \beta = \frac{1}{\sqrt{k_1+1}}.$$

With this result a guiding limiting value on the stability region can be calculated.

Finally, it should be noted that an increase in the ζ_1 damping ratio of dynamic vibration absorber "*stretches*" the stability region in the left direction, but in contrary to the Fig. 4.d., an ultimate stable strip at smaller absolute values of μ' at the right side of the stability region cannot be reached.

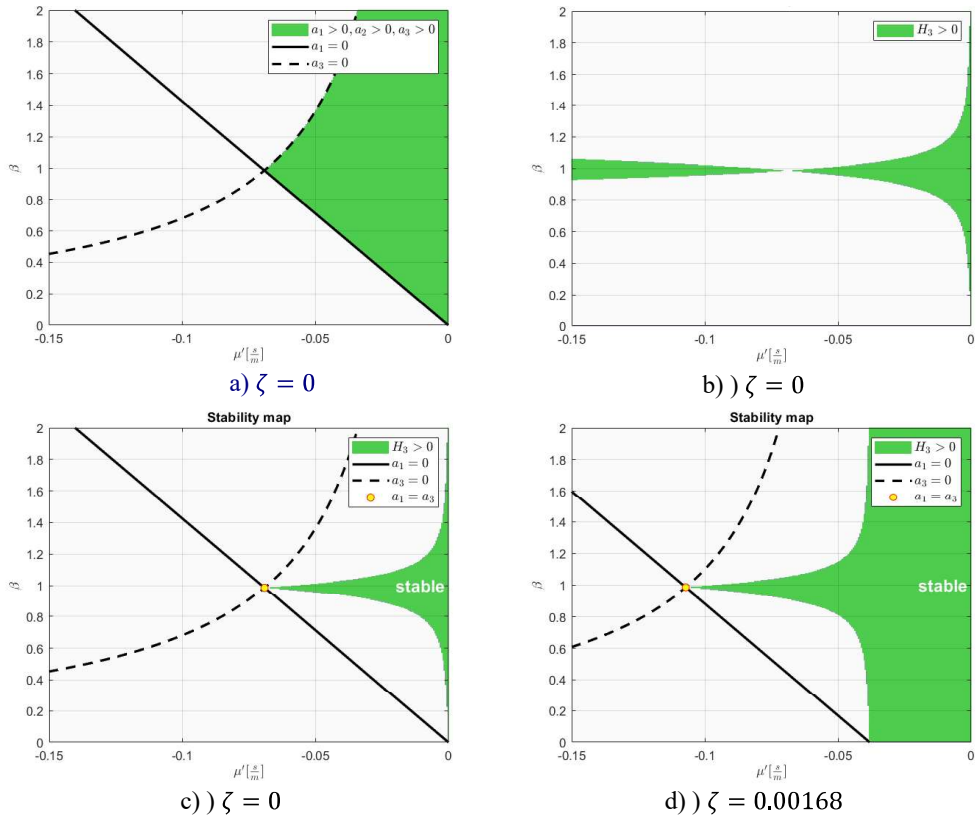

a) $\zeta = 0$ b)) $\zeta = 0$

c)) $\zeta = 0$ d)) $\zeta = 0.00168$

Fig. 4 Effect of the variation of the natural frequency of the dynamic vibration absorber on the system stability ($\zeta_1 = 0.003$)

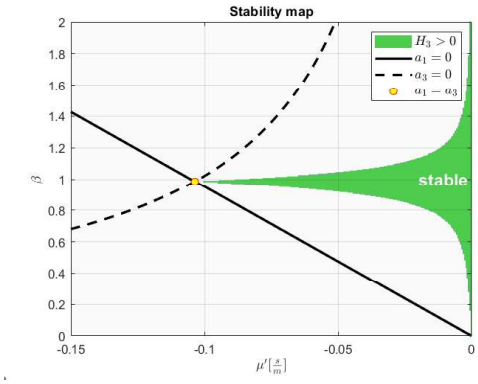

Fig. 4 Effect of increased damping of the dynamic vibration absorber on the system stability ($\zeta = 0,\ \zeta_1 = 0.0045$)

4 CONCLUDING REMARKS

Based on the models analysed in this study some short conclusions can be drawn regarding the application of a dynamic vibration absorber to attenuate the self-excited vibration of a disc brake system:

- An unstable base system cannot be stabilised at all by an *undamped* dynamic vibration absorber, so additional damping is needed anyway.
- A method for the determination of the minimal amount of damping of the dynamic vibration absorber is proposed, which is theoretically required to avoid friction induced vibration of a particular disc brake system.
- Practically it is hard to adjust and keep the natural frequency of the dynamic vibration absorber exactly at a theoretical value under operating conditions, therefore the effect of variations in this parameter has been evaluated. By the aid of the proposed evaluation method, a tolerance region on the parameter variation can be calculated and considered already in the design phase.
- Further investigation and experimental analysis are necessary to gain more insight into the manifold vibration phenomena of disc brake systems and to evaluate stability of the material properties of elastomers applied in dynamic vibration absorbers.

5 ACKNOWLEDGEMENT

I would like to express my gratitude to Professor István Zobory and Mr. Franz-Josef Weber for supporting this work with words and deeds.

6 REFERENCES

[1] Zobory, I.: Investigation into the vibration phenomena of the disc-brake system of a railway bogie, Technical Report, Technical University of Budapest, Faculty of Transportation Engineering, Department of Railway Vehicles, 1997 (in Hungarian)

[2] Németh, I. - Zobory, I.: Identification of Structural Damping in Railway Disc Brake Suspension Systems, Proceedings of the 7th VSDIA, Budapest Hungary, 2000. pp. 303-314.

[3] Németh, I.: How to avoid dynamical instability in disc-brake systems by using additional linear damping. Proceedings of the 7th VSDIA, Budapest Hungary, 2018. pp. 131-142.

[4] Csáki, F.: Szabályozások dinamikája (Control dynamics – In Hungarian), Akadémiai Kiadó, Budapest, 1974.

COMPUTER AIDED FATIGUE ANALYSIS AND VALIDATION OF A WELDED BOGIE STRUCTURE

Anna NAGY, László KOVÁCS, Tamás TURCSÁN and László TAKÁCS

Department of Analysis and Testing
Econ Engineering Kft
3 Kondorosi út, H-11161 Budapest, Hungary

Received: August 5. 2022

ABSTRACT

This paper introduces an extensive railway product development and validation process in close cooperation with Ganz Motor Kft. and Econ Engineering Kft, where we performed the fatigue assessment of a welded bogie. Structural simulations were based on EN 13749 standard and performed using Ansys general finite element software. We developed a custom tool for the fatigue assessment of the weld seams by enhancing the Volvo-Chalmers method and performed physical fatigue tests of fillet-weld and butt-weld specimens to determine the SN curves of the weld seams that serve as input for our evaluation method. A static test of the complete bogie was also performed to validate the FE model.

In the first phase, we modelled the welded frame as shell elements and the suspension parts as rigid beams with appropriate kinematic joints and real characteristics of primary and secondary springs. A static test was performed on a testing bench at Ganz for validation purposes. We measured the applied forces, spring travels, the reaction forces at the wheelbases, and strains with strain gauges at preselected locations. Force and strain data were compared to simulation results, and a good correlation was achieved. In the next phase, we performed structural simulations according to EN 13749 standard and evaluated the stresses in the weld seams that are the basis of the fatigue calculations. In the third phase, for the fatigue assessment, we developed our custom tool that calculates relevant stress ranges in the appropriate directions in each weld element and modifies the SN curves according to a custom mean-stress correction method. It also incorporates a weld-length correction method to consider the size effect. In the end, we used our custom tool to estimate the fatigue life of each weld seam of the bogie and made weld seam classification to highlight the safety level of them.

Keywords: railway bogie, structural analysis, simulation, weld seam, fatigue assessment, validation, physical test

1 INTRODUCTION

Nowadays, the importance of fatigue assessment and lifetime prediction using numerical simulation tools is out of question due to the ability to obtain fast and reliable results. Extensive research has been done on this topic [1]. Most of the works focus on the accurate consideration of the loadings, which can be determined either by using the accelerated test method [2], or by direct measurement of the loads [3]. In this paper, we took the loadings from a relevant EN standard and focused on the fatigue life evaluation method of the weldings.

For achieving a high level of confidence in the simulation-based lifetime estimation, there is a need to have a validated finite element (FE) model including reliable material characteristics in terms of fatigue life, and a proper method is needed to evaluate the results from the analysis and interpret them from lifetime point of view. This work of method development has entirely achieved the abovementioned criteria by implementing a complex workflow (Fig 1) on the process.

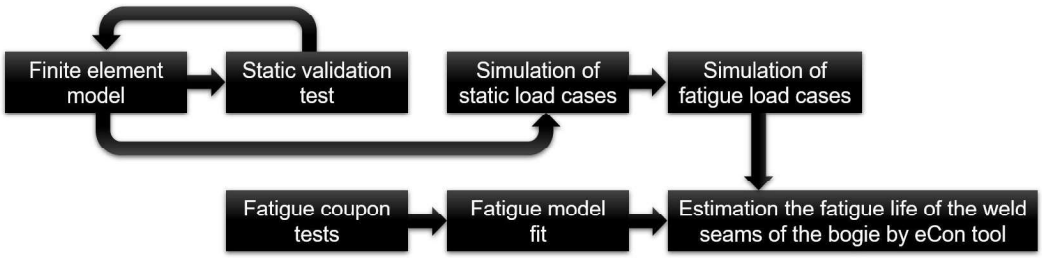

Fig 1. The workflow of the implemented bogie weld lifetime assessment procedure

2 STRUCTURAL ANALYSIS AND MODEL VALIDATION

In this section, the used FE model is introduced and the model validation process is revealed. This is based on comparing the static physical test bench and static structural simulation results, and the standardized structural calculations on the validated model are also detailed.

2.1 Finite element model

In the FE model of the bogie structure, welded steel plates were modelled using shell elements which typically run on the middle surface of each plate. High-thickness elements that cannot be represented adequately with shells e.g., machined brackets were modelled with solid elements. The geometry of the wheelset was modelled as rigid elements, allowing a representation appropriate for the task but significantly simplified. From a kinematical point of view, important points e.g., joints and springs, were connected with rigid rods, leaving the degrees of freedom corresponding to each articulated joint free. The elastic elements involved in the bogie frame-wheelset coupling were modelled with springs. The primary and secondary springs were connected to the bogie by RBE3 (rigid body element) elements which distribute the force/moment applied at the master node to a set of slave nodes. The suspension was connected to the bogie by CERIG (rigid constraint equations) elements which define a rigid connection region. The stiffness of the springs was defined by both longitudinal and lateral linear characteristics. The preload of the primary springs was 177 620 N, and with this value, the axle box was directed in a horizontal position due to the gravity load. The bogie was connected not only to the rail but also to the vehicle body through flexible elements in the FE model. For this, the pivot was represented with shell and solid elements. These elements were also connected to the rest of the frame by springs with proper stiffnesses.

This simplified model of the bogie can be seen in Fig 2. The average element size in the model was 10 mm. The mesh was created by taking into account the requirements of the fatigue evaluation (Volvo-Chalmers) method. The material model of structural steel elements was a linear elastic representing S355 NL material whose main properties can be found in 1 Table.

Table 1: Material properties of used S355NL

Property	Value
Modulus of elasticity (E)	210 [GPa]
Poisson's ratio (ν)	0.3 [1]
Yield strength ($Rp_{0.2}$)	355 [MPa]
Tensile strength (σ_t)	535 [MPa]

As the bogie is loaded in the standard load cases of the FE analysis (FEA) by forces, it is not necessary to define the mass of the body additionally. Only the masses of each element of the suspension and axles were modelled with concentrated mass points on the relevant rod models.

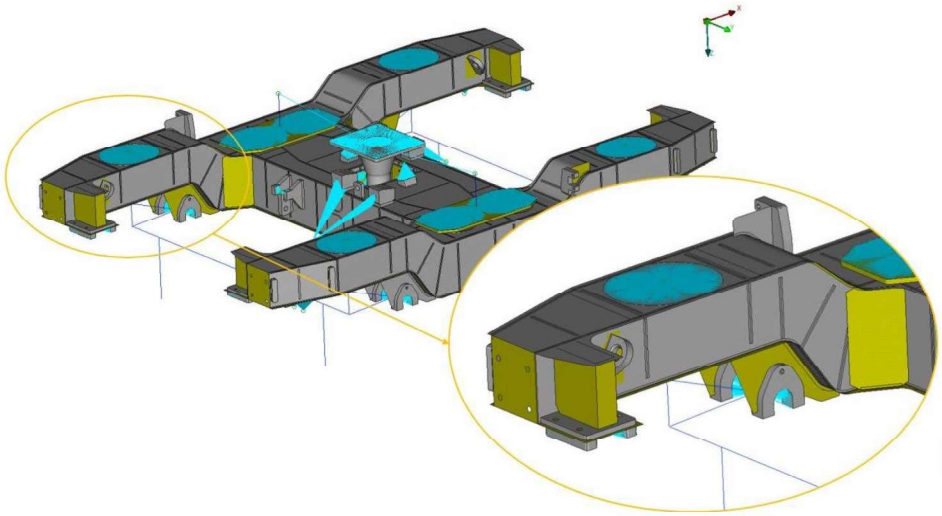

Fig 2. Simplified model of bushing block for the bogie

2.2 Quasi-static tests and simulation of the bogie frame

The main goal of this investigation was to validate the finite element calculation with a physical static test bench measurement. Physical tests were done on a BT-1.0-25/30 type testing bench previously developed by Ganz Motor Kft. It has two separately controlled hydraulic cylinder units for loading the investigated bogie structure at secondary springs. For validation, registered and FE-calculated elastic strains were compared at two targeted regions of the bogie. Placement and orientation of strain gauges were determined using preliminary FEA results, which has led to the identification of two regions with well-defined principal strain directions and levels. The first of them (Location 1) has been chosen due to the presumed pure tension-strain-state from the bending of the structure at the bottom of the bogie frame. The second region was selected because of its considerably high strains at the root of the side frame, and at this region, a biaxial strain gauge was placed.

The bogie FE model of this validation test is identical to the model used for the standard EN 13749 [4] simulations, but in this case, the assembly does not contain the powertrain system similarly to the physically tested frame. Measured strain values were registered

in 3 different load cases of the test bench static structural investigation. In the FE simulation, load cases of physical measurement were reproduced, and strains from the model were evaluated. Deformation results of these load cases can be seen in Table 2.

Table 2: Bogie structure deformation results (in mm) of 3 load cases

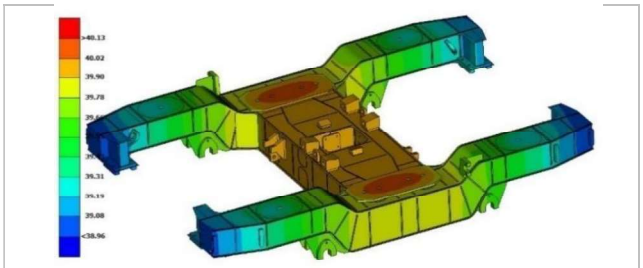

Load Case 1, Symmetrical load 110-110 kN

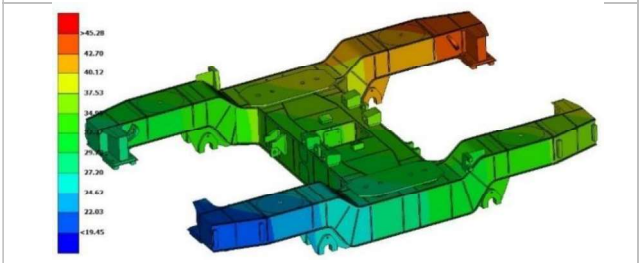

Load Case 2, Sym. load with wheel elevation (110kN)

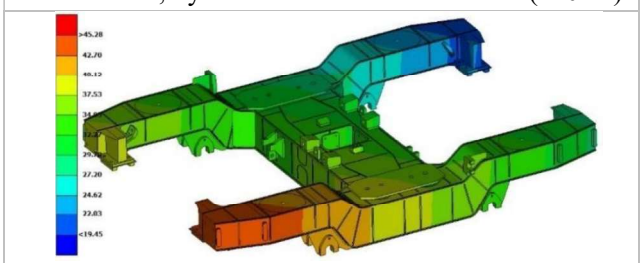

Load Case 3, Symmetrical load with opposite wheel elevation (110kN)

The comparison of the measured and calculated strain values are summarized in Table 3.

Table 3: Comparison of strain gauge measured and FEA resulted strain values

		Location 1			**Location 2, direction 1**			**Location 2, direction 2**		
		Gauge	**FEA**	**Diff.**	**Gauge**	**FEA**	**Diff.**	**Gauge**	**FEA**	**Diff.**
	Load [kN]	**Strain [1]**	**Strain [1]**	**[%]**	**Strain [1]**	**Strain [1]**	**[%]**	**Strain [1]**	**Strain [1]**	**[%]**
LC1	110	0.0065	0.0071	**9.2**	0.0038	0.0036	**4.5**	-0.0025	-0.0025	**0.9**
LC2	110	0.0067	0.0066	**1.3**	0.0046	0.0042	**7.6**	-0.0032	-0.0031	**3.2**
LC3	110	0.0065	0.0066	**1.5**	0.0047	0.0049	**5.0**	-0.0032	-0.0030	**7.4**

Based on the result, it can be stated that differences between calculated and measured strain values stayed under 10% in all cases and under 5% in 6 cases of 10.

Concluding the validation process, it can be stated that the accuracy of static FE simulation results was adequate, and this FE modelling approach is able to give accurate results for the operational and exceptional load cases of the EN standard as well.

2.3 Structural simulations according to EN 13749

The standard EN 13749 [4] contains different load cases for bogie strength testing to represent possible operating conditions. Loads, by their nature, can be divided into two main groups: exceptional and operational loads. The aim is to verify that the bogie does not suffer any fatal damage as a result of the exceptional loads. In contrast, in the case of service loads, the strength of the bogie must be tested not only for static failure but also for fatigue due to the repetitive nature of the load. Since the bogie is a welded steel structure, the fatigue of the welds was investigated as a characteristic failure mode in terms of durability.

Stresses of the exceptional load cases have been calculated according to clause C.4.1 of EN 13749 [4]. These relatively large loads occur only in exceptional cases; therefore, their effect is tested in comparison with the static strength of the structure. Loads for normal operating cases have been calculated according to clauses C.4.2 and F.2.2.2 of EN 13749 [4]. These loads are expected to be an upper prediction of the repeating loads during normal operation, and the supports of the structure are similar to those described in exceptional load cases.

3 FATIGUE ASSESSMENT

In the next section, some details are given on the custom fatigue evaluation tool developed by Econ Engineering, and lifetime calculations and their results are also shown.

3.1 Custom fatigue evaluation tool

A custom fatigue life evaluation approach was introduced that was derived from standard methods developed to assess weld fatigue based on weld nominal stresses.

The main steps of the weld seam safe cyclic life evaluation method are summarized in Fig 3. The entire approach is a modified implementation of the Volvo-Chalmers evaluation method [5], which is briefly introduced here.

For the method development, the basic concept of the method by Fermér et al. in [5] was invoked that is based on the approach described for spot-welds by Rupp et al. in [7] called the Volvo-Chalmers approach.

The baseline SN approach, including the majority of the correction methods proposed by the Volvo approach, was taken over. This is summarized in Fig 3. However, the FE inputs had to be adjusted to the shell element-based weld stress calculation methodology which by default returns linearized stress distribution along the weld seam. This basically involves the automated calculation of the in-plane stress component normal to the weld line as the anticipated driving stress component of the crack initiation process. This procedure is somewhat unique and does not follow the Volvo approach in this regard which only requires the acting forces and moments at the nodes representing the weld

lines and turns this information into linearized stress distribution across the thickness of the weld. The introduced approach acquires this information directly from the FE shell stress results.

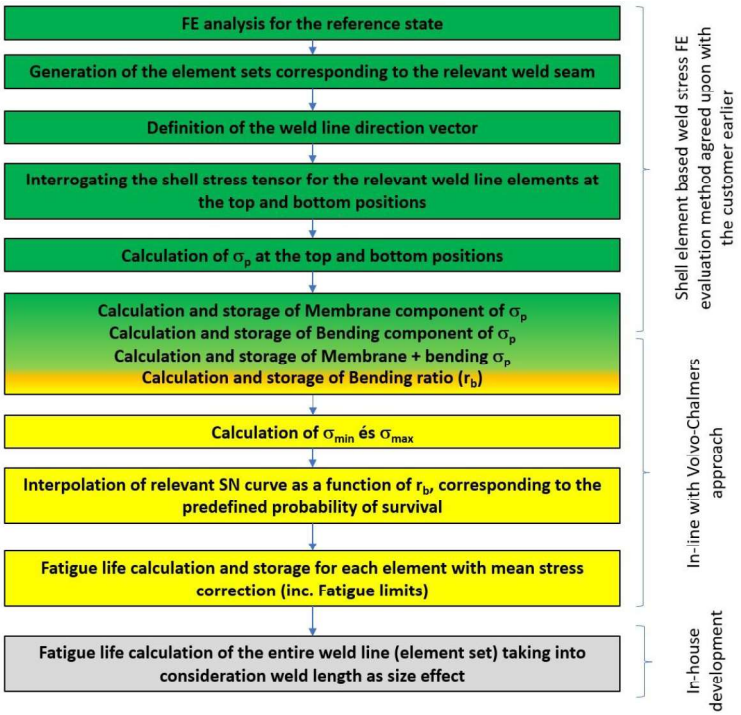

Fig 3. General workflow of the developed weld seam fatigue evaluation

Some extra features addressing some common fatigue-related dilemmas were added that are beyond the scope of the Volvo-Chalmers method, such as:

- Automatic SN curve parameter recalculation capability once the relevant fatigue curve covering the actual bending ratio and probability of survival has been found.
- Automatic method to shift the input 50% survival probability SN curve as a function of the predefined probability level.
- Size effect estimation takes into account the fact that the input SN curves represent a limited weld length compared to the real application. The introduced method is based on the weakest link approach.

With regards to all other fatigue-related aspects, the approaches implemented in the original Volvo-Chalmers method were followed, such as:

- Linear SN curve in log-log space with endurance limit defined,
- Bending ratio (r_b) dependent fatigue life data,
- FKM guideline [8] based mean stress correction (Haigh-diagram with multiple linear sections),

- Life pertaining to the predefined probability of survival is constructed by shifting mean life by the corresponding "number of σ_N" in log space, where σ_N represents the life standard deviation to be derived experimentally.

3.2 Correction of fatigue life for weld length

The fatigue life of a weld seam corresponds to the fatigue life of the weakest section of it. The weakest section is the one having the lowest expected life. However, from a statistical aspect, elements with equal life have never exhibit numerically identical values. Statistically, the finite elements corresponding to a weld seam are considered to have equal life if the actual calculated number of cycles are within a certain factor relative to the lowest calculated life.

The more elements are included in the cluster of weakest sections, the higher the probability of failing at a given number of cycles due to the fact that higher volume is subjected to the critical load, and therefore there is a higher chance of finding a microstructural flaw in these regions that initiate fatigue crack.

This phenomenon was considered mathematically using the Weakest Link theory [9]. In practice, the input SN curves are generated from specimens having significantly shorter weld lines than what the final product (motor bogie) has. This leads to the valid expectation that the longer weld line subjected to the same load level as the specimen shall have lower fatigue life than what the specimen experiments show based on the weakest link theory. Assume a weld line subjected to a constant load level having a total length of "B". The weld length of the specimens used in fatigue experiments has a weld length denoted as "b". The weld line with "B" length can be considered as being a chain of "b" long links as Fig 4 shows.

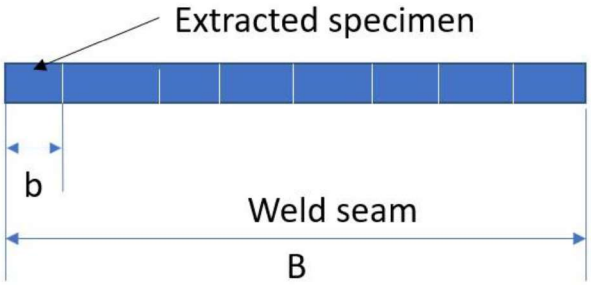

Fig 4. Interpretation of weakest link theory on a weld seam

Using the "chain of links" assumption above, the entire weld survives if all links forming it survive. Thus, the probability of survival of the weld seam is the product of the individual probabilities of the links. It can be proven that the likelihood of failure with regards to the entire weld can be calculated like this:

$$P_{fail}^{weld} = 1 - (1 - P_{fail}^{speciment})^{\frac{B}{b}} . \quad (1)$$

Using the equation above for a large number of cycle levels, the entire Cumulative Distribution Functions (CDF) of the specimen and the weld line can be built up, and the corresponding CDFs can be compared. This is shown in Fig 5. It follows from the figure

that a whole weld representing a larger volume than the baseline specimens is expected to fail earlier, but in return, the expected scatter in the fatigue behaviour is lower as well. This is manifested by the narrower CDF in Fig 5.

In order to implement the weakest link approach in connection with the presented fatigue life calculation method, the first step should be to quantify how much deviation from the minimum fatigue life along a certain weld line (N_{min}) is considered to be statistically equivalent to that. Based on this information, it is possible to select all elements of a weld seam that satisfy this condition. If the number of elements possessing statistically identical life to N_{min} is denoted as "n_{crit}" and the typical element length at the weld is "l" then the critically loaded weld seam length is to be calculated as:

$$B = n_{crit} \cdot l \, . \tag{2}$$

Using the weakest link approach, the expected life of the critically loaded weld line length can be computed by reading off the number of cycles at a corrected probability level on the fatigue life CDF of the experimental (specimen-based) results. The expected minimum life of the critically loaded weld line representing the predefined probability of survival (NA) is considered the expected minimum life of the entire weld line. Thus, this is considered to be the outcome of the weld seam fatigue assessment method.

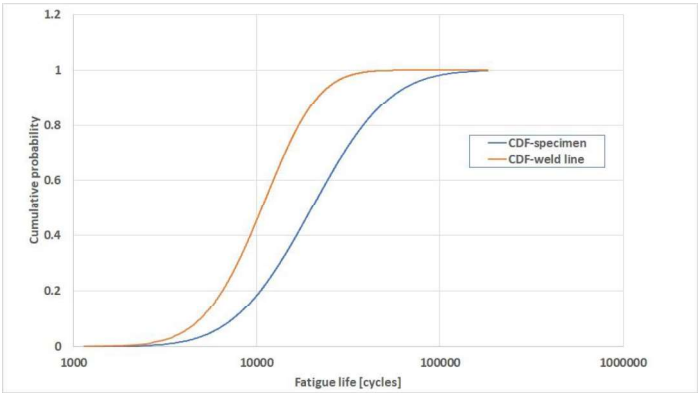

Fig 5. Comparison of specimen vs. weld line CDFs as per weakest link theory

3.3 Experimental weld-specific SN curves

In order to supply the fatigue life estimation method with the necessary experimental inputs, fatigue tests were conducted on samples containing typical weld seams used on the motor bogie in question, such as butt weld and fillet weld. Flexural fatigue experiments were carried out on an Instron 8801 type servo-hydraulic machine at high frequencies (f>5Hz), making sure that the acting stress level at the weld does not exceed the yield stress of the base material. Target lives fell into the High Cycle Fatigue (HCF) regime (> 100k cycles). The experiments were performed under load control at different positive R-ratios, where the actual loads were measured with Dynacell 100 kN dynamic load cell, and actuator displacement was also recorded to identify the onset of macro-cracking. A typical test setup for the two aforementioned weld types is shown in Fig 6.

Fig 6. Fatigue testing setup for butt welded (left) and fillet welded (right) samples

SN curves were then fitted to the experimental stress vs. fatigue life data pairs by using the Maximum Likelihood Estimation (MLE) method assuming lognormal life and fatigue strength distributions. This approach, as a result of Total Likelihood as Objective Function maximization, returns the slope (m) and intercept (C) of the 50% survival probability (mean) SN curve parameters as well as the life and fatigue strength standard deviations on a logarithmic scale. Due to the fact that the SN curves represented a very limited number of data points, the fitted standard deviation was corrected for the uncertainty of fitting to the sample using Chi^2 correction as follows:

$$f_{\chi^2} = \sqrt{\frac{N_{DOF}}{inv\_\chi^2(P_{conf},N_{DOF})}}, \tag{3}$$

where: inv_χ2 stands for the Inverse of right-tailed Chi^2 distribution function. The two parameters to define the function are the ones in brackets: P_{conf} and N_{DOF}. P_{conf} refers to the confidence level expressing the level of fidelity of the fitted parameters. It means what is the likelihood for the real scatter to be less than the corrected fitted value. Parameter NDOF is the statistical degrees of freedom corresponding to the given data sample. In practice, this number equals the quantity of independent data values that determine the theoretical (fitted) values. This is to be calculated by taking the number of available data points and reducing it by the number of SN curve parameters to fit. An additional constrain was imposed on the SN curve fitting problem: it was assumed that the slope of the SN curve is not dependent on the actual R-ratio. Thus, a different mean stress level only shifts the fatigue curve; therefore, only the intercept (C) varies with R-ratio. Fig 7 shows the R-ratio-dependent SN curves fitted to the experimental results.

Finally, the relationship between mean stress and stress amplitude was established by selecting a certain life level and back-calculating the stress range and mean stress from that using the fitted SN curve parameters at a given R-ratio. These discrete points in mean stress – stress amplitude space allowed fitting a straight line, and the slope of that is a direct input into the FKM guideline [5] based mean stress correction as the Goodman slope. The equations providing the required stress amplitude and mean stress levels at a preselected life level (N_{sel}) are as follows:

$$\sigma_a = \frac{10^{\frac{1}{m}\log(N_{sel})+c}}{2}, \tag{4}$$

$$\sigma_m = \sigma_a \cdot \frac{1+R}{1-R}. \tag{5}$$

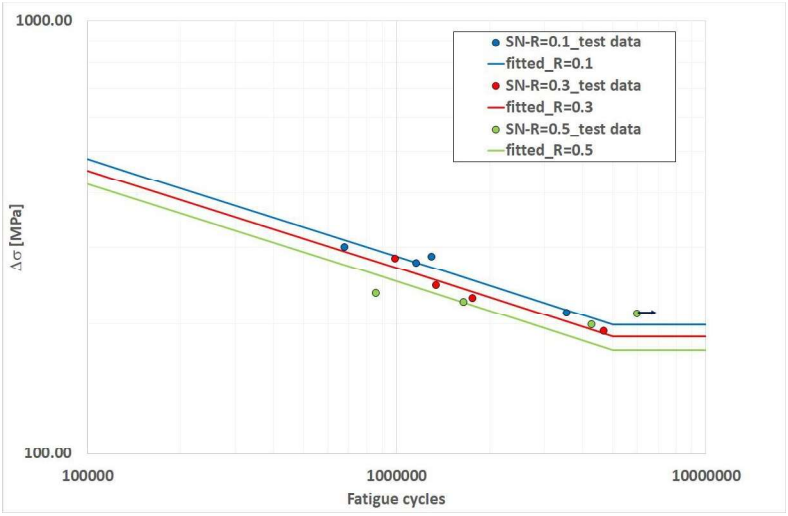

Fig 7. Mean fitted SN curves vs. test data; butt welded samples

A graphical example for a fitted Goodman slope is shown in Fig 8.

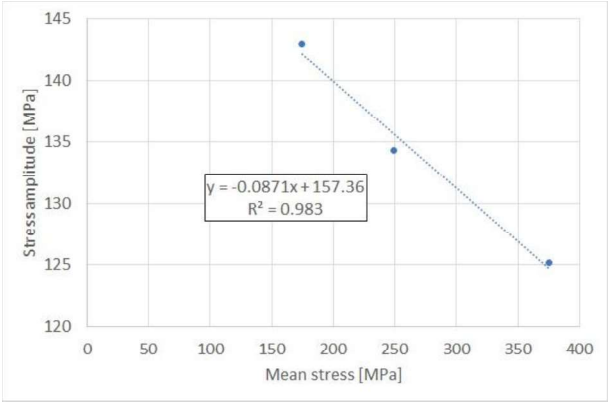

Fig 8. Mean stress vs. stress amplitude relationship from fitted SN curves and the fitted Goodman line in the range of R=0.1 - 0.5

3.4 Fatigue life estimation process of the bogie

The weld fatigue life assessment method was implemented in the form of an automated postprocessing code that directly evaluated the stress results extracted for all element sets associated with weld lines in the structural FE model of the bogie. The algorithm used the experimental SN curve parameters as inputs and returned the weld length – corrected, weld line specific fatigue lives, including mean stress correction and plate thickness effects representing the predefined survival probability level.

Based on the fatigue test described in EN 13749 [4], the total expected number of cycles is 10 million from the combination of vertical and lateral loads, described in the standard [4] in sections G.2. and G.3. The load cycle is dominated by vertical vibration and the expected number of cycles is 6×10^6 with a load multiplication factor of 1.0, and it is twice 2 million cycles when the multiplication factor equals to 1.2 or 1.4 respectively. The survival probability was specified to be 0.95 as per the requirement of the standard [4].

The fatigue test program was defined based on bogie category B-VII [6] in order to demonstrate the fatigue resistance of welds. The standard mandates to prove that the welded frame can withstand the predefined number of load cycles under several predefined combinations of static, quasi-static, and dynamic loads. According to that requirement, two high-frequency sinusoidal load clusters can be defined as fatigue load depending on the actual sign of the quasi-static part of loading. However, these load sequences are identical in terms of amplitude. Thus, using the one with a higher mean load is supposed to be the more conservative, which corresponds to the situation when the quasi-static loading is added to the static load ($F_s + F_{qs}$) in magnitude, as shown in Fig 9. This case was selected to define the loads on the FE model.

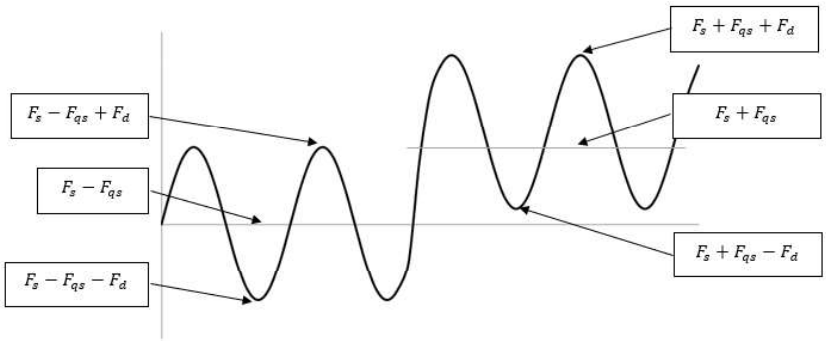

Fig 9. Fatigue load cycles example as per EN 13749 [4]

Since the requirement is to demonstrate crack-free behavior after imposing the standard load sequence, it can be done by summing up the fatigue damage estimated from each individual contributor by using Miner's inequality [4]:

$$D = \frac{n_1}{N_1} + \frac{n_2}{N_2} + \frac{n_3}{N_3} \leq 1\ , \tag{6}$$

where n_1, n_2 and n_3 corresponds to the prescribed number of loading cycles for the predefined load phases with different multiplication factors (1,1.2 and 1.4 respectively), as well as N_1, N_2 and N_3 are the fatigue lives for these load phases respectively, estimated with the fatigue evaluation method developed for the weld seams.

In case any of the estimated fatigue lives fell into the region of endurance, the corresponding damage is expected to be zero. During the welded specimen tests, it was demonstrated that the life level corresponding to the endurance limit of the welded joints is 5000k cycles meaning that the estimated cycles above 5000k can be treated as infinite life. For this reason, the standard requirement against 6×10^6 cycles for phase 2 of the representative load sequence means a design operating under the endurance limit.

3.5 Fatigue life evaluation results of the bogie

In all of the analyzed fatigue cases, the service life of the bogie turned out to be beyond the endurance limit. This numerically means that the calculated weld life has been maximized at 5×10^6 cycles at all locations. It also means that the associated damage is zero in all tested load cases, meaning that no significant aggregate fatigue damage occurs. Thus, an aggregate damage calculation with Miner sum was not necessary. The critical weld zone from the membrane and bending stress aspect is shown below in Fig 10 – Fig 12. These Figures highlight the bending ratio, the through-thickness bending, and membrane stresses respectively. The bending ratio of 0.931 implies a relatively bending-dominated situation. This is also demonstrated by the nearly zero membrane stress level.

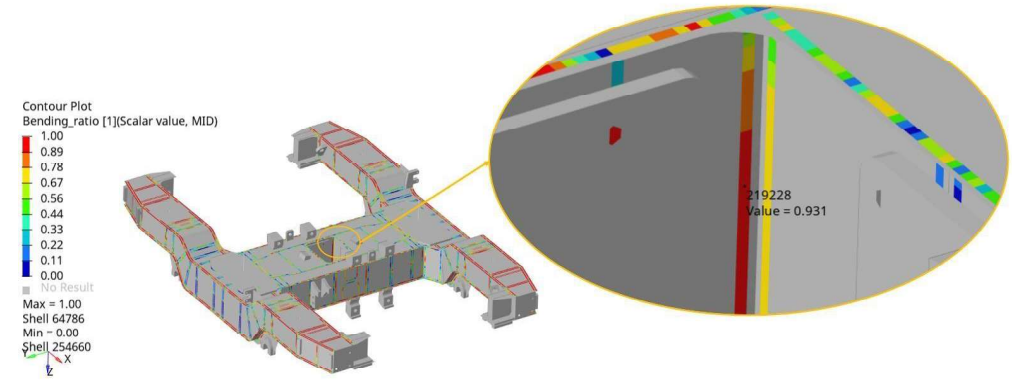

Fig 10. Bending ratio result with 1.0 multiplier and vertical force

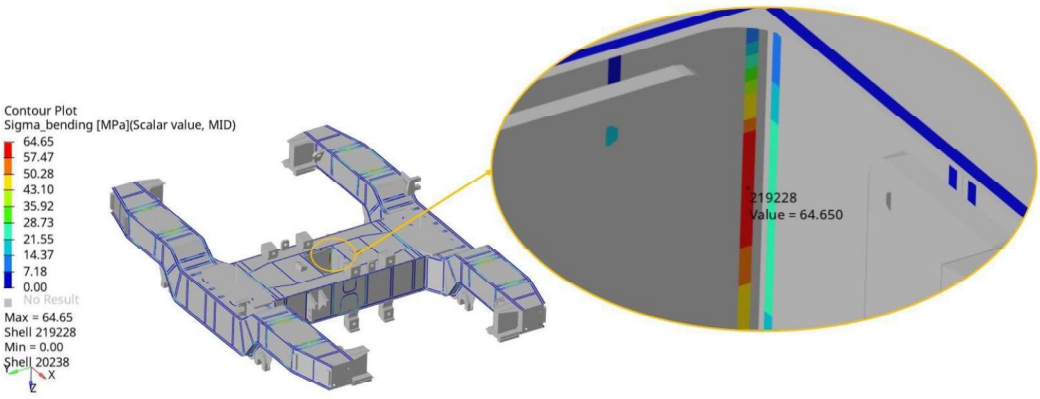

Fig 11. Reference bending stress result with 1.0 multiplier and vertical force

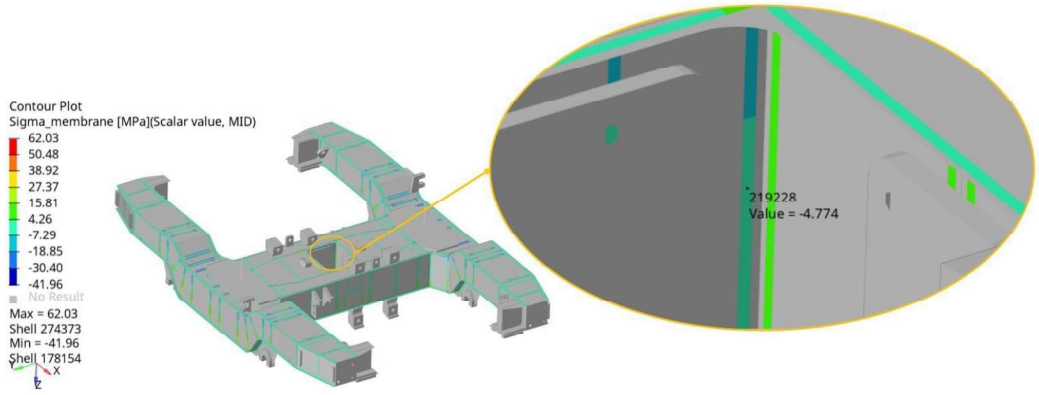

Fig 12. Reference membrane stress results with 1.0 multiplier and vertical force

To validate the results, based on the relevant experimental SN curve a conservative estimate of the endurance limit, including size effect, R-ratio and plate thickness was done, which is 50 MPa. At the critical location, the stress amplitude turned out to be 22 MPa. Thus, the safety against the endurance limit is 50/22 = 2.26. This essentially means that even at the critical location, the actual loading should be increased by 126% to reach the fatigue endurance limit and have ca. 5×10^6 cycles fatigue life. Since all welds have a large margin against fatigue endurance, the fatigue resistance of the entire structure was well demonstrated.

4 CONCLUSIONS

In summary, it can be concluded that a FE simulation-based strength and durability analysis of a welded structure like a bogie can significantly increase the accuracy of the analysis. We demonstrated that FEA-based stresses, even with simplifications like using shell-type elements for the plates, is an adequate representation of the real behavior from stiffness and strength point of view. Thus, these stress inputs can serve as reliable data for subsequent sophisticated fatigue assessment that can consider additional corrections such as mean stress effect, size effect, or consideration of plate thickness. Our assessment also proved that the investigated bogie structure has a significant built-in safety against fatigue, assuming the standard operational load sequence acting. This enables the bogie manufacturer to further optimize the thickness of the plates used as well as the weld types that can lead to reduced weight and more cost-effective solutions.

5 REFERENCES

[1] R. Xiu, M. Spiryagin, Q. Wu, S. Yang, Y. Liu: “Fatigue life assessment methods for railway bogie frames”. Engineering Failure Analysis, 116, 104725, 2020.

[2] Y. Lu, H. Zheng, J. Zeng, T. Chen, P. Wu: „Fatigue life reliability evaluation in a high-speed train bogie frame using accelerated life and numerical test”. Reliability Engineering & System Safety, 188, 221-232, 2019.

[3] B.J. Wang, S.Q. Xie, Q. Li, Z.S. Ren: “Fatigue damage prediction of metro bogie frame based on measured loads”. International Journal of Fatigue, 154, 106532, 2022.

[4] EN 13749:2011, Railway applications - Wheelsets and bogies - Method of specifying the structural requirements of bogie frames

[5] Fermér, M., Andréasson, M. and Frodin, B.: “Fatigue Life Prediction of MAG-Welded Thin-Sheet Structures”. SAE Technical Paper, 982311, 1998.

[6] EN 15085-3:2007, Railway applications - Welding of railway vehicles and components - Part 3: Design requirements

[7] A. Rupp, K. Störzel and V. Grubisic. “Computer aided dimensioning of spot-welded automotive structures”. SAE Technical Paper 950711, 1995.

[8] Analytical Strength Assessment of Components in Mechanical Engineering, FKM-Guideline, 5th edition, Frankfurt, 2003

[9] Wormsen, Anders, and Gunnar Härkegård. "A statistical investigation of fatigue behaviour according to Weibull’s weakest link theory." ECF15, 2004.

EXPERIMENTAL MEASUREMENT AND SIMULATION OF RUNNING RESISTANCE OF CONTAINER TRAINS

Tomáš MICHÁLEK[*a)], Martin KOHOUT[*a)], Jiří ŠLAPÁK[*a)], Jan PULDA[*a,b)], Jakub VÁGNER[*a)], Jan TÁBORSKÝ[*a)] and Martin KRÁLÍK[*a)]

[*a)] Department of Transport Means and Diagnostics, Section of Rail Vehicles
Faculty of Transport Engineering
University of Pardubice
CZ-53210 Pardubice, Czech Republic

[*b)] VÚKV a.s.
CZ-15800 Praha 5, Czech Republic

Received: August 5, 2022

ABSTRACT

This paper deals with research activities of the Faculty of Transport Engineering of the University of Pardubice in the field of running resistance of container trains. In the first part, results of run-down tests, which were performed with regular container trains in conditions of the Czech railway network, are summarized. On basis of their results, a modification of specific train resistance formulas was proposed. In the next part, the attention is paid to curve resistance. This resistance is influenced track-side (curve radius) as well as by vehicle parameters (radial wheelset steering capability etc.). A sensitivity analysis is performed by means of multi-body simulations in order to quantify a significance of the curve radius and cant deficiency. Evaluation of operational diagnostic data concerning the traction force of a locomotive in a curved track section is performed to verify the influence of curve radius on the total running resistance of a container train. Finally, a preparation of the instrumented screw coupling is briefly described. Actually, this measuring device is used by the Faculty of Transport Engineering for further investigation of vehicle running resistance of freight trains under the conditions of regular operation on the Czech railway network. The first measurement results, obtained with the instrumented screw coupling, are compared with the earlier results of operational run-down tests.

Keywords: container train, running resistance, run-down test, curve resistance, instrumented screw coupling

1 INTRODUCTION

Running resistance of railway vehicles plays a significant role in the branch of train dynamics. The running resistance of a train is influenced by many different factors, vehicle-side as well as track-side, and influences especially energy consumption of the train as well as the maximum weight of train which can be hauled by a given type of traction vehicle in a defined track section. Because some of these influencing factors show an accidental nature, an exact description of the running resistance is practically impossible. Therefore, the vehicle running resistance is usually expressed by empirical formulas to ensure its simple application in traction calculations.

As it is shown, e.g., in [1], sometimes the empirical formulas provide too inaccurate values which do not correspond to reality and affect especially the maximum allowed train weight. The reason of this disproportion can be based in outdatedness of the used formulas (in case of some older formulas which do not reflect the technical progress in railway system – e.g. the implementation of composite brake blocks with a positive influence on rolling resistance) or in a physical incorrectness of their application (in case of some formulas expressing the specific vehicle running resistance). Therefore, the problems of running resistance are still being actual and some research activities, realized at the Faculty of Transport Engineering of the University of Pardubice, are focused on this topic. The previous and current activities are summarized in this paper.

2 OPERATIONAL RUN-DOWN TESTS AND THEIR RESULTS

In years 2013 and 2016, a set of experiments was realized with regular container trains of the railway operator METRANS Rail (MTR) in order to quantify the vehicle running resistance of these trains. All the investigated trains consisted of a modern four-axle electric locomotive (type Bombardier TRAXX MS2e or Siemens ES64F4) and a set of 22 up to 25 four- and six-axle container wagons (types Sggnss 80', Sggrss 80', Sggmrs 90' and Sgns 60'). The total weight of the trains ranged from 650 to 1600 t and the total length was ca. 600 to 625 m (all the values include the locomotive). These experiments were performed in framework of regular operation on the railway line Brno–Břeclav (Czech Republic) and based on run-down tests – i.e. on coasting of the train without acting of any tractive or braking forces. The evaluation of these tests used the GPS data for speed measurement as well as train localization and the actual vehicle running resistance can be determined from the train equation of motion (see, e.g., [2]) as follows:

$$R_{\mathrm{tr}} = -\,s_{\mathrm{e}}\; g\; (M_{\mathrm{loc}} + M_{\mathrm{w}}) - 10^3\; [M_{\mathrm{loc}}\; (1 + \rho_{\mathrm{loc}}) + M_{\mathrm{w}}\; (1 + \rho_{\mathrm{w}})]\; \frac{\mathrm{d}v}{\mathrm{d}t} \qquad (1)$$

where:

- R_{tr} … vehicle running resistance of the train in [N];
- s_{e} … equivalent track gradient in [‰];
- g … gravitational acceleration (9.81 m·s^{-2});
- M_{loc} … total weight of locomotive in [t];
- M_{w} … total weight of the trainset (wagons) in [t];
- ρ_{loc} … coefficient of rotating masses of the locomotive;
- ρ_{w} … coefficient of rotating masses of the trainset (wagons);
- $\mathrm{d}v/\mathrm{d}t$ … actual value of train acceleration in [m·s^{-2}].

A detailed description of the performed operational run-down tests and their results can be found in [3, 4]. In the next, only the most significant conclusions of this stage of vehicle running resistance research are presented.

The first important result is the fact that the measured data allow to characterize the vehicle running resistance of the train by following formula:

$$R_{\mathrm{tr}} = a\; M_{\mathrm{tr}}\; g + C\; V^2 \qquad (2)$$

where:

- a … specific coefficient of constant resistance component in [N·kN^{-1}];
- M_{tr} … total weight of the train in [t];
- C … coefficient of aerodynamic resistance component in [N·h^2·km^{-2}];
- V … speed in [km·h^{-1}].

This formal description combines the specific expression of the constant component of vehicle running resistance (see the term defined by a) and the absolute expression of the aerodynamic component (see the term defined by C). This is the main difference of eq. (2) in comparison with the formulas using purely specific expression of the resistance, which is still being used e.g. by the Czech infrastructure manager. Besides to that, the results show that the specific coefficient a (given in N·kN^{-1}) can be expressed as:

$$a = 0.75 + 4/M_{\mathrm{a}} \qquad (3)$$

where M_a is the average axle load of the train (including the locomotive) in [t].

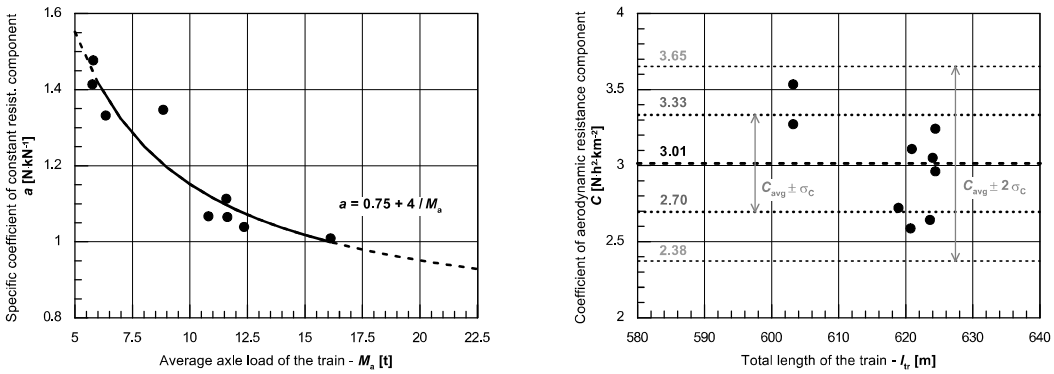

Fig. 1 Results of the operational run-down tests – values of the coefficients a and C

Results of the operational run-down tests are graphically presented in Fig. 1. These results are related to the whole train in accordance with eq. (1); i.e. the vehicle running resistance of the locomotive is also included. In the left graph, the approximation of the evaluated data by means of a dependence of the coefficient a on the average axle load of the train according to eq. (3) is demonstrated, as well. The hyperbolic shape of this dependence (i.e. the specific expression of a, given in $\mathrm{N \cdot kN^{-1}}$) reflects the physical base of the relevant resistance components:

- specific rolling resistance and specific axle bearing resistance (expressed by the value 0.75 $\mathrm{N \cdot kN^{-1}}$) which is generally not dependent on the train weight;
- friction components of the vehicle running resistance (e.g. the resistance of imperfectly released brake blocks) showing approximately constant absolute value (independent on the train weight).

In the right graph in Fig. 1, obtained values of the coefficient C – representing the aerodynamic resistance component – are depicted in dependence on the train length. Because a range of length of the investigated trains was small and the obtained values of the coefficient C show a relatively large dispersion (as a consequence of various shape inhomogeneity of the investigated trains – see [3, 4] for further details), no explicit dependency of the aerodynamic resistance component on the train length is observed. For application into the proposed formula (2), the average value of $C \approx 3$ seems to be appropriate for the common European container trains with a length of ca. 600–650 m.

3 CURVE RESISTANCE – SIMULATIONS AND EXPERIMENT

Besides to the vehicle running resistance, track resistances influence the train motion, too. The track resistances act on track gradients and in curves. The physics of the curve resistance lies in creep effects in wheel/rail contact during the vehicle run through the curve. In general, the specific curve resistance is usually expressed (see, e.g., [2]) as:

$$r_c = \frac{k_1}{R - k_2} \tag{4}$$

where:

- k_1 … the first coefficient of the specific curve resistance in $[\mathrm{m \cdot N \cdot kN^{-1}}]$;

- k_2 ... the second coefficient of the specific curve resistance in [m]; in case of some empirical formulas, this coefficient is equal to zero;
- R … curve radius in [m].

However, the (specific) curve resistance is really not influenced only track-side (i.e. by means of the curve radius). Because of a frictional nature of this kind of resistance, its value is significantly affected by the actual value of friction coefficient in wheel/rail contact. Operational conditions (flange lubrication, speed/cant deficiency, longitudinal forces in train) can also potentially influence the curve resistance value. Besides to that, vehicle parameters (dimensions, running gear design concept and characteristics of suspension) play a significant role, too.

3.1 Sensitivity analysis of selected parameters on the curve resistance

In framework of the diploma thesis [5], a sensitivity analysis of selected vehicle parameters on the curve resistance was performed by means of multi-body simulations (MBS) using a general four-axle vehicle model. On basis of its results it is possible to state that the most important vehicle parameter (from the point of view of specific curve resistance) is a longitudinal stiffness of wheelset guiding, influencing the radial steering capability of individual wheelsets. However, a possibility to change the value of wheelset guiding longitudinal stiffness of real railway vehicles is significantly limited by the requirement on stable run at higher speed. Therefore, in this work the attention is paid to a specific railway vehicle (a container wagon) and the influence of track parameters (curve radius) and vehicle speed (cant deficiency) on its curve resistance.

In order to quantify the significance of these parameters, a sensitivity analysis using MBS was performed. Computational simulations are suitable for the theoretical curve resistance analyses because they allow the vehicle to run without acting of vehicle running resistance (aerodynamic resistance, bearing resistance, etc.). SIMPACK model of an empty 60' container wagon was used. The vehicle model was equipped with a model of standard Y 25 bogie with frictional dampers developed in VÚKV. The basic design parameters of the model are listed in Tab. 1. The track flexibility and irregularities were considered and the FASTSIM method was used to calculate creep forces with a friction coefficient in wheel/rail contact equal to 0.36.

Tab. 1 Container wagon MBS model parameters

Parameter	*Value*
Bogie wheelbase	1 800 mm
Bogie distance	14 000 mm
Empty wagon weight	17 200 kg
Wheel/rail profile combination	S1002/e32.5 – 60E2/1:40

Curves with radii of 250, 325, 500 and 800 m were considered; the superelevation had a value of 100 mm in all these curves. And all these curves were run through at vehicle speed corresponding to values of cant deficiency of -50, -25, 0, 25, 50, 75 and 100 mm. For the calculation of the curve resistance, an assumption resulting from the law of conservation of energy was considered. The change in kinetic energy is equal to the work done by resistance force:

$$\frac{1}{2}\, m_{\mathrm{v}}\, (1+\rho_v)\, (v_2^2 - v_1^2) = F_R\, x \tag{5}$$

where:

- m_{v} … weight of the vehicle in [t];
- ρ_{v} … coefficient of rotating masses of the vehicle;
- v_2 … vehicle speed at the end of the monitored section in [m·s^{-1}];
- v_1 … vehicle speed at the beginning of the monitored section in [m·s^{-1}];
- F_R … resistance force in [N];
- x … length of the monitored section in [m].

Since the computational simulations consider only the curve resistance (and neglect the vehicle running resistance), it can be assumed that the resistance force is equal to the curve resistance. Then the formula for curve resistance calculation has following form:

$$R_{\mathrm{c}} = -\frac{m_{\mathrm{v}}\, (1+\rho)\, (v_2^2 - v_1^2)}{2\, x} \tag{6}$$

where R_{c} is the curve resistance in [N] and the minus sign before the fraction ensures a positive (absolute) value of the curve resistance. Then, the specific curve resistance (defined in N·kN^{-1}) can be expressed as follows:

$$r_{\mathrm{c}} = -10^{-3} \cdot \frac{(1+\rho)\, (v_2^2 - v_1^2)}{2\, g\, x}. \tag{7}$$

The simulation results (evaluated as described above) are presented in Fig. 2 in a form of dependency of the specific curve resistance on the curve radius. The results obtained in individual simulation scenarios (defined by the values of curve radius and cant deficiency) are depicted by points. On basis of the evaluation of simulations, it appears that a change in the cant deficiency has only a very small effect on the curve resistance. This effect is also confirmed by the results presented in Fig. 3 in form of dependencies of the (absolute) curve resistance on the cant deficiency for all investigated curve radii – only in case of a very small radius curve a slightly decreasing tendency is observed.

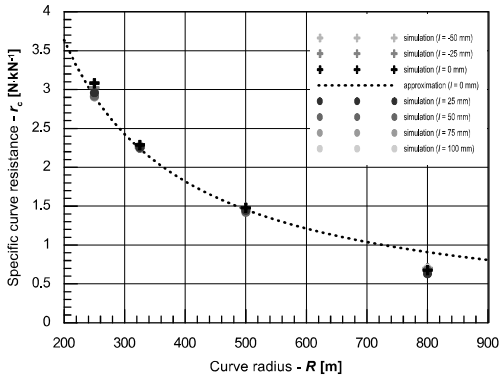

Fig. 2 Simulation results – the specific curve resistance vs. curve radius and calculated approximation function

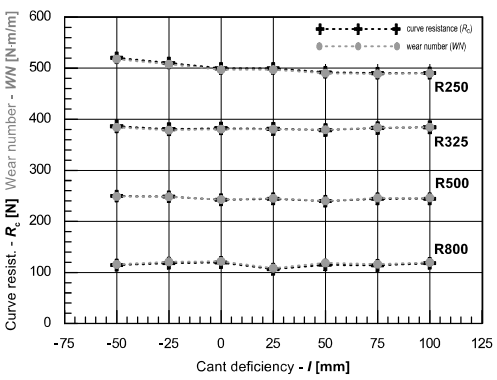

Fig. 3 Simulation results – dependency of the curve resistance and wear number on the cant deficiency

If the obtained set of results for individual values of the considered cant deficiency are approximated by the hyperbolic function in form of eq. (4) with $k_2 = 0$ m (using the least squares method), the values of the coefficient k_1 range approximately from 715 up to 750 m·N·kN^{-1}. In Fig. 2, the dotted line represents the approximation of results for the zero cant deficiency which can be expressed in following form:

$$r_c = \frac{727}{R}. \tag{8}$$

Because of the physical nature of curve resistance (i.e. the frictional effects in wheel/rail contact), so-called wear numbers were also observed during the simulations. The wear number represents the specific frictional work realized in the wheel/rail contact and the calculated values were compared with the absolute curve resistance values (defined by eq. (6)). The comparison is graphically presented in Fig. 3. The maximum difference between the calculated curve resistance values and wear number values is approximately 3.2 %. For the investigated MBS model this indicates a very good agreement of these two differently defined quantities.

3.2 Experimental verification of simulation results

Experimental methods for estimation of the curve resistance were checked in framework of the bachelor thesis [6] in 2017. In this case, traction force records from the locomotive diagnostic system TELOC were used and compared with theoretically calculated shape of forces acting on investigated trains in the track section Brno–Blansko (CZ) which can be characterized by numerous curves with radius of 250 up to 600 m. Three different container trains consisting of a locomotive type Bombardier TRAXX MS2e (Class 386) and 21 to 24 container wagons were considered. The total weight of these trains ranged from 1000 to 1700 t and their total length was ca. 560 up to 650 m (including the locomotive); all the wagons were equipped with Y 25 bogies. If the specific curve resistance in form of eq. (4) with $k_2 = 0$ m is applied, the results of the performed assessment show the values of $k_1 = 428$ up to 809 m·N·kN^{-1}. The average observed value of k_1 provides the specific curve resistance formula:

$$r_c = \frac{615}{R}. \tag{9}$$

Although the range of the observed results is relatively wide, they provide similar values of the coefficient k_1 as commonly used empirical formulas (see, e.g., [2]). It can be also stated that the results of multi-body simulation performed with an empty four-axle container wagon model (see section 3.1, eq. (8)) lies within the observed range.

4 EXPERIMENTAL MEASUREMENT OF FREIGHT TRAIN RUNNING RESISTANCE USING INSTRUMENTED SCREW COUPLING

As a next stage of the experimental research of running resistance of freight trains at the Faculty of Transport Engineering, an instrumented screw coupling was prepared for on-track measurement of traction force on the draw hook.

4.1 Preparation of instrumented screw coupling

It was decided to measure the traction force indirectly through deformation of screw coupling parts. Coupling links seems to be the optimal part for installation due to highest

relative deformation and low probability of hand contact during hanging of wagon and locomotive. The strain gauge technology in Wheatstone full bridge connection was chosen as a sensing element. This solution enables maximal sensitivity of measurement up to highest forces, static and dynamic sensing as well as full elimination of temperature effects during the measurement. Fig. 4 presents testing of the instrumented screw coupling before measurements in railway operation. These tests were realized on the dynamic test stand of the Faculty of Transport Engineering in Pardubice (CZ).

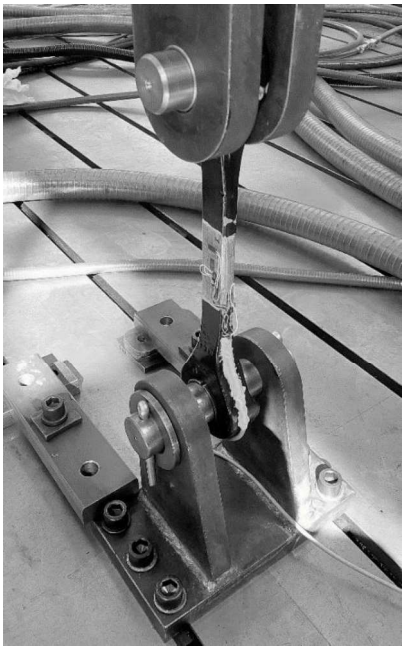

Fig. 4 Instrumented hanger of the screw coupling during laboratory tests

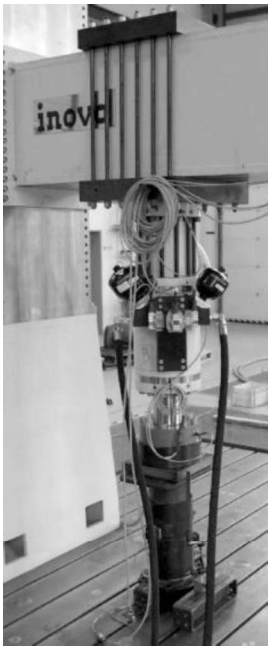

Fig. 5 Railway buffer during the laboratory tests of its dynamic characteristics

Although only the buffers compression was additionally checked during the realized operational tests, testing of the real dynamic characteristics of suspension elements applied in the draw- and buffing gear at different loading conditions is a next activity of the experimental research in the field of train dynamics at the Faculty of Transport Engineering (see, e.g., [7]). An example of the tested buffer is shown in Fig. 5.

4.2 Experimental measurement and examples of its results

The initial measurement of vehicle running resistance with the instrumented screw coupling (see Fig. 6) was realized with container trains of the METRANS Rail company on the Czech railway line Česká Třebová–Břeclav and back on November 5, 2021. The assessment of obtained data was performed in framework of the bachelor thesis [8].

As an example of results of the initial measurement, measured traction force and speed of the investigated train in the track section Brno–Břeclav are shown in Fig. 7. The speed was measured by an external GPS device (black dotted line) as well as registered by the system TELOC (grey dotted line). In case of the traction force, the record obtained by means of the instrumented screw coupling (i.e. the traction force on the draw hook) is presented by the black solid line and the TELOC record (i.e. the traction force on the

wheels) by the grey solid line. The train consisted of a locomotive type Bombardier TRAXX MS2e and 24 container wagons of the types Sggnss 80' and Sggrss 80'. The trainset had a total weight of 1408 t and a total length of 625 m (both values without the locomotive).

Fig. 6 Instrumented screw coupling on the locomotive

As described in [8], evaluation of these records in the relevant track section was done in two different ways:

- the vehicle running resistance value at the constant speed was calculated;
- the dependency of the vehicle running resistance on the speed was evaluated during the train acceleration.

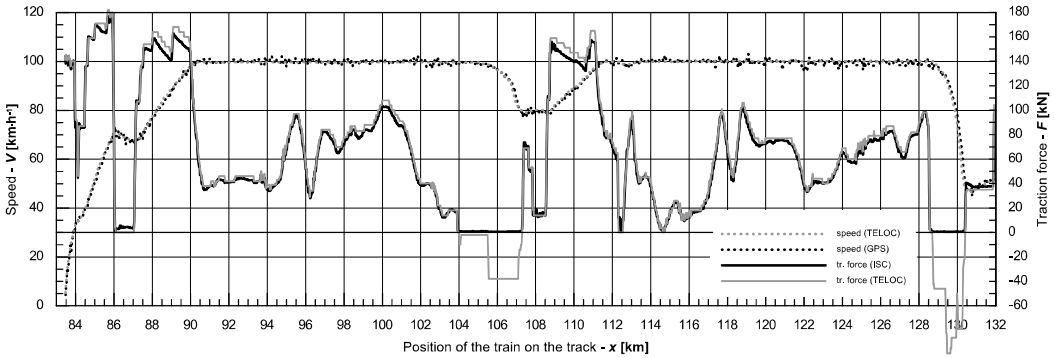

Fig. 7 Measured traction force of locomotive (on the wheels and on the draw hook) and speed of the train Nex 41736 in the track section Brno–Břeclav

Evaluation of the vehicle running resistance at constant speed is demonstrated in Fig. 8. The dotted lines represent the measured traction force (instrumented screw coupling: black, TELOC: grey) and the dashed line represents the total track resistance of the train following from the track gradient. Using the train equation of motion, the vehicle running resistance can be calculated. The solid lines represent the resistance:

- of the trainset (i.e. the wagons without the locomotive) – calculated from the measured force acting in the instrumented screw coupling (black line);

- of the whole train (i.e. including the locomotive) – calculated from the traction force on the wheels registered by the TELOC system (grey line).

Two important aspects of the measurement can be stated on basis of results in Fig. 8:

- for reliable evaluation of the vehicle running resistance value, a steady motion state of the train is needed (i.e. the constant speed as well as unchanging track gradient). This situation arises in km 91.5–93.0. The average value of the vehicle running resistance in this track section is 43.2 kN for the whole train and 41.4 kN for the trainset. The difference of 1.8 kN should correspond to the vehicle running resistance of the locomotive at the speed of 100 km·h^{-1};
- if any changes in traction force occur (e.g. as a consequence of regulation response on changing track gradient), effects of longitudinal train dynamics can be excited. These effects can complicate the evaluation of vehicle running resistance (see, e.g., the calculated resistance behaviour in km 97.0–103.0).

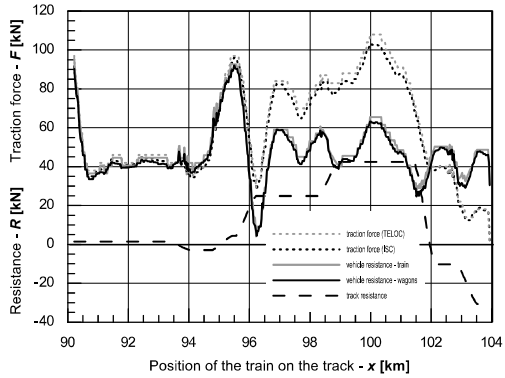

Fig. 8 Example of the vehicle running resistance evaluation at constant speed

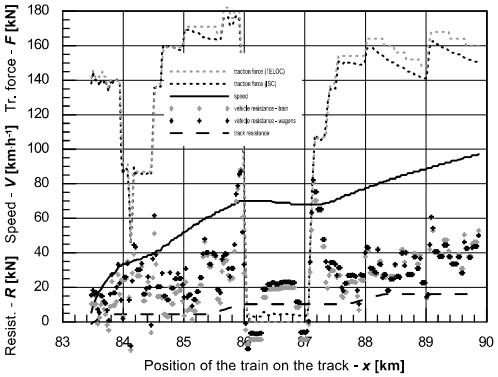

Fig. 9 Example of the vehicle running resistance evaluation during acceleration

Evaluation of the vehicle running resistance during train acceleration is demonstrated in Fig. 9. Again, the dotted lines represent the measured traction force on the draw hook (black) and on the wheels (grey) and the dashed line represents the total track resistance of the train following from the track gradient; the solid line shows the speed of the train (registered by TELOC). The individual points represent the calculated values of the vehicle running resistance of the trainset without locomotive (black) as well as the whole train (grey). Therefore, these points – calculated with using of the train equation of motion – correspond to relevant speed of the train. Generally, the relevant coordinates of these points $[V_i, R_i]$ can be subsequently approximated by a suitable function. However, this specific acceleration was affected by speed restriction on the throat of the Břeclav station (accompanied with a significant reduction of traction force – see km 84.0–84.5) and especially by coasting through a neutral section (see km 86.0–87.0). Therefore, the speed range of ca. 35–70 km·h^{-1} was not covered into the calculation of approximation function. Then, the characteristics of vehicle running resistance of the investigated trainset without locomotive can be expressed in following form:

$$R_{\mathrm{w}} = 11\,990 + 3.736 \cdot V^2. \tag{10}$$

5 CONCLUSIONS

This contribution summarizes previous and current research activities of the Faculty of Transport Engineering of the University of Pardubice in the branch of running resistance of container trains. The attention is paid especially to *experimental investigation of vehicle running resistance of trainsets using the instrumented screw coupling* and comparison of the obtained results with former results of operational run-down tests. If the obtained results should be mutually compared, it is possible to state that:

- the calculation of vehicle running resistance of the investigated container train at the constant speed of 100 km·h^{-1} gives a similar value (43.2 kN) as the formerly performed run-down tests (for the given train parameters: 45.4 kN);
- for the speed 100 km·h^{-1}, the vehicle running resistance formula (10) gives the result of 49.4 kN, i.e. a higher value than measured at the constant speed;
- in comparison with the currently used vehicle running resistance formula "T4" (see also [1, 2, 3]), the generalized conclusions of the operational run-down tests as well as the vehicle running resistance characteristics of the investigated train in form of eq. (10) indicate that the real vehicle running resistance of container trains of that type shows a lower constant component, but a higher aerodynamic component. This comparison is graphically presented in Fig. 10.

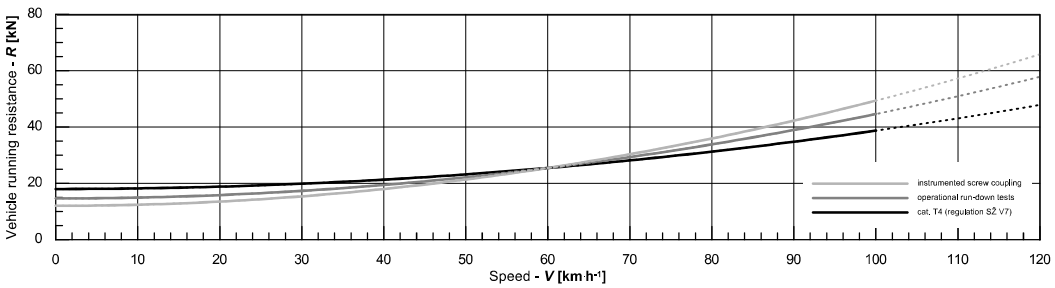

Fig. 10 Comparison of calculated characteristics of vehicle running resistance of the investigated container train (1408 t and 625 m without the locomotive)

On basis of the obtained results it can be stated that the mostly appropriate method for estimation of the vehicle running resistance characteristics is measurement of forces by the instrumented screw coupling at various speed levels and a separate evaluation of the partial results with a subsequent approximation of these partial results by a suitable approximation function. Evaluation of the vehicle running resistance characteristics should be possible during smooth accelerations without sudden changes of traction force (to avoid the longitudinal train dynamics effects). In case of evaluation of the TELOC records, the traction force record sometimes provided "dubious" values and therefore, their utilization can be problematical. All the acquired experiences will be applied within the further research of vehicle resistances at the Faculty of Transport Engineering.

In field of the *curve resistance*, multi-body simulations of a four-axle container wagon equipped with Y 25 bogies were used to estimate its curve resistance, including the estimation of influence of the curve radius and cant deficiency. Some tests using TELOC data were done in order to verify the MBS results. However, the range of results of the experimental measurements is too large to do unambiguous conclusions.

6 REFERENCES

[1] Šimral, P. - Michálek, T. - Králík, P.: On the problems of container train resistance. Proc. of the 21st International Conference on Current Problems in Rail Vehicles, 2013, p. 177-186.

[2] Michálek, T. - Zelenka, J.: Traction Mechanics. University of Pardubice, Faculty of Transport Engineering, 2022.

[3] Michálek, T.: Modification of train resistance formulae for container trains based on operational run-down tests. Proceedings of the Institution of Mechanical Engineers, Part F: Journal of Rail and Rapid Transit, 232(6), 2018, p. 1588-1597.

[4] Michálek, T. - Šimral, P.: Proposal of a modification of method for container train resistance calculation. Proc. of the 23rd International Conference on Current Problems in Rail Vehicles, 2017, p. 283-290.

[5] Králík, M.: Hodnocení odporu z jízdy obloukem s využitím simulačních výpočtů jízdy kolejového vozidla. [in Czech] Diploma thesis. University of Pardubice, Faculty of Transport Engineering, 2021. URL: https://dk.upce.cz/handle/10195/78875

[6] Králík, M.: Hodnocení jízdních odporů kontejnerových vlaků. [in Czech] Bachelor thesis. University of Pardubice, Faculty of Transport Engineering, 2018. URL: https://dk.upce.cz/handle/10195/70454

[7] Michálek, T. - Jaroš, P. - Vágner, J. - Kohout, M. - Šlapák, J. - Pulda, J. - Bílek, A. - Výmola, L. - Staněk, M.: Testing of draw- and buffing gear components on dynamic test stand at the Faculty of Transport Engineering of the University of Pardubice. Proc. of the 25th International Conference on Current Problems in Rail Vehicles, 2021, p. 199-206.

[8] Táborský, J.: Experimentální ověřování platnosti vzorců měrného vozidlového odporu nákladních vlaků. [in Czech] Bachelor thesis. University of Pardubice, Faculty of Transport Engineering, 2022. URL: https://dk.upce.cz/handle/10195/79935

ACKNOWLEDGEMENTS

This work was institutionally supported by the University of Pardubice, especially by the grant project No. SGS_2022_009 "*Research problems from the branch of transport means and infrastructure solved at the Faculty of Transport Engineering*". The authors thank to the METRANS Rail company for the cooperation on the experimental research of running resistance of container trains.

DYNAMICAL INVESTIGATION OF A RAILWAY WHEELSET RUNNING IN CURVE

Máté M. SZŰCS and Zoltán Zábori

Department of Railway Vehicles and Vehicle System Analysis
Faculty of Transportation Engineering and Vehicle Engineering
Budapest University of Technology and Economics
H-1521 Budapest, Hungary

Received: August 5, 2022

ABSTRACT

Since the beginning of the history of railway operation, experts have been concerned about gaining a deeper understanding of the rolling resistance of a railway vehicle, especially the energy loss in the operation when a vehicle is negotiating curves. Numerous studies have resulted resistance formulas, usually empirically based, that are useful for engineering practice. The growing safety requirements for railway operations, the increase of movement and the need to reduce traction energy require the need for a more thorough examination of the traction resistance forces generated during the running of vehicles and the application of technical measures to reduce the resistance.

A significant part of the losses during the operation of railway vehicles is necessarily present during traction, but a more thorough analysis of the parasitic movements during the running of the vehicle may show a way to reduce the losses. Among the running resistances generated during the operation of the vehicle, the loss related to the track-vehicle connection occupies a very significant place, which increases especially in curved sections.

In this study, we examine the energetic characteristics of an unsupported railway wheelset running in a curve applying a computer simulation method, whichdeterminese the losses from running a wheelset in a curve. In the course of the analysis, our purpose was to investigate the running resistance forces of a wheelset running in a curve and the reasons for their generation by simulating the known wheel-rail contact problem using the most fundamental model.

Keywords: railway single wheelset, conical tread, flange contact, curve resistance

1 INTRODUCTION

A significant part of the rolling resistance forces is generated from the wheel-track interaction. The rolling resistance appears both when running on a straight track and in a curve. Experience shows that these two different operating conditions result in different rolling resistance forces. It is easy to see that the displacement of two structural elements in contact with each other generates a frictional force, which can be interpreted as an energy loss in terms of traction energy, this loss derives from the main motion energy of the vehicle.

An in curve running wheelset outer and inner wheels' angular velocities are approximately the same (may differ depending on the torsional stiffness of the wheelset axle). If the wheelset is running in a curve with tread (one point) contact, the wheel running on the inside and outside rails can travel in the curve by creep or slip, depending on the operating conditions. The two wheels perform different resultant distances, in a so-called hunting motion with different amplitudes.

The dynamic behaviour of a free-running railway wheelset with a simple conical profile, launched at a given initial speed (and angular velocity) is simulated by computer modelling, as shown in Fig. 1. This allows the study of the dynamic processes of a wheelset running on a straight or on a curved track and of the position in the track axis.

The analysis determines the variation of the kinetic energy of the wheelset, the work of the creep and friction forces generated in the wheel-rail contact, from which the value of the energy dissipated during the travel in the curve can be deducted. For this purpose, the nonlinear wheel-rail contact model was taken as a basis according to [1]. From the results, obtained conclusions can be drawn about the increased resistance of the free-running wheelset in the track curve with regard to the variation of the curve resistance force.

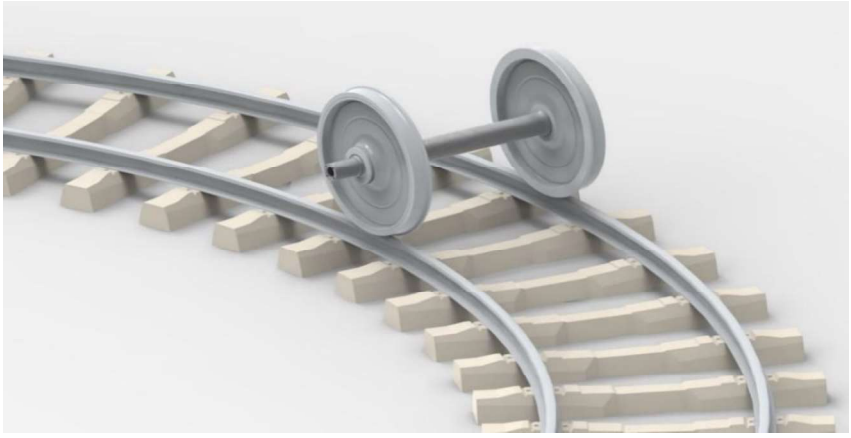

Fig. 1 Single wheelset running on a curved track

2 PURPOSE OF THE SIMULATION

Some of the known formulas for calculating the value of specific curving resistance are given in the first table based on [2]-[6]. The two types of the most used formulas are $\frac{c}{R}$ and $\frac{c}{R-R_{min}}$, can be given for curve ranges with different c and R_{min} values, where c is constant and R is the curve radius in metres as described in [7]. Some of the formulas are experimental and most of the measurements performed in the 1850s to the 1960s (I) and (IV). The other part of the formulas is the result of a quasi-static theoretical approach calculation [(II), (III) and (V)]. The specific curving resistance generally is stated in N/kN in respect of the weight of the vehicle.

Table 1 Curving resistance formulas based on the state of the art

Formula's author	Formula	No.
Röckl	$\frac{650}{R-55}$	(I)
Protopapadakis	$\frac{103{,}4a+158{,}4u}{R}$	(II)
Parodi	$1000\frac{\mu_s}{2R}(u+a^2+u^2)$	(III)
Astakhov	$\frac{100}{R}+1{,}5\lvert\tau\rvert, ahol\ \tau=\frac{v^2}{R}-\frac{h}{u}g$	(IV)
Schramm	$\frac{160a+162}{R}$	(V)

Where μ_s is the coefficient of friction in the contact surface; a is the wheelset spacing; u is the rolling plane distance; h is the height of the outer rail; g is the gravitational acceleration and v is the vehicle speed.

For (I) and (IV) the specific curve resistance is essentially given as a function of the radius, possibly with a velocity-dependent part added, where the velocity-dependent part is the unbalanced radial acceleration, thus the parameters are the moving speed, the curve radius, the height of the outer rail and the rolling plane distance.

In the formulas obtained by the theoretical approach, the parameters besides the radius are re usually the values of the wheelset spacing, the rolling plane distance and the friction on the wheel thread. Depending on which parameters are considered as constant values, one parametric (curve radius) or several parametric formulas are obtained.

In recent years, the results of experiments on test runs and roller rigs, as well as simulations with multibody dynamics software products, have usually been expressed in the form $\frac{c}{R}$ or $\frac{c}{R-R_{min}}$, as is well known from the literature sources [8]-[10]. Computer simulations were also carried out to investigate into influences of the coupler gear system generated forces in the curve resistance [11].

The aim of the simulation is to obtain a more accurate picture of the resistive forces generated during the travel of a single railway wheelset in a curve and describe characteristic features based on a dynamic approach.

The formulas described above provide a value for the curve resistance with a generally satisfactory accuracy for practical applications and reflects a quasi-static approach. In our experience, the curve resistance force manifests as a time-varying force.

3 DYNAMICAL MODEL

In this dynamic simulation, the free-rolling railway wheelset is considered as rigid body, rolling on a track with rigid support. The wheelset is free to move longitudinally, laterally and is free to rotate around the wheelset shaft, and a vertical axis passing through the wheelset's centre of mass. A four degrees of freedom dynamic model is considered. In the computation procedure, the wheel profiles are assumed to be purely conical (see Fig 2.).

In modelling the geometry of the wheel-rail contact, the tread contact and the flange contact were also considered as a purely conical profile. Wheel-rail contact model was discussed according to the nonlinear (heuristic) theory [1] with the addition that the dependence of the force-coefficient μ on creep was modelled according to [12]. A study of the dynamic model of the wheelset based on computer simulation can be used to determine the energy dissipation computed when the wheelset is running in curves, which is the basis of determination the curve resistance of the single wheelset in the curve.

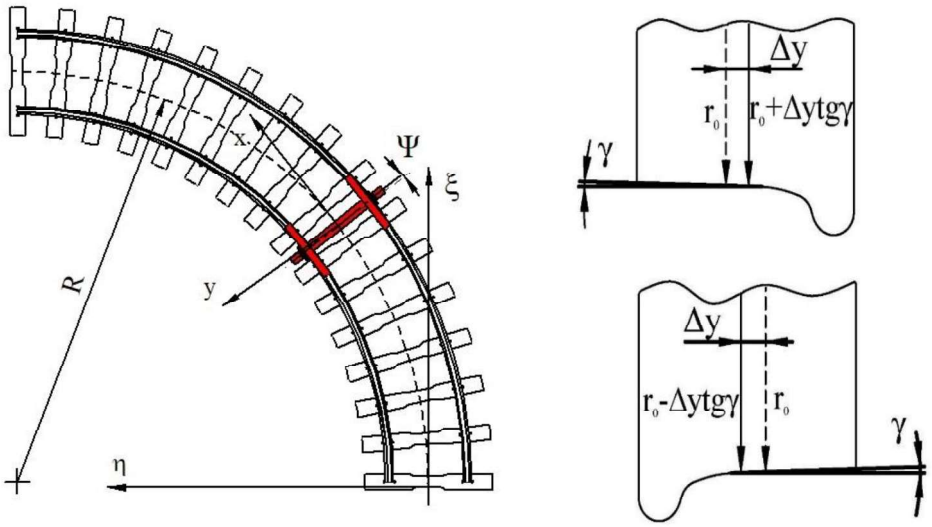

Fig. 2 Dynamical model of the single wheelset

3.1 Forces acting on the wheel tread – rail contact

The creep in the wheel-rail contact can be described by the movement of the outer and the inner wheels, formed to a vector (v_x is the longitudinal, v_y is the lateral and φ is the spin creepage):

$$\underline{v}_o(t) = [v_{xo}, v_{yo}, \varphi_o]^T, \underline{v}_i(t) = [v_{xi}, v_{yi}, \varphi_i]^T$$

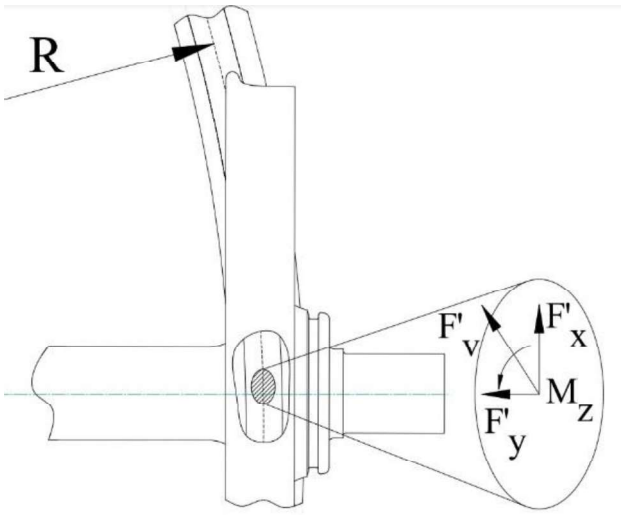

Fig. 3 Forces and moment acting on the contact ellipse

After determining the creepages, the forces and moments can be calculated according to Kalker's linear theory (see Fig. 3). According to the linear theory, the resultant tangential force at the wheel-rail contact surface can be computed as follows:

$$F'_{vo} = \sqrt{{F'_{xo}}^2 + {F'_{yo}}^2}, F'_{vi} = \sqrt{{F'_{xi}}^2 + {F'_{yi}}^2}$$

where F'_x is the longitudinal, F'_y is lateral creep forces arising in the contact surface, and F'_v is the resultant force.

In the case of slipping, the creep forces are replaced by friction forces according to eq. (1) and (2), which are limited by friction coefficient. Knowing the resultant tangential force, the nonlinear theory states that the relation between the creep and slip process can be calculated using the expression in [1] for the outside contact:

$$F_{vo} = \begin{cases} \mu Q_o \left[\frac{F'_{vo}}{\mu Q_o}\right] - \frac{1}{3} \cdot \left[\frac{F'_{vo}}{\mu Q_o}\right]^2 + \frac{1}{27} \cdot \left[\frac{F'_{vo}}{\mu Q_o}\right]^3, & if\ F'_{vo} < 3\mu Q_o \\ \mu Q_o, & if\ F'_{vo} > 3\mu Q_o \end{cases} \quad (1)$$

for the inside contact:

$$F_{vi} = \begin{cases} \mu Q_i \left[\frac{F'_{vi}}{\mu Q_i}\right] - \frac{1}{3} \cdot \left[\frac{F'_{vi}}{\mu Q_i}\right]^2 + \frac{1}{27} \cdot \left[\frac{F'_{vi}}{\mu Q_i}\right]^3, & if\ F'_{vi} < 3\mu Q_i \\ \mu Q_i, & if\ F'_{vi} > 3\mu Q_i \end{cases} \quad (2)$$

where Q is the vertical force comes from the weight of the vehicle, μ is the friction coefficient. The tangential and lateral contact forces can be computed according to the following expressions:

$$F_{xo} = \frac{F_{vo}}{F'_{vo}} \cdot F'_{xo}, F_{yo} = \frac{F_{vo}}{F'_{vo}} \cdot F'_{yo}, F_{xi} = \frac{F_{vi}}{F'_{vi}} \cdot F'_{xi}, F_{yi} = \frac{F_{vi}}{F'_{vi}} \cdot F'_{yi}$$

The lateral component of the forces in the normal direction on the running surface with the tread angle γ of the running surface on the outside is $T_{yo} = Q_o \cdot sin\gamma$, while on the inside $T_{yi} = -Q_i \cdot sin\gamma$.

The vector of tangential forces on the contact surface:

$\underline{F_o}(t, \underline{v_o}(t), Q_o, R, v_0) = [F_{xo}, F_{yo}, M_{zo}]$, and $\underline{F_i}(t, \underline{v_i}(t), Q_i, R, v_0) = [F_{xi}, F_{yi}, M_{zi}]$.

Combined performance of the wheel tread - rail forces:

$$P_T(t) = \underline{F_o}^T(t, \underline{v_o}(t), Q_o, R, v_0) \cdot \underline{v_o}(t) + \underline{F_i}^T(t, \underline{v_i}(t), Q_i, R, v_0) \cdot \underline{v_i}(t)$$

3.2 Approximate model of flange contact

For the simplified computation, there is always a two-point interaction assumed upon flange contacts the railhead.

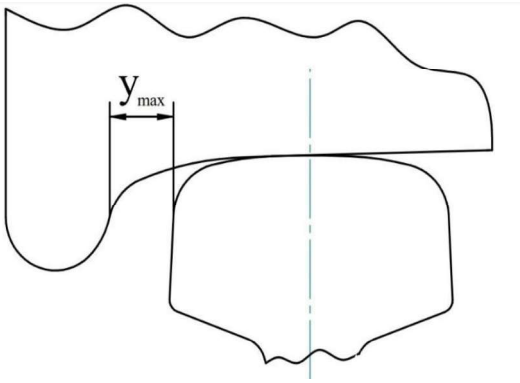

Fig. 4 Flange clearance

In the simplified model, the flange contact always occurs at the same point, so $y_{max}(\gamma)$ can be determined as a function of the running angle. In this model, a flange contact occurs when the lateral displacement reaches half of the predefined clearance (see Fig. 4):

$$y = f(y, \gamma) = y_{max}(\gamma)$$

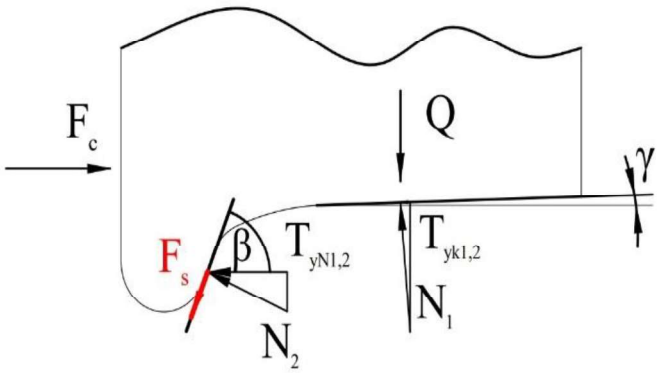

Fig. 5 Forces arising in the wheel-rail contact

The approximate determination of the normal force on the flange is based on the following simplifying assumption. The two-point interacted flange lateral contact force is balanced by two forces as of the normal force acting on the tread-flange and the lateral component of the flange arose friction force. Similarly, the vertical wheel load is balanced by the vertical component of the normal force applied on wheel tread points and the friction force applied on the flange. From this condition, two equations obtained from which the normal forces at the two interaction points can be determined (see Fig. 5).

Let the normal force in the case of two-pointed contact be N_1 on the running surface and N_2 on the flange, and the normal direction on the running surface is angle γ and the wheel flange angle is β.

The vertical wheel force Q and the wheelset has a lateral force F_c.

Then the following relations apply:

$$N_1 \cdot cos\gamma + N_2 \cdot cos\beta + \mu_N N_2 \cdot sin\beta = Q$$
$$N_1 \cdot sin\gamma + N_2 \cdot sin\beta + \mu_N N_2 \cdot cos\beta = F_c$$

Rearrange the equations, where μ_N is the sliding coefficient of friction in the wheel flange and rail contact:

$$N_1 = \frac{F_c \cdot (cos\beta + \mu_N sin\beta) - Q \cdot (sin\beta + \mu_N cos\beta)}{sin\gamma \cdot (cos\beta + \mu_N sin\beta) - cos\gamma \cdot (sin\beta + \mu_N cos\beta)}$$

$$N_2 = \frac{Q - N_1 \cdot cos\gamma}{cos\beta + \mu_N sin\beta}$$

From this, the longitudinal frictional forces on the flange are $F_{xN} = \mu_N N_2 cos\psi$, the lateral forces are $F_{yN} = \mu_N N_2 sin\beta$, and the lateral component of the normal force on the flange is $T_{yN} = N_2 cos\beta$.

To calculate the dissipation, it is also necessary to determine the value of the sliding velocity on the flange contact point. Assuming that the flange contact occurs at the same point on the wheel profile, the presumed wheel profile can be used to predetermine the value of the wheel radius difference Δr. For the hypothetical simplified profile used, the value of the wheel radius increasement was chosen to be 14 mm, so that the longitudinal slip velocity in the flange contact is:

$$v_{xN} = \frac{\dot{x}}{R - y_{max}} \cdot (R + b_A - y_{max}) + \dot{\psi} \cdot (b_A - y_{max}) - \dot{\chi} \cdot (r_0 + \Delta r) \cdot cos\psi$$

Lateral slip velocity:

$$v_{yN} = \frac{\dot{y} - (r_0 + \Delta r) \cdot \dot{\chi} sin\psi + (b_A - y_{max})\dot{\psi} sin\psi}{cos\beta}$$

where b_A is the half of the rolling plane distance. As vector:

$$\underline{F_N}(\tau, Q, R, v_0, \mu_N, \gamma, \beta) = [F_{xN}, F_{yN}, 0]$$

as well as the slip calculated at the contact of the flange:

$$\underline{v}_N(t) = [v_{xN}, v_{yN}, 0]^T$$

Friction power dissipated in the contact surface of the flange - railhead in the case of flange contact:

$$P_N(t) = \mu_N N_2 cos\psi \cdot v_{xN} + \mu_N N_2 sin\beta \cdot v_{yN} = \underline{F_N}(t, Q, R, v_0, \mu_N, \gamma, \beta) \cdot \underline{v}_N(t)$$

3.3 Equations of motion

The centrifugal force is defined as:

$$\underline{F_c} = -m\underline{\omega} \times (\underline{\omega} \times \underline{r})$$

In this case using scalar parameters:

$$F_c = -m \cdot (R - y) \cdot \left(\frac{\dot{x}}{R - y}\right)^2 = -m \cdot \frac{\dot{x}^2}{R - y}$$

Based on the above written the equations of motion of a free-running wheelset:

$$m \cdot \ddot{x} = F_{xo} + F_{xi}$$

$$\Theta_y \cdot \ddot{\chi} = -F_{xo} \cdot r_o - F_{xi} \cdot r_i$$
$$m \cdot \ddot{y} = +F_{yo} + F_{yi} + F_c + T_{yo} + T_{yi} + T_{yN}$$
$$\Theta_z \cdot \ddot{\psi} = M_{zxo} + M_{zxi} + M_{zo} + M_{zi}$$

$\underline{q}$ as a state vector: $\underline{q} = [x\ \chi\ y\ \psi\ ]$, also $\boldsymbol{M} = \langle m\ \ \Theta_y\ \ m\ \Theta_z\ \rangle$ mass diagonal matrix and introducing $\underline{F}(\underline{q}, \dot{\underline{q}}, R, \mu(v)\ , \underline{c}, t)$ excitation vector function we get

$$\ddot{\underline{q}} = \boldsymbol{M}^{-1} \cdot \underline{F}(\underline{q}, \dot{\underline{q}}, R, \mu(v)\ , \underline{Q}, \underline{c}, t)$$

second-order nonlinear differential equation system, where $\underline{c}$ is the vector containing the geometric parameters of the system ($\underline{c} = \underline{c}(b_A, \gamma)$), $\underline{Q} = [Q_o, Q_i]$ vertical wheel load vector. The solution of the system of differential equations is numerically generated using MATLAB.

3.4 Computation of the dissipated energy on the wheel-rail contact

The dissipated energy can be determined on basis of simulation run with duration time T. One can assume that the dissipated power generated in the wheel-rail contact is comes from the tread contact and occasionally from the flange contact. The structure of the dynamical model determines that while the wheel contact force on both wheel treads continuously exists, the occasionally appearing flange contact provides dissipated energy when the normal direction force N_2 acting on the flange is greater than zero.

$$P(t) = P_T(t) + P_N(t) = \underline{F}_o^T\left(t, \underline{v}_o(t), Q_o, R, v_0\right) \cdot \underline{v}_k(t) + \underline{F}_i^T\left(t, \underline{v}_i(t), Q_i, R, v_0\right) \cdot \underline{v}_i(t) + \underline{F}_N(t, Q_o, R, v_0, \mu_N, \gamma, \beta) \cdot \underline{v}_N(t)$$

At a given time t, the dissipated energy of the wheel-rail contact is computed by the integral

$$W = \int_0^t \underline{F}_o(\tau, \underline{v}_o(\tau), Q_o, R, v_0) \cdot \underline{v}_o(R, \tau) d\tau + \int_0^t \underline{F}_i(\tau, \underline{v}_i(\tau), Q_i, R, v_0) \cdot \underline{v}_i(R, \tau) d\tau + \int_0^t \underline{F}_N(\tau, Q_i, R, v_0, \mu_N, \gamma, \beta) \cdot \underline{v}_N(R, \tau) d\tau$$

In the following, to determine the value of the energy dissipation W per curve length unit, per curve radius unit.

The energy computed from the above expression can be used to determine a force of constant magnitude for a sufficiently long time or a sufficiently long distance. The energy generated by this force over a given distance, is equals to the energy computed above:

$$W = \int_0^S F_W(s) ds$$

where $S = \int_0^T \dot{x}(t) dt$. Based on all this, the curve resistance force that can be interpreted on a given section of track can be determined by the relation

$$F_W = \frac{W}{\int_0^T \dot{x}(t) dt}$$

The above expression also shows that the $F_W = F_W(R, v_0, Q_o, Q_i)$. Its specific value divided by the sum of $Q = Q_o + Q_i$ gives the specific value of the curve resistance:

$$f_w(R, v_0) = \frac{F_W(R, v_0, Q_o, Q_i)}{Q} \tag{3}$$

In eq. (3) the specific curve resistance is the total running resistance in curve, so it is not the resistance besides the resistance of running on straight track, but the total running resistance acts on the wheelset.

3.5 Simulation strategy

Several simulations have been carried out to determine the nature of the curve resistance. These simulations were considered:

- Initial speed: from 20 to 100 km/h with an increment of 20 km/h (5 situations).
- Curve radius: from 200 to 800 m with an increment of 100 m (7 situations).

The total simulation quantity (running in curve) is 35. In addition to the above cases, a straight section also considered, and the simulation run time was T=20 s.

4 RESULTS

The speed of the centre of gravity of the free-running wheelset appears to show a short time slight increase at the beginning of the simulation, as the wheelset drifts to the outer rail of the curve until contacts with the flange, so running on the increasing wheel radius causes a temporary increase, which is followed by a rapid decrease in speed. The wheelset continues to run at an apparently decreasing speed (see Fig. 6)

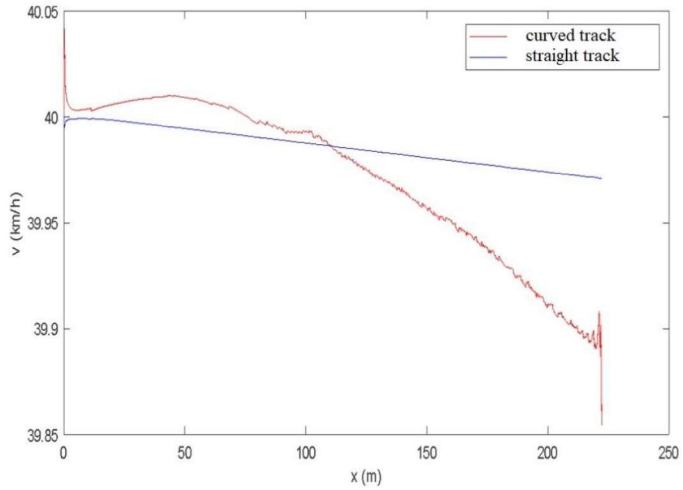

Fig. 6 The speed of the wheelset's centre of gravity

The specific curve resistance values determined for the different cases are shown in Fig. 7. The well-known dropping characteristics feature of the empirical formulas can be detected as a function of the curve radius.

A decreasing trend as a function of speed over the range investigated can also be recognised, in line with recent simulation results using multi-body dynamics software [10].

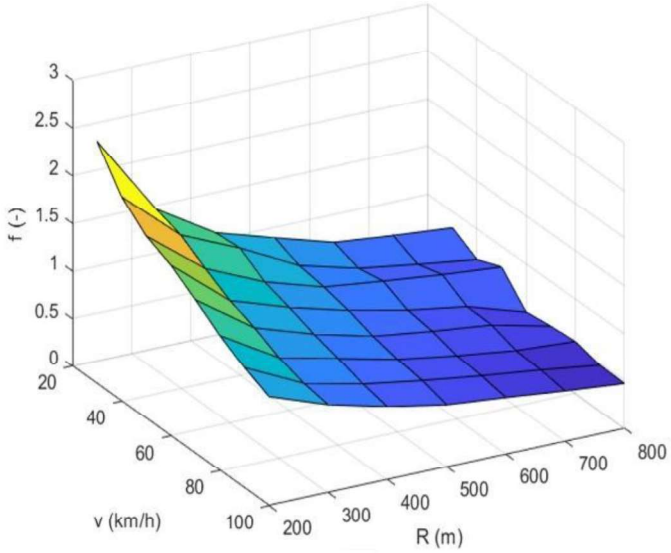

Fig. 7 The specific curve resistance as a function of speed and radius

5 CONCLUDING REMARKS

- In this research, the simple model shows the nature of the curve resistance lacking the impact of a possible suspension system and the entire body of the vehicle and the other vehicles.
- The conducted results of this research demonstrate that a free-running wheelset loses more kinetic energy via running in curve than running on a straight track. The loss is clearly coming from parasitic wheelset movements and the flange contact characteristics. This energy is originated from the main motion kinetic energy.
- The speed of the wheelset, the radius of the track and the length of the curve (the duration of the wheelset's run in the curve) are taken into account to calculate the curve resistance.
- In the future work, more simulations will be conducted by the current researcher, such as wider speed range and longer simulation run time. The scope of future research is to learn more about curve resistance particularly the property that decreases with speed.
- In order to investigate the loses of the suspension and coupler system, more accurate contact algorithms, profiled wheels, complete bogie and vehicle models, models consisting of several vehicles will be used in the proposed future work.

6 REFERENCES

[1] Shen, Z. - Hedrick, J.K. – Elkins, J.A.: A Comparison of Alternative Creep Force Models for Rail Vehicle Dynamic Analysis. Proc. Of the 8th IAVSD.Symposium: Swets and Zeitlinger B.V.Lisse, 1983, p. 591-605.

[2] v. Röckl, A.: Die Versuche der bayerischen Staatseisenbahn über die Widerstände der Eisenbahnfahrzeuge bei ihrer Bewegung in den Gleisen. Organ für die Fortschritte des Eisenbahnwesens in technischer Beziehung, 1881, p. 261-263. (In German)

[3] Protopapadakis, D.: Bemerkung über die zur Berechnung des Krümmungswiderstands w angegebenen Formeln. Monatsschrift d. Int. Eisenbahn-Kongress-Vereinigung, 1937, p. 1540-1555. (In German)

[4] Parodi, H.: La Traction électrique et le chemin de fer. Paris, 1935 (In French)

[5] Astakhov, P.N.: Resistance to Motion of Railway Rolling Stock. Moscow, 1965, p. 112-120. (In Russian)

[6] Schramm, G.: Bogenwiderstand und Spurkranzreibung. Eisenbahntechnische Rundschau, 1963, Heft 8, p. 390-392. (In German)

[7] Sapronova, S. - Tkacenko, V.: Rail Vehicles: The Resistance to the Movement and the Controllability. Duit State University of Infrastructure and Technology, 2017, p. 18-25.

[8] Lukaszewicz, P.: Running resistance - results and analysis of full-scale tests with passenger and freight trains in Sweden. Proceedings of the Institution of Mechanical Engineers, Part F: Journal of Rail and Rapid Transit, vol. 221, 2, p. 183-193.

[9] Ozaki, T. - Nakai, T.: Evaluation of a Steering Bogie about Running Resistance and Power Consumption. Proc. of the15th International Conference on Railway Bogies and Running Gears: Dep. of Rolling Stock of the SSME, 2016, p. 269-278.

[10] Wu, Q. - Wang, B.: Curving Resistance from Wheel-Rail Interface. Vehicle System Dynamics. Vehicle System Dynamics, 2020, p. 1-19.

[11] Wu, Q. - Wang, B.: Implications of Lateral Coupler Forces for Rail Vehicle Curving Resistance. Journal of Computational and Nonlinear Dynamics, vol. 16, 2021, p. 1-9.

[12] Zobory, I.: A kerék és a sín közötti gördülőkapcsolat hosszirányú erőkapcsolati tényezőjének modellezése kétparaméteres nemstacionárius sztochasztikus mezővel. GÉP, vol. LIX (2), 2008, p. 40-50. (In Hungarian)

AN UNCONVENTIONAL ROLLER TEST RIG FOR THE INVESTIGATION OF ROLLING CONTACT FATIGUE AND WEAR PHENOMENA IN RAILWAY WHEELS AND RAILS

Prasaenna RANGANATHAN and Christian SCHINDLER

Institute for Rail Vehicles and Transport Systems (IFS)
RWTH Aachen University
Seffenter Weg 8, 52074 Aachen, Germany

Received: August 05, 2022

ABSTRACT

Rolling contact fatigue and wear are the two most important phenomena that occur in railway wheels and rails. To test the fatigue and wear characteristics of the wheel and rail materials, roller test rigs are used in railway research. The contact patch between the wheel and rail is crucial as it directly influences their fatigue lives and the wear pattern on their contact surfaces. Therefore, it is imperative to reproduce the real wheel-rail contact patch between the rollers of a roller test rig. Current full-scale roller test rigs, which use the actual railway wheel for testing, produce contact patches narrower than in reality along the direction perpendicular to the axis of rotation due to the use of rollers with rail profile instead of straight rails. Since rolling contact fatigue at a point is dependent on the number of fatigue cycles, it takes a considerable amount of time for these test rigs to develop cracks and material wear as they employ actual railway wheels. Downscaled test rigs like the twin-disc machine can test specimens quickly due to their extremely small size. However, their rollers produce a miniscule contact patch. At the Institute for Rail Vehicles and Transport Systems (IFS), RWTH Aachen University, an unconventional roller test rig is being developed for the investigation of rolling contact fatigue and wear phenomena in railway wheels and rails. The unconventionality of the test rig stems from its 'internal rollers' roller orientation, which is novel to roller test rigs in railway research. One of the main advantages of this test rig is its ability to produce contact patches similar to reality with rollers that are smaller than real railway wheels. This paper discusses the drawbacks of the current roller test rig designs and presents the design and the operating modes of the new test rig. The results of the normal contact analyses of the rollers at different normal loads and with different contact profiles are also discussed.

Keywords: roller test rig, rolling contact fatigue, wear, wheel-rail contact, wheel-rail contact testing

1 INTRODUCTION

Roller test rigs are an intrinsic part of railway engineering and research. The purpose of a roller test rig (RTR) is to emulate the conditions on a real track and thereby enabling the rail vehicles or its sub-systems to be tested economically and efficiently. They are utilized for a variety of purposes like performance and safety testing of rail vehicles, testing the dynamics of new running gear and vehicle concepts, wheel-rail contact, rolling contact fatigue and wear investigations and NVH (Noise, Vibration and Harshness) testing.

1.1 Roller Test Rig Designs in Railway Engineering

There are several designs of a RTR. They can be categorized based on the tested specimen, the scale and the orientation of rollers [1]. All roller rigs consist of a wheel (or wheels) in contact with a rail (or rails). The rail is realized either as a straight or a curved bar or as a wheel with a rail profile on its circumference. The selection of a configuration is based on the type of experiments to be carried out in it. The specimen of a RTR can be a single wheel, a wheelset, a bogie or a vehicle depending upon the phenomenon that is investigated. Single wheel test rigs are used for investigations where the wheel-rail contact parameters are crucial. However, they are not suitable for simulating or studying the effect of the lateral dynamics of a wheel as the lateral movement of the wheel with

respect to the rail is usually arrested. Such investigations can be performed with a wheel-set, bogie or a vehicle RTR where the wheels are free to move in the lateral direction like in reality. This feature also enables investigations on the evolution of wear pattern on the wheel tread.

Based on the orientation of the wheel with respect to the rail, RTRs can be categorized into vertical roller, perpendicular roller, internal roller and oscillating roller as shown in Fig.1 [1]. The vertical plane roller is the most commonly used orientation and it is applied across all specimen types. The perpendicular roller design is shown in Fig.1b. As the arrangement is similar to reality, the wheel-rail vertical dynamics can be investigated with this orientation when the rail is fixed on the ground. In the oscillating rail set-up (see Fig.1d), the wheel is held stationary and the rail is moved back and forth or vice versa. Consequently, the wheel cyclically alters its direction of rotation. The speed of the wheel is usually slow and cannot be maintained constant throughout. Therefore, this orientation is suitable for rail fatigue investigations. The internal roller orientation (see Fig.1c) is the rarest of all. This orientation is more stable than rollers in external contact [2]. The radii of the rollers can be adjusted to reproduce the contact geometry of interest without major increase in size of the test rig.

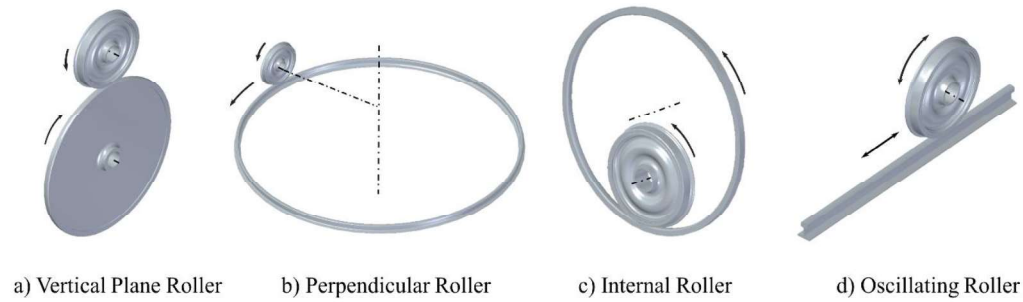

Fig. 1 Different orientations of the rollers in a roller test rig (According to [1])

Based on the size of specimen used they can be classified into full-scale and scaled RTRs. As the name suggests, the full-scale RTRs use real specimens and components for testing and the scaled test rigs use downscaled models as specimens. In a full-scale vehicle RTR both complete vehicles and running gears can be tested. A wide range of dynamic tests can be carried out at stability limits under different track conditions like curved track, tangent track, track with irregularities etc.

The name scaled RTR generally refers to a downscaled RTR. Scaled RTRs and models are downscaled using a scaling factor. The scaling factor usually ranges between 1:3 and 1:5. They are cheaper to manufacture and maintain. Amendments to the design can be done easily and quickly whenever necessary. Currently, scaled models are used only for testing new running gear concepts and for educational purposes.

Mini test rigs have been developed exclusively for testing rolling contact fatigue (RCF) and wear characteristics of materials. These test rigs were initially developed to test bearing steels and were later adapted for wheel-rail RCF and wear testing. They use the contact of two or more rotating metal balls, rods, discs or their combinations to develop

fatigue and wear. For investigating RCF in railway wheels and rails, disc on disc (or Twin-disc) test rig is commonly used. Twin-disc machines are mini RTRs specifically used for investigating rolling-sliding contact fatigue and wear characteristics of materials. It essentially has two thin discs contacting each other on their circumference. The diameter of the discs depends up on the manufacturer of the machine. Discs of different diameters ranging from 47 mm to 320 mm have been recorded in the literature ([3] - [7]). The thickness of the disc is usually around ten millimetres. Around 8 kN normal contact load can be applied using these machines, which is very low compared to full-scale test rigs. Fig.2 shows the configurations used in current roller test rigs in railway engineering (denoted by pink spheres).

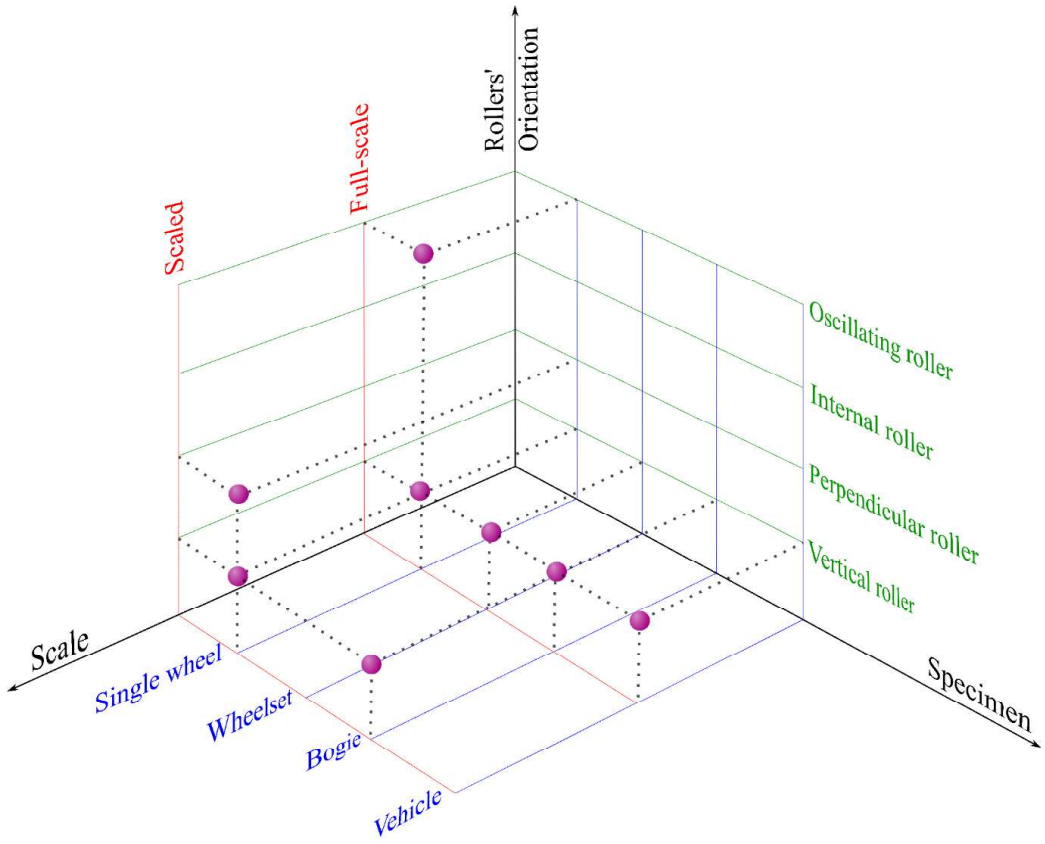

Fig. 2 Configurations used in current roller test rigs in railway engineering

1.2 Motivation for the New Roller Test Rig

The investigation of RCF and wear in a conventional full-scale RTR is time demanding. Rolling contact fatigue at a point in the wheel/rail material is dependent on the number of contact stress cycles and subsequently on the number of rotations of the wheel. Therefore, carrying out RCF tests until failure on a real wheel takes several months to complete, which is inefficient in terms of cost, time and energy. The contact patch in a full-scale RTR is also not accurate due to the use of wheel with rail profile instead of actual rails. In a full-scale RTR, rollers with rail profile on their circumference are employed

to provide traction to rotate the tested wheel. The diameter of these traction rollers is usually bigger than the tested wheel's diameter. The contact patch obtained from these test rigs are narrower than in reality due to the rollers' curvature.

Though full-scale RTRs can simulate accurate wear patterns along and across the wheel's circumference, they are not time-efficient with respect to testing of wear characteristics of materials. For example, in wear rate investigations, the rate of removal of material from contact surface is more critical than the pattern of wear along and across the wheel circumference. For such investigations, using real wheels is not prudent as they consume more time than scaled wheels to develop the same wear magnitude at identical contact conditions due to their size.

The disadvantage of a twin-disc machine is that, unlike wheel-rail contact, a rectangular contact patch develops between the discs due to flat contact profiles. Consequently, the pressure distribution is also in contrast with that of a wheel-rail contact. Therefore, conventional discs are not suitable for investigating RCF and wear of railway wheels and rails. Kumar et al. [6] and Galas et al. [7] have used bigger and modified rollers to replicate the pressure distribution of a wheel-rail contact; the size of the contact patch developed thereby is however several times smaller than a real wheel-rail contact patch. For example, the rollers used by Galas et al. produced an elliptical contact patch with extents 3.3 mm and 2.8 mm at 6 kN normal load.

The problem with using a smaller contact patch for RCF and wear investigations is that, in an asperity contact, the contact stresses from a smaller contact patch cannot be directly correlated with the stresses in a real contact patch. For Hertzian contacts, where zero friction is assumed, hertzian laws can be used to find the load required to produce a certain equivalent pressure, for any scale. However, in an asperity contact, the stresses are comparatively higher and they do not vary linearly with respect to loads. It is imperative to address these problems before correlating the results of a twin-disc machine or any downscaled test rig with the results from a real wheel-rail contact [8].

Thus, a test rig that can simulate the RCF and wear phenomena in railway wheels and rails under contact conditions similar to reality with minimal cost and time consumption is the need of the hour.

2 CONCEPT DESIGN OF THE NOVEL TEST RIG

Different views of the proposed test rig concept are shown in Fig.3. The test rig consists of two rollers in 'internal rollers' orientation. This orientation is chosen as it offers flexibility to adjust the geometry of the rollers and subsequently the contact patch shape and size, without major increase in size of the test rig. The test-roller, which is the tested specimen, represents the railway wheel, while the counter-roller represents the rail. The rollers are connected individually through hollow shafts to two geared asynchronous machines that can operate both in motor and generator mode. The calculated power of the motors is 160 kW. The test-roller is press-fitted (conical press fit) on an adapter, which in turn is mounted on the shaft as shown in cross section A-A of Fig.3. Two roller bearings on each shaft bear the wheel loads.

The counter-roller shaft is mounted on a lever arm, whose one end is pivoted by two journal bearings and the other end is fastened to an I-section frame through an assembly of Belleville spring washers and a load cell. The load is applied to the test-wheel by relaxing the pre-loaded set of Belleville spring washers. The magnitude of the applied load is controlled by adjusting the compression of the spring washer set. The free body diagram of the contact force generation system is shown in Fig.4.

The partial angular movement of the counter wheel shaft about the lever arm axis is realized by a flexible shaft coupling that connects the shaft and the motor. The above-mentioned parts are mounted on frame assemblies on both sides.

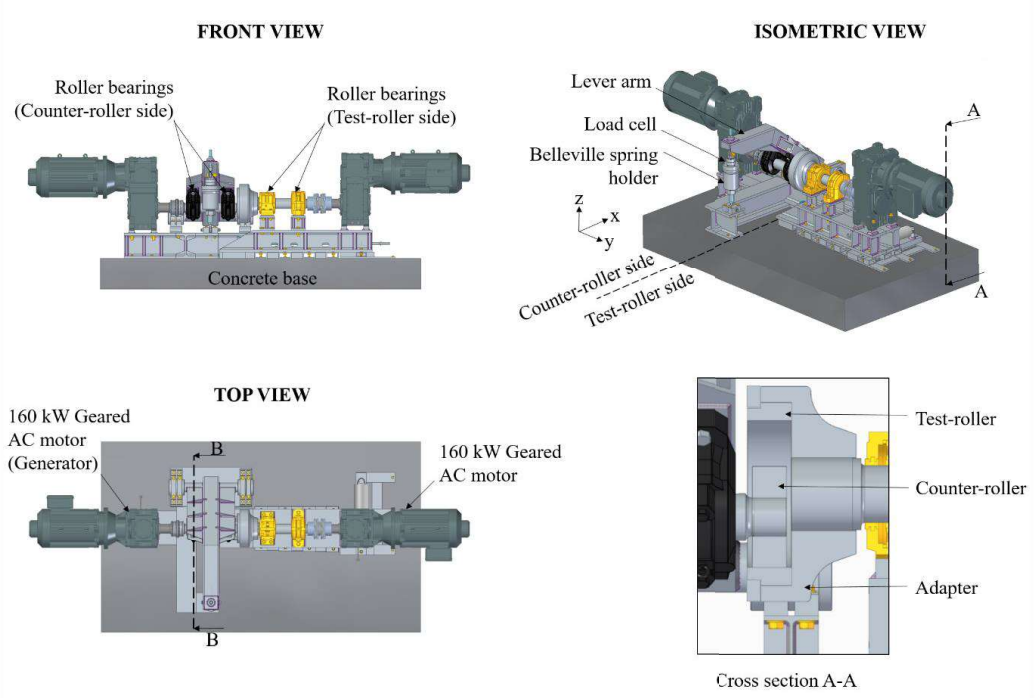

Fig. 3 Parts of the proposed test-rig

Once the contact load is applied on the test-roller by the counter-roller, the frictional contact binds them. The motor on the test-roller side acts as the drive motor and the counter-roller side motor, whenever activated, acts as a generator. The rollers rotate in the same direction due to their orientation

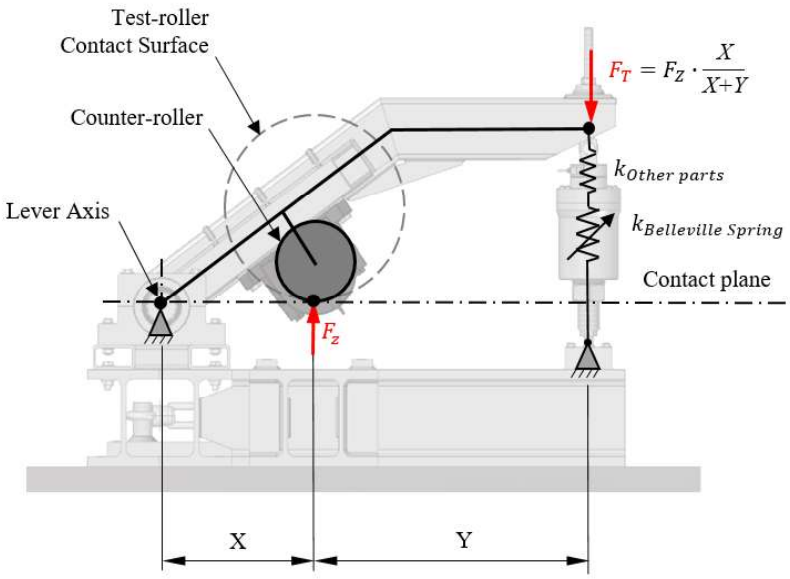

Fig. 4 Free body diagram of the contact force generation system (The figure represents cross section B-B mentioned in Fig.3 without motors, rollers and the test-roller side)

2.1 Modes of Operation

The test rig can be operated in free rolling and slipping modes. During the free rolling mode, the motor on the test-roller side drives the test roller, while the counter-roller side motor is electrically inactive such that no sliding occurs between the contact surfaces of the rollers.

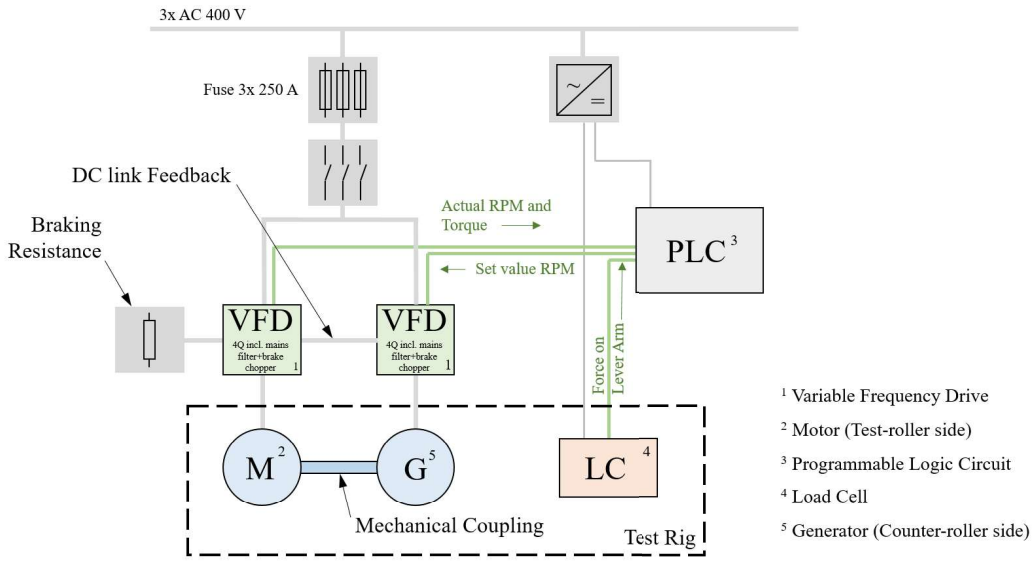

Fig. 5 Electrical circuit diagram of the test rig

In the slipping mode, in which accelerating or braking of a wheel is emulated, the motor on the counter-roller side is activated and switched to generator mode. This causes counter moment to act on the counter–roller shaft leading to relative motion between the contact surfaces. Simultaneously, the energy is recuperated and circulated back to the motor on the test-roller side by the variable frequency drives (VFD) (see Fig.5).

Tests can also performed with an angle of attack (up to two degrees) between the rollers. This is realized by rotating the test-roller side about the axis passing through the contact point.

2.2 Design of the rollers

As emulating the real wheel-rail contact patch is of primary importance, the rollers' radii are selected such that, the equivalent radius of the contact pair is similar to that of the real wheel-rail contact. The wheel-rail contact patch is sensitive to the orientations of the wheel and the rail. Contact patches of different shapes can be obtained just by shifting the wheel laterally with respect to the rail. For testing purposes, a simple quasi-circular contact patch is chosen. To produce a quasi-circular contact shape in the test rig, the equivalent radii of the contacting rollers should be similar in the vertical planes parallel and perpendicular to the direction of travel. The reference radius chosen for the test rig is 450 mm. Thus, the roller profiles generate equivalent radii around 450 mm in both the planes.

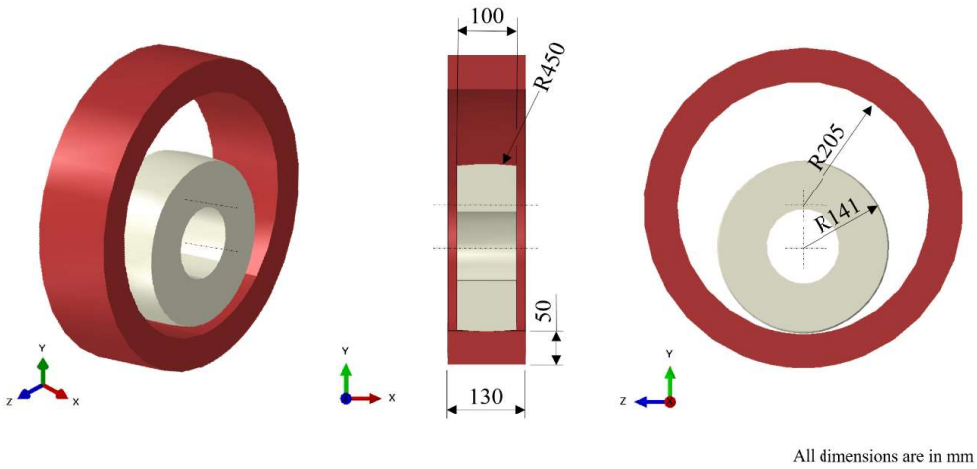

Fig. 6 Primary dimensions of the rollers

In a real railway wheel, the equivalent contact radii vary drastically especially in the vertical plane perpendicular to the direction of travel. This non-hertzian nature of the contacting surfaces results in a bigger contact width than when a constant contact radius is used. For simplicity, a constant contact radius is chosen for both the rollers in both the directions. Due to this, the area of the contact patch is slightly smaller than in reality. The dimensions of the rollers is shown in Fig.6. The rollers have not been scaled directly from a real wheel using a scaling factor. Instead, smaller rollers, the radii of which are mathematically calculated to attain the desired contact geometry, are used. However, the radii of the rollers can be adjusted to obtain different contact patch shapes.

2.3 The contact patch

To calculate the geometry of the contact patch and the pressure distribution within the contact patch Abaqus Standard FE solver has been used. The simulations were done in implicit dynamic quasi-static mode. The properties of the materials used for the simulation are shown in Tab.1. The material properties for the R7T and R260 materials have been taken from [9]. The plasticity models used for R7T and R260 steels are the Armstrong-Frederick kinematic hardening model [10] and the Lemaitre-Chaboche combined non-linear isotropic and kinematic hardening model [11] respectively.

Tab. 1 Material properties used for finite element analysis

Part	Material	Properties	
Test-roller	R7T	Elastic Parameters	E : 205000 MPa ϑ : 0.3
		Plasticity Model Parameters	C : 137000 MPa γ : 401 σ_y : 316 MPa
Counter-roller	R260	Elastic Parameters	E : 206000 MPa ϑ : 0.3
		Plasticity Model Parameters	C_1 : 2.47e^{+04} MPa C_2 : 6e^{+04} MPa C_3 : 2e^{+05} MPa γ_1: 55 γ_2: 600 γ_3: 2000 σ_y : 379 MPa Q_∞: -189 MPa b_m : 500
Test-roller Adapter	25CrMo4	Elastic Parameters	E : 210000 MPa ϑ : 0.3

The contact patch developed by the test rig and its pressure distribution are shown in Fig.7. The contact patch is quasicircular in shape and comparable to real wheel-rail contact in size. The ratio of its extents can be changed by adjusting the radii of the rollers.

Contact Geometry

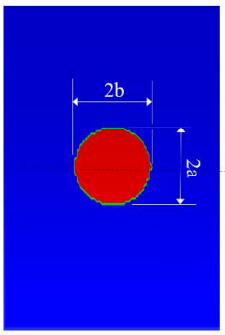

Load (kN)	Contact Area (mm^2)	Extents (mm)
70	121	2a : ~12.00 2b : ~12.50
90	146	2a :~14.00 2b :~13.50
100	159	2a : ~14.00 2b : ~14.50

a)

Contact Pressure Distribution

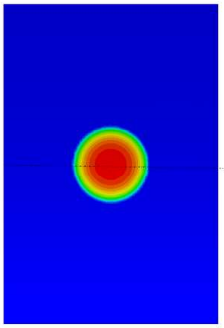

Load (kN)	Max. Contact Pressure (MPa)
70	809
90	845
100	862

b)

Fig. 7 a) Geometry of the contact patch between the rollers b) Pressure distribution inside the contact patch at different normal contact loads

The contact stress and equivalent plastic strain distribution inside the rollers at different contact loads are shown in Fig.8. The distribution of the von Mises stress is similar in both the x-y and y-z planes. The points of maximum von Mises stress and the equivalent plastic strain are found below the contact surface for both the rollers for all normal loads. For the 100 kN and 90 kN normal contact load, the maximum von Mises stress and the equivalent plastic strain occur at 3.4 mm and 4 mm below the contact surface for test-roller and counter-roller respectively. For the 70 kN normal contact load, the points are located at 3.37 mm and 3.14 mm below the contact surfaces of test-roller and counter-roller respectively. The values of equivalent plastic strain mentioned in Fig.8 correspond to single cycle of contact load application. The maximum equivalent plastic strain occurs in the test-roller for all the load cases.

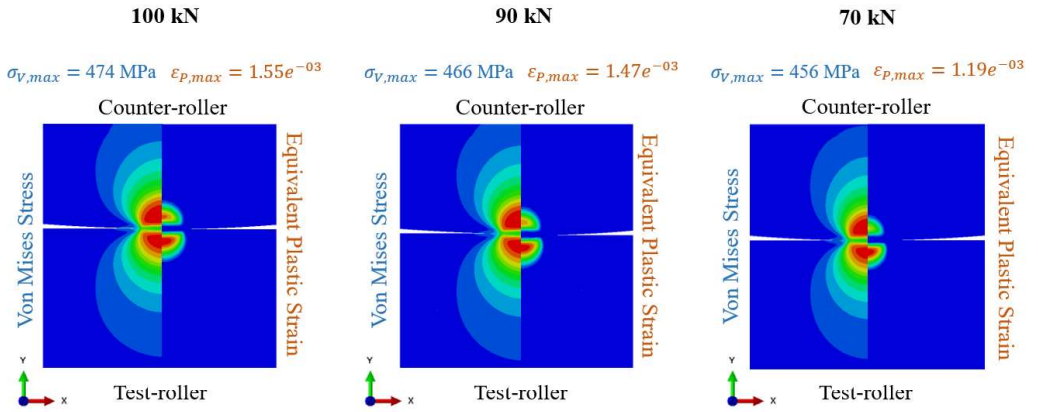

Fig. 8 Contact stress and equivalent plastic strain distribution in test-roller and counter-roller at different contact loads

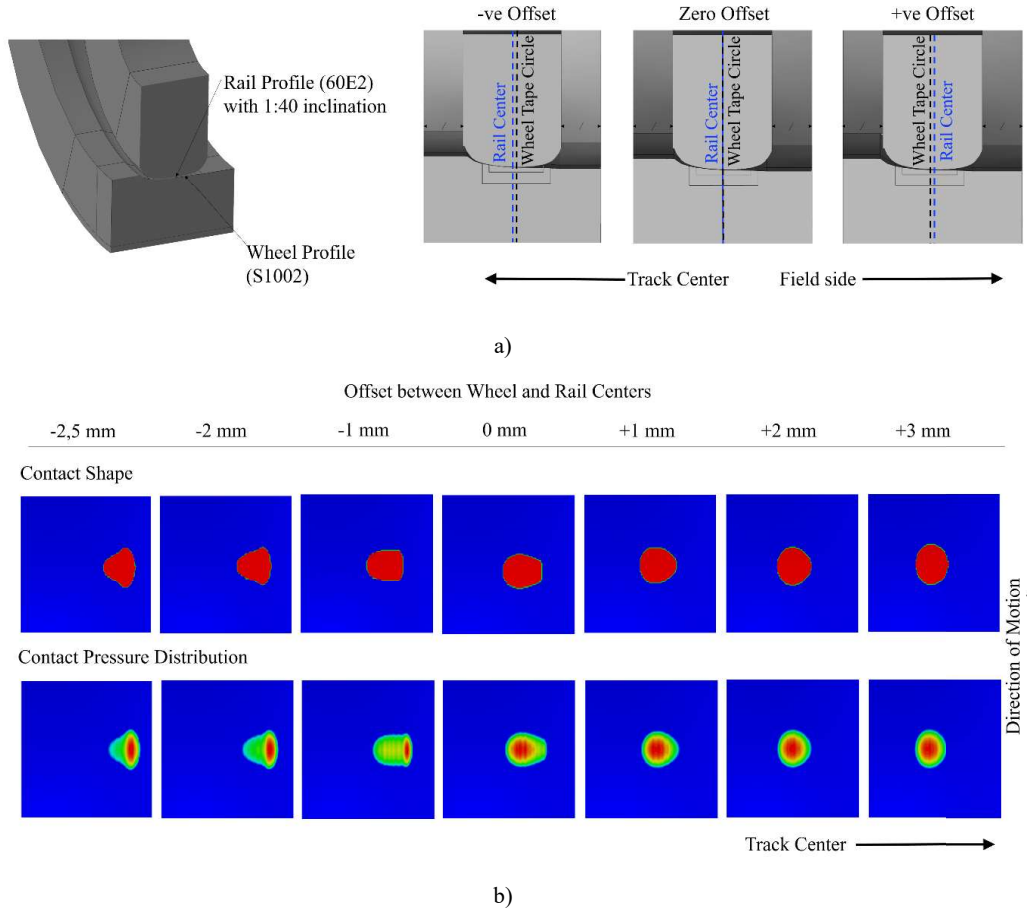

Fig. 9 a) Rollers with wheel and rail profiles b) Contact patches produced by the rollers at different offsets

The test rig is not limited to circular and elliptical contact patches. If the real wheel and rail profiles are employed in the test-roller and counter-roller respectively, contact shapes observed in a wheel-rail contact can be obtained. The process of reproducing the real contact patch is however complicated. In a real wheel-rail contact the first contact point between the wheel and rail shifts rapidly as the wheel is shifted laterally with respect to the rail. Since the radius of the rail is always infinity on the vertical plane parallel to the direction of motion of the wheel, it does not affect the equivalent radius on this plane. In contrast, for the roller test rig, the radius of the rail is not infinity as a wheel with rail profile, in this case the counter-roller, is used for representing the rail. Therefore, the equivalent radius also shifts in accordance with the first point of contact leading to larger or smaller contact width than in a wheel-rail contact along the rolling direction. Hence, the radius of one or both wheels have to be adjusted to maintain the same equivalent radius at the first point of contact.

Fig. 9 shows the cross section of the rollers with wheel and rail profiles embedded on test-roller and counter-roller respectively and the contact patches developed by shifting the wheel profile of the test-roller along the direction of the axis of rotation. The results shown here are preliminary, as the diameters of the rollers have not been adjusted to match the extents of a wheel-rail contact patch. The shapes of the contact patch and the pressure distribution are however similar to the real wheel-rail contact.

3 CONCLUSION

The issues with the present test rigs with respect to RCF and wear testing of materials for railway wheels and rails were discussed. The concept design of the proposed test rig was explained. The proposed test rig has two rollers in ‘internal rollers’ orientation. The rollers have a smaller diameter than a railway wheel, which allows quicker and cheaper testing of the specimens. Though the rollers are smaller, the contact patch developed by the test rig is similar to that of a real wheel-rail contact. The test rig can be utilized for research on general rolling contact, RCF and wear. It will be helpful in answering several questions related to RCF crack propagation, wear rate of wheel/rail materials, polygonal wear of wheels, influence of different friction modifiers on the adhesion coefficient etc.

4 ACKNOWLEDGEMENT

The authors express their gratitude to the Deutsche Forschungsgemeinschaft (DFG) for providing the financial support for the development of the test rig. Project No.: 471444469

5 REFERENCES

[1] Myamlin, S., Kalivoda, J., Neduzha, L.: Testing of Railway Vehicles Using Roller Rigs. Procedia Engineering, Volume 187, 2017, p. 688-695, ISSN 1877-7058.

[2] Meymand, S.Z.: State of the Art Roller Rig for Precise Evaluation of Wheel-Rail Contact Mechanics and Dynamics [Doctoral Thesis], in Mechanical Engineering, Virginia Polytechnic Institute and State University, Blacksburg, 2015.

[3] Lewis, R., Dwyer-Joyce, R.S.: Wear mechanisms and transitions in railway wheel steels. Proceedings of the Institution of Mechanical Engineers, Part J: Journal of Engineering Tribology, 218(6), 2004, p. 467-478.

[4] Hasan, S.M., Chakrabarti, D., Singh, S.B.: Dry rolling/sliding wear behaviour of pearlitic rail and newly developed carbide-free bainitic rail steels. Wear, Volumes 408–409, 2018, p. 151-159.

[5] Jouini, N., Revel, P., Thoquenne, G., Lefebvre, F.: Characterization of Surfaces Obtained by Precision Hard Turning of AISI 52100 in Relation to RCF Life. Procedia Engineering, Volume 66, 2013, p. 793-802.

[6] Kumar, S. and Rao, D. L. P.: Wheel-Rail Contact Wear, Work, and Lateral Force for Zero Angle of Attack—A Laboratory Study. ASME. J. Dyn. Sys., Meas., Control, 106(4), 1984, p.319–326.

[7] Galas, R., Smejkal, D., Omasta, M., and Hartl, M.: Twin-Disc Experimental Device for Study of Adhesion in Wheel- Rail Contact. Engineering Mechanics, 21(5), 2014, p. 329-334.

[8] Fletcher, D.I., Franklin, F.J., Kapoor, A.: Rail surface fatigue and wear. Editor(s): R. Lewis, U. Olofsson, Wheel–Rail Interface Handbook, Woodhead Publishing, 2009, p. 280-310, ISBN 9781845694128.

[9] Saint-Aimé, L., Charkaluk, E., Dufrénoy, P.: Three-dimensional finite element elastic-plastic model for wheel-rail rolling contact fatigue prediction. In: Proceedings of the 10th international conference on contact mechanics, 2015, Colorado Springs, Colorado, USA.

[10] Armstrong, P.J., Frederick, C.O.: A mathematical representation of the multiaxial Bauschinger effect. CEGB report RD/B/N 731, 1966.

[11] Chaboche, J.L., Lemaitre, J.: Mechanics of solid materials. Cambridge: Cambridge University Press, 1990.

ANALYSIS ASPECTS OF VERTICAL DYNAMIC MODEL IMPLEMENTATION INTO SIMULATION METHODS TO ASSESS INFLUENCES OF SECONDARY SUSPENSION SYSTEM ANOMALIES ON WHEEL PROFILE WEAR

Péter FERENCZ

Department of Railway Vehicles and Vehicle System Analysis
Faculty of Transportation Engineering and Vehicle Engineering
Budapest University of Technology and Economics
H-1521 Budapest, Hungary

Received: August 5, 2022

ABSTRACT

This paper describes the investigation process development goals and method into the impacts of bogie secondary suspension system anomalies with specially to focus on wheel wear propagation. The study is particularly focusing on analysis of vertical dynamics, evaluates changes of output characteristics of different stages of a development of vertical dynamics implementation into simulation method. The basis of study was originated from a past issue of an electric locomotive bogie design flaw. The results of the past study derived to a general correlation assessment between the origin of such anomalies and the resultant in an unexpected wheel wear phenomenon. The forming of thoughts covers the procedure of extension of current available simulation method to handle vertical, pitching, and tilting parasite movements to establish the possibility to evaluate the influence on the wear propagation process. The hereby study pictures the development of the application of the dynamics system simulation, observing the output features change effects of the simplest vertical system simulation realization solution. An important in-process goal emerged, which is to evaluate the output features provided by the different level complexity system stages. How deep-complex a model should be developed to get adequate answers for certain phenomena question on practical usage? This answer needs to be found as well. By searching correlation alongside the output data, the goal is to find the necessary minimum level and range of input parameters should be determined to be taken into consideration. This inspection results in a certain way of parameter sensitivity analysis, utilizing the preceding evaluations of quasi-static investigation results as influences of the secondary suspension system anomalies identified such as the resultant horizontal restoring torque, or the direct impact of vertical wheel force deviations.

Keywords: stochastic simulation, railway wheel profile, correlation analysis, system anomaly, stochastic system analysis, system deterioration, lifetime

1 INTRODUCTION

The subject of the paper is originated from a dynamic anomaly phenomenon occurred on a large quantity of an electric locomotive type. Solution of the problem was hidden in the dynamic parameters of the suspension system. The phenomena turned out to show intensive asymmetric wheel profile wear, which by the computations and simulations confirmed, caused by the secondary suspension spring elements' feature alterations. The question was formed, how a certain phenomenon can be identified by examination of the wheel profile wear propagation process. The investigation process by application of parameter sensitivity checks pointed out the importance of the secondary horizontal resultant torque if it is present due to the possible asymmetry of suspension features. This paper searches for possible general statements to describe the effects of simple suspension system parameter variations by using the acceptable simplest dynamical models. This is to establish the ground to find the general answer how a suspension system anomaly can have influence on the wheel profile wear propagation processes.

2 2. ON THE ORIGINAL CASE STUDY

The case-study was dealing with the MÁV No. 431 series electric locomotives suffered from dramatically fast wheel profile wear propagation after bogie and wheelset revisions were carried out. In several cases during the years 2000 - 2006 more than 3 mm difference could be measured between the two flange thickness values of certain wheelsets performed approximately only 80 000 kms of mileage (see Fig.1)

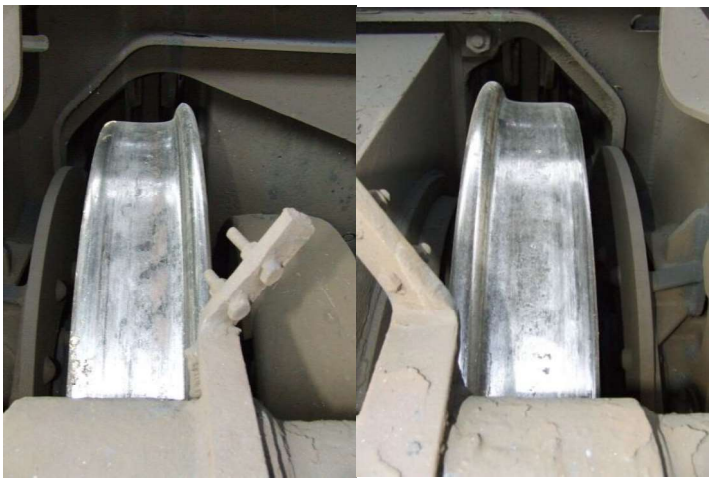

Fig. 1 The phenomenon of the asymmetric profile wear, picture of left and right wheel of an affected wheelset

The phenomenon appeared in a random way, in different combinations, it could not be stated that affected regularly left or right-side wheels. The chart of Fig.2 shows sample secondary suspension spring characteristic measurements on a certain locomotive with large asymmetric flange wear values. With an implementation of a modernization purpose change of the bogie - loco-body interface design, rubber springs had been applied since 1998 instead of a pendulum structure. The re-usage of these rubber to metal spring units became necessary in large amount during the overhaul of the bogies. After more than hundreds of measurements turned out that the stiffness parameters can show grate deviations.

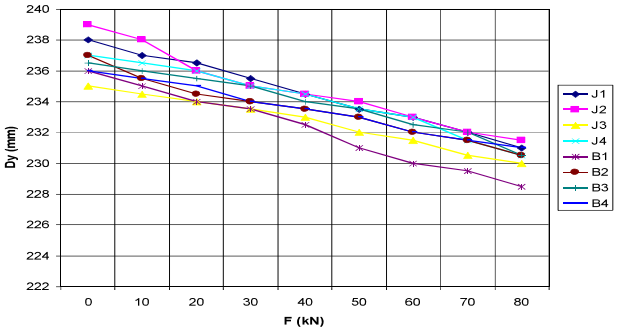

Fig. 2 Sample data of vertical spring force characteristic, all units in one loco attached could show high deviation

To eliminate this problem, the wheel-profile wear simulation method and software (developed by BME, Department of Railway Vehicles) were used. Considering the several elastic components of the bogie design, it was necessary to use non-linear models built into the existing wear simulation method (software named ELDACW), which contains the lateral dynamical model of a rail-vehicle of two bogies with 2 wheelsets each, described by 30 degrees of freedom. The simulation processes focused on the wear propagation process appearing on the wheels one by one.

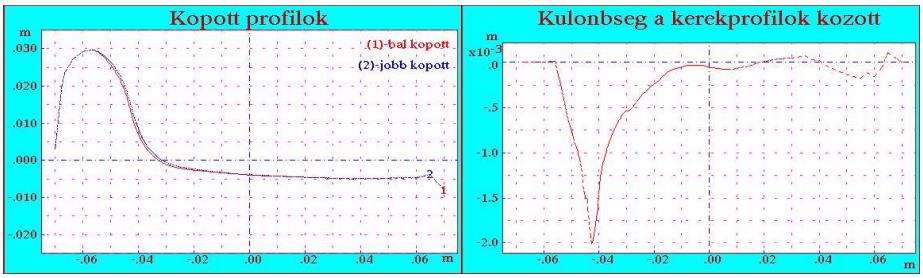

Fig. 3 Difference between right and left worn wheel profiles, the left figure shows the simulated worn profiles, whilst the wear difference in the right one

The spring characteristic tests revealed that the probable randomly re-mounted secondary spring units could cause great stiffness differences in the suspension gear that gave rise to a special effect which was recognized in the simulation results as a variation in the resultant horizontal torque appeared at the bogie - body interface.

It was proved that differences among the characteristics of the built-in secondary springs caused the strongest influence on the mentioned abnormal wear process, bringing about asymmetric wheel flange wear. As an edification of the simulation-based study it became a real necessity the emphasized control of the secondary suspension characteristics of the applied secondary suspension springs of rubber-to-metal sandwich structure. Several modifications were realized according to the results of the examinations (i.e., secondary suspension design, as well as the maintenance and overhaul technology were modified).

3 RESULTS USED OF QUASI STATIC COMPUTATIONS

To evaluate vertical force variations depending on the secondary suspension stiffness deviation of each side, evaluation was carried out by using the classic linear, simplified in vertical quasi static plane model to determine characteristic vertical displacements and relevant rotation values.

The evaluation of the resulted vertical force variations caused by the vertical dynamical asymmetry due to measure of the secondary suspension stiffness deviations was handled as follows. The considered percentile measures of the input stiffness deviations from the rated stiffness value were arranged into vector **Δ**.

$$\mathbf{\Delta} = [1, 8, 16, 25, 33]\ (\%) \tag{1}$$

These values were applied as direct impacts to introduce conscious artificial stiffness asymmetry into the later described computations.

The case study showed that the lateral and the vertical dynamical models of the locomotive reflected the real behavior of the structure. It proved that differences in the characteristics of the secondary suspension elements could cause effective asymmetric wheel wear. These investigations into the asymmetric wheel flange wear phenomenon proved that the differences in characteristics of the secondary suspension elements caused the most intensive influence, for details see citation [6].

4 SIMPLIFIED MODEL AND SIMULATION METHOD

Such described phenomenon is identified as a detectable system anomaly, originated from suspension system parameter deviations that cause unexpected formations in wheel wear propagation. The goal is now to set up the most simplified simulation model to examine the dynamical effects of the suspension element parameter deviation variations.

Utilization of MATLAB Simulink modules, a 5 degrees-of-freedom model was selected. The model is characterized in Fig. 4. The three masses are representing in order one wheelset, the portion of a bogie over it, and the portion of the car-body. The considered elastic and dissipative parameters of the system components are set according to the above-described locomotive suspension gear.

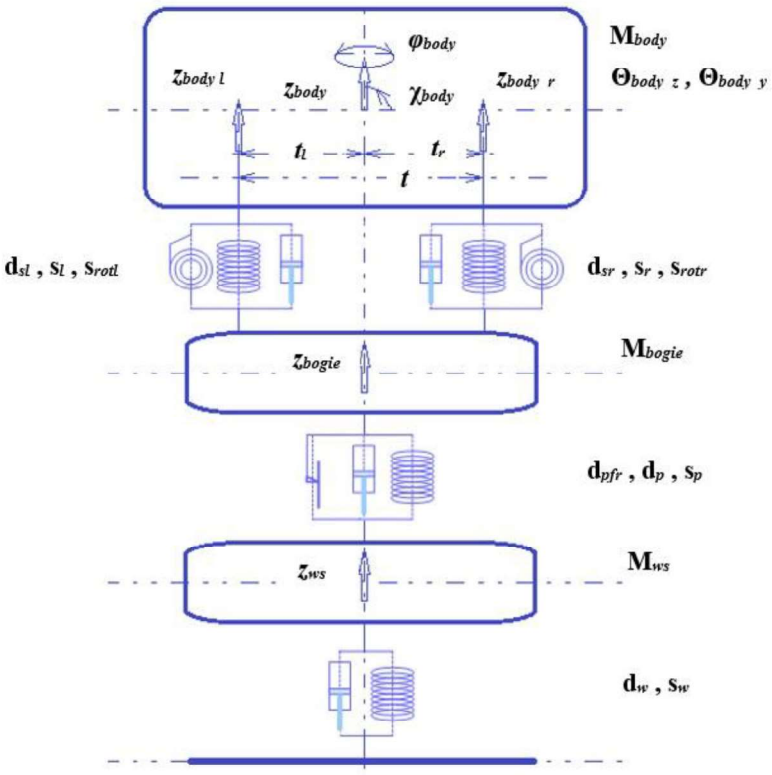

Fig. 4 Simplified model of vertical dynamics

Equations of motions were constructed and expressed as listed below.

$$M_{body}\, z''_{body} = s_{sr}\left(z_{bogie} - z_{body\_r}\right) + s_{sl}\left(z_{bogie} - z_{body\_l}\right) + d_{sr}\left(z'_{bogie} - z'_{body\_r}\right) + d_{sl}\left(z'_{bogie} - z'_{body\_l}\right) \quad (1)$$

$$\theta_{body\_y}\, \chi''_{body} = \left(s_{sr}\left(z_{bogie} - z_{body_r}\right) + d_{sr}\left(z'_{bogie} - z'_{body_r}\right)\right) t_r - \left(s_{sl}\left(z_{bogie} - z_{body_l}\right) + d_{sl}\left(z'_{bogie} - z'_{body_l}\right)\right) t_l \quad (2)$$

$$\theta_{body\_y}\, \varphi''_{body} = s_{rot_r} t_r - s_{rot_l} t_l \quad (3)$$

$$M_{bogie}\, z''_{bogie} = s_p\left(z_{ws} - z_{bogie}\right) + d_p\left(z'_{ws} - z'_{bogie}\right) + d_{pfr}\left(z'_{ws} - z'_{bogie}\right) - s_{sr}\left(z_{bogie} - z_{body_r}\right) - s_{sl}\left(z_{bogie} - z_{body_l}\right) - d_{sr}\left(z'_{bogie} - z'_{body_r}\right) - d_{sl}\left(z'_{bogie} - z'_{body\_l}\right) \quad (4)$$

$$M_{ws}\, z''_{ws} = s_w z_{ws} + d_w z'_{ws} - s_p\left(z_{ws} - z_{bogie}\right) - d_p\left(z'_{ws} - z'_{bogie}\right) \quad (5)$$

The model component nominal parameters' dataset consists of as cited from values used in [5]:

a) The masses:
M_{body} = 20 900 kg

M_{bogie} = 4305 kg

M_{ws} = 3640 kg

b) Moment of inertia for the "z" body axis:
θ_{body_z} = 208 500 kgm^2

Moment of inertia for the "y" body axis:
θ_{body_y} = 139 000 kgm^2

c) Elastic and dissipative parameters of springs and dampers of the structural connection joints:
At the reference point (rail) – wheelset:

s_w = 590 kN/mm

d_w = 100 kNs/m

At the wheelset - bogie connection

s_p = 10 kN/mm

d_p = 8,882 kNs/m

Parameters of the frictional damper elements:

d_{pfr} = 10 kNs/m

Computational indicated Coulomb friction force: 10 N

Computational friction velocity: 1 m/s

Bogie and car-body interface parameters:

$s_{sl} = s_{sr}$ = 2,07 kN/mm

$d_{sl} = d_{sr}$ = 5436 kNs/m

$s_{rotl} = s_{rotr}$ = 268.32 kNm/rad

d) Simulation computational initiative parameters applied as of the:
Initial velocity of the car-body mass portion vertical movement:

V_{0_Mbody} = 1 m/s

Initial angular velocity of the car-body mass inertia around the vertical axis:

$\omega_{0\ 0Body}$ = 0,01 rad/s

The output measured values are the three mass vertical displacement functions vs. time, and the body – bogie interface torque function on the body mass around the axis vs. time, they are included in the nominated vector **δ**.

$$\boldsymbol{\delta} = [\, z_{body}(t),\, z_{bogie}(t),\, z_{ws}(t),\, T_{body}(t)\,] \quad (6)$$

Where the function of $T_{body}(t)$ over time represents the computational output value referred above as equation (3), the torque to be calculated of $\theta_{body\_y}\ \varphi''_{body}$.

Simulation runs were carried out with systematically changed secondary vertical and the rotational linear spring stiffness values in accordance with the planned percentual parameter deviations introduced in vector **Δ** (1).

5 RESULTS AND EVALUATION

At first, the simulation contained only linear elements with no damping within the system joints. The simulation duration was 60 + 2 seconds long. As Fig. 7 shows, from top the first pair of charts reflects the vertical displacement vs. time functions of the three masses in a common diagram. The second row shows the vertical displacement of the body mass, the third the vertical displacement of the bogie mass, whilst the fourth shows the vertical displacement of the wheelset.

As the body mass motion initiates the system, it aligns in harmonic oscillation, such as the bogie does, with the addition of the impact of the wheelset motions. The wheelset displacement function shows strengthening oscillation with disharmonic features aligns in a limited cycle. This is caused with high probability by the solver function's numeric noise effect.

Simulation runs were performed in accordance with the described **Δ** parameter change values. The results showed periodic behavior of the system, with the expected changes in time-periods (wavelengths) and absolute maximum amplitudes.

Comparison made between the largest deviated stiffness applied and the standard basic runs that is shown in Fig.8. The stiffness parameter changes caused expected harmonic displacement motion characteristics. The comparison of the wheelset mass vertical displacement functions showed that the numerical noise enters perpetuating, aligning on limited cycle that is within range of 10.4 meters, likely caused by computational solver noise disturbance (numerical instability).

As second series of simulation runs, vertical damping, through viscous like linear damping parameters were introduced according to the model described.

Fig. 9 shows the solution functions got via these runs. The expected behavior was experimented with the simulation results: damped vibrations were given. The wheelset disturbance noise due to numerical instability remained in the same range.

Comparative figures (Fig, 10.) show on top left the deviation of body displacement function from the standard oscillation, while the bogie and wheelset comparative function show the 33% stiffness deviation effect.

The third series of simulation runs were carried out with switching in a non-linearity to the model by application of frictional damping between the bogie mass portion and the wheelset mass elements. The frictional impact caused significant larger damping effect as it was seen in Fig. 11 and Fig. 12. The non-linearity introduced by the frictional elements caused significant increase in the numerical computational noise, it can be checked in Fig 12. bottom right plotted comparative functions.

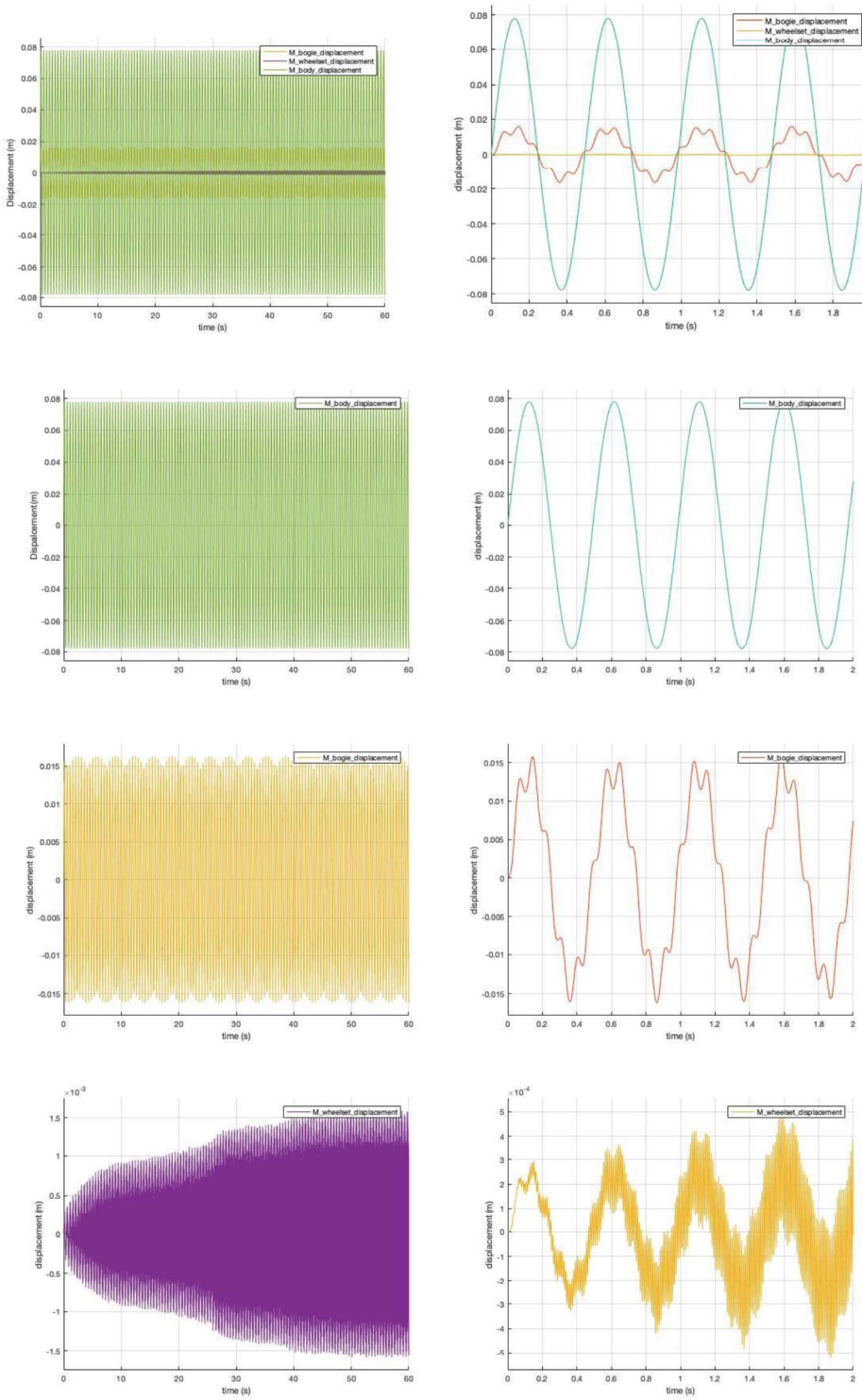

Fig. 7 Results of runs with no spring stiffness deviation and no damping

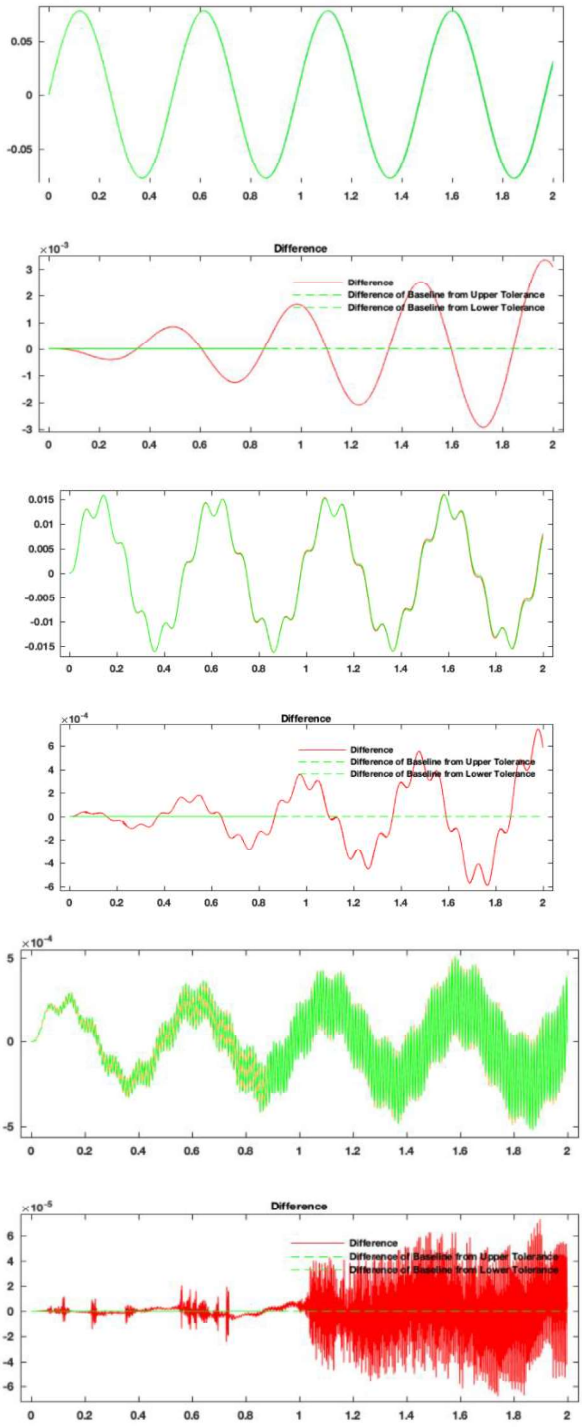

Fig. 8 Comparison of the vertical displacement vibration functions, difference functions of standard and the 33% enlarged secondary suspension (body, bogie) connection stiffness application (body, bogie, wheelset)

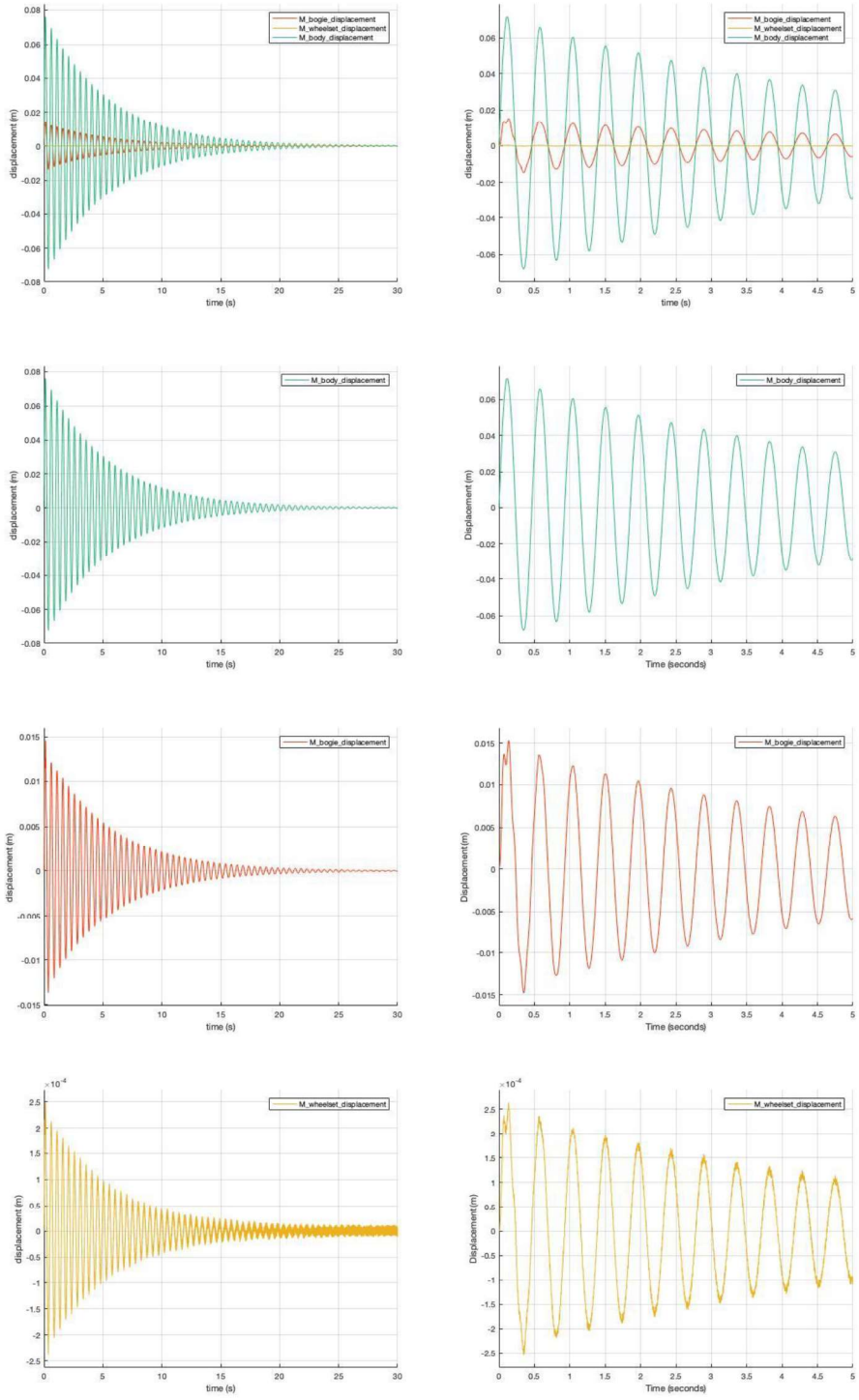

Fig. 9 Simulation results of runs with damping parameters applied

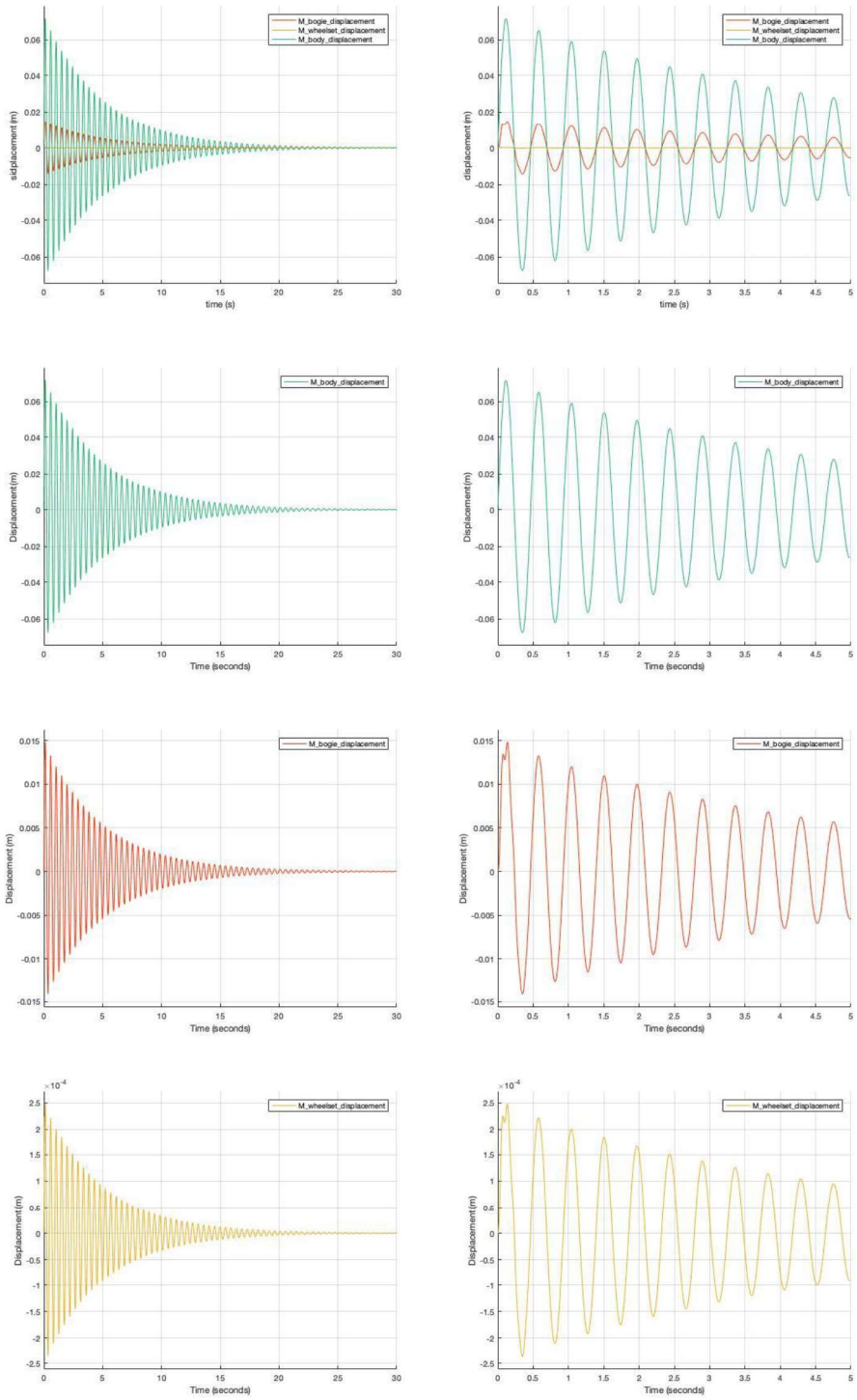

Fig. 10 Simulation results of runs with damping and frictional damping parameters applied

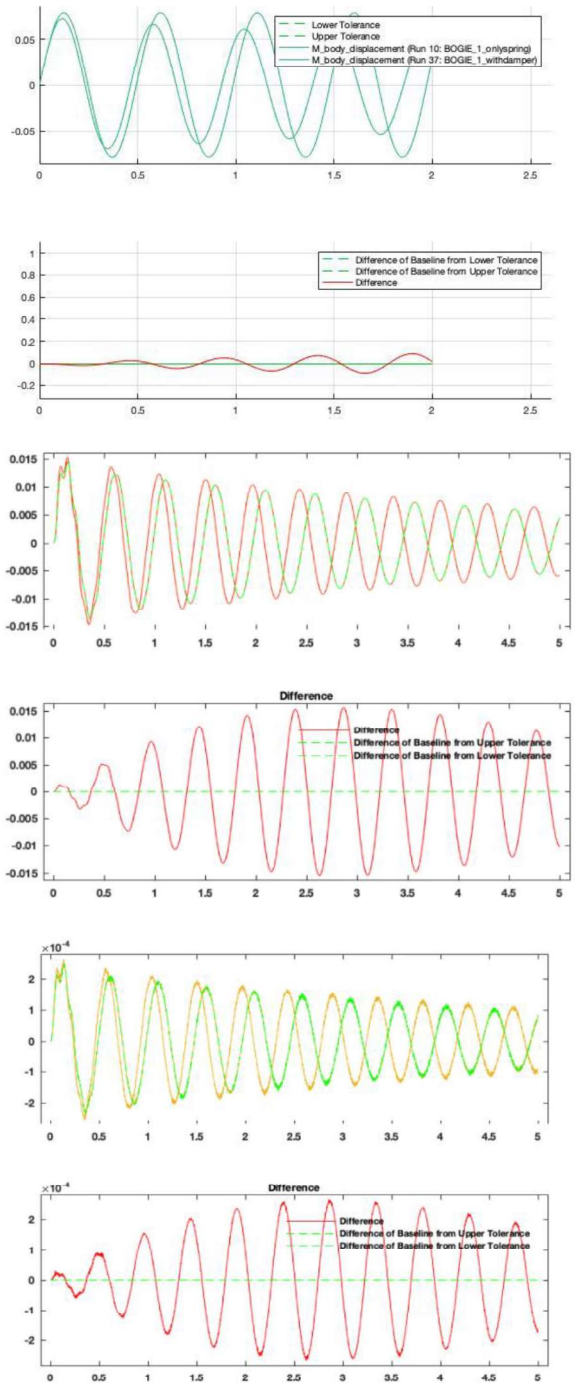

Fig. 11 Vibration displacement function comparison with linear damping, difference functions of standard and the 33% enlarged secondary (body, bogie), suspension stiffness application (body, bogie, and wheelset)

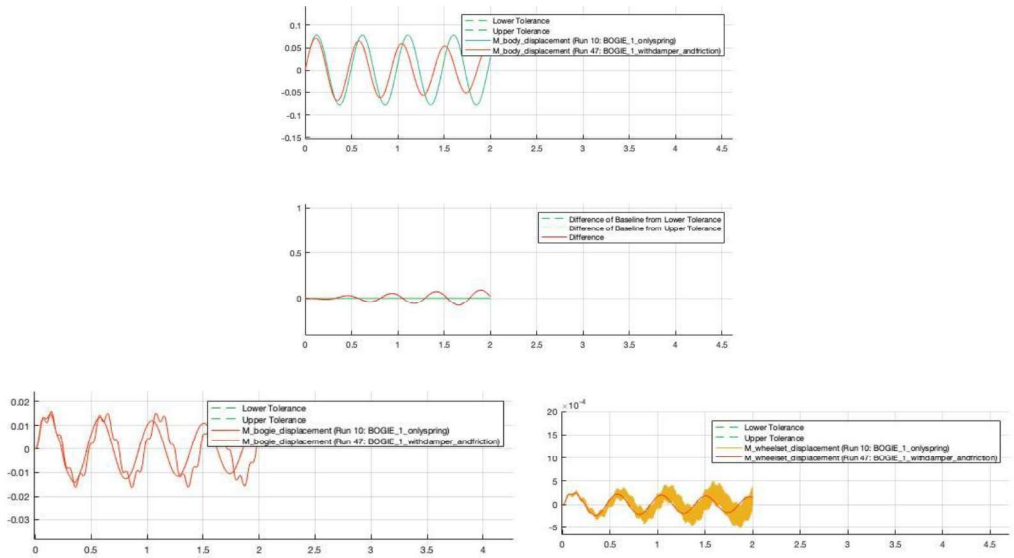

Fig. 12 Vertical vibration displacement function comparison with linear and frictional non-linear damping, difference functions of standard no damped and the 33% enlarged damped secondary suspension (body, bogie) stiffness application (body, bogie, and wheelset)

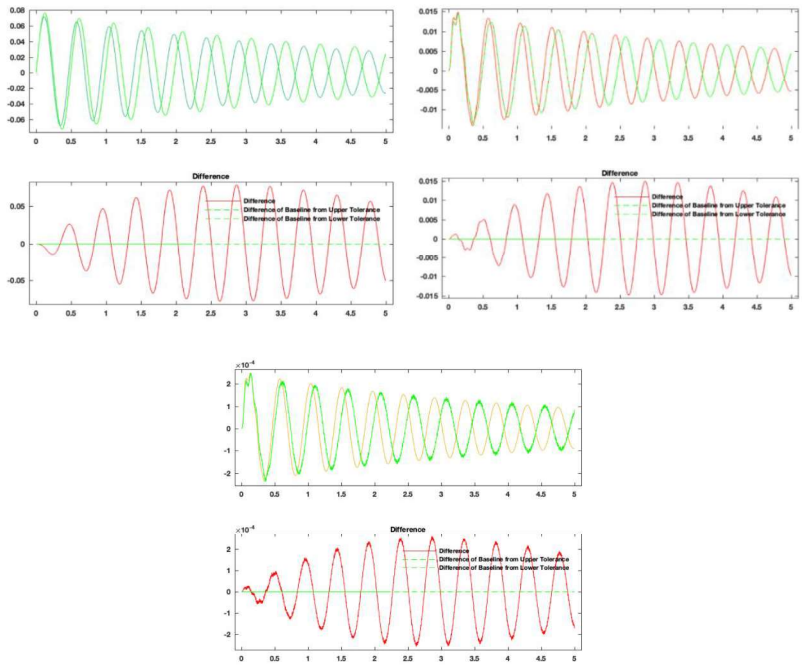

Fig. 13 Vibration displacement function comparison with linear and frictional (bogie and wheelset) non-linear damping, difference functions of standard and the 33% enlarged secondary suspension (body, bogie) stiffness application (body, bogie, and wheelset)

Taking into consideration the entire simplified model, orderly applied the stiffness parameter deviations according to the described portions, with observation of the absolute maximum displacement (amplitude) values, for each mass element its displacement motion can be determined depending on the stiffness change.

By creating the related functions over the stiffness change percentage, based on the simulation results simple linear regression lines can be drawn, orderly shown in Fig. 14, Fig. 15, and Fig. 16.

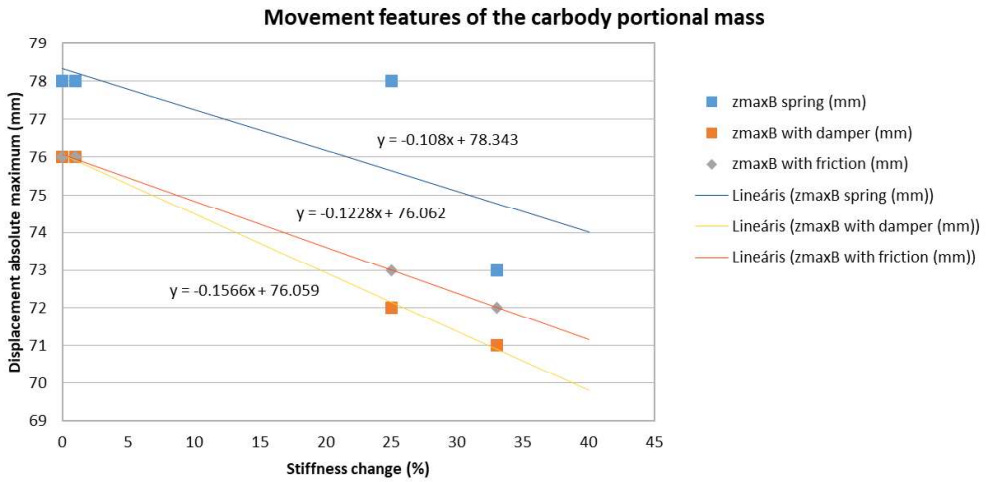

Fig. 14 Motion characteristics of the car-body portion mass

Because of the linear regression lines, stiffness change can be measured over the amplitude change intensity, expectedly the derivative function of each line is constant.

These linear regression derivative values formed to vectors following the order as the first with no damping, on second place with linear damping, and on third with linear and frictional non-linear damping effects.

$$\boldsymbol{D}_{\mathbf{Body}} = [-0.108, -0.122, -0.157]\ \text{mm} \tag{7}$$

$$\boldsymbol{D}_{\mathbf{Bogie}} = [0.028, 0.026, 0.020]\ \text{mm} \tag{8}$$

$$\boldsymbol{D}_{\mathbf{Wheelset}} = [0.0008, 0.0003, 0.0003]\ \text{mm} \tag{9}$$

By this the influence of stiffness parameter changes, transformed via the interfaces to each mass elements have been described.

The impact on wheelset mass element movement is much less, by scale of the thousand decreased.

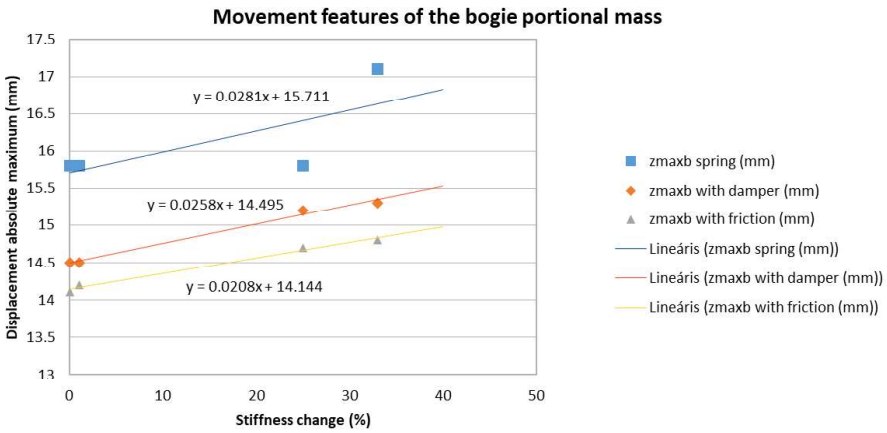

Fig. 15 Motion characteristics of the bogie portion mass

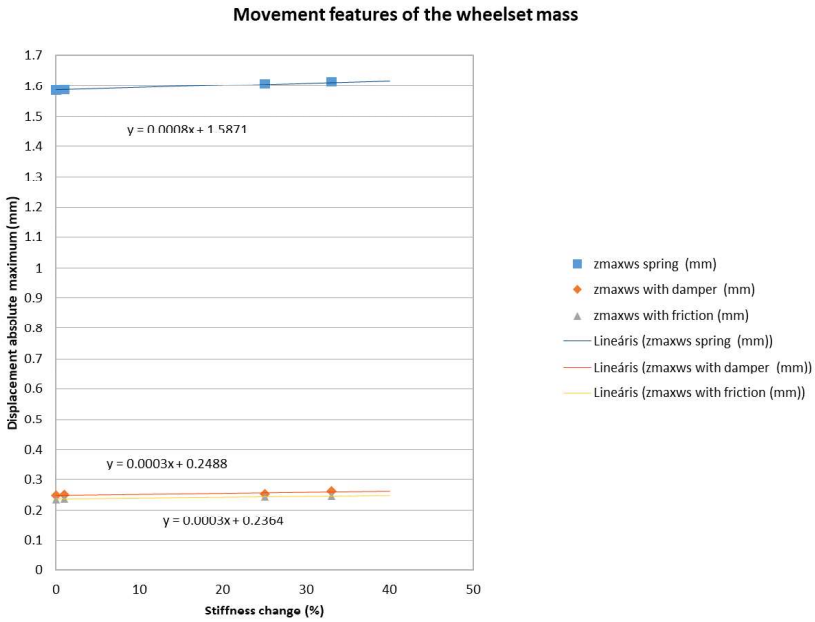

Fig. 16 Motion characteristics of the wheelset portion mass

An extra examination carried out by only torsional spring application, with no damping. The impact scale concerning the torque change represented by the maximal torque values resulted in linear regression line, results shown in Fig.17, Fig.18, and Fig.19. The intensity of the torque change per percentage is computed.

$$\boldsymbol{D}_{\mathbf{Torque}} = \ 5.696 \text{ Nm} \tag{10}$$

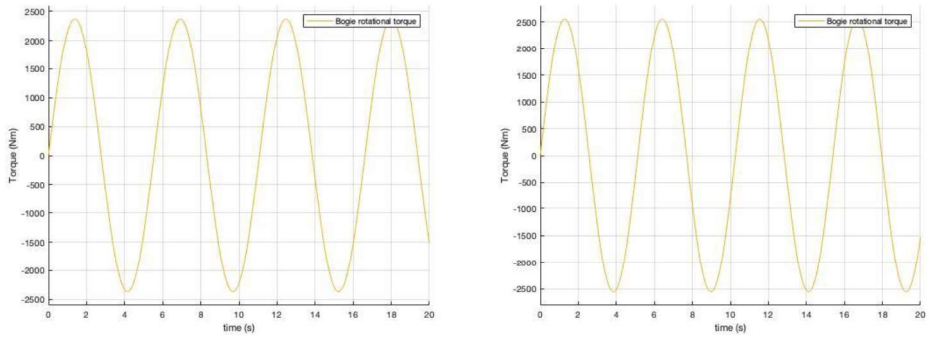

Fig. 17 Torque oscillation functions evolved in the body–bogie interface

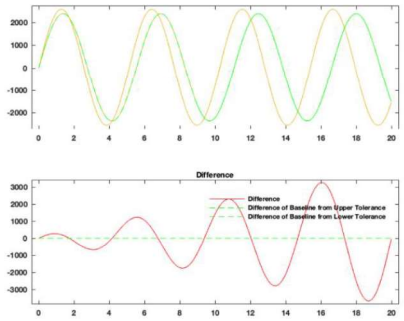

Fig. 18 Comparison of time dependent response functions received with the standard and with the case of 33% stiffness parameter change (upper curves) and the difference function (lower curves).

Considering the effect of the torsional stiffness parameter change by the percentages described in vector **Δ**, significant influence was detected.

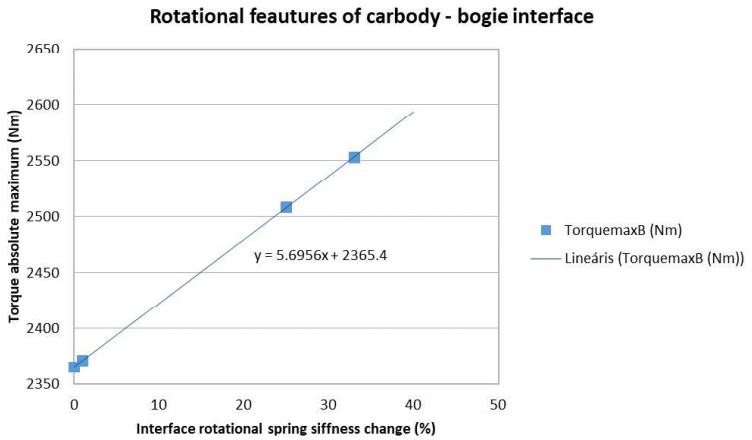

Fig. 19 Effect of the change in rotational spring stiffness in the car-body and bogie interface

6 THE INFIRM DEFINITION OF DETECTABLE SYSTEM ANOMALY

It can be declared that the described dynamical system asymmetric behavior is an anomaly process, which is the significant and detectable cause of the unexpectedly appeared irregular wheel profile wear phenomenon described in the original case study.

It can be declared that the presence of the anomaly process can be detected by regular wheel profile measurement evaluations. Nevertheless, the performances of the secondary suspension system elements cannot be as easily controlled especially in regular operation.

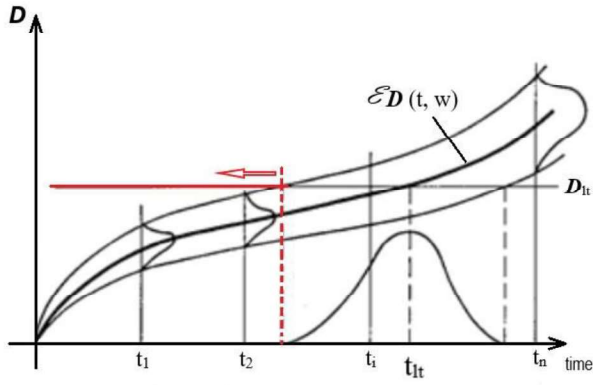

Fig. 20 Band-with of the deterioration process vs. time

Certain phenomena can definitely be described by the instationary stochastic deterioration process $D(t,w)$ curve. The curve shows with increasing operation time an increasing standard deviation around the expectation function indicated $\mathcal{E}D(t,w)$.

The natural physical process of normal material and structural damage, the stochastic process of deterioration, as shown in Fig. 20 over the time axis. The natural wheel profile wear can be determined accordingly. The deterioration of the natural state of the components is the classic description of the statistical evaluation of the process of system degradation. The individual realization curves running within the band-with consist of two main sections divided by an inflexion point, since the second derivative (the curvature) of the realization functions are negative if the time is taken under the inflexion time abscissa, whilst the second derivatives are positive if the considered time is over the inflexion time abscissa. In the close neighborhood of the inflexion time abscissa the curvature is very small, thus a shorter or longer quasi-linear middle part can also be recognized.

The speed of deterioration is exactly defined by the time-derivative process of $D(t,w)$, it is also a stochastic process: it depends on time t and on the elementary event w.

$$V_{D(t,w)} = \frac{dD(t,w)}{dt} \tag{11}$$

An average rate of the deterioration speed $\overline{V}_D(t)$ is defined as a time function by the derivative function of the expectation function $\mathcal{E}D(t,w)$ of the deterioration process:

$$\overline{V}_D(t) = \frac{d}{dt}\mathcal{E}D(t,w). \tag{13}$$

The expected value function $\mathcal{E}\boldsymbol{D}(t,w)$ can approximatively be described from an initial increasing non-linear section, then with a quasi-linear section, from the end of which the increase of deterioration is much faster than it was in the preceding middle linear section. This accelerating process shall be avoided, thus arbitrarily a preceding point can be assigned as limit point. Let $\boldsymbol{D}_{lt}$ designate a tolerable level of deterioration and t_{lt} designate the time point where the expected value function $\mathcal{E}D(t,w)$ intersects level $\boldsymbol{D}_{lt}$. In this way the expected lifetime of a certain structure is $\mathcal{E}D(t,w) = \boldsymbol{D}_{lt}$. If for a set of structural items the value-pair $[t_{lt}, \mathcal{E}D(t,w)]$ is specified, then if the deterioration realisation function $D(t,w_i)$ of an individual item intersects the tolerable deterioration level $\boldsymbol{D}_{lt}$ (i.e. $D(t_i,w_i)= \boldsymbol{D}_{lt}$) and t_i is less than $t_{lt} - 3\sigma(t_{lt})$, then the **item anomaly is detected**. Here $\sigma(t_{lt})$ stands for the standard deviation of random variable $\tau_{D_{lt}}(w)$ordered to level $\boldsymbol{D}_{lt}$ in the following way: let $t_i(w)$ denote that random (i.e. w-dependent) time point, where the realization function intersects level $\boldsymbol{D}_{lt}$ (thus $D(t_i,w) = \boldsymbol{D}_{lt}$), then $\tau_{D_{lt}}(w)$ $t_i(w) - t_{lt}$. Random variable $\tau_{D_{lt}}(w)$ is of zero expectation and is normally distributed, furthermore $\sigma(t_{lt})=\sigma(\tau_{D_{lt}}(w))$ In short, anomaly is detected if

$$t_i(w) < [t_{lt} - 3\sigma(t_{lt})] \text{ or } \tau_{D_{lt}}(w) < -3\sigma(\tau_{D_{lt}}(w)). \tag{14}$$

This gives the hereby described infirm definition of the detectable system anomaly.

7 CONCLUDING REMARKS

Based on the recognized phenomenon that the asymmetric wheel profile wear can be traced back to the stiffness parameter deviations in the secondary suspension system, my present study revealed that the dynamic system anomalies can cause significant deviation of the dynamic processes in the vehicle that can result in detectable measures.

As important influences, the relative asymmetry of vertical stiffness parameter values and impact of the body-bogie interface torque were identified, that can be resulted in remaining (permanent) influences on the dynamics of the vehicle system and on the system deterioration processes, basically the lifetime.

Based on this train of thoughts, the infirm definition of system anomaly was described by usage and stochastic extension of the traditional deterioration function curve.

The present investigations into the model-based simulations with varied system parameters showed the influence of the parameter deviations on the wheel dynamics, therefore further studies are needed to point out the dependence of wheel profile wear process on any suspension system parameter changes, in other words: how the vertical dynamics of the suspension system influences the evolution of wheel-profile wear processes.

8 REFERENCES

[1] Zobory, I. – Benedek, T. – Győri, J.: Járműdiagnosztika–oktatási segédlet, BME, Vasúti Járművek Tanszék, Budapest, 2004. (In Hungarian)

[2] Zobory, I.: Prediciton of Wheel/Rail Profile Wear, Vehicle System Dynamics, 28, (1997), p. 221-259.

[3] Szabó, A.: Vasúti járművek keresztirányú dinamikai és kerékkopási folyamatainak meghatározása digitalis szimulációval; Kandidátusi értekezés, Budapest 1993 (In Hungarian).

[4] VM14 kezelési utasítás: Járműszerkezeti rész, Ganz-MÁVAG Budapest, 1985. (In Hungarian).

[5] Ferencz, P.: Investigation into wheel profile wear processes influenced by parameter anomalies in suspension characteristics of electro-locomotive bogies, Proceedings of the 8th International Conference on Railway Bogies add Running Gears (BOGIE'10), (Ed. by Prof. I. Zobory), SSME, Department of Rolling Stock, Budapest, 2010. p. 201-212.

[6] Ferencz, P.: Investigation into impacts of bogie secondary suspension system anomalies on wheel wear propagation, Proceedings of the 11th International Conference on Railway Bogies add Running Gears (BOGIE'19), (Ed. by Prof. I. Zobory), SSME, Department of Rolling Stock, Budapest, 2019. p. 323-336.

DEVELOPMENT OF A TOOL FOR ESTIMATING THE CHARACTERISTIC CURVES OF RUBBER-METAL PARTS

Christian BUZZI[1], Andreas DUTZLER[2], Tobias FAETHE[2], Johannes LASSACHER[1], Martin LEITNER[1] and Franz-Josef WEBER[2]

[1]Graz University of Technology, Institute of Structural Durability and Railway Technology, Graz, Austria
[2]Siemens Mobility Austria GmbH, Graz, Austria

Received: August 11, 2022

ABSTRACT

The development of rubber-metal parts used as load-carrying components in bogies of rail vehicles is mainly guided by their mechanical properties. Nonlinear force-deflection behaviours of such mainly elastic structural components are influenced by both the geometry of the rubber as well as the ratio of the vulcanized rubber-metal surface in relation to the free surface of the rubber. Analytic calculation methods exist for the elastic moduli at the undeformed state, whereas a characteristic curve estimation tool is developed for multi-layer springs with circular cross sections to enhance the development of rubber-metal parts during the design phase. Beside three representative verification tests, the estimation tool is applied on selected multi-layer springs. A primary layer spring with two layers and a hole inside serves as demonstration model. The resulting characteristic curves and stiffness properties are compared with the experiments, results from literature as well as with numerical results based on a detailed finite element simulation.

Keywords: rubber-metal parts, characteristic curves, hyperelasticity, numeric simulation

1 INTRODUCTION

Bogies of rail vehicles contain rubber-metal parts, which are used as load-carrying components within the primary or secondary suspension stage. The technical development of these mainly elastic components is driven by specified mechanical properties. Force-deflection curves are typically nonlinear and are affected by the geometry and the loading type of the rubber. The compressive behaviour has a strong influence on the ratio between the vulcanized rubber-metal interface and the free surface of the rubber. At the undeformed state, analytic calculation methods based on experiments are well established in literature [1, 2]. However, rubber-metal parts in bogies of rail vehicles are typically pre-deformed or pre-stressed. Hence, the elastic properties are required at a given point of operation [3]. Detailed numeric simulations in the design phase are comparably time- and cost-extensive in this very iterative stage of development. A common use case of rubber-metal parts are layer springs in the primary suspension stage of a bogie of a rail vehicle, which acts between the wheelset and the bogie as shown in Fig. 1. Here, a layer spring is used as a serial support for the coil spring within the primary suspension stage.

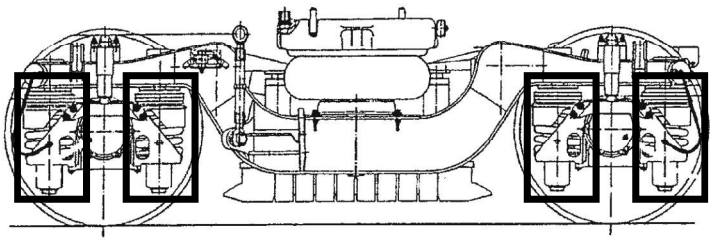

Fig. 1 Primary suspension stage (rectangles) within the bogie for the second generation of the ICE [4]

2 MATERIALS AND METHODS

Inspired by analytic calculation methods for the elastic stiffness properties at the undeformed state for rubber-metal components [1, 2], the estimation of characteristic curves and stiffness properties at an operation point is enabled by the development of a software-based estimation tool. Multi-layer springs with circular disk-shaped cross sections are chosen as a demonstration model. Numeric simulations utilizing an isotropic hyperelastic material formulation at discrete combinations of geometry parameters provide the characteristic curve and stiffness data. A normalization technique for the characteristic curves enables well-suited data for interpolation [5]. The characteristic force-deflection or moment-rotation curves in axial, lateral and torsional directions are evaluated for a given set of geometric parameters. The Mullins effect as a load-history dependent structural softening of rubber is evaluated in the post-processing stage. Finally, a shape and deformation dependent lateral shear correction factor is applied. Material parameters for the hyperelastic material formulation and the Mullins material model are calibrated on uniaxial cyclic normal force versus stretch experiments on carbon-black reinforced natural rubber mixtures [6] based on the shore hardness. The resulting stiffness properties at the operation point of axial compressive and lateral shear experiments are used as reference values against which the calculated properties are compared.

2.1 Numeric simulation model for the estimation tool

Numeric simulations are carried out by nonlinear finite element method, using both MSC.Marc Mentat and an open source software package [7]. The geometry of a layer spring is idealized to a cylindrical shape, see Fig. 2. The thickness of the intermediate plates in multi-layer springs is neglected. Eventually occurring contact situations as self-contact of the rubber or between the rubber and the steel plates are not considered. The isotropic hyperelastic material formulation takes only the primary elastic part of the material behaviour into account. Secondary properties like volumetric shrinkage after vulcanization, aging, temperature dependency, viscoelastic hysteresis or permanent set effects are also not part of this analysis.

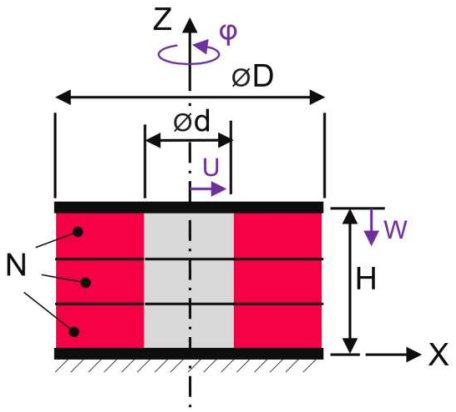

Fig. 2 A multi-layer spring with outer and inner diameters D and d, height H and N layers. The compressive displacement W acts along the rotation axis Z. Lateral shear displacements U are applied in direction X.

The geometry is defined by the outer D and inner diameters d, the total height H as well as the number of layers N. The deformation of a layer spring is described by the compressive axial displacement W, the lateral displacement U as well as the axial torsional twist. Kinetic quantities include the applied axial compressive force, the applied lateral shear force as well as the applied torsional moment. The area ratio between the vulcanized surface and the free surface of the rubber is denoted by the layer-related $k_{A,N}$ and component-related k_A shape factors from Eq. (1) and Eq. (2).

$$k_{A,N} = \frac{D - d}{4\,H\,N} \tag{1}$$

$$k_A = \frac{D - d}{4\,H} \tag{2}$$

2.2 The equivalent strain energy function of a layer spring

The most basic hyperelastic strain energy function formulation is used to provide sound scalability of the simulation results. Hence, an isotropic first strain invariant formulation is chosen. The Mullins-softening is not considered by the numeric simulations, instead it is evaluated within the post-processing by an appropriate equivalent strain energy, representing the one of the non-homogenous deformed component. The strain energy function ψ on the incompressible part of the deformation as shown in Eq. (3),

$$\psi = 2\,C_{10}\,I_1 \tag{3}$$

based on the first strain invariant I_1 from Eq. (4), where E_1, E_2 and E_3 are the three principal strain components,

$$I_1(E) = E_1 + E_2 + E_3 \tag{4}$$

and on the one-dimensional principal strain $E-$stretch λ relation from Eq. (5) with the strain exponent k

$$E = \frac{1}{k}(\lambda^k - 1) \tag{5}$$

is used within the numeric simulations. For an incompressible uniaxial deformation and a strain exponent of two as denoted in Eq. (6),

$$I_1(E) = \frac{1}{2}\left(\lambda^2 + \frac{2}{\lambda} - 3\right) \tag{6}$$

this results in the Neo-Hookean material formulation as given in Eq. (7) for the uniaxial normal force N per undeformed area A. Herein, C_{10} is the primary stress-like material parameter of the hyperelastic force stretch relation, with the physical meaning of the half initial shear modulus.

$$\frac{\partial \psi}{\partial \lambda}\left(= \frac{N}{A}\right) = 2\,C_{10}\left(\lambda - \frac{1}{\lambda^2}\right) \tag{7}$$

The inverse relation (evaluated by a cubic spline) enables a relation for the equivalent uniaxial stretch λ_{eq} for a given normal force N per undeformed area A, see Eq. (8).

$$\lambda_{eq}\left(\frac{N}{A}\right) = \left\{\frac{\partial \psi}{\partial \lambda}\right\}^{-1} \tag{8}$$

An equivalent strain energy $\tilde{\psi}$ is used for the evaluation of the Mullins softening. It is composed out of contributions from the global and the local deformation. The contributions of the local and global deformations are shape-dependent by the ratio of the vulcanized and the free surface. The proposed formulation is purely empirical, based on the numeric simulation results, see Eq. (9). For slim shapes, where the cross-sectional area is small compared to the length, the global deformation contribution is dominant. Due to the introduced shape dependency, the local deformation contribution changes with growing cross-sectional areas.

$$\tilde{\psi} = 5\left(1 + 5\,k_{A,N}^2\right)\frac{\psi(W/H)^2}{2} + k_{A,N}\frac{\psi\left(\lambda_{eq}\right)^2}{2} \tag{9}$$

The maximum deformation induced Mullins softening is formulated by a simplified version of the isotropic Ogden-Roxburgh model formulation [8], i.e. independent of material directions with no permanent set effects. The relative softening is a function of the current $\tilde{\psi}$ and maximum $\tilde{\psi}_{max}$ occurred equivalent strain energies, see Eq. (10). Herein, the amount of the relative softening is controlled by the relative softening parameter r. Contrary to the original formulation, the stress-like parameter m is replaced by the elastic constant C_{10} in Eq. (10) to reduce the number of parameters while preserving a realistic material response behaviour.

$$\eta = 1 - \frac{1}{r}\,\mathrm{erf}\left(\frac{\tilde{\psi}_{max} - \tilde{\psi}}{2\,C_{10}}\right) \tag{10}$$

The Mullins-softened force-displacement relation $\tilde{N}(W)$ is finally evaluated by Eq. (11).

$$\tilde{N}(W) = \eta\,N \tag{11}$$

2.3 Lateral shear factor

A lateral shear stiffness correction is applied on the numerical results to give the component shear stiffness $\tilde{c}_X$. The lateral shear stiffness correction factor f_S is empirically determined due to the geometric idealization as well as from deviations between results from detailed numeric simulations and experimental data, see Eq. (12) and Eq. (13).

$$f_S = 1 + \frac{1}{2}\frac{W}{H} + \frac{k_{A,N}}{4} \tag{12}$$

$$\tilde{c}_X = f_S\,c_X \tag{13}$$

3 VERIFICATION AND DEMONSTRATION MODELS

This section contains applications of the characteristic curve estimation tool on artificial and real-world examples. First, the axial characteristic curves of the estimation tool are compared against the results of the hyperelastic numeric simulations with the idealized geometry. This ensures both a valid interpolation of the data as well as the correct evaluation of the Mullins softening applied on the results of the simulation models. In a second step, a real-world example of a layer spring, used in the primary suspension stage of a bogie, is shown.

3.1 Validation of Mullins-softening applied on equivalent strain energy

Representative *slim*, *medium* and *massive* shapes of layer springs in terms of the ratio between the diameter and the height are considered for a comparison of the axial characteristic curves of the estimation tool and the numeric simulations, see Fig. 3. The axial force of the massive shape is about 50 times higher than the axial force of the slim shape at 10 mm axial displacement. Due to the overall good agreement between the estimation tool and the numeric simulations, both the interpolation and the Mullins softening of the estimation tool are validated.

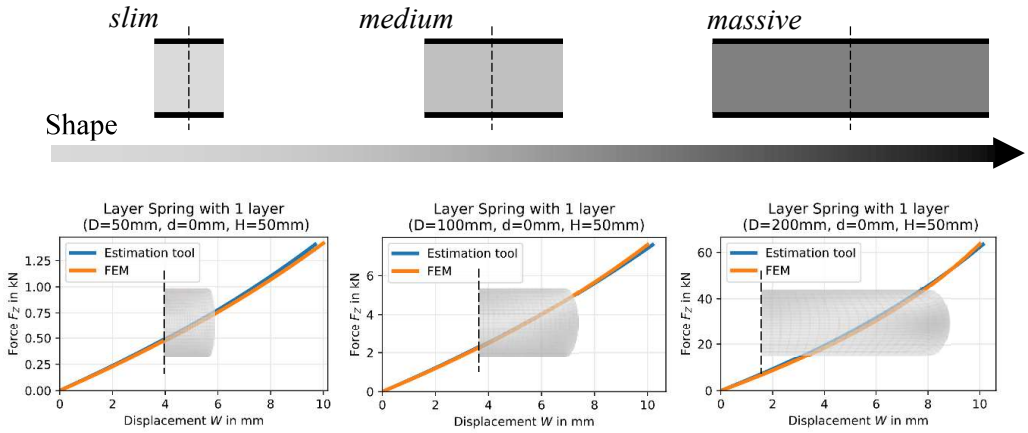

Fig. 3 Influence of the shape factor as ratio of the vulcanized and free surfaces on the axial force-displacement curve. Characteristic curves from finite element simulation models and the estimation tool, both including the Mullins softening.

3.2 Primary layer spring

The considered primary suspension stage contains a layer spring with two layers of circular ring cross-sections of the rubber blocks as shown in Fig. 4. A pre-deformed operation point results from the axial compressive force induced by the weight and the loading condition of the rail vehicle. The layer spring is subjected to a multi-axial loading situation on top of the operation point. Hence, stiffness properties are required at the deformed configuration of the layer spring at its operation point. Stiffness values determined by experiments are summarized in Table 1.

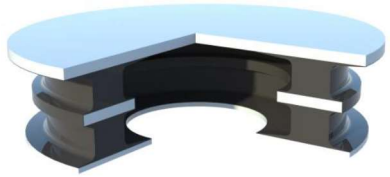

geometric parameter	symbol	value and unit
outer diameter	D	245 mm
inner diameter	d	180 mm
total height	H	58 mm
Number of layers	N	2

Fig. 4 Primary layer spring (sectional view): ground, intermediate and top metal plates in light grey and rubber blocks in black (left). Geometric parameters of the primary layer spring (right).

Table 1 Structural properties at the operation point determined by experiments on the primary layer spring.

structural property	symbol	value and unit
axial stiffness	c_Z	7.2 kN/mm
lateral stiffness	$c_{X,Y}$	400 N/mm

Results of the characteristic curve estimation tool

The estimation tool reveals realistic axial and lateral stiffness properties at the operation point with reasonable deviations compared to the stiffness values determined by the experiments, see Fig. 5 and Table 2. The axial force-displacement characteristic curve shows a sound correlation up to the operation point. For higher axial compressive states of deformation, the deviation of the axial stiffness, determined by the estimation tool and the experiment, increases.

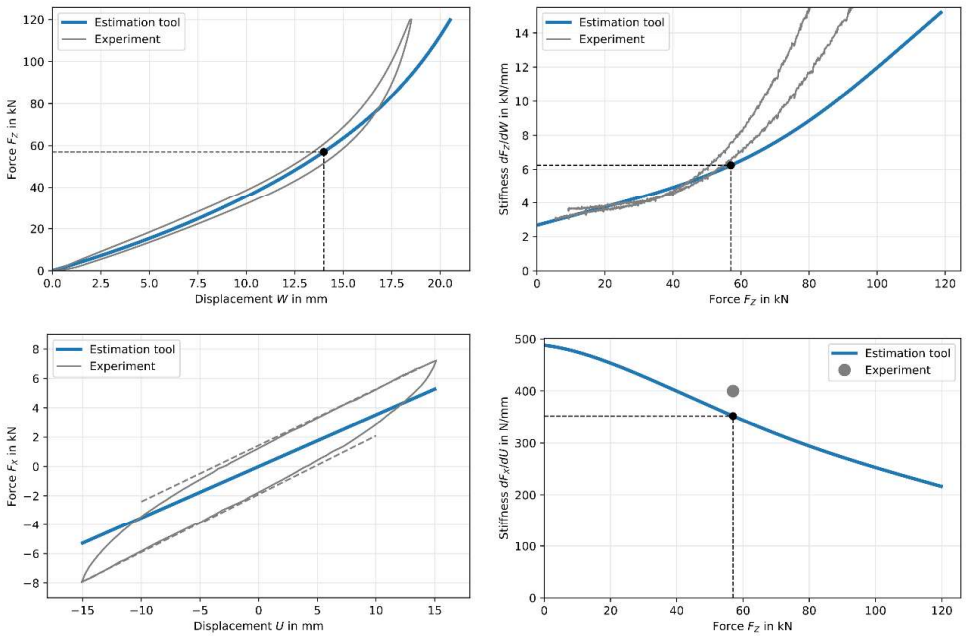

Fig. 5 Primary layer spring results of the characteristic curve estimation tool. Axial compressive force - displacement curve (top left), axial compressive stiffness - displacement curve (top right), lateral shear force - displacement curve at the operation point (bottom left) and lateral shear stiffness - axial compressive force behavior (bottom right). Material parameters: C_{10} = 0.8 N/mm^2, r = 3.4.

Detailed Numeric Simulation Model by the Finite Element Method

The detailed numeric simulation model is built upon the real geometry of the layer spring. The geometry of the rubber block, the intermediate plate as well as contact situations are considered within the simulation. Therefore, the geometry is meshed by eight-node hexahedral elements with linear shape functions. The simulation is carried out by

nonlinear finite element method, using MSC.Marc Mentat. The Neo-Hookean isotropic hyperelastic material formulation is used in combination with an isotropic Mullins-softening formulation [8] with identical material parameters used within the estimation tool. Due to the nearly incompressible material behaviour of rubber, a mixed-field approach effectively prevents volumetric locking [9]. The finite element simulation model is shown in Fig. 6. The external force is applied on the top plate. The axial force-displacement curve after a calibration cycle is given in Fig. 7. Herein, the upper branch of the simulated axial force-displacement characteristic curve hysteresis represents the first loading path, while the lower branch reflects the Mullins-softened elastic characteristic. The lateral force-displacement curve at the operation point of 57 kN axial force is shown in Fig. 8.

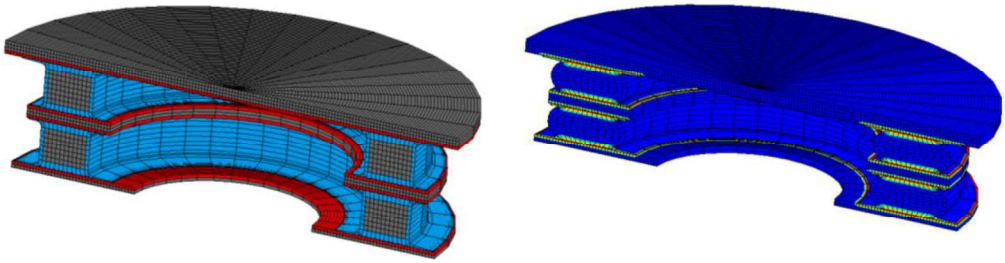

Fig. 6 Finite Element Simulation Model (3D half-symmetric). Undeformed model with defined contact areas at the metal plates in red and rubber blocks in blue (left). Deformed model with a compressive force of 120 kN and highlighted contact areas (right).

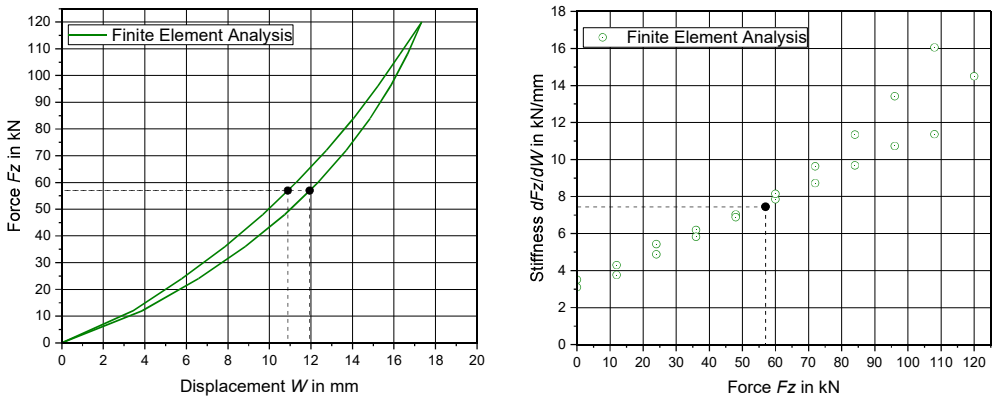

Fig. 7 Primary layer spring results of the finite element analysis. Axial compressive force - displacement curve (left), axial compressive stiffness – axial compressive force results (right)

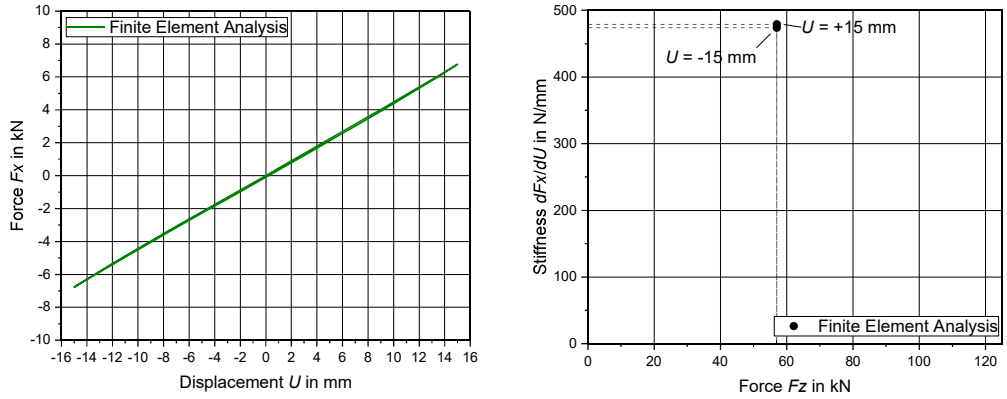

Fig. 8 Primary layer spring results of the finite element analysis. Lateral shear force - displacement curve at the operation point (left) and lateral shear stiffness - axial compressive force results (right)

In Table 2, the calculated stiffness properties of the primary layer spring are compared against the stiffness values determined by experiments. The estimation tool underrates the axial and lateral stiffness values at the operation point by -12% compared to the experimental data. The numeric simulation matches the axial stiffness, while the lateral stiffness at the operation point is overestimated by +19% compared to the experiment.

Table 2 Structural properties at the operation point determined by experiments and the estimation tool on the primary layer spring.

structural property	symbol	experiment	estimation tool	simulation
axial stiffness in kN/mm	c_Z	7.2	6.3 (-12%)	7.5 (+3%)
lateral stiffness in N/mm	$c_{X,Y}$	400	351 (-12%)	475 (+19%)

3.3 Comparison with other Parts

Stiffness properties at the specified operation points of several layer springs with two to five layers are given in Table 3. Stiffness properties determined by experiments, evaluated by the estimation tool and analytically calculated according to [1] are compared in Figure 9. The deviations of the stiffness properties from the experiments and the estimation tool are lower than 15% for four out of five parts. For one part, the deviation of the lateral shear stiffness is as great as 57%. However, the experimental data has indicated some uncertainties in terms of the material as well as the geometric properties may lead to the increased deviation.

Table 3 Geometric properties of several layer springs used as longitudinal buffers or primary layer springs of bogies for rail vehicles.

Part	*D* in mm	*d* in mm	*h* in mm	*N*
PLS	245	180	29	2
LS-A	313	236	17	4
LS-B	327	230	14	5
LS-C	320	210	24	3
LS-D	120	0	10	6

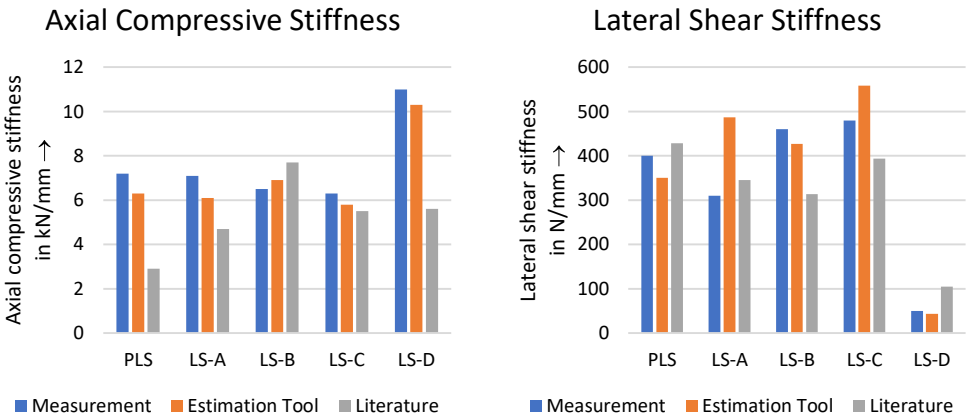

Fig. 9 Axial compressive stiffness (left) and lateral shear stiffness (right) properties of several different layer spring geometries determined by experiments and the estimation tool as well as stiffness properties at the undeformed state according to [1].

4 CONCLUDING REMARKS

It is shown that the characteristic curves of the estimation tool are in good agreement with experimental results of the chosen reference example. The deviation of the axial and lateral stiffness properties at the operation point are lower than 15%. However, the increase of axial stiffness with rising axial deformation above the operation point is underrated by the estimation tool compared to the experimental data. It is assumed that this is mainly due to the simplified geometry without any considered contact between the rubber and the steel plates.

For all other parts considered, the deviations of the stiffness properties determined by experiments and the estimation tool are of similar order and are lower than 15%. However, the deviation is markedly higher for one part concerning the shear stiffness. It must be investigated if this is an outlier due to uncertainties in the experimental data or if the estimation quality for the shear stiffness is lower than the one from the presented sample parts.

Contrary to common methods in literature, the proposed tool enables the estimation of realistic stiffness properties at a deformed operation point up to finite deformation states of axial compression. It is planned to extend the estimation tool to rectangular cross-

sections. It must be evaluated whether new simulations with rectangular blocks must be carried out or if the results of circular cross-sections may be projected to rectangular cross-sections by an equivalent shape factor without a significant loss in accuracy.

In the next step, local stress and strain quantities must be derived and assessed to provide an estimation for the durability in addition to the component characteristic curves.

5 REFERENCES

[1] E. F. Göbel, Gummifedern. Berechnung und Gestaltung, Springer, 1969.

[2] W. Battermann and R. Köhler, "Elastomere Federung. Elastische Lagerung", Wilhelm Ernst und Sohn Berlin München, 1982.

[3] D. F. Lalo, M. Greco, and M. Meroniuc, "Numerical Modeling and Experimental Characterization of Elastomeric Pads Bonded in a Conical Spring under Multiaxial Loads and Pre-Compression", Mathematical Problems in Engineering, vol. 2019. Hindawi Limited, pp. 1–14, Feb. 04, 2019. doi: 10.1155/2019/5182629.

[4] K. Knothe and S. Stichel, Schienenfahrzeugdynamik. Springer Berlin Heidelberg, 2003. doi: 10.1007/978-3-642-55766-8.

[5] A. Dutzler, C. Buzzi, and M. Leitner, "Nondimensional translational characteristics of elastomer components", Journal of Applied Engineering Design and Simulation, vol. 1, no. 1. UiTM Press, Universiti Teknologi MARA, Sep. 21, 2021. doi:10.24191/jaeds.v1i1.20.

[6] F. Carleo, E. Barbieri, R. Whear, and J. Busfield, "Limitations of Viscoelastic Constitutive Models for Carbon-Black Reinforced Rubber in Medium Dynamic Strains and Medium Strain Rates", Polymers, vol. 10, no. 9. MDPI AG, p. 988, Sep. 04, 2018. doi: 10.3390/polym10090988.

[7] A. Dutzler, „FElupe - Finite Element Analysis", Zenodo, 2022. doi:10.5281/zenodo.4817406.

[8] R. W. Ogden and D. G. Roxburgh, "A pseudo–elastic model for the Mullins effect in filled rubber", Proceedings of the Royal Society of London. Series A: Mathematical, Physical and Engineering Sciences, vol. 455, no. 1988. The Royal Society, pp. 2861–2877, Aug. 08, 1999. doi: 10.1098/rspa.1999.0431.

[9] J. Bonet and R. D. Wood, "Nonlinear Continuum Mechanics for Finite Element Analysis", Cambridge University Press, Mar. 13, 2008. doi: 10.1017/cbo9780511755446.

RESEARCH OF THE AERODYNAMIC LOAD INFLUENCE ON THE CAR-BODY HUNTING MOTION OF HIGH-SPEED TRAIN

Xin Ding[1,2], Helmut Netter[1], Gang Chen[1], Qiang Sun[1], Xianwei Cao[1], Bernd Markert[2]

1. CRRC CHANGCHUN GERMANY RailTech GmbH, Kackertstraße 11, 52072 Aachen, Germany.
2. Institute of General Mechanics, RWTH Aachen University, Eilfschornsteinstraße 18, 52062 Aachen, Germany

Received: August 5, 2022

ABSTRACT

The car-body hunting motion is more frequently occurring on the trailing car of the train because of the aerodynamic wake effect while the train is operating at high speed. It is necessary to study the aerodynamic loads (ALs) influencing the running dynamic characteristics of the high-speed train. In this paper, a hunting motion case occurred on the tail car of a high-speed train was analysed by both experiment and numerical simulation methods. The hunting motion features and the potential influence factors including wheel-rail contact relationship, vehicle assembly status, and suspension components were investigated by the experiments. Then the vortex effect of a high-speed train was simulated to get the ALs. It was observed that the yaw moment values of the tail car were quite larger than these of the head car and middle car. The main frequencies of this pulsing excitation were 1.45Hz and 4.37Hz, which are close to the main hunting frequencies. A running dynamic model considering the effect of ALs was established to study the dynamic characteristics. It is found that the aerodynamics loads on the tail vehicle make the vehicle dynamic characteristics more sensitive to the suspension parameters while the equivalent conicity of wheel-rail contact relationship is low. Finally, several suggestions for the maintenance strategies and parameter optimization are discussed to avoid the hunting motion.

Keywords: high-speed train, hunting motion, aerodynamic loads, dynamic simulation, dynamic experiment

1 INTRODUCTION

The running dynamic behaviour of the high-speed trains are always influenced by different factors, such as the external excitation, the wheel-rail contact relationship, and the performance of the suspension components, et al [1]. During the long-term service of the high-speed trains, all the above factors always vary randomly. The abnormal vibration phenomenon like hunting motion may happen while problematic operational conditions like low equivalent conicity [2] or a damage of a suspension component [3] appeared, which are harmful to deteriorate the ride comfort, increase the wheel wear and increase the risk of vehicle damage. While the hunting motion occurred on the high-speed train, these issues are always firstly selected to be verified. Then the running dynamic model of the vehicles were also established to reproduce the hunting motion and find the possible solutions for countermeasures [4]. However, the influence of the aerodynamics on the investigated vehicle were usually ignored.

The most common method of considering the effect of aerodynamics on vehicle dynamics is to add the ALs to the car-body of the vehicle dynamic model [5], [6]. Currently, only the crosswind condition was calculated according to EN-standard 14607 for the high-speed train in the initial design stage [7]. But according to the research of aerodynamics, different kinds of ALs except crosswind, such as the sudden wind loads [8], tornado-like vortex [9], tunnel exit winds [10] and random turbulent winds [11], may be generated when the train operates at a high speed under different conditions. In addition, higher operating speed transient aerodynamic loads will more and more effective to the

vehicle dynamics and complex [12]. Therefore, it is important to focus on the special operating conditions while considering the aerodynamics influence.

In the following, an actual case of hunting motion occurred on a high-speed train is followed. The hunting features and potential reasons are firstly analysed by experiments in Section 2. The simulation method of the aerodynamics according to the special case is introduced in Section 3. Then the different parameter sensitivity of suspension components whether to consider the aerodynamic influence are analysed. Finally, several suggestions were proposed to maintain the high-speed train in service and avoid the hunting motion, respectively.

2 PHENOMENON OF LOW FREQUECNY CAR-BODY HUNTING

2.1 Setup of experiments

A high-speed train operating on the railline from Haerbin-Dalian was chosen as the test object while all of the wheels were new re-profiled. Fig.1 shows that the accelermeters were mounted on the 8th vehicle, both on the car-body floor and the main components of bogie, such as axlebox, bogie frame, bolster, gearbox and motor. The HBM data acquisition system was used to record the acceleration data. The sampling frequency was 2500Hz. The train was round-trip operated from Changchun to Shenyang with a speed of 300km/h.

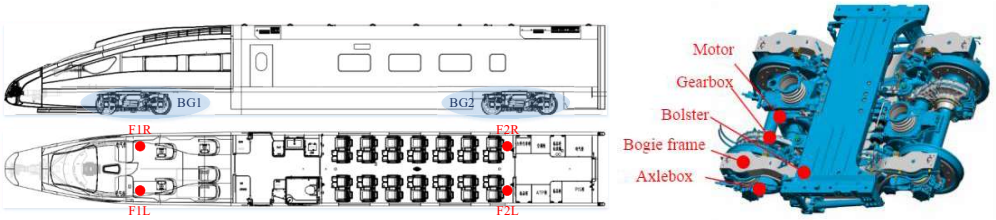

(a) car-body (b) bogie

Fig. 1 Arrangement diagram of vibration test points and test equipment

2.2 Hunting motion features

The Spering Index and lateral acceleration on the bogie frame band pass filtered by 0.5Hz and 10Hz while the tested vehicle operated as the head car and tail car are shown in Fig.2. The hunting motion occurred only when the tested vehicle operated as the tail car. In Fig. 2(b), the hunting motion occurred when the train in the acceleration and deceleration phases, and the train operated through the stations with high speed. The lateral Sperling index of the car-body were close to 3.5, which was quite higher than the required value of 3.0 according to GB5599, the related national standard of China. The acceleration on the bogie frames were close to 0.4~0.5g after filtered by 0.5~10Hz while the vehicle hunting, which were not exceed the limit value of 0.8g. Meanwhile, all the acceleration values on the floor and bogie frame of the second bogie location were larger than the first bogie location. Fig.3 shows the lateral and vertical acceleration filtered by 0.5~10Hz at the measuring points on the floor while vehicle hunting. Both the roll and yaw actions of car-body were found according to the acceleration on the floor. In Fig.4, the main hunting frequency of the lateral acceleration on the floor were 1.3~1.4Hz, while

some lower multiple times of the hunting frequency were found on the bogie frame and axle-box.

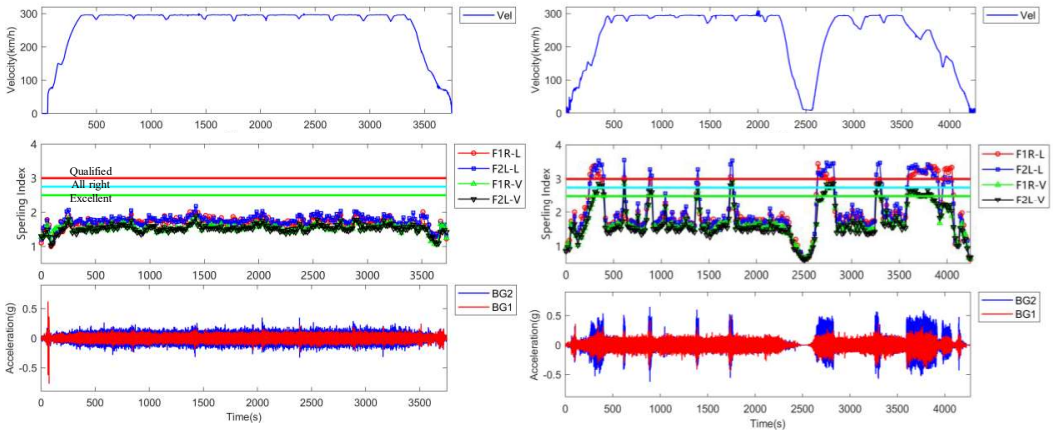

(a) operated as the head car (b) operated as the tail car

Fig.2 The dynamic index value while the tested vehicle operated as the head car and tail car

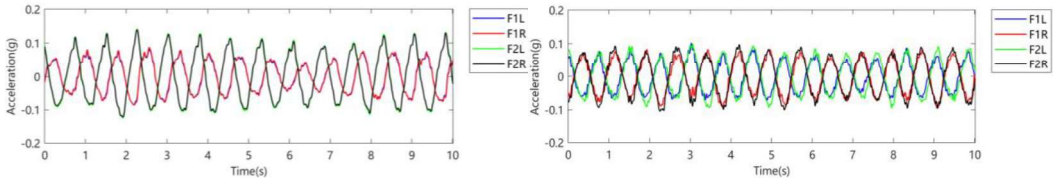

(a) lateral (b) vertical

Fig.3 Lateral and vertical acceleration filtered by 0.5~10Hz of the measuring points on the floor while vehicle hunting

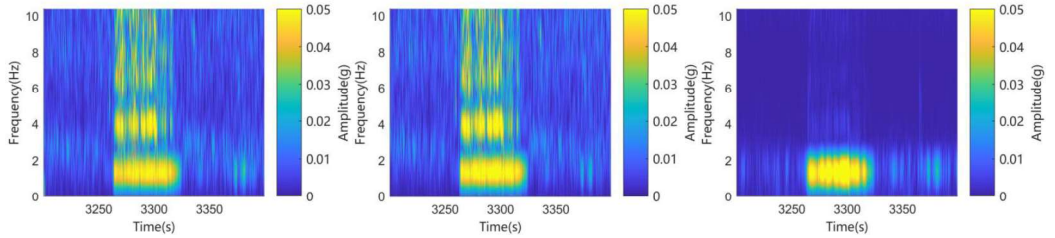

(a) axle-box (b) bogie frame (c) floor

Fig.4 Time-frequency diagram of the acceleration measured on the axle-box, bogie frame and floor

2.3 Potential influence factors analysis

According to the above-described test results, the tested vehicle only hunted when it operated as the tail car, which means that the ALs generated by the vortex effect on the tail car has obvious influence on the vehicle dynamic characteristics. However, there was no hunting motion occurred on the 1st Vehicle, no matter operated as the tail car or head car. This means that the ALs are not the only influencing factors. Therefore, other potential influence factors, including wheel-rail contact relationship, vehicle assembly

status, and the suspension components were checked for both cars and compared to each other.

1) The hunting motion phenomenon occurred when the wheel profiles were new re-profiled. After re-profiling the wheel profile as the worn profile indicate an equivalent conicity of 0.24 as shown in Fig. 5(a), the hunting motion disappeared.

2) The wheel radius difference between the 7th vehicle and 8th vehicle reaches 40mm as shown in Fig. 5(b). After changing new wheelsets for the 8th vehicle with the same radius of the 7th vehicle, the maximum lateral Sperling index value slightly reduced to 3.18, which means the hunting motion still occurred.

3) The dynamic stiffness values of the anti-yaw damper mounted on the 8th vehicle were tested larger than the initial design value under each frequency as shown in Fig.5(c), despite the static damping ratios all met the requirement (Fig. 5(d)). After exchanging them with the 1st vehicle, the maximum lateral Sperling index value reduced to 2.69, which means the hunting motion was almost disappeared.

In summary, the aerodynamics loads on the tail vehicle make the vehicle dynamic characteristics more sensitivity to the vehicle assembly status and the suspension parameters while the equivalent conicity of wheel-rail contact relationship is low. It is necessary to analyse the running dynamic characteristics considering the influence of aerodynamics, especially at the new re-profiled stage.

Tab.1 The potential influence factors verified by experiments

Factor	Status check	Measure	Result
Wheel-rail contact relationship	Lower conicity (0.11) of the new re-profiled profile	Worn profile with the conicity of 0.24	Lat. Sperl. 2.18
Vehicle Assembly Status	Higher wheel radius difference between the neighbouring vehicles	New wheelsets to eliminate the radius difference	Lat. Sperl. 3.18
Suspension components	Larger dynamic stiffness of anti-yaw damper	Exchange the anti-yaw dampers with the 1st vehicle	Lat. Sperl. 2.69

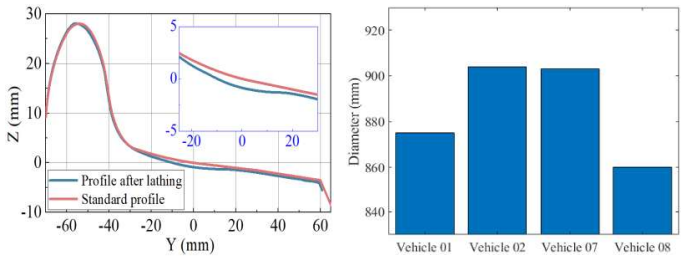

(a) wheel profiles (b) wheel radius difference

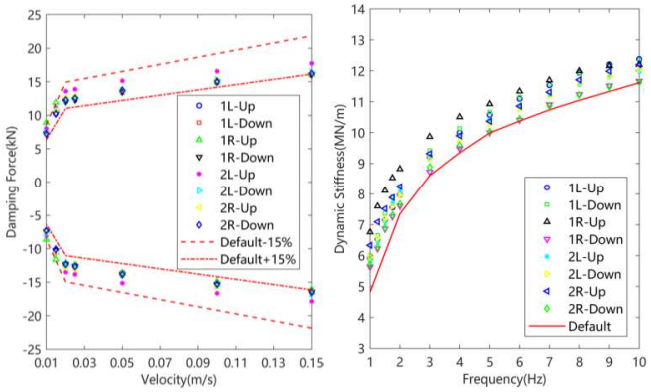

(c) static damping ratio (d) dynamic stiffness

Fig.5 Status check results of the tested vehicle with hunting motion

3 DYNAMIC SIMULATION CONSIDERING AERODYNAMIC LOADS

3.1 Analysis of aerodynamic loads

According to the EN 14067 standard, the components of forces and moments shall be expressed as follows.

$$F_i = \frac{1}{2}\rho A C_i |\mathbf{V} + \mathbf{U}|^2 \quad (i = x, y, z) \tag{1}$$

$$M_i = \frac{1}{2}\rho A L C_{Mi} |\mathbf{V} + \mathbf{U}|^2 \quad (i = x, y, z) \tag{2}$$

Where ρ, A, and L are the air density, reference area, and reference length respectively. $\mathbf{V}$ and $\mathbf{U}$ are the velocity vectors and the running speed of the vehicle and the crosswind. C_i represents the coefficients of the aerodynamic drag force, lateral force, and lift force. C_{Mi} represents the coefficients of the aerodynamic roll moment, pitch moment, and yaw moment.

Computational Fluid Dynamics (CFD) method was used in ANSYS Fluent to calculate the force and moment coefficients. The original eight-car marshalling train was simplified into a three-car mixed marshalling train model as shown in Fig. 5. The finite volume method is used to solve Reynolds-averaged Navier–Stokes (RANS) equations. Improved delayed detached eddy simulation (iDDES) method with k-ω-SST turbulence model was used in this paper. Fig.6 shows the Q-criterion iso-surface map of the simulated train. Vortex structures are formed behind the tip of the tail car nose, on both sides and on both sides of the track. On the tail vehicle, the vortex structure, which was composed of vortices with different time and space scales, was generated at the behind and two sides of the nose point, and the two sides of the rail. Continuously varying aerodynamic loads were formed by the evolution, shedding, and breaking of these vortices.

Fig. 8 shows the time and frequency domain curves of simulated yaw moment results. The yaw moment values of the tail car are quite larger than the head car and middle car. The main frequencies of the yaw moment on the tail car are 1.45Hz and 4.37Hz, which are close to the main hunting frequencies introduced in Section 2.2.

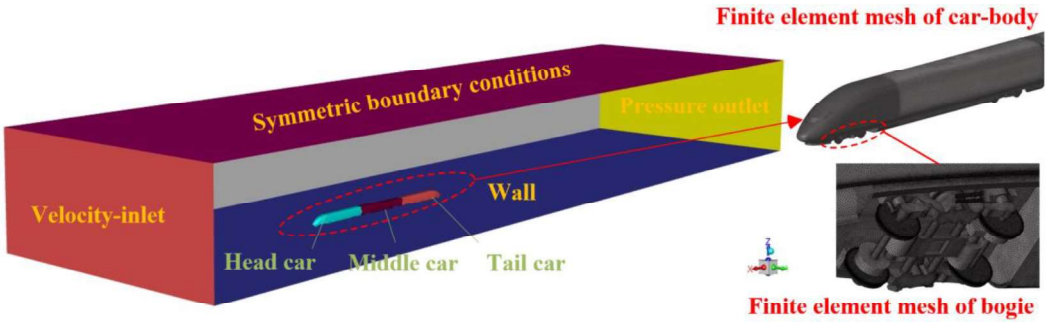

Fig.6 Schematic diagram of flow field calculation domain

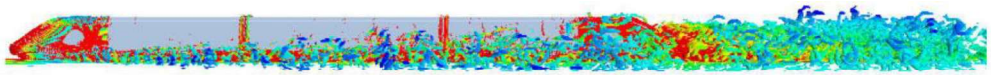

Fig.7 Vortex effect on the trailing car of the high-speed train.

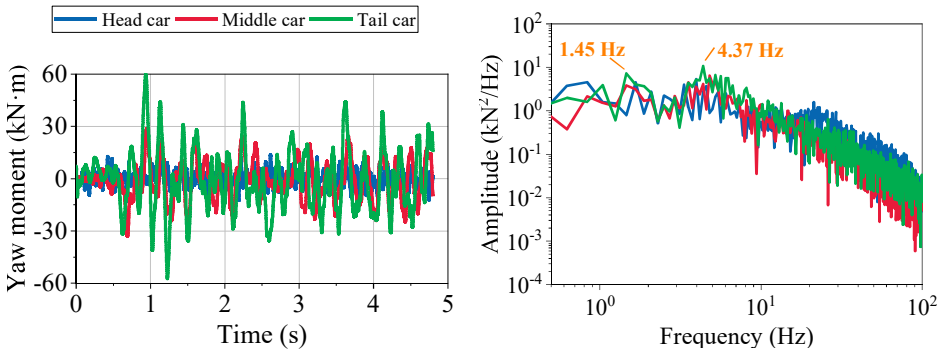

(a) time domain (b) frequency domain

Fig.8 Time and frequency domain curves of simulated yaw moment results

3.2 Setup of dynamic simulation

The muti-body running dynamic model of one vehicle was established in SIMPACK software. The original wheel profile “LMB10” and the rail profile “60N” were set as the wheel-rail contact relationship in the dynamic model. Chines standard high-speed track irregularities were considered as the wheel-rail excitations. The ALs analyzed for the tail car were applied to the centroid position of the car-body to meet the consistency to the aerodynamic model output. The 50%~150% varied range of both stiffness and damping ratio of the anti-yaw damper are considered in the calculation model as well.

3.3 Parameter sensitivity analysis results

Fig.9 shows the time history curves and spectrum of the lateral acceleration on the floor filtered by 0.5~10Hz for the cases of the stiffness value of anti-yaw damper changing. Without considering the ALs by the dynamic model, the acceleration on the car-body is almost unchanged while increasing the anti-yaw damper’s stiffness, which means no hunting motion occurred. However, considering the influence of ALs, the hunting motion occurred while increasing the stiffness of anti-yaw damper a little. The main hunting frequency in this case is 1.49Hz, which is close to the tested result. In Fig. 10, the maximum lateral Sperling Index values show more sensitivity to the variation of the anti-yaw damper’s stiffness and damping ratio. Therefore, the ALs on the vehicle make the

vehicle dynamic characteristics more sensitivity to the suspension parameters while the equivalent conicity of wheel-rail contact relationship is low. I.e., the appearance of pulsive aerodynamic loads reduces the stability margin due to working point of designed yaw damper at low conicities by about 20%.

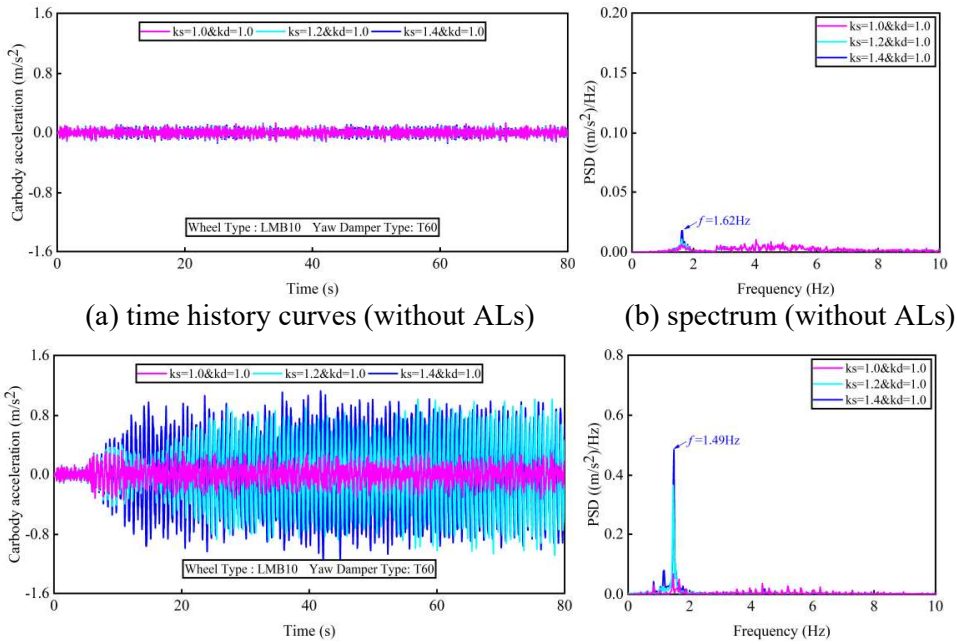

(a) time history curves (without ALs) (b) spectrum (without ALs)

(c) time history curves (with ALs) (d) spectrum (with ALs)

Fig.9 Time domain curves and spectrum of the lateral acceleration on the floor filtered by 0.5~10Hz in the cases of the stiffness value changing

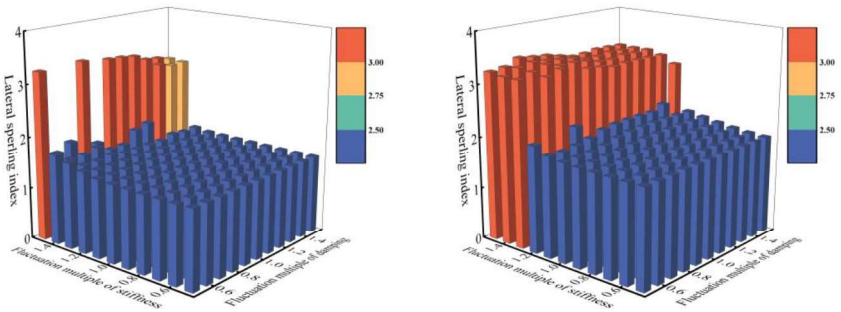

(a) without ALs (b) with ALs

Fig.10 Variation of the lateral Sperling index values in the cases of the values of stiffness and damping ratio changing

4 SUGGESTIONS AND DISCUSSIONS

According to the experiment and simulation results, several suggestions about the maintenance strategies and parameter optimization are discussed to avoid the hunting motion.

1) The parameter sensitivity of the suspension components to the vehicle dynamic performance should be analysed by using the dynamic model considering the ALs, especially for the low conicity condition. The performance of the suspension components such as anti-yaw dampers should be checked in each advanced repair process. Both static and dynamic performance tests for the suspension components are mandatory, which need to be added in the technical requirement for the supplier.

2) The strategies to reduce the ALs, such as maintaining the similar wheel diameter between the neighbouring vehicles, installing appropriate inter-vehicle dampers are suggested to considered in the future high-speed train's designing and maintenance.

3) The new wheel profiles with better wheel-rail contact relationship are suggested to be continuously concerned for the high-speed train.

5 CONCLUSIONS

In this paper, a hunting motion case occurred on the tail car of a high-speed train was analysed by both experiment and numerical simulation methods. The hunting features and the potential influence factors were analysed by the measuring data. Then, the analysis method of running dynamic performance considering the simulated aerodynamic loads was studied. Different parameter sensitivity of the suspension components to the vehicle dynamic under the conditions whether considering the ALs are got. Finally, several suggestions to avoid the hunting motion were proposed. Based on the study, the following conclusions are drawn.

- The hunting motion occurred when the train in the acceleration or deceleration phases, and the train operated through the stations with high speed. The main carbody's hunting frequencies were 1.3~1.4Hz. There were also some lower multiple times of the hunting frequencies on the bogie frame and axle-box.
- The yaw moment values of the tail car are quite larger than the head car and middle car. The main frequencies of the yaw moment on the tail car are 1.45Hz and 4.37Hz, which are close to the main hunting frequencies.
- The aerodynamics loads on the tail vehicle make the vehicle dynamic characteristics more sensitive to the vehicle assembly status and the suspension parameters while the equivalent conicity of wheel-rail contact relationship is low.
- Several suggestions about the maintenance strategies and parameter optimization are discussed to avoid the hunting motion.

6 REFERENCES

[1] Zhai W.: Vehicle-track coupled dynamics: theory and applications. Springer Nature; 2020.

[2] Wu, Y., Zeng, J., Qu, S., Shi, H., Wang, Q., & Wei, L.: Low-frequency carbody sway modelling based on low wheel-rail contact conicity analysis. Shock and Vibration, 2020, 6671049, p.1-17.

[3] Xu, K., Feng, Z., Wu, H., Li, F., & Shao, C.: Investigating the influence of rail grinding on stability, vibration, and ride comfort of high-speed EMUs using multi-body dynamics modelling. Vehicle System Dynamics, 2019, 57(11), p. 1621-1642.

[4] Xia, Z., Zhou, J., Liang, J., Ding, S., Gong, D., Sun, W., & Sun, Y.: Online detection and control of car body low-frequency swaying in railway vehicles. Vehicle System Dynamics, 2021, 59(1), p. 70-100.

[5] Montenegro, P. A., Carvalho, H., Ortega, M., Millanes, F., Goicolea, J. M., Zhai, W., & Calçada, R.: Impact of the train-track-bridge system characteristics in the runnability of high-speed trains against crosswinds-Part I: Running safety. Journal of Wind Engineering and Industrial Aerodynamics, 2022, 224, p. 104974.

[6] Montenegro, P. A., Ribeiro, D., Ortega, M., Millanes, F., Goicolea, J. M., Zhai, W., & Calçada, R.: Impact of the train-track-bridge system characteristics in the runnability of high-speed trains against crosswinds-Part II: Riding comfort. Journal of Wind Engineering and Industrial Aerodynamics, 2022, 224, p. 104987.

[7] Baker, C., Cheli, F., Orellano, A., Paradot, N., Proppe, C., & Rocchi, D.: Cross-wind effects on road and rail vehicles. Vehicle system dynamics, 2009, 47(8), p. 983-1022.

[8] Liu, D., Zhou, W., Lu, Z., Gu, H., Li, T., & Zhong, M.: Effect of car-body initial dynamic sway on overturning before high-speed trains negotiate wind speed variations. Vehicle System Dynamics, 2021, 1902540, p. 1-18.

[9] Xu, R., Wu, F., Zhong, M., Li, X., & Ding, J.: Numerical investigation on the aerodynamics and dynamics of a high-speed train passing through a tornado-like vortex. Journal of Fluids and Structures, 2020, 96, 103042, p. 1-17.

[10] Ishihara, T., Zhang, D., & Nagumo, Y.: Numerical study of dynamic response of railway vehicles under tunnel exit winds using multibody dynamic simulations. Journal of Wind Engineering and Industrial Aerodynamics, 2020, 211, 104556, p. 1-21.

[11] Montenegro, P. A., Barbosa, D., Carvalho, H., & Calçada, R.: Dynamic effects on a train-bridge system caused by stochastically generated turbulent wind fields. Engineering Structures, 2020, 211, 110430, p. 1-16.

[12] Diedrichs, B., Krajnović, S., & Berg, M.: On the aerodynamics of car body vibrations of high-speed trains cruising inside tunnels. Engineering Applications of Computational Fluid Mechanics, 2008, 2(1), p. 51-75.

FROM INSTABILITY TO LOW FREQUENCY BODY MOTION - CONTACT GEOMETRY VERSUS DESIGN OF THE VEHICLE

Thomas KOLBE

Department of Running dynamics testing
DB Systemtechnik GmbH
32423 Minden, Germany

Received: August 11, 2022

ABSTRACT

In the German-speaking railway infrastructures, the rail inclination was changed from 1:20 to 1:40 in the past in order to create better contact conditions for higher speeds. In addition, this should also be favored with a low distance between the active faces and a small gauge. Based on these conditions, the standard wheel profile ORE S1002 was developed and established itself as a recognized wear profile in a many European countries (with different rail inclinations). But the wear of the rail heads and the sleepers led to an increase of the contact geometry parameter equivalent conicity which reached very high values in some sections of lines and characterizes the vehicle design and the proof of stability to this day. You can find these levels in national notified technical rules (NNTR) of Germany and Austria.

With the introduction of a new rail profile and headcheck-preventing geometries and, in particular, preventive rail processing by grinding and milling, this high level of equivalent conicity has not only been reduced, it is now approaching zero. This means a comeback of the conditions of the rail inclination of 1:20 on the one hand and even more extreme conditions on the other hand, since the frequent maintenance no longer allows greater wear on the rail head. The resulting long-wave sinusoidal running of the wheelsets increasingly leads to low-frequency body motions, to which the railway vehicles react due to insufficient damping. In addition, there is the issue of high equivalent conicities too, which are now caused by wheel profile wear in the no longer coordinated wheel-rail contact system .

If this situation stays that way, the requirements for a vehicle design will continue to increase. Beside the avoidance of instability at high equivalent conicities, more attention must be paid also to damping to prevent low-frequency body motions

Keywords: contact geometry, instability, low frequency body motion, running behaviour

1 INTRODUCTION

The problem of instability is omnipresent. An essential parameter for describing the causal contact conditions is the equivalent conicity. An instable running behaviour is characterized by a high value of the equivalent conicity, which in the past was mainly caused by the contact partner rail in the form of small gauges and worn rail heads. About 10 - 15 years ago, the situation in Germany began to change due to a change in the shape of the rail head (new rail profiles 60E2, 54E4 [2]), the correction of small track gauges and modified maintenance procedures to avoid head checks and rolling contact fatigue (RCF). This led to changed wheel profile wear and the loss of the form stable standard wheel profile S1002 [1]. High equivalent conicities now determine worn wheel profiles, which can lead to stability problems even with mileages of more than 100,000 km, depending on the vehicle or bogie construction. In addition, a new, previously avoided problem of low frequency body motion (LFBM) arose, which again, depending on the vehicle or bogie construction, can more or less affect the running comfort and also the running safety.

1.1 The equivalent conicity as a basic criterion

There are several parameters defined in EN 15302 [1] to analyse the wheel-rail contact geometry. The equivalent conicity as a basis for further considerations is described in this standard [1] as follows: " By definition, the equivalent conicity is equal to the tangent of the cone angle of a wheelset with coned wheels whose kinematic movement has the same wavelength as the given wheelset for a particular amplitude of the lateral wheelset movement."

This parameter is controversial among mathematicians and it is an auxiliary quantity developed by engineers, which describes the movement of a free, unbound wheelset based on the simplification of a conical wheel. Practice has proven, however, that this parameter can be used to describe and test the running behaviour with regard to instability and low frequency body motion very well.

1.2 The changes in the infrastructure/ on the track

The contact geometry between wheel and rail has changed significantly, especially on the German network. Unintentionally, conditions have been approached that were previously only known on railway networks with a rail inclination of 1:20. And metrologically proven, these conditions have been surpassed in a negative sense.

The rail profiles used in the past (60 E1 [2]) have a flank radius of 13 mm. Due to the wear of the rail under the rolling wheel, this radius becomes smaller (see Figure 1 left). This has a negative effect on the parameter equivalent conicity, making it larger. In combination with a track gauge of less than 1435 mm, a sine wave is stimulated in the vehicles, which can lead to instable vehicle running if there is insufficient damping.

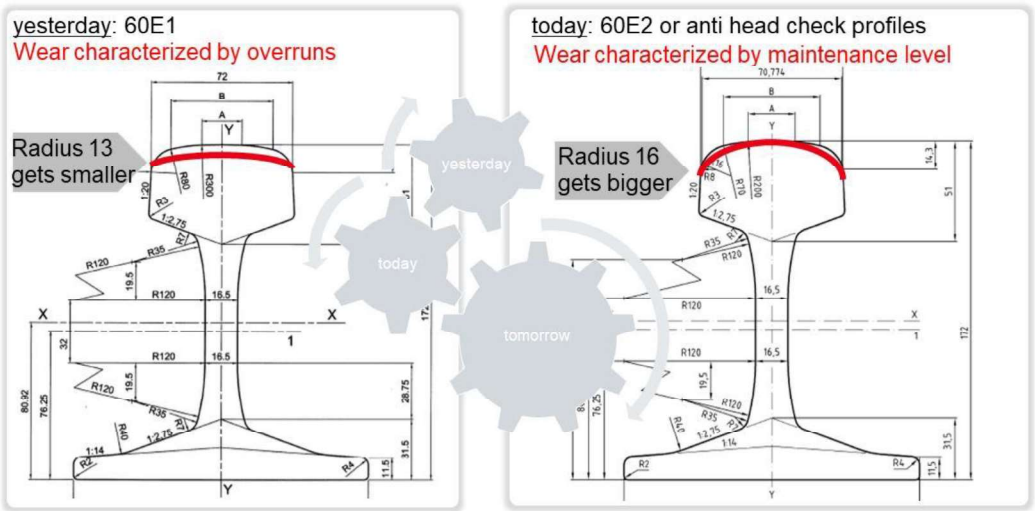

Fig.1 rail wear - yesterday and today

The rail profiles used today (60 E2 [2]) have a flank radius of 16 mm and larger if special profiles are applied by grinding or milling to prevent head checks. The wear of the rail head due to wheel-rail contact is now negligible and very small. The maintenance work of the rail head processing only characterizes the wear of the rails.

This leads to conditions that guarantee a flank radius at the rail head that is always greater than 16 mm (see Figure 1 on the right). This results in very small equivalent conicities when using the standard wheel profile S1002, which can lead to low frequency body motions, to an excitation of a specific carbody mode if there is insufficient damping. At least on the German network this phenomenon was not exist from so far.

1.3 The changes on the vehicles / on the wheelsets

The wear of the wheel profile S1002 [1] was previously characterized by the fact that the geometric shape remained constant and thus the influence of the contact geometry on the running behaviour remained stable with also relatively constant rail conditions. This can be described by an almost constant value of the equivalent conicity (see Figure 2, green gradient in the optimal range). Due to the change in the wheel flange thickness of the wheel profile (e.g. due to a desired low material removal during reprofiling), very low equivalent conicities arose, but after a certain wheel profile mileage they again reached an optimal level (see Figure 2, blue gradient).

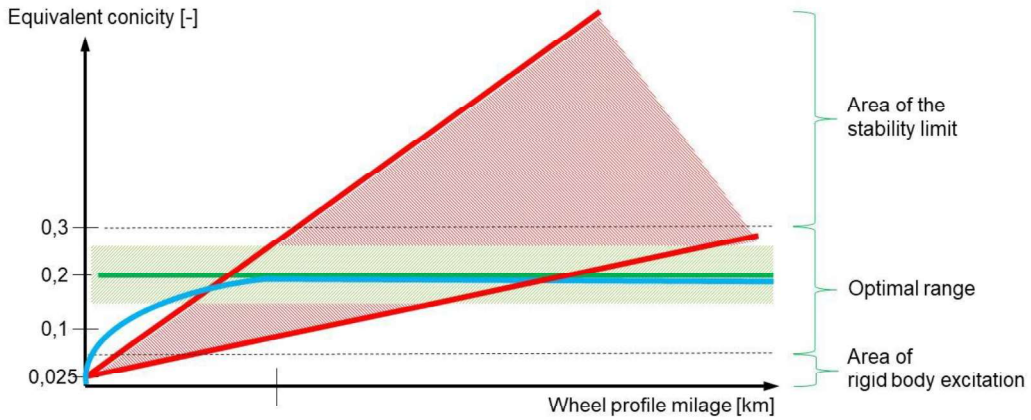

Fig.2 wear development of the wheel profile S1002

However, it became more and more evident in almost all vehicle types that the wheel flange thickness increased during operation and reached the operating limit very quickly. The nominal dimension of the wheel flange thickness was further reduced. The shape of the wheel profile now changed during operation in such a way that there was a constant increase in the equivalent conicity without visible saturation (see Figure 2, red curves). Ultimately, depending on the vehicle design, this also leads to instable vehicle running. There are now vehicles showing low frequency body motion with a new wheel profile and tend to have instable running behaviour after a certain wheel profile mileage.

2 EFFECTS ON RUNNING BEHAVIOUR

Based on a form stable wear of the wheel profile, the running behaviour of a railway vehicle is characterized not only by the track geometry irregulations but also by the change in the contact geometry. These changes can be described very well with the parameter equivalent conicity and correlate with the vehicle reaction (see Figure 3).

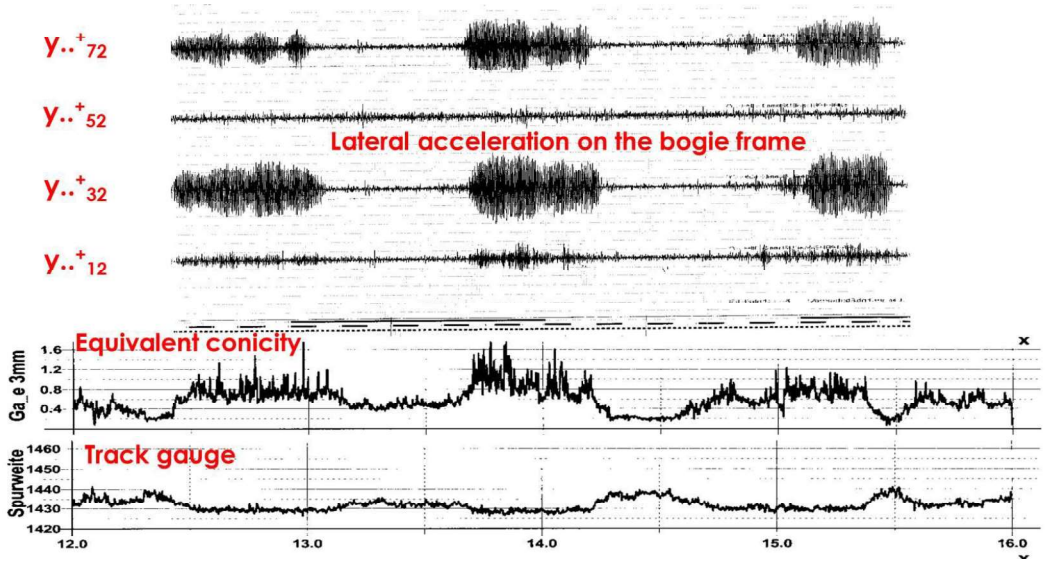

Fig.3 vehicle reaction based on contact conditions

In the past local vehicle reactions could be assigned locally to the contact conditions. Reports of instable behaviour led to maintenance procedures on the track. Basically these were concrete hot spots in the network and could be eliminated by maintenance after detection. Today there are relatively constant conditions of equivalent conicity from the point of view of the track, but the wheel profile no longer wears in a form stable way. The wheel profile S1002 [1], which is still predominantly used, starts under these track conditions with very low values of equivalent conicity, which increase with increasing wheel profile mileage (see Figure 4).

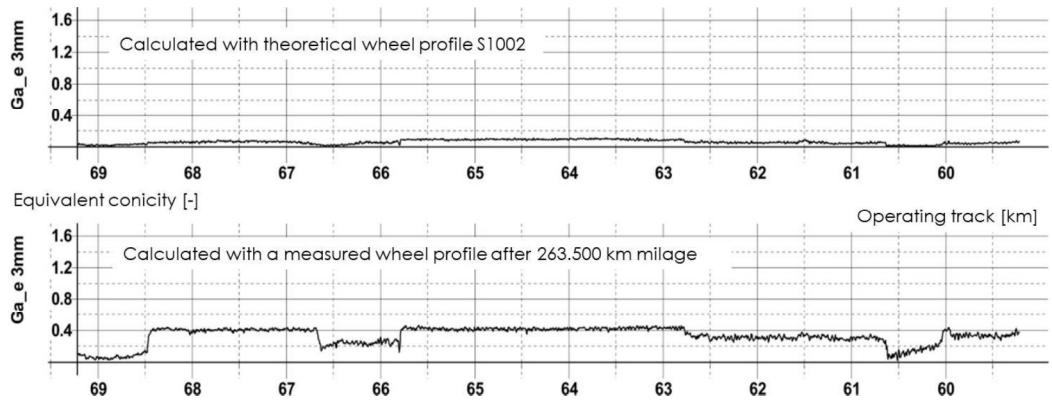

Fig.4 change of equivalent conicity based on the wear of the wheel profile S1002

The running behaviour is no longer influenced by the hot spots on the track, but by the change in the contour of the wheel profile over its mileage. Depending on the vehicle design, there are problems with the low frequency body motions and stability. There are examples where vehicles come from maintenance with a new wheel profile and low frequency body motion effects occur, sometimes associated with a noticeable loss of comfort. The running behaviour improves with increasing mileage, but after a mileage of more than 150,000 km, the vehicle running becomes instable.

Due to the decisive influence of the wheel profile, the running behaviour is no longer only problematic locally, it extends over all lines of the network depending on the respective speed. The boundary conditions for good behaviour of a railway vehicle have deteriorated at the present time from the point of view of the wheel-rail contact geometry. The full range of wavelengths of the sine wave can occur, but only a frequency range between approx. 2 and 4 Hz of it offers optimal conditions for conventional vehicle constructions (see Figure 5).

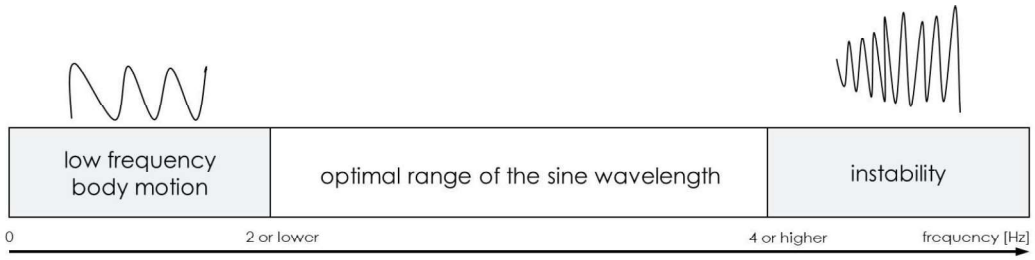

Fig.5 influence of the wavelength of the sine wave

This makes clear that the currently existing wheel-rail contact conditions place very high demands on the vehicle design. Although this requirement can be met with the current state of the art, it leads to higher development and construction costs, and depending on the implementation, e.g. with active elements in the running gear, also to higher maintenance costs.

An optimized wheel-rail contact geometry with dimensionally constant conditions on both the wheel and the rail side would be more simple and more cost-effective. Due to the development in the maintenance of the track and a significantly improved track geometry through better measuring systems and better maintenance tools and machines, the influence on the vehicle running behaviour due to deviations in the track geometry is minimized and the wheelset movement is mainly influenced by the wheel-rail profile pairing. Unfortunately, this enormous importance of the contact geometry has not yet arrived in the maintenance of the vehicles and the track. In the high-speed range beginning with 200 km/h, however, you can no longer avoid it.

Since the problem lies precisely at the interface between the vehicle and the track or wheel and rail, it is not easy to correct or optimize the contact geometry. The separation of operation, vehicle and infrastructure as well as maintenance has created more interfaces than ever before.

The few technical experts with the knowledge of the overall railway system have to do a lot of convincing on several fronts in order to achieve improvements, especially at the interface between vehicle and track. DB Systemtechnik makes a significant contribution to this.

3 CONCLUDING REMARKS

Despite its simplicity, the wheel-rail system is very complex. A high-quality construction of a railway vehicle is and will always be very demanding. In the past, the design of the spring-damper systems was essentially relevant for compensating the irregularity of the track geometry. It will continue to be so, but there is a decisive factor in the lateral direction – the wheel-rail contact geometry. Up to now, this was mainly decisive for running stability and compliance with the instability criterion from the point of view of running safety. Due to the changes in the profile geometry, which, starting with the changes to the rail, has significantly changed the wear on the wheel, another factor, the low frequency body motion influencing running behaviour is becoming more concise and requires increasing attention. This development has been taken into account by the standardisation committee of the European standardisation organisation, the CEN TC256 Working Group 10 Vehicle - Track – Interaction as part of the revision of the EN 14363 standard for the approval of a railway vehicle in view of running behaviour and will be of greater importance in the future for testing and verification.

It would be desirable if the vehicle designers could adjust to these influences timely and avoid surprises during vehicle homologation or later in operation.

In the medium term, however, the aim should be for the wheel-rail contact geometry to move within a framework that is characterized by a constant parameter of the equivalent conicity and the radial steering index and is based on form stable wear of both partners, the wheel and the rail.

4 REFERENCES

[1] EN 13715 „ Railway applications – Wheelsets and bogies – Wheels – Tread profile“, July 2020

[2] EN 13674-1:2011 +A1 „ Railway applications – Track – Rails – Part 1: Vignol railway rails 46 kg/m and above“, May 2017

[3] EN 15302 Railway applications – Wheel-rail contact geometry parameters – Definitions and methods for evaluation, October 2021

[4] CEN/TR 17792 Railway applications – Wheel-rail contact geometry parameters – Technical report and background information about EN 15302, February 2022

[5] Kolbe, Thomas: Das in den 70er Jahren entwickelte und europaweit eingesetzte Radprofil S1002 ist heute kein Verschleißprofil auf dem deutschen Streckennetz mehr. Tagungsband 14. Internationale Schienenfahrzeugtagung Dresden 2015, p. 38-41

STRENGTH VERIFICATION OF DYNAMICALLY STRESSED COMPONENTS OF ROLLING STOCKS OUTSIDE THE MAINSTREAM ACTIVITIES OF DYNAMIC TESTING LABORATORY VZU PLZEN

Jan CHVOJAN and Jiri NEMET

Department of Dynamic Testing Laboratory
Research and testing institute Pilsen Ltd.
CZ-30100 Pilsen, Czech Republic

Received: August 29, 2022

ABSTRACT

The abstract concisely reports the role and possibilities of the VZUP Dynamic Testing Center in the development process of new rolling stocks. The mainstream of Dynamic Testing Laboratory VZU Plzen is the performing of extensive long-term strength tests of rolling stock bogie frames using electrohydraulic loading system for simulation of static and fatigue loading with simultaneous measurement of deformation responses at critical points and their evaluation and fatigue strength prediction. The result of these tests is the basis for the certification of the bogie frames according to the TSI regulation.

Unlike these core activities of the Dynamic Testing Laboratory, the paper focuses on ensuring the vibration resistance of rolling stock equipment and demonstrating its ability to safely handle the operational vibrations of the places where this equipment is mounted on the rolling stocks. By simulating the load spectra, both their service life and their function are checked so that these electrical devices can perform features for which they were designed. Special electro-hydraulic shaker tables with advanced control software are used for these vibration simulations of a power spectral density of load signals.

Finally, the paper describes tests to verify the strength of couplings of rolling stock both statically and dynamically.

Keywords: vibration, power spectral density of load signals ASD, clamping points, transfer function, durability test, shock test, functional test, couplings, static loading, dynamic loading, coupling head

1 INTRODUCTION

Developing of the new rolling stocks is a demanding process involving development project, design, computational verification, testing, and operational measurement. All this under the strong scrutiny of countless standards, leaflets, ordinances, TSI regulations and so on, which are to guarantee the safety of passengers, the flow of traffic and the operational reliability of rolling stocks and their components.

Most of these components are exposed to dynamic force effects in operation, which are associated with the phenomenon of fatigue damage to their integrity. In the case of welded steel parts, technological and structural notch effects also come to the fore. Some components that are fixed on the vehicle body, floor, bogies, or unsprung mass are exposed to vibrations in operation and thus form a separate chapter in their experimental verification - resistance to vibrations.

1.1 Railway stocks components resistance to vibrations

The European standard [1] deals with the vibration resistance of rail vehicle components. Vibration simulation is divided into categories according to where the components are located on the rail vehicle. The largest vibrations occur in components

mounted on unsprung masses, while smaller vibrations occur in the bogie and the floor or the vehicle body. The tested object was subjected to the following tests:

- Simulated long-life testing at increased random vibration levels
- Shock testing

Checkpoints have to be determined for each of the three orthogonal load directions, and acceleration sensors for measuring the reference signal were installed at these locations. The location of the control checkpoints was as close as possible to the mounting points of the device and were firmly connected to it. Based on the data from all these accelerometers from the control points, the reference signal at the fictitious reference point is calculated, where the reference signal spectrum is defined as the arithmetic mean at each frequency of the spectral acceleration density (ASD) values of the signals from all control points. The total rms value of the reference signal is equivalent to the root mean square value of the rms values of the signals from the control points. The reference signal at the fictitious point is used to confirm the test requirements - the vibration levels at this point were used to determine the ASD and the effective acceleration values at the beginning and end of the test for each orthogonal direction.

Usually based on an agreement with the customer, measuring points are defined on the tested object, where other accelerometers were installed. The measuring point is the specific location on the testing device from which data are obtained to examine the vibration response characteristics of the device. Data from these accelerometers are used to determine the frequency transfer functions (FRF) throughout the testing for each orthogonal direction. Thus, the FRF expresses the ratio of the acceleration amplitude at a given frequency at a measuring point to the acceleration amplitude at a given frequency at a control point. If there are no changes in the mechanical properties of the test item, the FRF does not change during the test.

The order of the individual tests (in individual orthogonal test directions x, y, z) is determined with regard to the complexity of assembling the tested object on vibrating tables in order to minimize assembly work when fastening to vibrating tables. After each subtest in a given orthogonal direction, a visual inspection of the test item, including fixation, for visible mechanical damage body of tested subject and anchor points are performed.

An objective of the simulated long-duration life test by the specified test levels is to determine the mechanical integrity of the equipment under increased levels of vibrations. In compliance with [1] it is necessary to keep the curve of the values of the acceleration spectral density (hereinafter referred to as ASD) in g2/Hz on frequency Hz and a size of an RMS value of acceleration in m/s2 for the period of 5 hours in each direction. The shape of ASD loading and its limits defined for frequency area are given on Fig. 1.

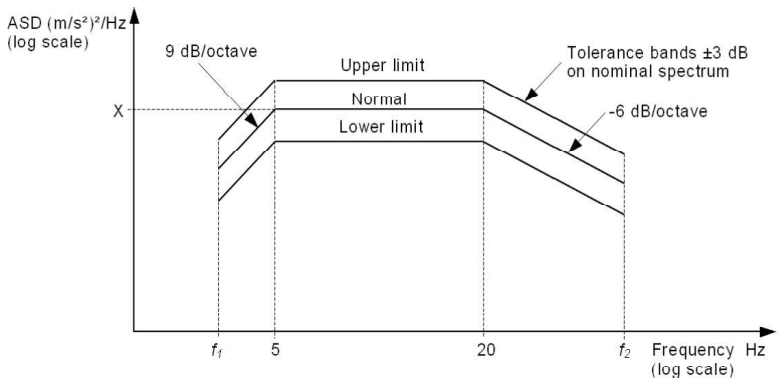

Fig. 1 Prescribed shape of ASD loading and ASD limits

The frequency range is calculated using empirical formulas based on the weight of the tested subject and the category and class of its attachment to the vehicle. Power spectral density (ASD) for **x** orthogonal direction in the fictitious reference point at the beginning and end of the simulated long-duration life tests at increased levels of random vibrations (5 hours) is visible on Fig. 2. An example of frequency response functions H3 between response point 1 and mounting point 1 (left) and mounting point 2 (right) during the simulated long-duration life tests at increased levels of random vibrations (5 hours) are shown on Fig. 3.

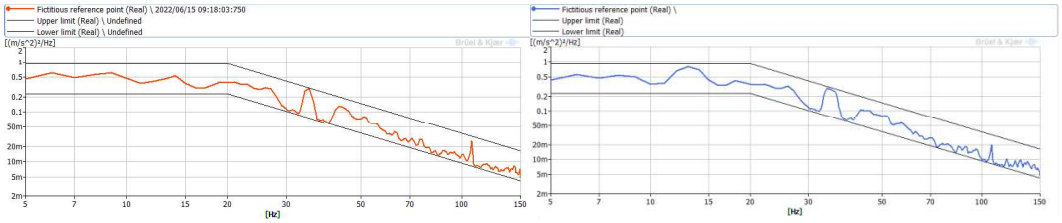

Fig. 2 Real shape of ASD loading and ASD limits at the beginning and end of testing

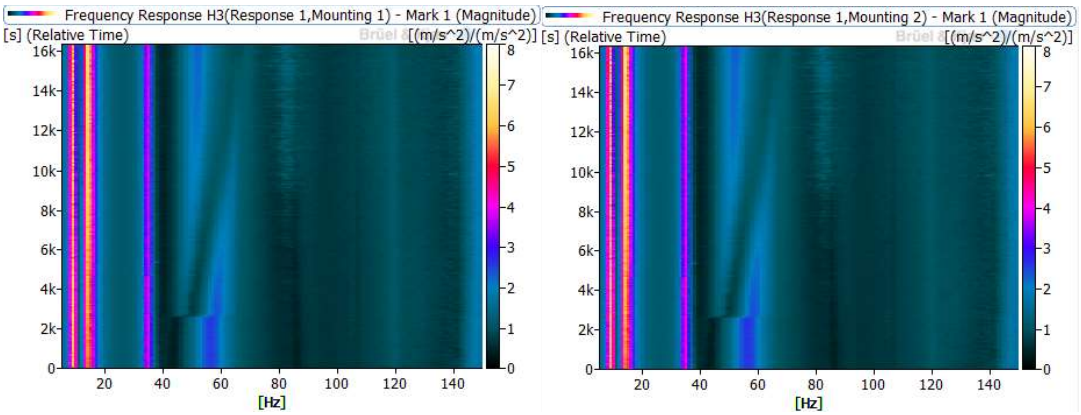

Fig. 3 An example frequency response functions H3 between response point 1 and mounting points 1 (left) and 2 (right)

During the shock testing the tested object is put to the effect of a train of individual half-sine pulses, each of a rated value of duration D [ms] with a nominal amplitude A, which gives a peak acceleration. The shape of loading is given in Fig. 4 which was taken from [1]. Duration of a pulse D was 30 ms in all the excitation cases, the peak acceleration amplitude for the direction X was 5g and for the directions Y and Z 3g. The tested object will be exposed to 18 shocks in total, 3 positive and 3 negative in each of three orthogonal directions of loading.

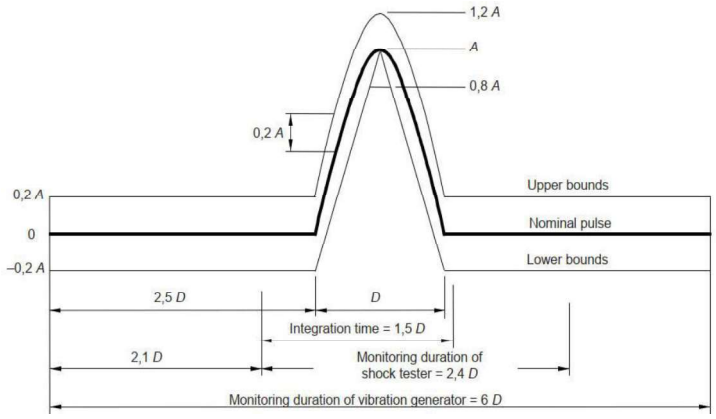

Fig. 4 The shape of loading during shock testing

Finally, the tested device has to be tested successively by partial tests in the following order:

- long-life testing at increased random vibration levels test (5h) direction x
- shock test direction x 5g/3x positive, 3x negative
- long-life testing at increased random vibration levels test (5h) direction y
- shock test direction y 3g/3x positive, 3x negative
- long-life testing at increased random vibration levels test (5h) direction z
- shock test direction z 3g/3x positive, 3x negative

1.2 Experimental verification of a coupling

An important verification method is the experimental testing of the head connecting two couplings of railway vehicles. Type tests are carried out according to the specifications and technical parameters determined by the manufacturers and their customers and reflecting the specific conditions of their operation. The actual test is preceded by the installation of strain gauges in specific critical locations as well as lift sensors in the vertical and longitudinal directions. The basic verification is the application of a static force alternately in tension and compression in partial steps up to 200kN or 300kN, exceptionally 400kN. This test can be completed by a load leading to destruction or a fatigue test with a prescribed number of cycles and load amplitude. A typical shape of the coupler is shown in Fig. 5.

Fig. 5 Typical design of a coupling

The test bench for an experimental verification consists of a robust support structure for clamping both couplings and a connecting head. Static or dynamic force is developed by an electro-hydraulic loading system. An example of mentioned test stand is showed on the Fig. 6.

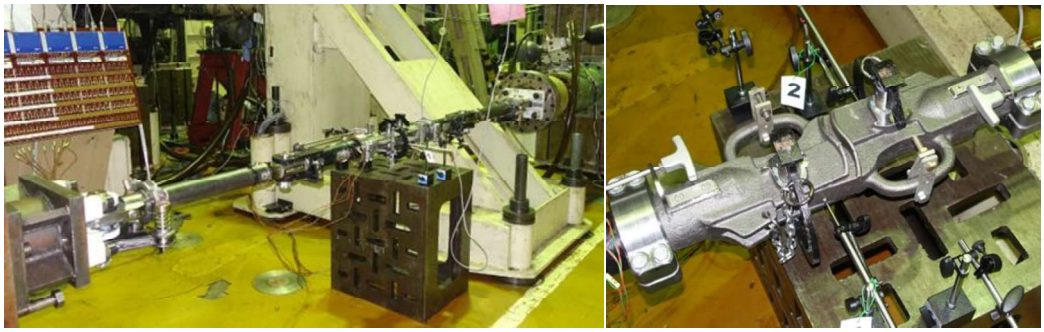

Fig. 6 Coupling in the test bench and coupling head

The aim of the test is to verify the behaviour of two coupled together couplers under the action of axial loads given in the Table 1. Negative sign signifies pressure force.

Step. No:	1	2	3	4	5	6	7	8	9	10
Force (kN)	100	-100	200	-200	200	-200	200	-200	-300	-400

Table 1 Possible static loading scenario

Sometimes, the fatigue type test of the coupler is required and can be performed on one serial piece. There is no need to perform the test with two complete couplers, one coupler and the head of the second coupler could be enough in order to validate the coupling interface. During the test these quantities will be measured:

- Loading electro-hydraulic cylinder force
- Angles and forces during coupler turns

The coupler shall resist fatigue life of 1.200.000 longitudinal loading cycles. The fatigue load due to service to considered is a load amplitude of 100kN, it means 1 cycle is (+50KN traction, -50KN compression). In order to facilitate the test, the cycle could be a complete traction cycle (0KN; +100 KN traction). In addition to longitudinal forces, simultaneously it shall be applied ± 5° and ± 25° in horizontal direction according to table 1. In addition to longitudinal forces, simultaneously it shall be applied ± 2° in vertical direction according to table 2.

Phase	Configuration	Movement	Cycles	Forces/displacements
1	Straight	Longitudinal	500.000	0 – 100KN (Traction)
		Horizontal	-	-
		Vertical	-	-
2	± 5º Horizontal	Longitudinal	400.000	0 – 100KN (Traction)
		Horizontal	1.000.000	± 5º
		Vertical	-	-
3	± 25º Horizontal	Longitudinal	100.000	0 – 100KN (Traction)
		Horizontal	25.000	± 25º
		Vertical	-	-
4	± 2º Vertical	Longitudinal	200.000	0 – 100KN (Traction)
		Horizontal	-	-
		Vertical	200.000	± 2º

Table 2 Possible fatigue loading scenario

Based on this table the fatigue test shall be carried out in 4 phases as indicated in following table:

- Straight longitudinal load
- Longitudinal load combined with ±5º horizontal turns
- Longitudinal load combined with ±25º horizontal turns
- Longitudinal load combined with ±2º vertical turns

2 CONCLUDING REMARKS

This paper summarizes some methods and procedures for the experimental verification of equipment of railway vehicles which are exposed to vibrations and shocks in operation. These devices must not only ensure their integrity in operating conditions, but must also meet the requirements for their function, which they have in the railway vehicle. The strength verification of the integrity of these devices can also be performed computationally, but these computational methods are not capable of guaranteeing their correctness and completeness throughout the entire development process of these railway devices and their production technology. Experimental verification, i.e. physical simulation of operating conditions or their equivalents, unlike computational ones, also affects in its conclusions the quality of the production process of railway vehicle equipment. Modern measuring methods are capable of graphically detecting integrity disturbances caused by operational vibrations and shocks.

3 REFERENCES

[1] European standard EN 61373 ed2.:2011- Railway equipment - railway vehicle equipment - impact and vibration tests.

PRISMA SINUSJET GEN. 3.0 AT SIEMENS GRAZ: HIGH SPEED WHEELSET TESTING. FIRST EXPERIENCES AND OUTLOOK

Gábor NÉMETH[1], Jochen MARX[2], Franz-Josef WEBER[2]

[1]Prisma Engineering Maschinen- u. Motorentechnik GmbH.
Kärntner Straße 311.
A-8054 Graz, Austria

[2]Siemens Mobility Austria GmbH.
Eggenberger Straße 31.
A-8020 Graz, Austria

Received: August 12, 2022

ABSTRACT

The scope of this work is the introduction of the testing possibilities of the latest generation railway resonance testbed, the Prisma SinusJet Gen. 3.0.

Testing of railroad wheelsets for bending has always been a crucial topic of bogie development. The EN 13103, EN 13260 and the EN 13261 standards for example clearly define certain bending fatigue limits for 10^7 cycles, although they do not set further requirements regarding the testing frequencies or higher (or lower) cycle counts. The common vibration testbeds (see EN 13103 such as the Minden-type or the Vitry-type) provide a bending moment distribution in the axle which differs significantly from the real bending moment distribution observed in operation. More realistic introduction of the bending moment in the press fit (via 2-point or 4-point bending) also remains an open topic. Apart from these points, the standards lack the directives for torsional testing, which is nowadays a factor for wheelset homologation in some countries.

The idea behind the Prisma SinusJet Gen 3.0 testbed is to remove these limitations and enable not just 2-point or 4-point bending but also torsion and their combination at much higher (40-60 Hz) frequencies. To save up space and manufacturing costs, a completely isolated (force-free) and easy-to-mount support system has been designed, which does not require any special foundation. As test specimens, 1:1 production wheelsets (as manufactured for service) can be used. To demonstrate the capabilities of the new system, variable load sequences have been applied, resulting in stable stress distributions and reliable testbench running performance.

Keywords: wheelset testing, wheelset dynamics, testbed development, torsion, bending

1 INTRODUCTION

Testing of railroad wheelsets for bending has always been a crucial topic of bogie development. The EN 13103, EN 13260 and the EN 13261 standards for example clearly define certain bending fatigue limits for 10^7 cycles, although they do not set further requirements regarding the testing frequencies or higher (or lower) cycle counts. The common vibration testbeds (see EN 13103 such as the Minden-type or the Vitry-type) provide a bending moment distribution in the axle which differs significantly from the real bending moment distribution observed in operation. More realistic introduction of the bending moment in the press fit (via 2-point or 4-point bending) also remains an open topic. Apart from these points, the standards lack the directives for torsional testing, which is nowadays a factor for wheelset homologation in some countries.

The idea of an “all-in-one” lightweight solution for a wheelset testing device was conceived back in 2013 by the Austrian company *Prisma Engineering*. The concept was a resonance testbed with multiple actuators to introduce bending and torsional load to a “floating” sample (one which has not been rigidly fixed to the ground but rather hung on a system of elastic spring-like structures). As the plan seemed too ambitious at the time, the final solution has materialized over multiple generations of more and more

complex prototypes of increasing functionality, culminating in the 3rd generation of the SinusJet testbed in 2021.

1.1 Design of the SinusJet Gen 3.0 test bench

In order to accomplish both excitation modes (bending and torsion), the principal design of the machine had to be done with two sets of actuators in mind – one set for each vibration eigenform. This was a major upgrade compared to the previous generations of the SinusJet testbeds, one that required a completely new engineering philosophy. To obtain the closest possible results to the real operation of the wheelset, in which bending and torsional moments are introduced on both sides of the axle, the testbed had been designed in a symmetric manner: two vibrational actuators (one for bending and one for torsion) had been placed on each side of the wheelset, which had been connected to the wheel through a stiff, clampable adapter structure. The main 9,6 kW electric servo motor had been placed in the middle of the structure, under the axle of the wheelset, connected to the vibrational actuators with long axial shafts. Fig. 1 shows the exact layout of the testbed as designed by *Prisma Engineering*.

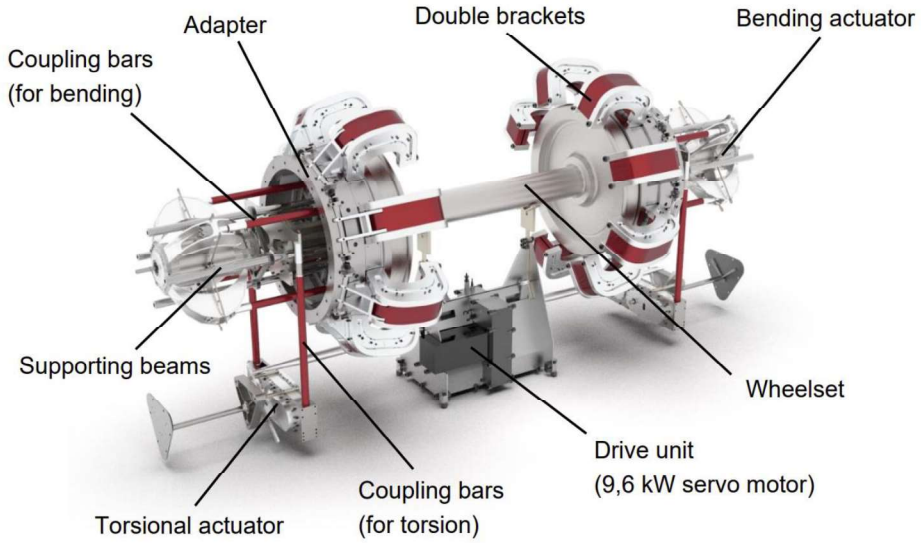

Fig. 1 Principal design and components of the Prisma SinusJet Gen 3.0 testbed

The true challenge of this straight-forward design lies in the decoupling of the different eigenfrequencies from each other and – most importantly – from the ground. Without it, a massive additional foundation must be considered to keep the environmental resonance under a safe limit (as it has been a common practice in the field of dynamic testing). Since the use of such foundations tends to introduce other (mostly logistical) problems, a three-way elastic decoupling system had been developed: first of all, a large central clutch-like decoupler had been inserted between the test sample (which is the assembly of the wheelset and the large adapter) and the vertical support to keep the bending resonance away from the housing, therefore protecting the close environment of the testbed. This central clutch is soft in bending direction but stiff in all other degrees of freedom. To decouple the harmful torsional vibration from the static structure, a special torsional pipe had been put between the vertical support and the test sample, with a

similar functionality as the central clutch, only in torsional direction. Thirdly, the vibrational actuators had also been partially decoupled from the static holding structure by the use of elastic beams which act as radial and axial bearings. Fig. 2 depicts the position of the central clutch and the torsional pipe within the machine.

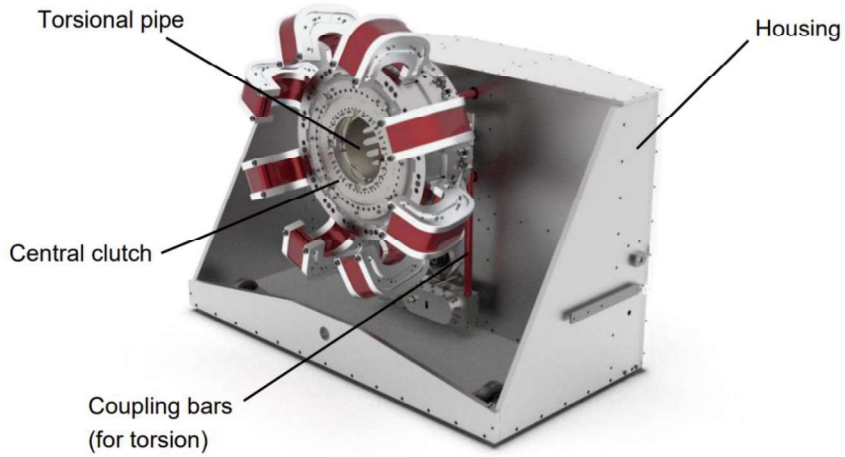

Fig. 2 The elastic decoupling systems of the Prisma SinusJet Gen 3.0 testbed

Fig. 3 shows the machine in its final form as it has been completed in December 2021.

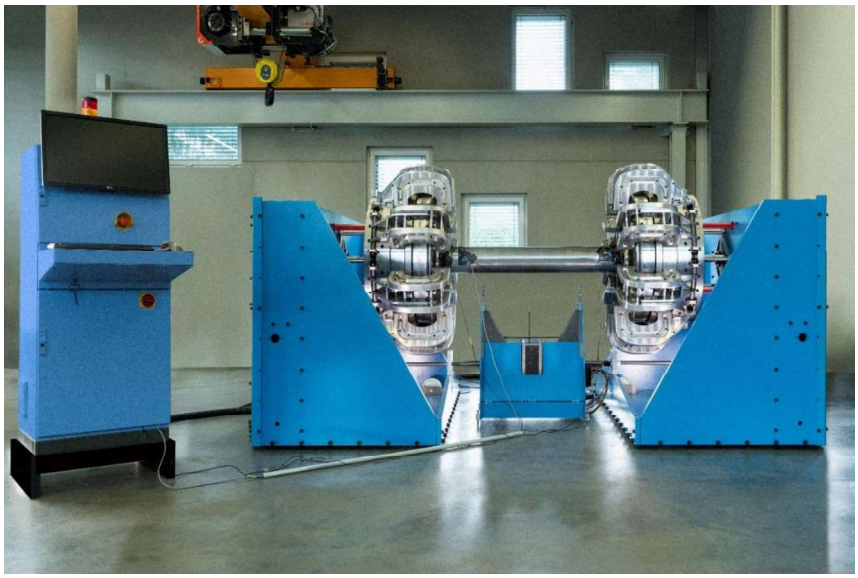

Fig. 3 The final product with a sample wheelset and the electrical control unit (left)

1.2 Testing capabilities

From the specification side, Prisma SinusJet Gen 3.0 has been designed to have many unique qualities compared to the current wheelset testbeds mentioned in the standards e.g. EN 13261 [3].

First and foremost, the four-actuator setup (two for bending and two for torsion) and the hanging support of the test piece make SinusJet capable of testing both sides of an axle without the need to re-configurate and set up the sample and start the whole analysis again from the beginning. Thanks to the higher testing frequencies (see Table 1) the testing duration of such tests can be reduced by an additional factor of 2-3, making the Gen 3.0 testbed approximately 4 times faster than any other test rig operating in the usual 15-28 Hz frequency range. This makes it possible to validate new wheelset materials and concepts in a shorter timeframe, thus reducing the necessary development time [7].

Technical parameter	**Value**
Applicable wheel tread diameter	Max. 1.250 mm
Overall frequency range of tests	40 – 60 Hz
Ideal frequency range for bending	50 – 60 Hz
Ideal frequency range for torsion	40 – 50 Hz
Max. bending angle of the axle	±1,0°
Max. torsional angle of the axle	±0,3°

Table 1 Testing limits of the Prisma SinusJet Gen 3.0 testbed

One of the biggest benefits however is the range of feasible tests: apart from the standard bending tests required by the EN standards, non-standard torsional tests as well as combined bending and torsional tests can also be performed with the machine, which all are essential in the evaluation of crack propagation, wheel seat fretting and operational durability scenarios.

The features of the Prisma SinusJet Gen. 3.0 testbed:

- Testing for bending with different bending moment introductions:
  - 2-point bending (bending load introduced through the wheel)
  - 4-point bending (bending load introduced partially through the wheel and the axle journal)
- Testing for torsion
- Testing for combinative bending and torsion
- Variable load sequences
- Crack propagation evaluation
- Fretting examination in the wheel seat
- Operational durability scenarios with different load cycles

2 FIRST EXPERIENCES

The following test reports are based on acceptance tests to examine the testing performance of the Prisma SinusJet Gen 3.0 testbed.

2.1 Measurement set-up

As a first step in the evaluation process, a fitting measurement system had to be set up. In order to achieve that, the following factors were chosen as benchmarks to determine the quality of the results:

- Left and right symmetry of the load distribution, using a symmetric axle as test piece
- Circumferential symmetry of the load distribution („roundness" of the stress results over the axle central diameter)

For the left and right symmetry, the system was simple: 5 full-bridge strain gauges were symmetrically distributed along cross sections that have been chosen as measuring positions (POS1-5), with the first position being exactly in the middle of the axle and acting as the regulatory plane for the control of the testbed. Fig. 4 shows the schematic of the measuring planes, including the 2 additional positions in the transition zones from shaft to the wheelseats (these planes were chosen according to the EN 13260 standard to define the exact load levels in the critical cross section).

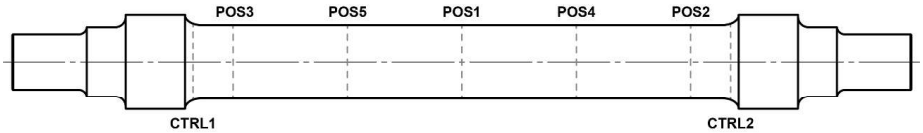

Fig. 4 Position of the measuring planes (POS1-5)

After the selection of the appropriate measuring planes, the number of strain gauges had to be determined. To evaluate the circumferential symmetry of the operational load, POS2 and POS3 had been fitted with 10 linear strain gauges (in addition to the already installed full-bridge strain gauge) to obtain more data over the circumference, thus providing a precise overview of the dynamic load distribution in the wheelset axle. Fig. 5 shows the angular distribution of the 12 measuring points at POS2 and POS3.

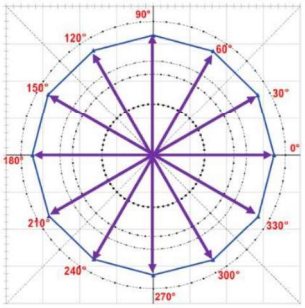

Fig. 5 Angular distribution of the strain gauges at POS2 and POS3

As mentioned, the electrical control of the testbed is done by monitoring the amplitude stresses at the critical cross section (namely at the basket curves). In compliance with the EN 13260 standard, this amplitude stress serves as the nominal dynamic stress in the shaft [2].

2.2 Initial results

The first analyses had been conducted with the so-called *4-point bending* load case. This load case is a simple bending load case where the bending load is partially introduced

through the wheel as well as through the journal area of the axle. For this purpose, a sample wheelset was used to complete the tests. This particular wheelset had initially been used in other tests before, where it had been subject to additional preliminary machining.

Altogether 6 test runs were done using this set-up. The first in line was a test with the wheelset without dynamic balancing or additional weights used to decrease its natural bending frequency. The second test already included dynamic balancing to compensate the loss of inertia caused by the asymmetric preliminary machining of the wheels from the preceding tests. Tests 3-6 all included the aforementioned balancing in addition to a pair of additional weights to reduce the bending frequency of the wheelset.

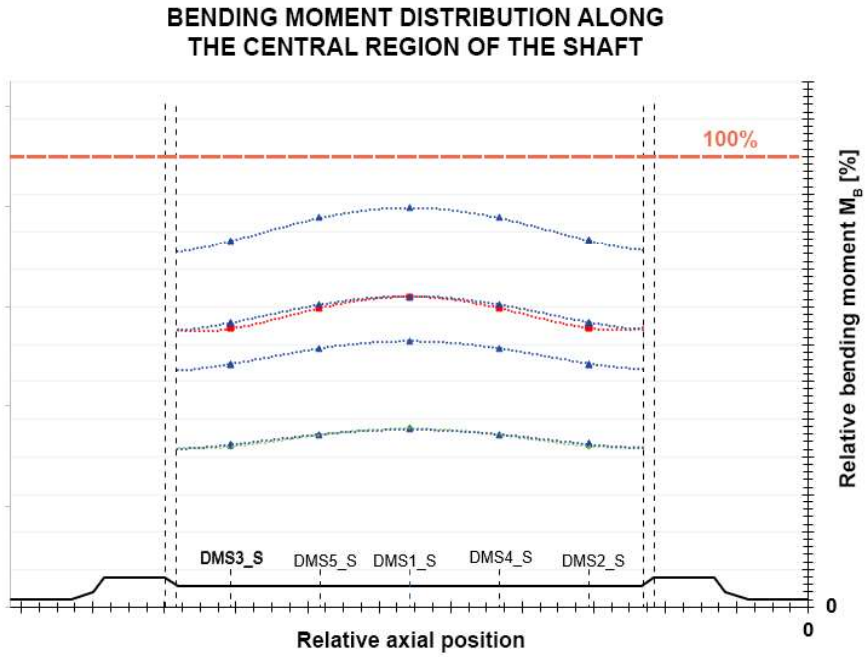

Fig. 6 Bending moment distribution and left-right symmetry along the shaft

As it is pictured on Fig. 6 the distribution of the bending moment shows a symmetric, although slightly uneven trend. The uneven behaviour of the distribution (namely the peaks in the middle of the shaft) seems to get stronger with the nominal bending moment, typically up to +10%. This effect is rooted in the dynamic behaviour of the vibrating wheelset: the higher the dynamic load magnification (and therefore the bending moment), the more significant the vibration of the unsupported mass located in the centre of the shaft is (this corresponds to the results of other relevant references, such as [8]). However, the left-right symmetry shows especially good results, with a typical stress deviation of ≤0,3% between the opposite measuring point (POS2-3, POS4-5).

The circumferential symmetry of the moment distribution also provided similarly promising results: apart from the dynamically unbalanced first test run (see the visibly elliptical curve on Fig. 7), tests 2-6 show less than 2% deviation in the bending moments along the circumference.

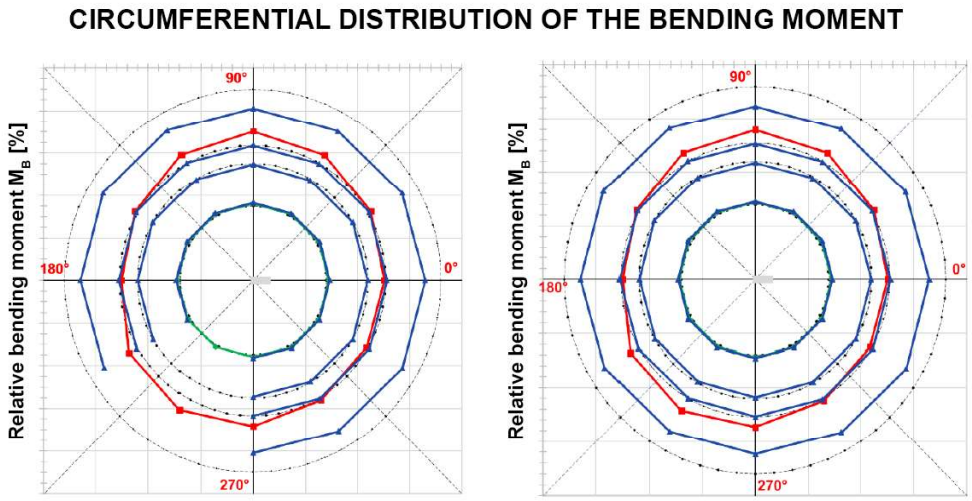

Fig. 7 Circumferential distribution of the bending moment (POS2 and POS3)

After the preliminary investigations with 4-point bending, a similar set of tests had also been conducted using the *2-point bending* set-up: in this load case the complete bending load is introduced through the wheels without radial support on the bearing areas. Leaving the radial support out of the set-up means the wheels are subject to much higher bending stresses than normal, leading to a rather conservative load scenario. (Most testbeds on the market provide this kind of load introduction, therefore requiring custom – stiffer – test wheels rather than the production ones.)

Impressively, the 2-point bending investigations provided almost as good results as the tests with 4-point bending: the left-right symmetry showed nearly perfect distributions on the two sides, resulting in a deviation of a mere ≤0,2% between the opposite measuring point (POS2-3, POS4-5). As for the circumferential distribution, the discrepancy increased from an average of 2% to 5%, which clearly shows that this set-up is more sensitive to the machining and assembly tolerances than the 4-point bending.

2.3 Testing for torsion and combinative load cases

Following the preliminary bending evaluations, two sets of additional test runs had been done: the first set only with torsion and the second with torsion and 4-point bending at the same time.

The purpose of the torsional test was to determine the exact torsional frequency, which was required for the combinative load case. Since torsional load is an axisymmetric load, no further tests were required since the symmetrical conditions had been met.

The combinative load case on the other hand represents a more challenging problem: since both torsion and bending are present, an equivalent stress has to be calculated to obtain a reliable output. The calculation of the equivalent stress can be calculated according to the EN 13103-1 standard [4]:

$$\sigma_V = \sigma_1 - \sigma_2 = \sqrt{(\sigma_n)^2 - 4(\sigma_t)^2} \quad (1)$$

where σ_n represents the bending stress and σ_t represents the torsional stress.

In addition to the necessary calculation of the equivalent stress, the phase shift between the two eigenforms (bending and torsion) must be considered. However, due to the different eigenfrequencies, this phase shift is not constant. Since the two eigenmodes are acting in two different dynamic planes, the test bench may be used to validate multiaxial damage criteria as well.

As for the results, the combinative load case showed comparable behaviour to the original 4-point bending load case without significant deviations in the symmetry or in the circumferential distribution.

3 CONCLUDING REMARKS AND FUTURE OUTLOOK

The design and delivery of the SinusJet testbed has been a long and challenging task but it has also paved the way for many exciting research projects for the years to come.

For the time being, the current industrial standards only consider bending as the primary quality factor when it comes to wheelset durability, even though torsional and combinative load cases all present real-life challenges during the development phase. Being able to consider these problems before a new prototype goes into production means an obvious economic and strategic advantage over the "classic" R&D approach.

As we can see from the first tests, the current (3rd) generation of SinusJet performs admirably: with a deviation in symmetry of just 0,3% the testbed already outperforms the market leaders by allowing simultaneous testing of both ends of the axle. Combined with the overall good circumferential symmetry as well as with the high testing frequency, the machine brings a great addition to the dynamic testing field. Finally, the aforementioned extra possibilities (torsion and combination of torsion and bending) make it a potentially ideal device for every wheelset designer and manufacturer in this field.

As for the future outlook, further tests are being (and will be) conducted on the machine to investigate current production-ready wheelsets as well as prototypes with the new load cases including possible evaluations for crack propagation and for fretting. The long-distance target is to shift the physical evaluations to the principal development stage as much as possible.

The development of the testbed is however not done. Based on the primary results the effect of the bending peaks is yet to be addressed further and the possibility for a second servo motor to independently control the torsional excitation will be investigated (the current testbed runs only with one servo motor using a mechanical belt drive to activate the combined load case). This obviously increases the power requirement from the current maximum of 10 kW but it also makes the test rig more flexible when it comes to field use.

All in all, the Prisma SinusJet Gen 3.0 has a great potential based on the primary tests and the full range of possibilities is yet to be investigated in future projects such as this.

4 REFERENCES

[1] Eisenbahnfahrwerke 3 (EBFW3) – Probabilistic Fracture Mechanical Concept for the Assessment of Railway Wheelsets. International Research Project, 2014.

[2] EN 13260 Railway applications – Wheelsets and bogies – Wheelsets – Product requirements.

[3] EN 13261 Railway applications – Wheelsets and bogies – Axles – Product requirements.

[4] EN 13103-1 Railway applications – Wheelsets and bogies – Part 1: Design method for axles with external journals.

[5] EURAXLES: Minimizing the risk of fatigue failure of railway axles. Final project report, 2014.

[6] Foletti, S. et al: Experiments on crack propagation and threshold at defects in press-fits of railway axles. Procedia Structural Integrity, Vol. 7, 2017, p. 484–491.

[7] Rieger, M. et al: Fatigue crack growth in full-scale railway axles – Influence of secondary stresses and load sequence effects. International Journal of Fatigue, Vol. 132, 2020.

[8] Traupe, M. – Meinen, H. – Zenner, H.: Sichere und wirtschaftliche Auslegung von Eisenbahnfahrwerken. Abschlussbericht, Band I – Hauptteil, 2004, p. 101–110.

EXPERIMENTAL INVESTIGATION ON THE FORMATION OF RAILWAY WHEEL POLYGONIZATION

Pascal GIL, Martin RAKOWITSCH and Christian SCHINDLER

Chair and Institute for Rail Vehicles and Transport Systems
RWTH Aachen University
Seffenter Weg 8, 52074 Aachen, Germany

Received: August 5, 2022

ABSTRACT

Polygonization in railway wheels is the periodic out-of-roundness caused by uneven tread wear. It affects several types of rail vehicles including high-speed trains and it impedes both ride comfort and safety. The current countermeasure to correct polygonization by re-profiling leads to high annual costs and reduces wheelsets' service life. Therefore, it is desirable to obtain a better understanding of the underlying polygonization formation mechanisms. Previous investigations have predominantly used simulation software to analyze the root causes of polygonization. To provide an experimental verification, a scaled test rig was built at the Institute for Rail Vehicles and Transport Systems (IFS), RWTH Aachen University, Germany. The test rig is equipped with a roller of 50 mm diameter, representing the railway wheel, and a disc of 670 mm diameter, representing the rail. The wheel normal load, which is applied using a coil spring, is chosen in a way that the stresses in the contact patch resemble the stress condition of the real wheel-rail contact. In addition, the test rig contains two motors, one that is used to drive the disc and the other to apply a continuously oscillating angle of attack to the roller. With this configuration, the test rig has the ability to imitate the natural bending vibration of a real wheelset. In the course of the first trials, the test rig was evidently able to generate polygonization with a significant wear depth within a short period of time. The experimental setup offers a wide range of possibilities for the variation of parameters that influence polygonization. For example, by changing the ratio of the rotational speeds of the motors, different polygonization orders can be generated. This paper illustrates the design and the functioning of the polygonization test rig and presents the first test results.

Keywords: wheel-rail contact, railway wheel polygonization

1 INTRODUCTION

Polygonization is a periodic out-of-roundness with a varying wear depth over the wheel circumference. It occurs in railway vehicles of various designs, but especially in high-speed trains, and reduces ride comfort and safety.

During operation, polygonization leads to fluctuations in the normal force of the wheel. The exposure to the generated vibration causes damage to critical vehicle parts such as the wheelset, the axle bearing housings or the coil springs [1]. Not only rail vehicles, but also the railway infrastructure is affected by polygonization. Due to vibration caused by polygonization, the trackway faces accelerations of up to 250 m/s^2 [2]. As a result, damage to rail fastening systems or, especially at low ambient temperatures, rail fractures may occur [3].

Besides the impact on safety, the excitation of the rail vehicle by out-of-round wheels leads to further negative effects which are directly perceptible to the passenger. Polygonization causes vibrations of railway vehicle components and increases the noise exposure of passengers measurably [4].

To comply with the standardized requirements for operational safety, re-profiling on wheel lathes is necessary at short maintenance intervals. This is unfavorable for railway

vehicle operators in many aspects: Additional maintenance ties up workshop personnel while the affected vehicles are not available for revenue service. Moreover, each wheel re-profiling leads to a removal of tread material until the wear limit is exceeded and a replacement of the wheelset becomes necessary.

Because of these negative effects of polygonization, it seems appropriate to gain a better understanding of its formation mechanisms. Today, the most widespread assumption is that natural vibrations within the rail vehicle or in the interaction between wheel and rail are the root cause of the occurrence of polygonization. Natural bending or torsional eigenmodes of the wheelset, for example, cause lateral slip in the wheel-rail contact point which leads to polygonal wear.

The formation mechanisms of polygonization have already been investigated by several researchers conducting simulations or field tests [1]. Experiments on test rigs, on the other hand, were rarely carried out. Mädler [5] and Wu [6] were able to generate polygonization on full-scale single-axle roller test rigs. Experiments on full-scale test rigs, however, suffer from the disadvantage of long test durations, high costs, and fixed excitation frequencies. Therefore, at the Institute for Rail Vehicles and Transport Systems of RWTH Aachen University, a scaled test rig for the investigation of polygonization formation mechanisms has been designed and constructed.

2 EXPERIMENTAL SETUP

The test setup realized at the Institute of Rail Vehicles is capable of freely selecting driving speed while simulating any excitation frequencies. Fig. 1 shows a rendering of the test rig. Fig. 2 shows a photograph of the setup. The main parts are a drive disc of 670 mm diameter, representing the rail, and a small disc of 50 mm diameter, representing the wheel. The drive disc has been made from a former light rail vehicle wheel provided by the light rail operator from the city of Stuttgart. It is connected to a 75 kW three-phase induction motor which can accelerate the drive disc up to a circumferential velocity of 100 km/h. For the polygonization experiments, however, it is not planned to exceed a speed of 15 km/h.

The wheel is connected to an excitation mechanism that is able to impose a yaw movement on wheel, wheel holder, and support arm. The propulsion of the excitation mechanism is realized by another, far smaller motor: A brushed 0.25 kW DC motor actuated by a separate motor controller connected to an Arduino microcontroller board. This DC motor drives a timing belt which powers a flywheel. The flywheel is necessary to ensure a constant operating speed without any speed fluctuations. As the transmission ratio of the timing belt is 1:1, DC motor and flywheel always have the same angular frequency.

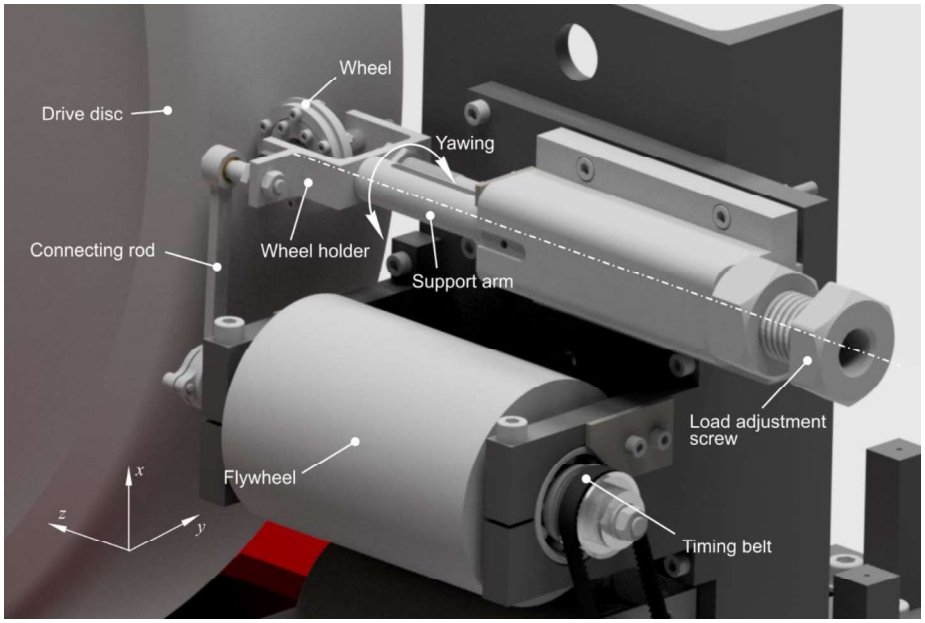

Fig. 1: Test rig being developed at IFS, based on [7]

On the shaft of the flywheel facing away from the timing belt, a connecting rod is mounted. The connecting rod directly links the flywheel to the wheel holder. With this mechanism, a yaw movement of the wheel is enforced whenever the DC motor is operating.

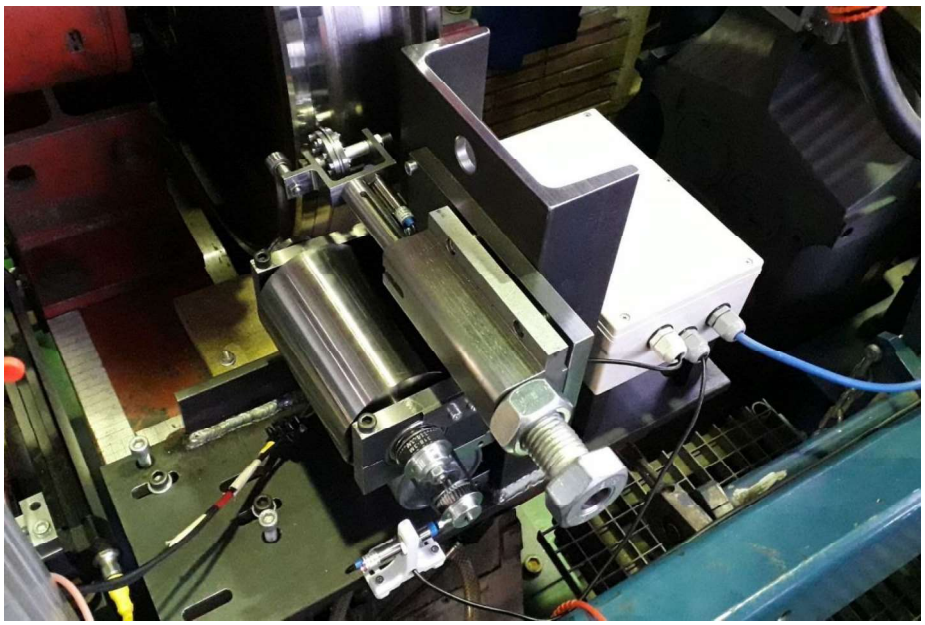

Fig. 2: Photograph of the test rig

As induction motor and DC motor are completely separated from each other, the ratio between excitation frequency and drive disc speed can be varied to any extent. Inductive sensors measure the speeds of specimen wheel and DC motor and provide their information to a closed loop PI controller running on the Arduino board. Therefore, a constant speed ratio between specimen wheel and drive disc is ensured.

To provide realistic operating conditions, a wheel load needs to be applied. This task is fulfilled by a coil spring acting on the support arm. A load adjustment screw helps the operator to vary the normal load on the specimen wheel.

3 WEAR DEPTH ESTIMATION

To investigate the general applicability of the presented test bench concept, a wear depth estimation shall be conducted. The test rig can only be beneficial for research on polygonization if the generated wear depth is high enough to be measured reliably with reasonable effort. A common dial gauge, for example, is capable to conduct measurements with a resolution of 1 µm. Therefore, the mean wear depth of the polygonised specimen wheel should at least reach an order of magnitude of 10 µm. If polygonization is assumed to be the only occurring wear pattern, for a mean wear depth of 10 µm, the difference between maximum and minimum radius deviation is 20 µm.

The first step of the wear depth estimation is to choose an approach to calculate the expected wear rate. In this paper, the approach of Krause and Poll described by Zobory [8] is being used. If $\dot{m}$ is the wear rate, k^* the wear coefficient and $P(t)$ the friction power, it applies:

$$\dot{m} = k^* \cdot P(t) \tag{1}$$

In the wheel-rail contact, friction can occur due to different reasons. According to [9], longitudinal adhesion force T_x, lateral adhesion force T_y and spin moment M_φ are present in the contact patch. The general equation for the friction power is:

$$P(t) = w_x(t) \cdot T_x + w_y(t) \cdot T_y + \omega_\varphi(t) \cdot M_\varphi \tag{2}$$

In eq. 2, w_x and w_y denote the relative velocities between wheel and rail in longitudinal and lateral direction, while ω_φ denotes the spin slip.

Due to the test rig concept, the lateral adhesion force is decisive for the wear development. Consequently, longitudinal adhesion force and spin moment can be neglected. Therefore, eq. 2 can be simplified:

$$P(t) = w_y(t) \cdot T_y \tag{3}$$

The lateral adhesion force T_y of a cylindrical wheel profile depends on the adhesion coefficient f_y and the wheel normal load Q:

$$T_y = f_y \cdot Q \tag{4}$$

The relative velocity $w_y(t)$ is dependent on the longitudinal speed v_x and the angle of attack $\alpha(t)$:

$$w_y(t) = v_x \cdot \sin(\alpha(t)) \tag{5}$$

In the present test rig, the angle of attack continuously varies due to the yaw movement of wheel holder and support arm. The angular velocity of the excitation mechanism is from now on denoted as ω_e in order to distinguish it from the angular velocity of the specimen wheel. Using ω_e, the angle of attack can be described as:

$$\alpha(t) = \alpha_{max} \cdot \sin(\omega_e t) \tag{6}$$

Inserting eq. 4, eq. 5, and eq. 6 into eq. 3 yields:

$$P(t) = f_y \cdot Q \cdot v_x \cdot |\sin(\alpha_{max} \cdot \sin(\omega_e t))| \tag{7}$$

A sine function can take values from +1 to -1, but the friction power always has a positive value. Therefore, the absolute value of the sine function is used. The small angle approximation $sin\varphi \approx \varphi$, which leads to good results for $\varphi < 10°$, helps to simplify eq. 7:

$$P(t) = f_y \cdot Q \cdot v_x \cdot \alpha_{max} \cdot |\sin(\omega_e t)| = P_{max} \cdot |\sin(\omega_e t)| \tag{8}$$

In eq. 8, P_{max} denotes the friction power at the moment when the angle of attack reaches its maximum value.

$$P_{max} = f_y \cdot Q \cdot v_x \cdot \alpha_{max} \tag{9}$$

The wear rate from eq. 1 can be determined by multiplying the mass of removed material Δm during one period of vibration by the frequency f_e of the excitation mechanism:

$$\dot{m} = f_e \cdot \Delta m = \frac{\omega_e}{2\pi} \cdot \int_0^{T_e} k^*(t) \cdot P_{max} \cdot |\sin(\omega_e t)| \; dt \tag{10}$$

During one excitation period, the wheel holder yaws to the left and to the right side. Each of these yaw movements consists of back-and-forth movement. Therefore, one excitation period can be split into four different parts. The absolute values of the integrals are equal for each of these parts. Consequently, it is possible to modify eq. 10 performing an adjustment of the integration limits:

$$\dot{m} = 4 \cdot \frac{\omega_e}{2\pi} \cdot P_{max} \cdot \int_0^{\frac{T_e}{4}} k^*(t) \cdot \sin(\omega_e t) \; dt \tag{11}$$

According to [8], the wear coefficient k^* assumes different values dependent on the current friction power. Below a fixed limit friction power P_{lim}, mild wear occurs. Above this value, severe wear is present.

$$k^* = \begin{cases} k_m^* = 6 \cdot 10^{-10} \dfrac{kg}{Nm}, & P < P_{lim} = 4 \cdot 10^6 \dfrac{W}{m^2} \cdot A \\ k_s^* = 22 \cdot 10^{-10} \dfrac{kg}{Nm}, & P \geq P_{lim} = 4 \cdot 10^6 \dfrac{W}{m^2} \cdot A \end{cases} \tag{12}$$

During the yaw movement of the wheel, the angle of attack changes continuously. For small angles, the friction power assumes a value below the limit and the wear coefficient for mild wear must be applied. Large angles of attack lead to an excess of the friction power limit causing severe wear. At the time t_{lim}, the instantaneous friction power equals the friction power limit. The integral from eq. 11 can now be transformed into a

sum consisting of one integral for the section of mild wear and one integral for the section of severe wear:

$$\dot{m} = 2 \cdot \frac{\omega_e}{\pi} \cdot P_{max} \left(\int_0^{t_{lim}} k_m^* \cdot \sin(\omega_e t)\ dt + \int_{t_1}^{\frac{T_e}{4}} k_s^* \cdot \sin(\omega_e t)\ dt \right) \tag{13}$$

Now, the time point t_{lim} shall be determined. After inserting $t = t_{lim}$ and $P_{\mathrm{lim}} = P(t_{lim})$, eq. 8 can be rearranged as follows:

$$t_{\mathrm{lim}} = \frac{1}{\omega_e} \cdot \arcsin\left(\frac{P_{lim}}{P_{max}}\right) \tag{14}$$

In eq. 14, ω_e, P_{lim} and P_{max} are still unknown and need to be determined. The excitation frequency depends on the desired order of polygonization n_P, the chosen test bench longitudinal velocity v_x and the wheel diameter d_{wheel}. For a polygonization of 3rd order and a longitudinal velocity of 8 km/h, it applies:

$$\omega_e = \frac{n_p \cdot v_x}{d_{wheel}} = \frac{3 \cdot \frac{8}{3.6}\frac{m}{s}}{0.05\ m} = 133.3\ s^{-1} \tag{15}$$

To determine P_{lim}, knowledge of the contact patch is necessary. The size of the contact patch can be estimated using the Hertzian theory of contact. With a normal force of $Q = 141\ N$ applied by the coil spring, the contact patch has an area of $A = 0{,}45 \cdot 10^{-6}\ m^2$. This value can be inserted into eq. 12:

$$P_{lim} = 4 \cdot 10^6 \frac{W}{m^2} \cdot 0.45 \cdot 10^{-6}\ m^2 = 1.8\ W \tag{16}$$

Using eq. 9, the calculation of P_{max} can be performed easily. For this reason, a realistic value of the friction coefficient f_y has to be assumed. As the test rig is located in the institute's indoor testing facility, the friction coefficient for dry rails, $f_y = 0.35$, is being chosen. The maximum angle of attack was set to $\alpha_{max} = 5°$during the design period of the test rig. It applies:

$$P_{max} = 0.35 \cdot 141\ N \cdot \frac{8}{3.6}\frac{m}{s} \cdot 5° \cdot \frac{2\pi}{360°} = 9.57\ W \tag{17}$$

Inserting eq. 15, eq. 16 and eq. 17 into eq. 14 yields:

$$t_{lim} = \frac{1}{133.3\ s^{-1}} \cdot \arcsin\left(\frac{1.8\ W}{9.57\ W}\right) = 1.419\ ms \tag{18}$$

The last value to be determined is the upper integration limit from eq. 13:

$$\frac{T_e}{4} = \frac{\frac{2\pi}{\omega_e}}{4} = 11.78\ ms \tag{19}$$

Now, all necessary parameters to perform the integration of eq. 13 are known. First, the integral for mild wear is being solved:

$$\int_0^{1.419 \cdot 10^{-3} s} 6 \cdot 10^{-10} \frac{kg}{Nm} \cdot \sin(133.3\ s^{-1} \cdot t)\ dt = 8.03 \cdot 10^{-14} \frac{kg \cdot s}{Nm} \tag{20}$$

Afterwards, the procedure is repeated with the integral for severe wear:

$$\int_{1.419\cdot10^{-3}s}^{11.78\cdot10^{-3}s} 22\cdot10^{-10}\frac{kg}{Nm}\cdot\sin(133.3\,s^{-1}\cdot t)\;dt = 1.62\cdot10^{-11}\frac{kg\cdot s}{Nm} \tag{21}$$

It is noticeable that the contribution of mild wear, which occurs at low angles of attack, is negligibly small compared to the amount of severe wear, which occurs at high angles of attack. Therefore, the influence of mild wear can be neglected during the further calculation. With the help of eq. 13, the wear rate calculation is being conducted:

$$\dot{m} = 2\cdot\frac{133.3\,s^{-1}}{\pi}\cdot 9.57\,W\cdot\left(1.62\cdot10^{-11}\frac{kg\cdot s}{Nm}\right) = 1.32\cdot10^{-8}\frac{kg}{s} \tag{22}$$

Assuming that the calculated wear rate remains constant over the entire test period, the following applies:

$$\dot{m} = \frac{\Delta m}{\Delta t} = \rho\cdot\frac{\Delta V}{\Delta t} = \rho\cdot\frac{\pi\cdot\left(r_R^2-\left(r_R-\bar{h}\right)^2\right)\cdot b}{\Delta t} \tag{23}$$

In eq. 23, Δt denotes the experiment duration, ΔV the wear volume, ρ the density of steel, r_R the wheel radius, $\bar{h}$ the mean wear depth, and b the wheel profile width. For the assumption of the mean wear depth, eq. 23 has to be rearranged as follows:

$$\bar{h} = r_R - \sqrt{r_R^2 - \frac{\dot{m}\cdot t_V}{\rho\cdot\pi\cdot b}} \tag{24}$$

The following values can be inserted into eq. 24:

- Wheel radius $r_R = 0.025\,m$
- Wear rate $\dot{m} = 1.32\cdot10^{-8}\frac{kg}{s}$
- Experiment duration $\Delta t = 2400\,s$
- Density of steel $\rho = 7.8\frac{g}{cm^2}$
- Wheel profile width $b = 1.5\cdot10^{-3}\,m$

As a result, the estimation of the mean wear depth of the polygonised wheel is:

$$\bar{h} = 0.025\,m - \sqrt{(0.025\,m)^2 - \frac{1.32\cdot10^{-8}\frac{kg}{s}\cdot 2400\,s}{7800\frac{kg}{m^3}\cdot\pi\cdot1.5\cdot10^{-3}m}} = 17.2\,\mu m \tag{25}$$

The estimated mean wear depth assumes a value of 17.2 µm. This is a sufficient wear depth to be measured by a dial gauge. Therefore, the experimental validation of the test bench concept has been conducted.

4 RESULTS

For the validation of the test rig concept, in addition to the experiments already presented in [7], six measurements have been conducted. All experiments were conducted with a wheel load of 141 N and a control loop aiming to generate polygonization of 3rd order. The parameters which were varied are shown in Tab 1. In the last column, the resulting wear depth of each experiment is indicated.

Tab. 1: Experiment data

Experiment no.	Initial wheel diameter	Experiment duration	Operating speed	Generated mean wear depth
1	50.002 mm	1200 s	3 km/h	20 µm
2	49.967 mm	2400 s	3 km/h	55 µm
3	49.984 mm	3600 s	3 km/h	132 µm
4	49.972 mm	3600 s	8 km/h	358 µm
5	49.999 mm	2400 s	8 km/h	426 µm
6	50.001 mm	1200 s	8 km/h	96 µm

The measurements of the specimen wheels after the experiments are shown in Fig. 3 and 4. For experiment 5, it can be observed that a significant polygonization with dominating 6th and 7th has been generated. This is also clearly visible in the polar plot, which shows the deviation from the mean radius. As already stated in [7], the desired order could not be reached. For the other experiments, i.e. 1 to 4 and 6, the goal of polygonization has not been achieved. This result has to be seen in contradiction to [7], where the specimen wheels could be reliably polygonized. The reason for this is not clear so far.

Fig. 3 indicates with significant values for the first order that the test wheels are eccentric after the experiments. However, this cannot be said with certainty, since another likely cause is the eccentric clamping of the wheels during measurement.

In all tests, a notable decrease of the wheel radius could be observed. Fig. 4 shows the difference between the initial radius before the experiment and the mean radius after the experiment. It is obvious that all measurements exceed the estimated mean wear depth by far. A possible reason is the usage of free-cutting steel for the specimen wheels instead of using steel for railway wheel applications. The high shear stresses in the contact patch were leading to an occurrence of plastic deformation instead of abrasive wear. A significant burr at the tread edge, shown in Fig. 5, supports this theory.

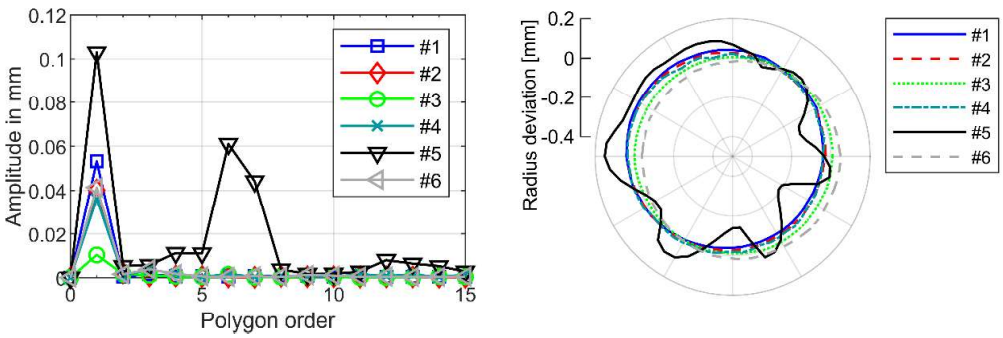

(a) (b)

Fig. 3: Radius deviation from mean radius after experiments, (a) Fourier transform revealing the order amplitudes, (b) Exaggerated out-of-roundness

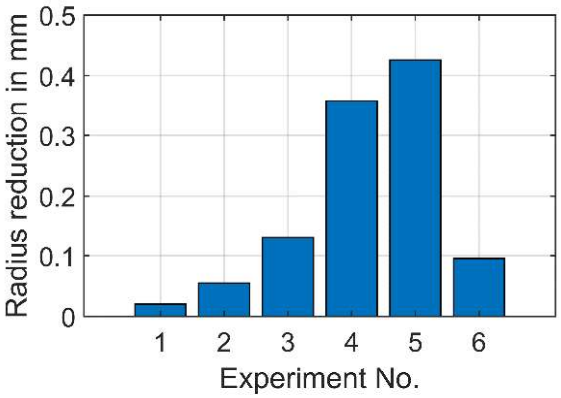

Fig. 4: Mean radius reduction of each test wheel

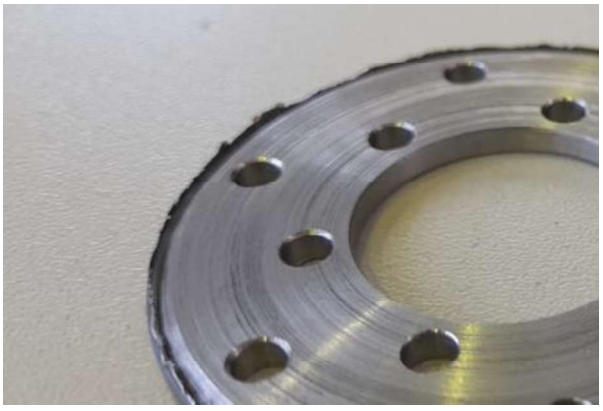

Fig. 5: Burr at tread edge

5 CONCLUSION

Polygonization is a severe issue in railway operation as it reduces the ride comfort of railway vehicles and poses a risk to safety. Therefore, an in-depth understanding of the formation mechanisms of polygonization is necessary. Investigations with test rigs can play an important role in solving this task.

The small-scale test rig designed and built at the Institute for Rail Vehicles and Transport Systems is able to generate a significant wear depth within a short period of time. It is also feasible to generate polygonization, however, the order of the wheel polygonization does not yet meet the expectations. Moreover, currently there are no reliable estimations possible in which of the experiments polygonization will be created.

To face this issues, further investigations on the small-scale test rig are already planned. The usage of steel grades used for railway wheels could lead to more realistic results regarding the mean wear depth. The reliability of the polygonization generation could be improved by an optimized control algorithm running on the Arduino microcontroller.

6 REFERENCES

[1] Tao, G. - Wen, Z. - Jin, X. - Yang, X.: Polygonisation of Railway Wheels: A Critical Review. Railway Engineering Science, 28, 2020, p. 317–345.

[2] Schubert, S.: Technischer Bericht über das Vorhaben TV 9410: Unrundheiten und Abhilfemaßnahmen bei Eisenbahnrädern. Forschungs- und Technologie-Zentrum Minden der Deutschen Bahn AG, 1997.

[3] Nielsen, J. - Johansson, A.: Out-of-round railway wheels - a literature survey. Proceedings of the Institution of Mechanical Engineers, Part F: Journal of Rail and Rapid Transit, 12, 2000, p. 79–91.

[4] Cai, W. - Chi, M. - Wu, X. - Li, F. - Wen, Z. - Liang, S. - Jin, X.: Experimental and numerical analysis of the polygonal wear of high-speed trains, Wear, 440-441, 2019.

[5] Mädler, K. - Bannasch, M.: Werkstoffeinsatz in Schienenfahrzeugrädern: Alternativen und Grenzen. ZEVrail, 130, 2006, p. 428–435.

[6] Wu, Y. - Wang, J. - Liu, M. - Jin, X. - Hu, X. - Xiao, X. - Wen, Z.: Polygonal wear mechanism of high-speed wheels based on full-size wheel-rail roller test rig, Wear, 494-495, 2022.

[7] Rakowitsch, M. – Gil, P. – Schindler, C.: Experiments on Polygonization of Railway Wheels based on a Small-Scale Test Rig. Proceedings of the Fifth International Conference on Railway Technology, Railways 2022, Montpellier, France.

[8] Zobory, I.: Prediction of Wheel/Rail Profile Wear. Vehicle System Dynamics, 28, 1997, p. 221-259.

[9] Schindler, C.: Handbuch Schienenfahrzeuge: Entwicklung, Produktion, Instandhaltung. Eurailpress, Hamburg 2014.

INVESTIGATION OF THE PRESSING PROCESS OF RAILWAY WHEELS USING PHOTOSTRESS ANYLYSIS

Lajos BORBÁS* and Péter FICZERE**

*2800 Tatabánya, Stúdium tér 1., borbas.lajos@edutus.hu
**1111 Budapest, Műegyetem rkp. 3., ficzere.peter@kjk.bme.hu

Received: August 5. 2022

ABSTRACT

In most cases, the connection of railway wheels to the axles is realized by pressing procedure. After the pressing procedure, lateral beating of the wheels may occur, which affects the accuracy of the running of the rim. The main goal of our investigation was to control the surface deformation of the wheel-pair during the pressing phase, and determine the size of the deformation using photo-elastic coating technique (Photo-stress analysis).

The task was to decide whether:

- the experimental method applied is suitable for the investigation of the surface deformation of railway wheels originating from pressing procedure,
- it is possible to measure differences between the pressing procedures of the two wheels based on the analysis of surface deformation,
- the surface deformation measured on the wheels can be connected to the measurement data of the axial failure of the wheels measured after the pressing procedure.

In case of the present investigation both wheel surfaces around the wheel hub (shaft/wheel connection) up to about 400 mm diameter was covered by photo-elastic coating material (optical sensor).

In case of the evaluation of the measurement results on railway wheels, fringe distributions were drawn together from recorded polarization pictures. Based on the fringe distribution we were able to calculate the principal strain differences on the outer surfaces of the wheels.

Keywords: railway wheels assembly, Photress analysis, interference fit

1 INTRODUCTION

The main goal of the investigation was to control and determine the surface deformation of the wheel-pair under the pressing procedure using photo-elastic coating technique (Photo-stress analyses).

The mounted railway wheel pair and the contact surface after the pressing procedure shown in Fig.1.

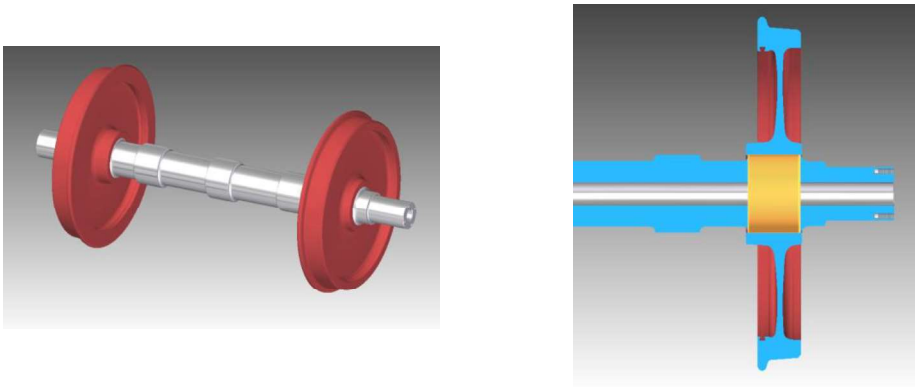

a) b)

Fig. 1. Mounted railway pair a), and the contact surface after the pressing procedure b)

Monitoring deformation and stress conditions during pressing procedure is extremely difficult task. Even for the most sophisticated finite element methods, we are facing still many, mostly unresolved issues.

2 INTERFERENCE FIT CALCULATION BASED ON CLASSICAL STRENGTH OF MECHANICS THEORY

The combined stress distribution in a shrink fit composite cylinder is made up of stress distribution in the inner and outer cylinders and this is shown in figure 2 below. [1]

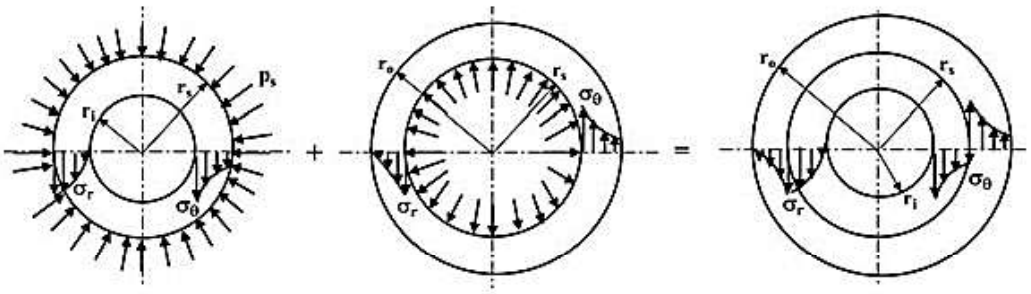

Fig. 2. The combined stress distribution in a shrink fit composite cylinder

Residual circumferential stress is maximum at r = ri for the inner cylinder and is given by equation 1:

$$\sigma_{\theta(max)}\Big|_{r=r_i} = -\frac{2p_s\ r_s^2}{r_s^2 - r_i^2} \tag{1}$$

Residual circumferential stress is maximum at $r = r_s$ for the inner cylinder and is given by equation 2:

$$\sigma_{\theta(max)}\Big|_{r=r_s} = -p_s\frac{r_0^2 + r_s^2}{r_0^2 - r_s^2} \tag{2}$$

Stresses due to fluid pressure must be superimposed on this to find the complete stress distribution.

In order to find the radial displacements of the cylinder walls at the contact area our consideration is shown in equation (3):

$$\varepsilon_\theta = \frac{u}{r} = \frac{1}{E}(\sigma_\theta - \nu\sigma_r)\ . \tag{3}$$

This gives the radial displacement of the inner wall of the outher cylinder as indicated in equation (4):

$$u_{r1} = \frac{p_s r_s}{E}\left[\frac{r_0^2 + r_s^2}{r_0^2 - r_s^2} + \nu\right] \tag{4}$$

Similar for the inner cylinder the radial and circumferential stresses at the other wall can be given by equation (5):

$$\begin{aligned}\sigma_r|_{r=r_s} &= -p_s \\ \sigma_0|_{r=r_s} &= -p_s\frac{r_s^2+r_i^2}{r_s^2-r_i^2}\end{aligned} \tag{5}$$

And following the above procedure the radial displacement of the contact surface of the inner cylinder is given by the equation (6):

$$u_{r2} = -\frac{p_s r_s}{E}\left[\frac{r_s^2 + r_i^2}{r_s^2 - r_i^2} - \nu\right] \tag{6}$$

The total interference is at the contact therefore given by equation (7):

$$\delta = -\frac{p_s r_s}{E}\left[\frac{r_0^2 + r_s^2}{r_0^2 - r_s^2} + \frac{r_s^2 + r_i^2}{r_s^2 - r_i^2} - \nu\right] \tag{7}$$

This gives the contact pressure in terms of the known variables as follows (equation (8)):

$$p_s = \frac{E\delta}{r_s\left[\frac{r_0^2 + r_s^2}{r_0^2 - r_s^2} + \frac{r_s^2 + r_i^2}{r_s^2 - r_i^2}\right]} \tag{8}$$

In the equations (1)…(8):

r_i: radius of the shaft,
r_s: radius of the shaft and wheel,
σ_0: tangential stress
σ_r: radial stresses
E: Material property, Modulus of Elasticity,
δ : total interference at the contact

The theory presented above gives us a picture of a static state, but it cannot reproduce the changes that occur during the pressing process.

3 POSSIBILITIES OF FINITE ELEMENT CALCULATION

The contact surface of the shaft/wheel connection – marked by in Fig 3. - is actually not a surface, but a cylindrical space, the overlap between the parts to be pressed.

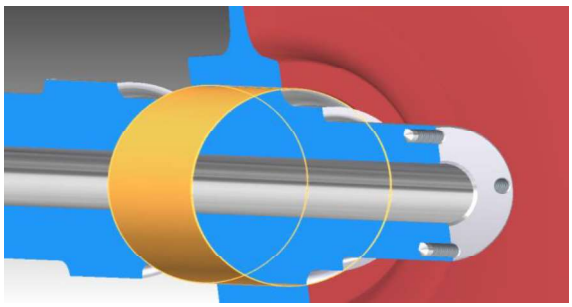

Fig. 3. The overlap between the parts to be pressed

It can be clearly observed that in numerical simulation, even for a large number of elements (small mesh size), the polygon effect appears, i.e., the geometry is only approximated by the mesh.

The possibility of exploiting cylinder symmetry is raised, whereby the problem could be solved with planar elements. Unfortunately, however, this solution has to be rejected

because, although the geometry is cylindrically symmetric, the load is not (C-shaped press tool).

The shaft and the mesh can be seen in Fig. 4.

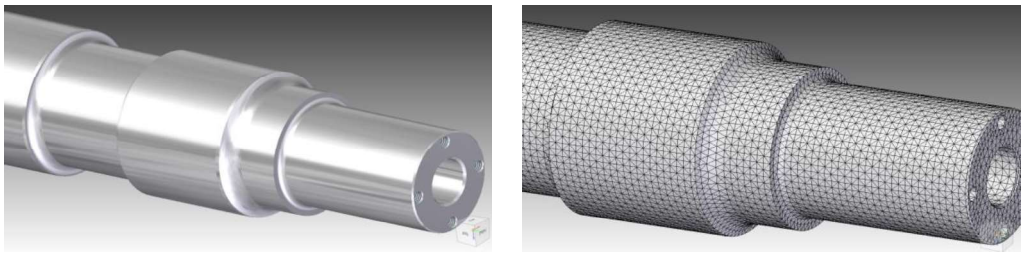

a) b)

Fig. 4. The shaft a), and the finite element generated mash b)

The assembled state with finite element mesh can be seen in Fig. 5. It can be clearly also observed in the figure that if the nodes do not fall in the same position relative to each other, then we do not expect cylindrical contact, but a line contact.

This results in much higher stress values, local peaks are created, which gives a false picture compared to the real stress distributions.

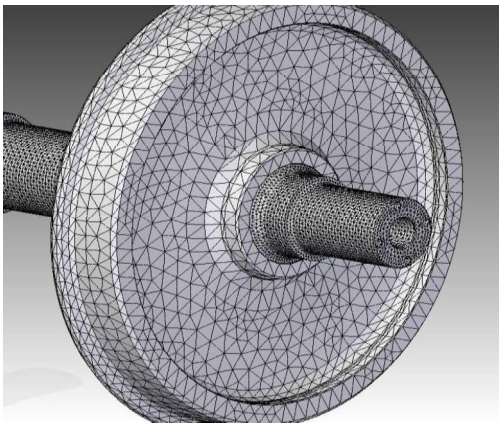

Fig. 5. The assembled state with finite element mesh

4 PHOTOSTRESS (PHOTOELASTIC COATING) INVESTIGATION

The measurement method used for the surface deformation and stress-state determination of the investigated specimen using optically active coating glued upon the surface and investigated in polarized light was supposed to be known [2].

In case of the present investigation both wheel surfaces around the wheel hub up to about 400 mm diameter was covered by photo-elastic coating. Some possibilities of the measurement method for investigation of machine elements can be found in more details in the literature attached [3], [4], [5], [6].

Railway wheels under test on the assembly table are shown in Fig. 6.

Fig. 6. Railway wheels under test on the assembly table

Two component epoxy resins were used for the preparation of the coatings. The epoxy resin was molded on a tray of A4 size, and in semi polymerized state was taken away and was formed to the investigated surface. Both surfaces of the wheels around the hubs were coated.

The wheel-pair prepared for investigation with photoelastic coating, with a network for the evaluation of the results can be seen on Fig. 7.

Fig. 7. The wheel-pair prepared for investigation with coating and network

In the pressing process, the “A” wheel was pressed first, followed by the “B” wheel (second in the process).

The investigation results based in the evaluation of fringe distribution of the measurement technique. Some of the results of the fringe distribution after the pressing procedure shown in Fig. 8.,

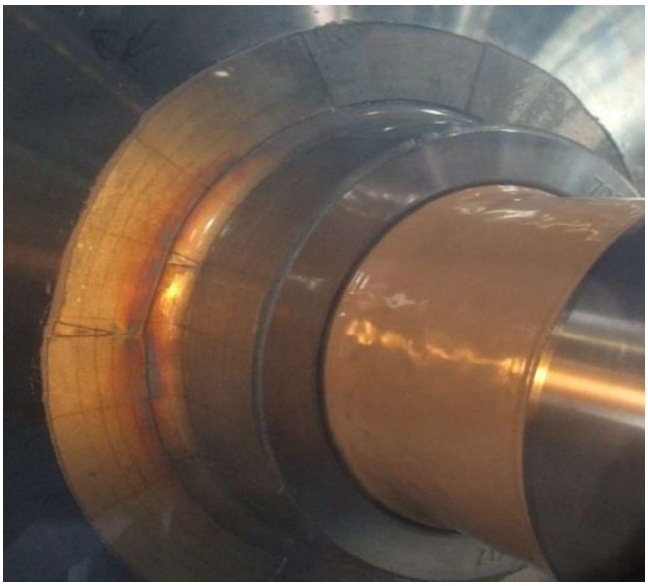

Fig. 8. The fringe distribution of inner surface B/I in crossed polarisation state of pressed wheel “B”

The evaluation of the fringe pattern based on the sensitivity of the applied photoelastic coating, as indicated in the following:

In case of the evaluation of the measurement results on railway wheels fringe distributions drawn together from recorded polarisation pictures were prepared. From the fringe distribution principal strain differences were calculated (1). During the conversion of the strain results to stresses the elastic modulus E = 2.068 [MPa], and a Poisson ratio ν = 0.29 of the investigated specimen were calculated. Calculated by these values the stress level belonging to the unit fringe order (m=1, the colour of this in the fringe distribution pictures is purple) is the following equation (9):

$$\sigma = \sigma_1 = \frac{k \cdot E}{1+\nu} = \frac{0,68 \cdot 10^{-3} \cdot 2,068 \cdot 10^{5}}{1+0,29} = 109,01\ MPa \tag{9}$$

The connection between the principal strain differences (ε_1 és ε_2) and the principal stresses σ_1, és σ_2 can be described by the following (10) equation:

$$\sigma_1 - \sigma_2 = \frac{E}{1+\nu}\left(\varepsilon_1 - \varepsilon_2\right) = m\frac{kE}{1+\nu} \tag{10}$$

where: E and ν are the material parameters of the investigated structure.

Based on the upon introduced evaluation, on the outer surface of the wheel “B” the stress level was calculated for an interval of 115.0 ….125.0 MPa stress value (see Fig. 9.)

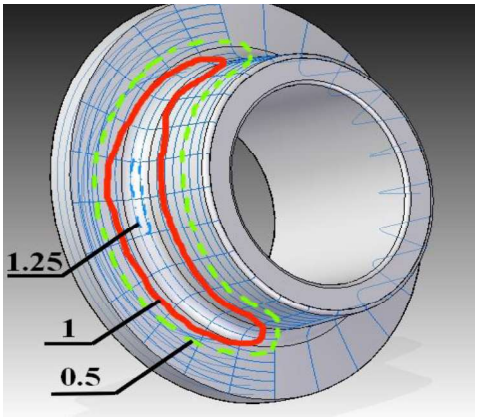

Fig. 9. The deformation distribution on „B" wheel (disk), which was pressed for the second time (second work phase).

5 EVALUATION/FINAL REMARKS OF THE RESULTS, CONCLUSIONS

a) The photo-elastic measurement coating technique is a suitable procedure to determine surface deformation of railway wheel-pair originating from the pressing up action,

b) The surface deformation on the railway wheel originating from the pressing procedure measured by photo-stress analysis appears on the surface in asymmetric way. The deformation on the open surface of the pressing tool is significantly higher than the area where the tool touches the wheel,

c) The place of the surface deformation measured by photo-stress analysis can be connected to the place of the axial deformation of the wheels. The maximum of the axial deformation of the wheels can be measured opposite (180 ^{0}) the maximum stress area.

6 REFERENCES

[1] Mechanical Engineer´s Handbook 2nd Ed [Wiley 1998]

[2] J.W. Dally, W.F. Riley: Experimental Stress Analysis, 3rd ed. McGraw-Hill, New York,1991.

[3] Borbás, L.: Fotoelasztikus rétegbevonatos mérési módszer használata gépalkatrészek vizsgálatánál és az eredmények értékelési lehetıségei (in Hungarian). Gép, 1986. nov. pp 359...363.

[4] Thamm, F., Borbás, L.,: Application of photoelastic coating at connecting points of bus under-carriage. IMEKO Congress on Experimental Stress Analysis, and 4th Danubia-Adria-Symposion. May 25-29./1987. Plzen. Proceedings: pp 71...76.

[5] Borbás, L. Zsáry, Á.,: Untersuchung von geschweisten Fahrgestell –Knottenpunkten mittels des Spannungsoptischen Oberflachensichtverfahren. Österreichishe Ingenieur und Architekten Zeitschrift. (ÖIAZ) 1988. 133.évf. 7.szám. pp 362...365.

[6] Thamm, F., Borbás, L.,.: Investigation of the optimum design junctions with respect to the welding procedure. Österreichishe Ingenieur und Architekten Zeitschrift. (ÖIAZ) 1989. 134.évf. 7/8.szám. pp 415...418.

ESTIMATION OF INPUT DATA FOR DYNAMIC SIMULATIONS BASED ON FIELD MEASUREMENT DATA

Tamás DEMUS

Department of Railway Vehicles and Vehicle System Analysis
Faculty of Transportation Engineering and Vehicle Engineering
Budapest University of Technology and Economics
H-1521 Budapest, Hungary

Received: July 20, 2022

ABSTRACT

During the design and development of railway vehicles and their components, the understanding and precise quantification of vehicle loads plays an important role. One approach is to derive the component loads by means of railway vehicle dynamic simulations. Such simulation requires reliable input data regarding railway track and vehicle parameters and control functions of the traction and brake application. These parameters highly depend on the actual setup of the railway track-vehicle system, in a wider range from the overall transportation system as there are characteristic differences between these parameters related to a commuter or long-distance train ride.

The current paper presents a method for obtaining the necessary data for dynamic simulations based on a case study. A series of measurements is carried out utilising handheld GPS positioning system based on the ARDUINO platform to acquire train ride characteristics.

Track parameters such as altitude information and speed limitations were estimated by means of statistical evaluation. A known vehicle type was chosen for the measurement that allows the calculation of the resulting traction and braking power. The control functions of the train that can be used as an input function of the dynamic simulation are derived from the force information. A characteristic histogram can be drawn up which can be later used for validating the results of the dynamic simulation.

In later steps of the research, the described method can be extended to other railway lines and vehicles, allowing comparison of the train rides and simulation results that might reveal characteristic differences between load cases related to different rail transport services.

Keywords: field measurement, train control, dynamic simulation, Markov process

1 INTRODUCTION

The design of railway vehicles requires a deep understanding of loads occurring during operation. The loads taken as an input to the design can be based on different standards, field measurements or simulations. As an example, an overview can be found in [1]. The target of the research is to get an insight to these loads and identify whether any characteristic difference is present related to different transportation services. Following up with an example, one can think that braking happens much more often in commuter traffic than in long distance transit resulting in higher loads induced by the brake equipment. Such characteristic is influenced by the driving style of the train driver. Therefore, our aim is to define the characteristic difference not only on a load spectrum basis but to consider different control functions given by the train driver.

The current paper acts as a pre-study for this approach, focusing on developing the necessary tools and methods to obtain the characteristic condition and to collect the first experiences.

The principle of the approach is to develop a simple and cheap device that records the route profile of a train, then by estimating the track parameters from this information a calculation on the traction and braking forces can be done considering the known ve-

hicle parameters. These forces allow us to define a control function. Assuming an underlying Markov-process a transition matrix can be defined along with the distributions of the hold times for each control positions.

2 METHODOLOGY

2.1 Track information and measurement circumstances

The lines no. 80 and 80a between Budapest-Keleti and Füzesabony railway stations were selected for the trial measurements (Fig. 1). The line is operated by MÁV-START Co. and part of the Budapest-Keleti to Eger route. It has two standard gauge track with an electrification of 25kV and 50 Hz. The Inter Regio type of train was selected for the measurements which has 10 stops during this section and consists of 2 STADLER FLIRT EMUs coupled together except for the early and late periods of the day with an overall of 16 pairs of trains every day. The journey takes 1 hour and 31 minutes, the route is 125 km long and can be divided into three main sections:

1 Budapest-Keleti to Rákoscsaba: lower speed limits, urban area of Budapest, many obstacles around the railway tracks,

2 Rákoscsaba to Hatvan: Gödöllő Hills area, curves with lower radius, wooded area,

3 Hatvan to Füzesabony: plain area, no obstacles, mainly straight sections.

The section between Rákos and Hatvan is recently renovated and thus giving good track condition. The EMUs are relatively new ones (in operation since 2007) resulting in a good running characteristic.

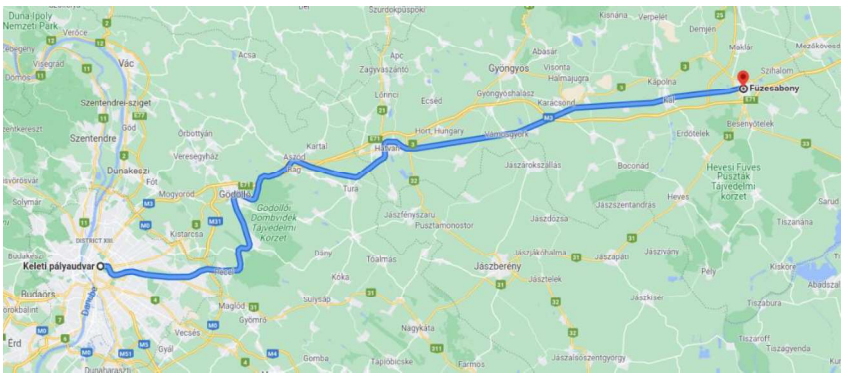

Fig. 1 Line no. 80 / 80a – Budapest-Keleti to Füzesabony

2.2 Measurement setup and device

In the scope of this pre-study the target was to obtain a device (Fig. 2) that is easily accessible, can be taken on-board and available on low cost to acquire the first experiences already in an early stage. Due to this the ARDUINO platform was selected and was equipped with GNSS receive type NEO-M8N from U-Blox, an SD card and an external antenna that allowed better positioning inside the car body. The following parameters were recorded with a sampling frequency of 5 Hz:

- longitude and latitude coordinates,

- altitude from sea level,
- date and time,
- current speed,
- number of satellites,
- position of dilution of precision.

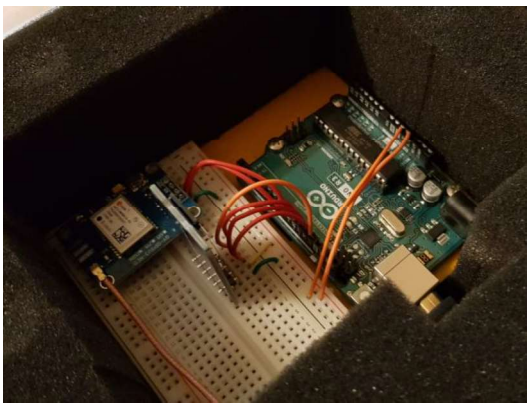

Fig. 2 Recording device

The measurements were done between October 2021 and March 2022. Overall, more than 30 profiles recorded as part of the tool development on the given route back and forth. However only a limited number of realizations are used in the further steps to represent the final variant of the tool. Each realization obtained is stored in a database for post-processing.

2.3 Data processing

The recorded data is processed further with a script developed in Python programming language. During the post-processing of the data two different status of the processing is distinguished. Raw data refers to the recorded data without any alteration. Conditioned data refers to the status after general data cleansing is done.

The raw data is checked for consistency and the acceleration is calculated to obtain the full extent of the parameters that are needed in later calculations.

The data cleaning process aims to find single data points that needs to be excluded from further processing, e.g., speed information recorded above the maximum allowed speed of the vehicle or corrupted data points. The first step is to identify and drop if any corrupted data is present in the time series of the recordings.

Second step of the conditioning is to remove highly uncertain points (e.g. data points with uncertain position information due to lack of GNSS signal) from the evaluation, therefore the dilution of precision (DoP) information is analysed and measurement points with DoP value above 20 are removed as these considered to be inaccurate according to [2]. Low number of satellites present for a GNSS fix is removed due to low accuracy. The minimum number of satellites of 7 is selected for the current study.

The remaining time series were then analysed for outliers by calculating the rolling means with a window of 50. The rolling means are used to normalize the recorded values and the standard deviation of the normalized series calculated. The threshold is that each recorded point must be in ± 3 standard deviation range. The calculation is performed for the longitude, latitude, altitude, and speed values. Once all the corrupted and outlying points are removed a Savitzky-Golay filter was applied to the series to smooth the dataset as proposed by [3] considering the parameters in Table 1. At this point, the conditioned dataset is produced.

	Window	Order
Longitude	11	2
Latitude	11	2
Altitude	21	2
Speed	21	2
Acceleration	151	3

Table 1 Parameters of Savitzky-Golay filter

Increasing the number of points for a later statistical analysis on the stochastic behaviour of the route realizations requires several recordings to be done under similar conditions as far as possible. The resulting realizations needs to be aligned to each other. As no reference point of the measurements given the offset between the different realizations need to be determined by searching the maximum value of the correlation for the position coordinates of the realizations in all three dimensions for longitude, latitude, and altitude as a function of the distance travelled. Afterwards an average value can be taken and the offset of the distance between two realizations can be calculated. The next realization is fitted to the already aligned set of realizations.

Merging these realizations into a single series result in position coordinates accompanied with speed and altitude information. This is referred as aggregated dataset and allows statistical analysis of the longitude, latitude, altitude, and speed values.

Once the conditioned and aggregated datasets are available the calculation of track and route profile parameters can be executed.

2.4 Parameter estimation

Considering the aggregated dataset, a moving average on the altitude values calculated with a window of 32 elements followed by a Butterworth filter of 5^{th} order. To ensure smooth transition, the altitude series were resampled and filtered with a Butterworth digital filter with an order of 5 and critical frequency of 0.001 of the Nyquist frequency. These parameters were experimentally fitted to the trial dataset only. Once the filter is applied the series are back sampled and a piecewise linear function is fitted. The track resistance is calculated based only on the altitude according to the equation below, where e is the track gradient and M is the vehicle mass taken as *124 t*. Other factors such as curve resistance is neglected in the first investigations.

$$F_{track} = e \cdot M \cdot g \tag{1}$$

The vehicle resistance is estimated based on the equation below, where *a, b, c* is assumed to be 2, 0 and 0.022 respectively based on engineering practice at MÁV Ltd.

$$F_{vehicle} = \left(a + b \cdot v + c \cdot \frac{v^2}{100}\right) \cdot M \cdot \quad (2)$$

The traction and braking forces can be calculated for each realization based on the acceleration data according to the equation given in (3) taken γ as 0.1.

$$F_{traction} = (1 + \gamma) \cdot M \cdot a + F_{track} + F_{vehicle} \quad (3)$$

Once the traction forces are known a comparison between the actual value and the F(v) traction curve of the vehicle can be done. Assumed that the brake characteristics are the same in magnitude as the traction characteristic but with opposite direction a segmentation of the traction-brake characteristics is possible. Taking speed intervals of 10 km/h from 0 to 160 km/h, at each interval the maximum traction force is distributed to 8 traction positions and 8 brake positions representing partial load of the traction or brake equipment. Classifying the actual traction force values to these intervals over the route profile results in a control function of the route. The traction-brake characteristics is presented on Fig. 3 according to [4].

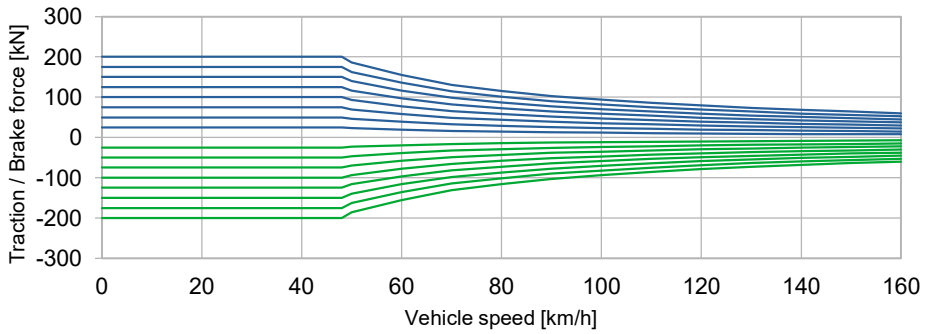

Fig. 3 Traction and brake characteristics of the vehicle

The control function over a route profile can be observed and the state changes between the traction or brake positions can be recorded leading to a transition matrix that is defined by the following, considering a transition from the actual position ξ from *i* to *j*. The current study considers transitions between neighbouring positions, however this restriction is not necessary and can be extended to allow transitions between all statuses.

$$M_{ij} = P(\xi = j \vee \xi = i) \quad (4)$$

Assuming an exponential distribution of the hold times that is taken on each position before shifting to another position, the parameter of the distribution can be estimated based on the histogram of each route profile by counting the duration taken in each step over the full route profile for each realization.

3 RESULTS

The trial runs were taken between 2021 December and 2022 April, altogether 7 realizations were recorded. The main parameters of the recorded datasets can be found in Table 2.

Dataset	No. of recorded points	No. of removed points during pre-processing	Offset applied during aggregation [m]
1	29143	1654	0
2	28394	2181	-209
3	25818	1935	4741
4	27566	1833	201
5	27591	2745	3024
6	30690	1720	23
7	29466	4306	2179

Table 2 Trial data basic information

To illustrate the effects of the dataset cleansing an example is shown on Fig. 4, where the altitude and speed series before and after pre-processing is shown.

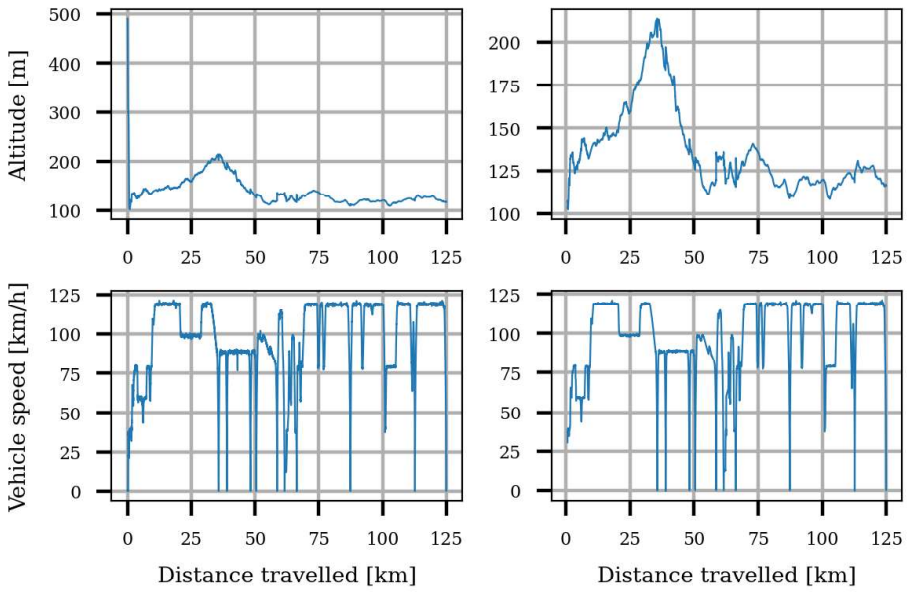

Fig. 4 Altitude and vehicle speed before and after conditioning

The estimated track altitude is shown on Fig. 5. The realizations together with the calculated moving average are shown on the upper part, whilst the filtered moving average and the linear approximation are shown on the lower part.

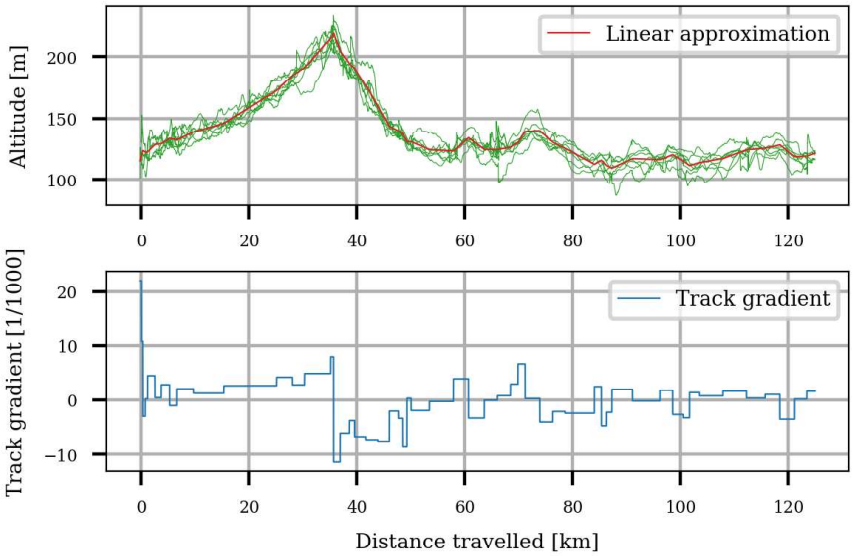

Fig. 5 Estimation of track altitude and gradient

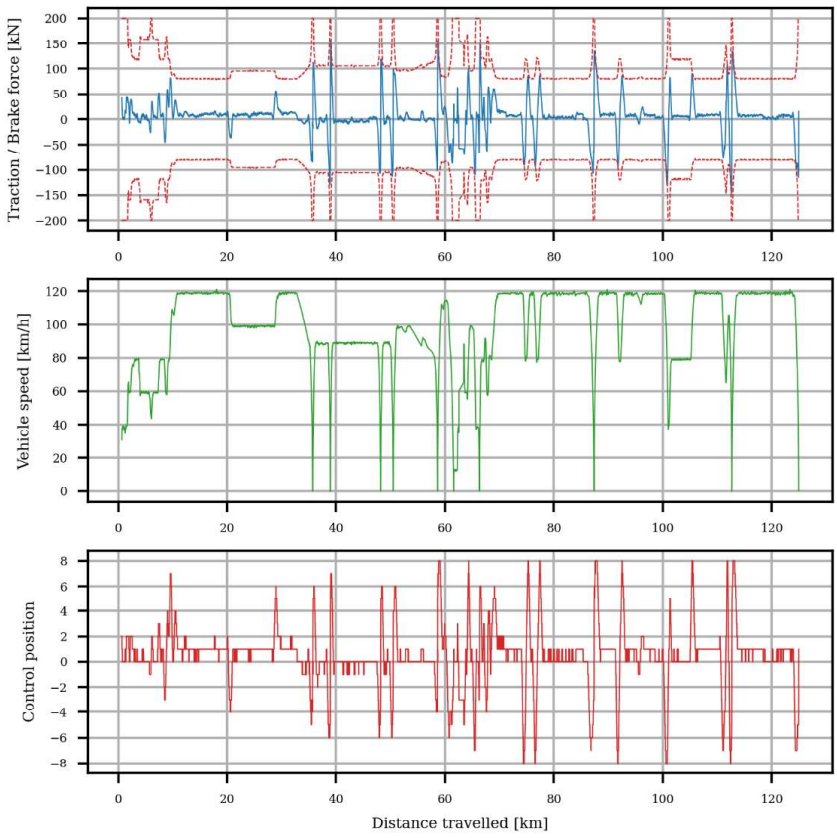

Fig. 6 Traction and brake forces, control function

Once the tractive and braking forces are available, the classification of the force value into the control positions considering the actual speed value is possible. The result for an exemplary realization is shown on Fig. 6.

The transition matrix for traction and brake position changes are shown on Fig. 7. The numbers indicated in each cell refer to the probability of a status change happens from the given row to the given column, e.g.: a state change from traction position 3 to 4 has a probability of 0.459.

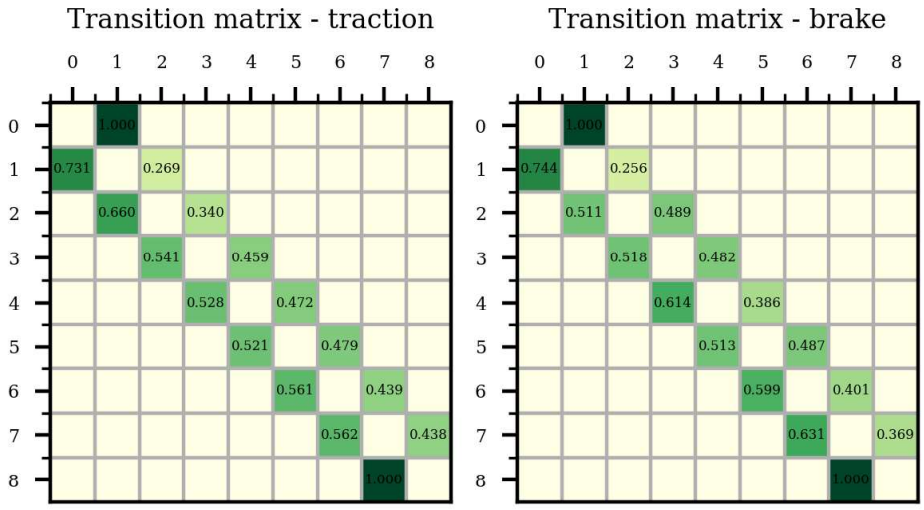

Fig. 7 Transition matrices

Table 3 shows the average hold times taken on each position in seconds considered as the expected value of the Poisson-distribution fitted to the histogram defined by the durations taken on each step.

Position	0	1	2	3	4	5	6	7	8
Traction	8.044	7.928	2.883	3.177	2.706	2.509	2.566	2.436	5.87
Brake		3.011	4.183	3.904	2.977	2.65	2.18	3.683	4.543

Table 3 Average hold times in each control position

4 DISCUSSION

The raw recorded data includes 25,000-30,000 data points, out of those approximately 1,500-2,500 is removed during the data cleaning process leading to a loss of 7% to 10%. During the last realization this loss is reached up to almost 15%. The Savitzky-Golay filter successfully removed the high frequency changes from the data series acting as a low pass filter, however large changes still present, for example in the altitude. The resulting conditioned dataset allowed further processing of the data as all extreme values were removed and the consistency of the dataset was given for each realization.

The estimation of the altitude and the track gradient lead to a first linear approximation. The resulting values correspond well to official track data given in [5] as shown in Fig. 8 as the calculated values exceed the reference values only in a few cases. The precision is limited and far as not as accurate as track data recorded with equipment dedicated to that purpose. However, for the current study it is enough to estimate the track resistance.

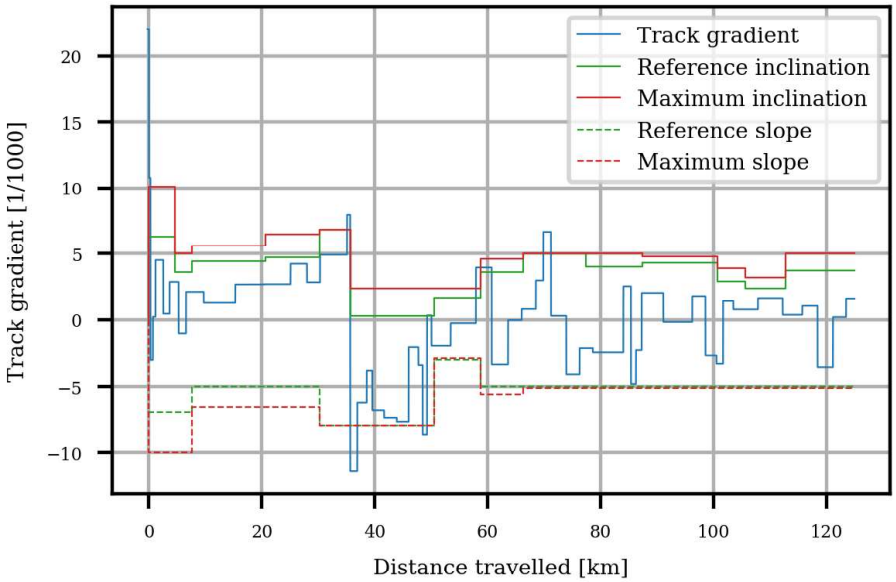

Fig. 8 Track gradient comparison

Comparing the available traction and brake forces with the actual ones over the route profile shows that neither the traction motors, nor the brakes are fully utilized as shown in Fig. 6 where the maximum traction and brake forces are shown with red dotted lines. More emphasis is put on the utilization if we visualize the vehicle load calculated from the aggregated dataset in a form of a histogram over the F-v plane as shown in Fig. 9. Phase trajectories can be observed on the F-v plane indicating the accelerating and decelerating motions. The load conditions align around the track speed limits. This emphasise that the train is only very seldom subject to traction or braking, mostly the coasting and cruising motions prevail. A shift can be seen on the force axis towards the traction, more load cases can be found on the positive area. This is because the input energy must be fed to the vehicle to realize the motion and the track and vehicle resistance is prohibiting the movement. This inefficiency is then depicted that more tractive energy needed than consumed by the brake process. It is to be noted that the calculation of the track forces is done with the mass of the vehicle only, not considering the passenger load. This additional load could be considered if the number of passengers would be known to each realization. Also, an assumption could be taken, which would lead to higher traction and brake forces resulting in higher utilization of the motor and brake power.

It is obvious to see on the control function that in a significant part of the route it alternates between the free position (no traction or brake happens) and the first traction position. This is because the low traction forces needed to maintain the vehicle speed between stations. There is only a seldom cases when higher traction or brake forces appear. The control function follows stepwise the build-up of such forces. This is because of the classification methodology. It is to be noted that this is an insufficiency of the model as the ramp up of the forces might be controlled by the vehicle control even if the control function is set to maximum by the driver. Further considerations to be done on refining the model that will most probably lead to allow the control function to jump more states in one step.

The relatively low cases of traction and braking is also depicted by the transition matrices. The state changes to reduce the position number is much more likely to happen then advancing to higher control states.

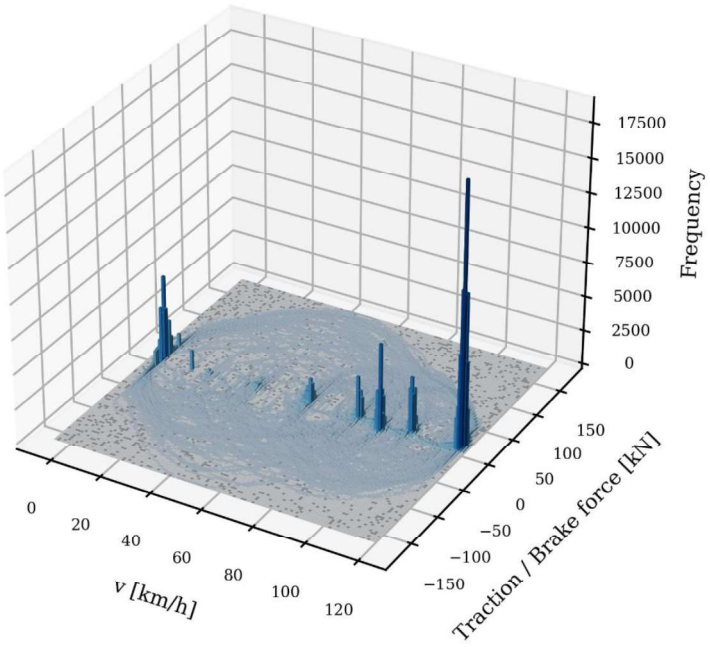

Fig. 9 Vehicle load histogram

5 CONCLUSION

The current research aimed as a pre-study on identifying load cases of rail vehicles based on hand-held measurement devices and statistical analysis. The measurements taken during the study were evaluated and the following concluding remarks can be drawn.

- A hand-held device was developed that was capable to record route profile information.
- The used data cleansing led to a loss of approximately 7% to 9% but retaining enough information for further processing.

- The altitude data were estimated, and the calculated track gradient was within the reference values of the investigated railway line.
- The calculated traction and braking forces were also inside the limitations supporting data consistency.
- The load case of the vehicle was evaluated based on a histogram over the F-v curve showing observation of concentrated load case around the speed limitations and shift towards the traction forces.
- Transition matrix and hold times were calculated that could be used for later comparison and simulation input.

Although the results are quite promising several aspects of the method is to be worked further. The accuracy and precision must be characterised along with the used data processing methodology and the dependency on the parameters used in the calculations. Further realizations are to be collected to investigate the statistical behaviour of the results. The transition matrix calculation can be developed to allow any kind of status changes. Final validation of the methodology is also needed, by building a simulation model of the vehicle and feeding it with the control functions generated by the transition matrices and the hold times. Resulting load cases should be comparable with the measured ones.

6 ACKNOWLEDGEMENTS

Researching is never a lonely journey; therefore, I would like to express my highest gratitude to Professor István Zobory for his long-lasting support on this endeavour and his constructive feedback during this study and in general. Additionally, I would like to thank Mr. Máté M. Szűcs taking the time and fighting all the hurdles while collecting the measurement data with the recording devices for many months long. Without them this study could have not reached to this point.

7 REFERENCES

[1] R. Xiu, M. Spiryagin, Q. Wu, S. Yang, and Y. Liu, “Fatigue life assessment methods for railway vehicle bogie frames,” Engineering Failure Analysis, vol. 116, p. 104725, Oct. 2020, doi: 10.1016/j.engfailanal.2020.104725.

[2] M. Tahsin, S. Sultana, T. Reza, and M. Hossam-E-Haider, “Analysis of DOP and its preciseness in GNSS position estimation,” in 2015 International Conference on Electrical Engineering and Information Communication Technology (ICEEICT), Savar, Dhaka, Bangladesh, May 2015, pp. 1–6. doi: 10.1109/ICEEICT.2015.7307445.

[3] A. Wilk et al., “Digital filtering of railway track coordinates in mobile multi–receiver gnss measurements,” Sensors (Switzerland), vol. 20, no. 18, pp. 1–20, 2020, doi: 10.3390/s20185018.

[4] Z. Dunai, Cs. Kiss, “Bemutatjuk a MÁV START Zrt. Nagykapacitású járműbeszerzési tenderére adott győztes Stadler választ, a KISS emeletes villamos motorvonatot”, Vasútgépészet, pp. 18-29, 2019/2.

[5] MÁV Zrt., “Műszaki Táblázatok I.”, 2003

INVESTIGATION OF A DERAILMENT PROCESS OF A RAILWAY WHEELSET CONSIDERING THE EFFECT OF THE TRACK SUPPORTING STIFFNESS

Zoltán ZÁBORI

Department of Railway Vehicles and Vehicle System Analysis
Faculty of Transportation Engineering and Vehicle Engineering
Budapest University of Technology and Economics
H-1521 Budapest, Hungary
Received: September 12, 2016

ABSTRACT

The derailment mechanism is a complex mechanical process in railway transport. This problem has got interested in a lot of research studies for determining the derailment criteria for avoiding the accidents and damage. A lot of different effects influence the risk of the derailment especially the quality of the track support, the track geometry, the wheelset suspension as well as the wheel-rail contact including the contact geometry (the wheel and rail profiles) and the friction conditions. These effects define a parameter space containing the masses of the vehicle and the track, the elastic and dissipative track parameters in lateral and vertical direction, the longitudinal, lateral and vertical elastic, dissipative suspension parameters, the radius of the curve, the railhead profile, the sliding friction coefficient, well as the travelling speed. All the mentioned parameters influence contact forces arising in the course of a derailment process.

This article deals with a dynamical investigation of the derailment processes of a railway wheelset running in a curve on an elastically supported track. The main point of the analysis is to determine the effect of the elastic parameters of an elastically supported curved track to the derailment of a wheelset running on it.

The paper also introduces a computation method which is based on a spatial wheelset-rail contact model, where the creep or slip contact forces and torques including the flange contact are modelled as a 3-D wheelset and rail-element model, which connect elastically to the vehicle chassis (or bogie) and the rail support.

The mentioned computation method proposes some new criteria of derailment. This investigation would like to press for an answer to the question of the rail elasticity of the track can affect such inconvenient events.

The main possible effects are taken into account like the rail elastic support failure.

Considering this effects an element of parameter-space can be defined which has a relationship between it and the derailment criteria. Evaluating of the numerical results of the dynamical investigation a recommendation can be given for the operators of railways and the maintainers for help them to decrease the chance of the derailment process. The risk of train derailment associated with rail transportation is an ongoing concern for the rail industry, government, and the public. Various approaches have been considered or adopted to analyse, manage and reduce risk. Upgrading track quality has been identified as one possible strategy for preventing derailment.

Keywords: derailment, *dynamical sim* simulation, railway wheel profile, track elastic support

1 INTRODUCTION

The risk of train derailment associated with rail transportation is an ongoing concern for the rail industry, government and the public. Various approaches have been considered or adopted to analyse, manage and reduce risk. Upgrading track quality has been identified as one possible strategy for preventing derailment.

A lot of different effects influence the risk of the derailment especially the quality of the track support, the track geometry, the wheelset suspension as well as the wheel-rail contact including the contact geometry (the wheel and rail profiles) and the friction conditions. These effects define a parameter space containing the masses of the vehicle and the track, the elastic and dissipative track parameters in lateral and vertical direction, the

longitudinal, lateral and vertical elastic, dissipative suspension parameters, the radius of the curve, the railhead profile, the sliding friction coefficient, as well as the travelling speed. All the mentioned parameters influence contact forces arising in the course of a derailment process.

This paper introduces a dynamical investigation into the railway wheelset running in a curve. In the course of the investigations an in-space model is taken into account. The goal of the dynamical investigations is to present the characteristic effects of the parameters, especially the elastic parameters of the track support influencing the derailment process.

The parameters of the wheel-rail contact geometry and the frictional conditions play a decisive role in the tribo-dynamical process of derailment.

2 THE DYNAMICAL MODEL OF THE WHEELSET-RAIL

In this section the applied dynamical model is introduced.

In Figs 1 and 2 the dynamical model of a 2-axle railway vehicle is shown. The front wheel-set of the vehicle model is connected to the vehicle body in longitudinal, lateral and vertical directions by elastic and dissipative joints. The model mentioned is apt for the analysis of the derailment process occurring in the course of negotiating a given curve at a constant velocity *v*. The dynamical model makes it possible to analyse the emerging *inclination for derailment*, the *danger of derailment* and the *actually occurred* derailment processes. It is clear that for the investigations into the derailment process it is necessary to take into consideration the dynamical environment of the complete wheel-set, thus the longitudinal, lateral and vertical elastic and dissipative connections of the wheel-set and the vehicle underframe should be included into the model and the dynamical analyses. The rear wheel-set is also a component of the simplified model, the role of the former is to guide the geometrical midpoint of the vehicle body always in the actual track direction.

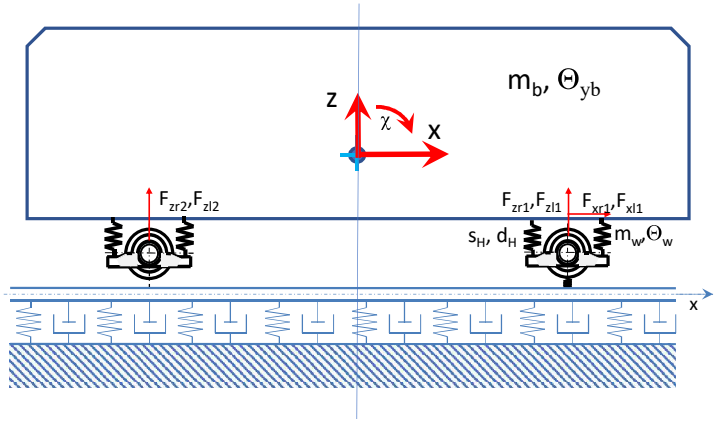

Fig 1 Side elevation of the dynamical model track/vehicle

Furthermore, in the dynamical model the treatment of the elastic behaviour of the railway track is also a basic condition of the investigations. In this respect the rails are

modelled in an approximate way, namely under the wheels of the considered leading wheel-set rail-replacing masses of rail profile are allocated, the two rail-masses are connected vertically and laterally in elastic and dissipative way to the stationary environment.

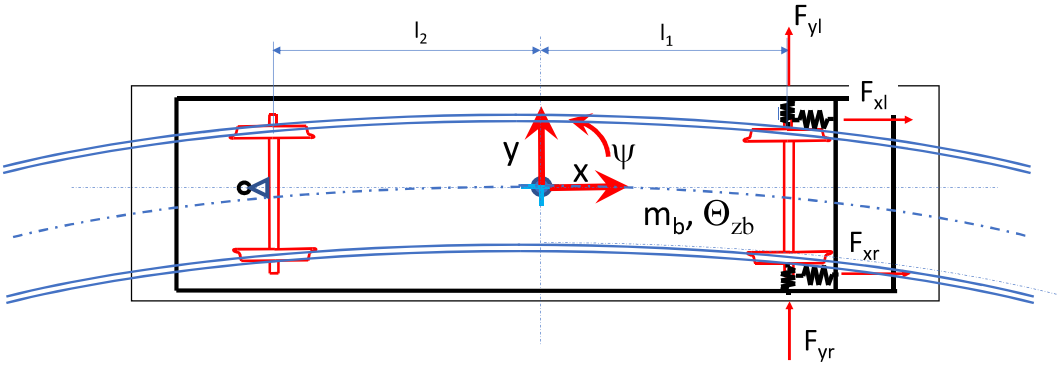

Fig. 2 Top view of the dynamical model track/vehicle

The dynamical model introduced above represents the motion of a two-axle vehicle in curved track. In the course of negotiating the curve inertia force of radial direction is acting on the vehicle body, the vector of the mentioned centrifugal force is oriented radially out of the vehicle. The magnitude of the centrifugal force is proportional to the square of the travelling speed.

The cross section profiles of both the wheels and the rails were taken into account in the analyses since the position of the wheel/rail contact spots give rise decisive influence on the contact forces and torques acting on the contact spots of the wheel-sets. It can be stated that one of the central problems in derailment dynamics is the treatment – determination – of the forces and torques arising in the contact spots.

Furthermore, the dynamical model is apt for taking into consideration the longitudinal variation of the position of the contact spots [1], due to the position variation mentioned the arisen contact forces generally constitute in space system of forces [2], [3].

The rear elevation of the front wheel-set is shown on Fig. 3.

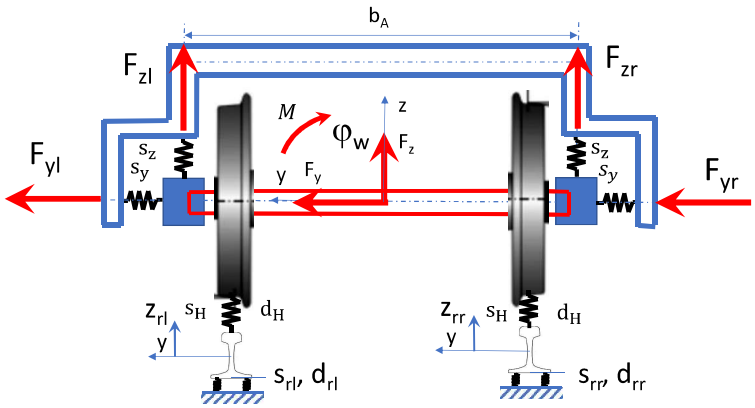

Fig. 3 The rear elevation of the front wheel-set

A proper mathematical model apt for computing the forces arising on the wheel/rail at the contact spot was established, which on the one hand helped the adequate description of the dynamical environment of the wheel-set, made it possible to compute the forces arising at the wheel/rail connection, on the other.

As for the track model, the two top site profiled rail masses were vertically and laterally connected to the stationary environment by elastic and dissipative members, and the possibility of angular displacements of profiled rail masses in the vertical plane perpendicular to the track longitudinal axis and around the vertical was also ensured in the presence of appropriate elastic and dissipative restoring torques.

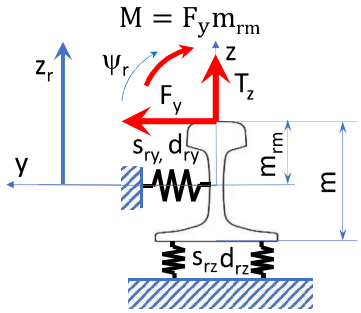

Fig. 4 Cross section of the rail beam and its elastic and dissipative connections with the stationary environment

In Fig 5. the wheel-set running in central position is shown. The longitudinal axes the wheel-set and the track are overlapped. When examining the derailment process it is assumed that the wheel-set displaces outward in the track-arch, and takes the position plotted in Fig. 6. The peak of the flange gets on the rail-head, while the wheel-set ran on the inner rail falls into the inter-rail space. Thus, *throughout the possible domain of the wheel/rail connection* the mechanical wheel/rail contact permanently vanishes at both wheels of the wheel-set.

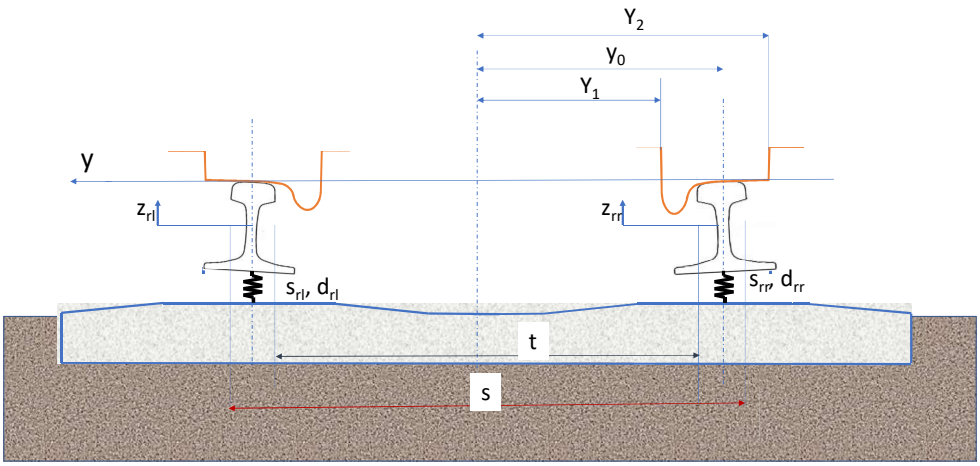

Fig 5 The wheel-set is running in central position along the track

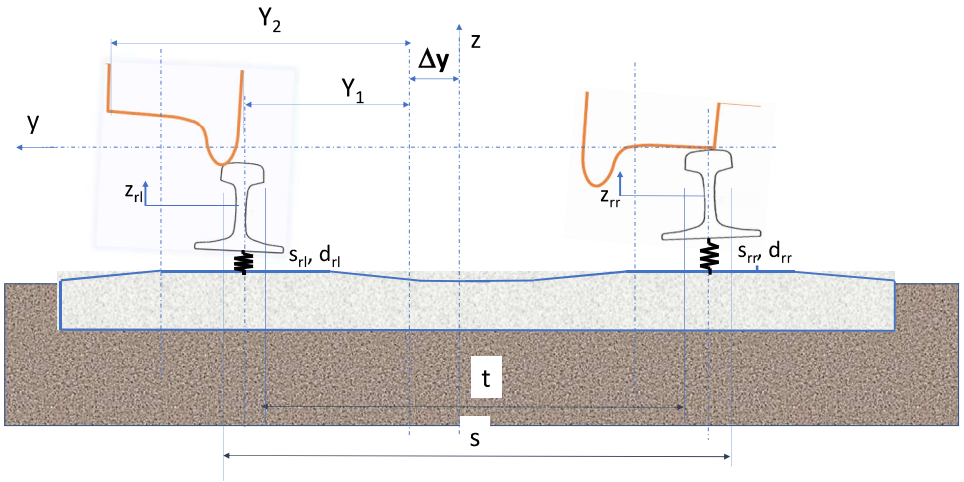

Fig. 6 The wheel-set in extremal-position prior to derailment

In the Figure, Y_1 means the distance of the *inner* plane of the wheel-tyre (in case of block wheels the flange) from the own vertical symmetry axis of the wheel-set, and Y_2 stands for the distance of the *outer* plane of the wheel-tyre (in case of block wheels the wheel disk) from the own vertical symmetry axis of the wheel-set. Furthermore, Δy stands for the relative displacement of the centre point of the wheel-set with respect to the tack central axis, while the displacement of the individual rails from their nominal position is permitted. The Figure also shows that the plane of trad plane of the right side rail is in higher position than the left side rail's because the elastic parameters (s_{rl}, d_{rl}) of the left side rail is not equal to the right side one's (s_{rr}, d_{rr}).

The derailment process is basically divided into three sections [8]. In the first section the outer wheel of the curving wheel-set is running with two-point-contact, i.e. wheel/rail force transfer occurs both through wheel tread contact and flange contact. In this running state appears the *inclination for derailment*.

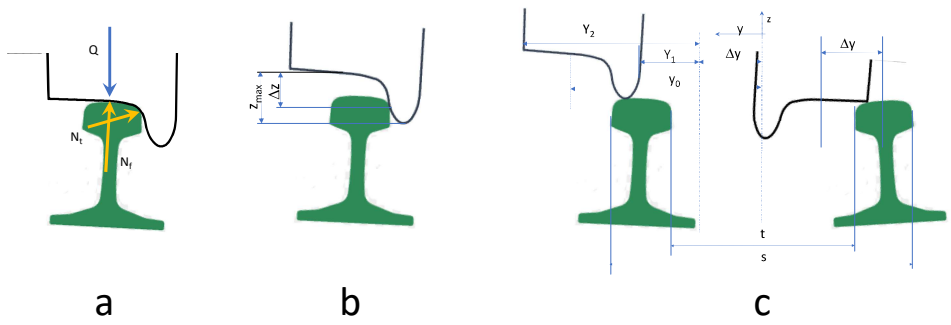

Fig. 7 The derailment event: a: inclination for derailment, b: danger of derailment, c: occurrence of derailment

The *inclination for derailment h* is defined as a ratio of the vertical wheel/rail forces acting on the wheel upwards divided by the static wheel load *Q*:

$$h = min\{1, \frac{N_t cos\beta_t + N_f \cos\beta_f + N_f \mu cos\beta_e}{Q}\} \quad (1)$$

Here N_f stands for the tread contact force and N_f for the flange contact force. Angles β_t and β_f are defined between the rail profile tangent lines and the horizontal axis. Angle β_e is defined in the vertical plane P_e which goes through the nominal flanging point and is perpendicular to the wheel-set axle. Angle β_e can be measured between the horizontal tangent plane of the rail profile and the straight line interconnecting the nominal flange contact point and the point defined by lateral projection of the tread contact point in plane P_e.

In the second section the flange of the outer wheel is continuously contacting with the rail and the inclination to derailment achieves the value 1 and there appears the *danger of derailment,* which is defined by the formula below:

$$v = min\{1, \frac{\Delta z}{z_f}\} \quad (2)$$

Here Δz stands for the vertical distance between the rail head and the wheel-tread and z_f system designates the height of the flange. If $v > 0$, then only flange contact is present at the outer wheel. The necessary condition of the occurrence of $v > 0$ is the equality h = 1. In this section the creep-dependent force transfer on the wheel-tread of the outer wheel terminates, and exclusively flange contact occurs in the presence of sliding friction in the outer wheel/rail connection. Meanwhile in the wheel/rail connection of the wheel running on the inner rail henceforward wheel tread contact remains present and brings about pure creepage-dependent force transfer.

The case of the actual derailment, when the necessary condition $v = 1$ is already in force can be identified by the occurrence of event *D* that has been defined by the geometrical position of the rail-pair/wheel-pair according to the following expression:

The complete derailment is indicated by the occurrence of the following event:

$$D = \left\{Y_1 + \Delta y > \frac{s}{2} \cap Y_2 - \Delta y < \frac{t}{2}\right\} \quad (3)$$

If the flange is running on the rail-head, conditions $h = 1$ and $v = 1$ are in force. In this motion state there is a wide possibility of the occurrence of an actual derailment, since the lateral inertia forces incite the curving wheel-set for further radially outward motion. The actual occurrence of the derailment depends first of all on the track radius, on the longitudinal velocity of the vehicle and on the parameters of the dynamical environment of the wheel-set (the elastic and dissipative parameters of the suspension of the wheel-set, the elastic and dissipative parameters of the rail supports, furthermore the friction between the contacting wheel and rail surfaces).

Thus, the condition of derailment is that either the flange of the wheel running on the outer rail leaves off the region of contact with the railhead, or the inner wheel plane of the inner wheel leaves off the railhead [8].

Considering Fig 1 and Fig 2 the model is an 18 degree of freedom dynamical model describing the introduced derailment event problem. The free-coordinates describing the motions of the selected dynamical system model are represented by the following time dependent vector of the 18-dimension Euclidean space:

$$\underline{\boldsymbol{q}} = [y_b, z_b, \varphi_b, \chi_b, \psi_b, y_w, z_w, \varphi_w, \chi_b, \psi_b, y_{rr}, z_{rr}, \varphi_{rr}, \psi_{rr}, y_{rl}, z_{rl}, \varphi_{rl}, \psi_{rl}]^T.$$

Furthermore, the geometrical characteristics are important parameters of the dynamical system these parameters are included into vector $\boldsymbol{g}$ shown below:

$$\underline{\boldsymbol{g}} = \left[l_1, l_2, b_A, r_0, t, s, Y_1, Y_2, m, l_{rs}, w_g(y_w), r_g(y_{rr}), r_g(y_{rl})\right]^T.$$

Further indispensable parameters are the inertial (mass)-, elastic and dissipative parameters included into vector $\boldsymbol{e}$ see below:

$$\underline{\boldsymbol{e}} = [m_b, \theta_{b\varphi}, \theta_{b\chi}, \theta_{b\psi}, m_w, \theta_{w\varphi}, \theta_{w\chi}, \theta_{w\psi}, m_r, \theta_{r\varphi}, s_x, s_y, s_z, s_{Hr}, s_{Hl}, d_x, d_y, d_z, d_{Hr}, d_{Hl}\,].$$

Finally those operation parameters were taken into account which take decisive effect on the analysis of the derailment process of the considered wheel-set and the role of the dynamical environment of the examined wheel-set in causing the derailment event, namely the track and vehicle body. The operation parameters in question are included into vector $\boldsymbol{w}$:

$$\underline{\boldsymbol{w}} = [v, R, \mu(\mu_0, \mu_\infty, \nu_0, \nu_\infty)].$$

where $\mu(\mu_0, \mu_\infty, \nu_0, \nu_\infty)$ is the friction coefficient in nonlinear contact model [6]. A basic pre-condition for analysing derailment processes is to fix the accurate concept of derailment. As a general definition it can be formulated that *the condition of the occurrence of complete derailment is that throughout the possible domain of the wheel/rail connection the mechanical wheel/rail contact permanently vanishes at both wheels of the wheel-set.*

In this paper it has been focused on the effect of the elastic parameters of the track. The elastic parameters can be described by the following formulas:

$$s_r = s_r(x - vt - l_i), \qquad i = 1,2 \tag{4}$$

$$d_r = d_r(x - vt - l_i), \qquad i = 1,2 \tag{5}$$

where x is the longitudinal coordinate, s_r is the stiffness, d_r is damping coefficient of the track support, l_i distance of the ith wheelset from the initial point of the coordinate system, v is the vehicle speed, t is the independent time-coordinate.

The x, t dependent elastic and dissipative parameters of the rail support can be defined by vector:

$$\underline{\boldsymbol{s}}(x - vt - l_i) = [s_{rr}(x - vt - l_i), s_{rl}(x - vt - l_i, d_{rr}(x - vt - l_i, d_{rl}(x - vt - l_i] \qquad i = 1,2 \tag{6}$$

where r and l indexes indicate the right- or left side rail support parameter.

It is obvious that the elasticity of the rail support is a very important factor of the derailment process. Furthermore, the dynamical model of a double-axle railway vehicle and an elastically supported curved track is taken into account for investigating the effect of

the rail support for the derailment process. In this model the track elasticity function can be modelled as an elastically supported Winkler beam on a variable stiffness and damping coefficient foundation. The problem solution can be approached by discretized rail model [7].

3 SIMULATION THE DERAILMENT PROCESS

The method of investigations into the derailment process was the numerical solution of the equations of motion of the selected track/vehicle model. The essence of the method was the description of the behaviour of the front wheelset by motion equations, in which all longitudinal, lateral and vertical elastic and dissipative connections were reckoned with. At the same time the motion equations of the profiled rail masses were also constructed, continuously taking into consideration the actual contact conditions with the wheels. When constructing the system equations first the positions of the geometrical contact points were determined for the wheel/rail profiles, as functions of the lateral displacements of the rail-pair and wheel-pair and as functions of the angular displacements of the latter around the vertical axis. Knowing the contact points the parameters of the contact surfaces were determined by assuming *Hertzian*-contact.

The dynamical model constructed for the vehicle/track system was treated numerically, by solving the initial value problem below:

$$\ddot{\underline{q}}(t) = \underline{f}(\dot{\underline{q}}(t), \underline{q}(t), \underline{g}, \underline{e}, \underline{w}, \underline{s}(x - vt - l_i)), \forall t \in I \tag{7}$$

$$t_0 \in I, \underline{q}(t) = \underline{q}_0, \dot{\underline{q}}(t) = \dot{\underline{q}}_0 \tag{8}$$

As vectors $\underline{g}, \underline{e}$ and $\underline{w}$ are constants, $\underline{s}$ is longitudinal coordinate and time dependent function. They can be considered as vector components of hipervector $\underline{\boldsymbol{p}}(x,t) = [\underline{g}, \underline{e}, \underline{w}, \underline{s}]^T \in \mathcal{P}$ where $\mathcal{P}$ is the parameter space of the considered vehicle/track dynamical system.

As the first step of the simulation, we are looking for an answer to the question of what effects the change in the support stiffness of the track has on the derailment process. To this end, we simulate the running of a dynamic model presented above on a curved track at a speed of $v = 80km/h$, where the support stiffness of the track's outer rail is reduced by 8% compared to the nominal (inside) rail over a $30m$ long section.

During this run, we examine the change in derailment tendency, i.e. we look for function

$$h = h(\underline{\boldsymbol{p}}(x,t)) = h(\underline{g}, \underline{e}, \underline{w}, \underline{s}(x - vt - l_i)), \; i=1,2. \tag{9}$$

4 NUMERICAL EXAMPLES

Figure 8. a. shows the value of the track stiffness in a 3-dimensional diagram, where the support stiffness of the 30 m long, nominal (300kN/mm) track support stiffness reduced by 8% can be seen on the outer rail strand. Figure 8. b. shows the function of the track stiffness with nominal stiffness.

Figure 9. a., b. shows the lateral displacement of the wheelset in a 3-dimensional diagram, the planar view of which is shown in Figures. 10. a and b. Moreover, Figure 10 a. and b. also show the function of the track stiffness.

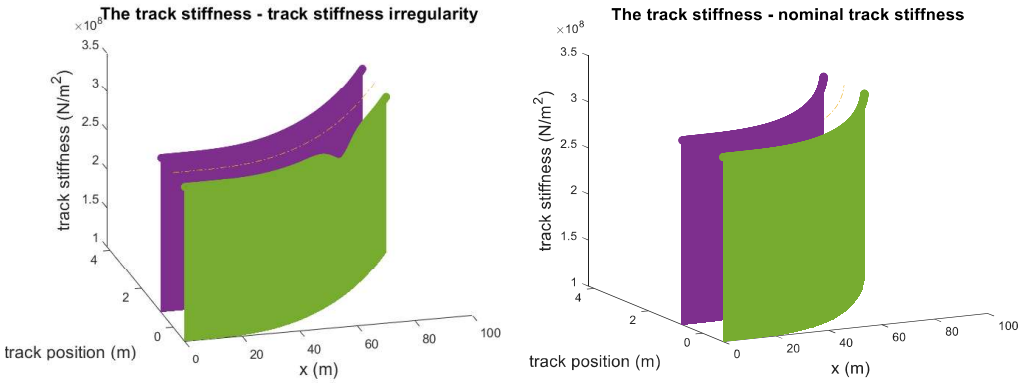

a. b.

Fig.8 Track stiffness function

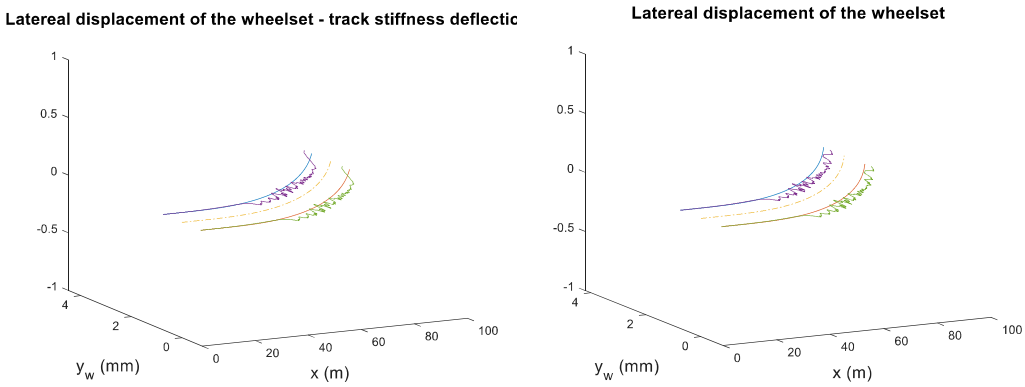

a. b.

Fig.9 Lateral displacement of the wheelset

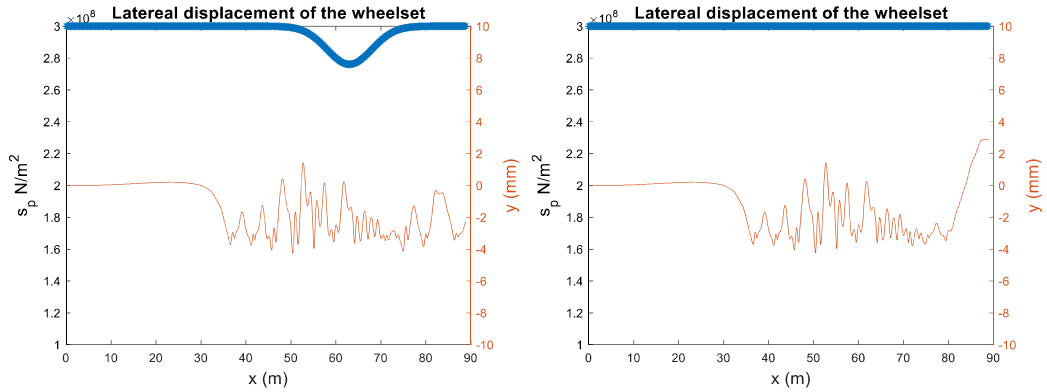

a. b.

Fig. 10 Lateral displacement of the wheelset layed down in plane

Figures 11. a, b. show the inclination for derailment function $h = h(\underline{\boldsymbol{p}}(x,t)) = h\left(\underline{g},\underline{e},\underline{w},\underline{s}(x - vt - l_i)\right), i = 1,2$ as a function of the length coordinate.

Figures 11. a. and b. show the function $h = h(\underline{\boldsymbol{p}}(x,t))$ obtained as a result of the simulation test conducted with inhomogeneous and the nominal stiffness of the track support. The figures additionally show that in both cases the value of the function $h(\underline{\boldsymbol{p}}(x,t))$ is

$$1 > h(\underline{\boldsymbol{p}}(x,t)) \geq 0. \tag{10}$$

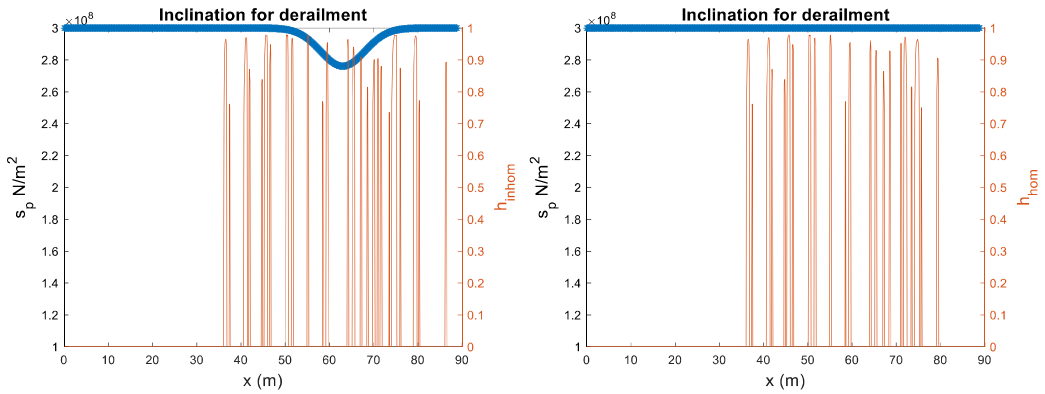

a. b.

Fig.11 Inclination for derailment function

In the following, we start from the assumption that the inclination for derailment depends not only on the value of the function $h(\underline{\boldsymbol{p}}(x,t))$ but also on the duration of contact with the flange during the simulation. This is typically characterized by the integral of the function $h(\underline{\boldsymbol{p}}(x,t))$:

$$I_{inhom} = \int_0^T h_{inhom}\left(\underline{\boldsymbol{p}}(x,t)\right) dt,\ I_{hom} = \int_0^T h_{hom}\left(\underline{\boldsymbol{p}}(x,t)\right) dt, \tag{11}$$

where $h_{inhom}\left(\underline{\boldsymbol{p}}(x,t)\right)$ is the inclination for derailment for the track with inhomogeneous stiffness, while $h_{hom}\left(\underline{\boldsymbol{p}}(x,t)\right)$ is the inclination for derailment for the track with homogeneous stiffness. The result of the simulation showed that

$$q = \frac{I_{inhom}}{I_{hom}} \approx 1.12 \tag{12}$$

during the dynamic simulation of the examined model, the simulation of passing through the inhomogeneous track section demonstrably increases the inclination for derailment.

5 CONCLUDING REMARKS

1. A lumped parameter dynamical model apt for the simulation of the derailment process of a railway wheel-set has been elaborated, which is connected to the vehicle underframe longitudinally, laterally and vertically by elastic and dissipative components and through rolling contact and sliding friction to the elastically and dissipatively supported track components (profiled rail masses).
2. The above model has been upgraded for the examination of the effects of the operation parameters.
3. Parameter sensitivity analysis of the above model has been carried out for the case where the stiffness function of the vertical support of the track has a given irregularity. During this simulation the vehicle speed and other operational parameters had been constant value.
4. The research activity should be extended for a more detailed description of the rolling contact and sliding friction processes, with respect of the possibility of changing friction parameters along the distance covered by the vehicle.

6 REFERENCES

[1] Kalker, J.J.: Simplified theory of rolling contact. Delft Progress Report, Series C 1, 1973, p. 1–10.

[2] Ping Wang – Kaize Xie1 – Liyang Shao2,3 – Lianshan Yan2 – Jingmang Xu1 – Rong Chen1,3: Longitudinal force measurement in continuous welded rail with bi-directional FBG strain sensors: Ping Wang et al 2016 Smart Mater. Struct. 25 015019

[3] Santamaria, J. – Vadillo, E.G. – Gomez, J.: Influence of creep forces on the risk of derailment of railway vehicles. Vehicle System Dynamics, 47:6, p.721-752, DOI: 10.1080/00423110802368817

[4] Xin Ge – Kaiyun Wang – Lirong Guo – Min Yang – Kaikai Lv – Wanming Zhai: Investigation on Derailment of Empty Wagons of Long Freight Train during Dynamic Braking. Published 6 September 2018, DOI: 10.1155/2018/2862143

[5] Haigermoser, A. – Luber, B. – Rauh, J. – Gräfe, G.: Road and track irregularities: measurement, assessment and simulation. Vehicle System Dynamics: International Journal of Vehicle Mechanics and Mobility, 53:7, 2015, p.878-957, DOI:10.1080/ 00423114.2015.1037312

[6] Zobory, I: A kerék és a sín közötti gördülőkapcsolat hosszirányú erőkapcsolati tényezőjének modellezése kétparaméteres nemstacionárius sztochasztikus mezővel. Gép : a gépgyártás műszaki folyóirata, LIX (2). pp. 40-50. ISSN 0016-8572 (in Hungarian)

[7] Zobory I., Békefi E., Zábori Z. Simulation backed identification of vertical track stiffness function by using wavelets, 6th Mini Conference on Vehicle System Dynamics, Identification and Anomalies VSDIA, Budapest, Hungary, 9-11 November 2000, pp. 151–159.

[8] Zábori, Z, Zobory, I.: Dynamical Investigation into the Derailment Process of a Railway Wheel-set Running in a Curve, 17th Mini Conference on Vehicle System Dynamics, Identification and Anomalies VSDIA, Budapest, Hungary, 9-11 November 2020, pp. 153–166.

IDENTIFICATION AND PARAMETERIZATION OF WEAR MECHANISMS BY SCATTERED LIGHT MEASURMENTS ON A SINGLE-WHEEL ROLLER TEST RIG

Patrick Schneider*, Ina Stratmann*, Marcel Wegener* **, Paul Schneider*, Christian Schindler*

* Institute for rail vehicles and transport systems, 52074 Aachen, RWTH Aachen University
** DB Systemtechnik GmbH, 80939 München

Received: August 05, 2022

ABSTRACT

The prediction of the development of wheel and rail profiles due to wear is of high interest regarding cost and safety of the operation of railway vehicles. In common approaches, multi-body simulations to represent the operation conditions are done. From the results of these simulations, the evolution of the wheel and rail profiles is calculated with experimentally determined wear laws. In common wear laws, the removed material between wheel and rail is often considered proportional to the frictional energy transferred in the contact surface or other auxiliary variables calculated from the occurring forces and relative movements. Due to different wear mechanisms acting in the contact, this proportionality however changes non-linearly. This non-linear function of the proportionality coefficient can be defined by certain parameters. They depend on the materials of the contact partners and further tribological conditions. In different works on the prediction of wheel profile wear, those parameters vary. To develop a method for improved investigation of the parameters defining the function of the wear coefficient for different materials and conditions, the authors implement an innovative experimental approach for continuously measuring the evolution of the state of the wheel and rail surfaces during tests on a single-wheel roller test rig. It is assumed, that the current dominant wear coefficient resulting from the dominant wear mechanism can be identified in continuous measurements of the evolution of the wheel surface. To this end, the scattered light technique is applied to the wheel surface of the roller rig and a system measuring the contact position is implemented on the test bench. Those added functions are described in detail and the first results of the experiments with possible identified changes of the wear behaviour are shown in this work.

Keywords: wheel-rail contact, light scattered technique, wear calculation

1 INTRODUCTION

Wear in the wheel-rail contact is one of the main problems, which needs to be solved and adjusted in the maintenance of a railway vehicle and a railway network. The forces resulting from the interaction between wheel and rail, which occur in its contact under different environmental conditions, lead to a wide spectrum of possible wear behaviour. To improve the adjustment of the wear of vehicles to their tracks and other operation conditions, the research aims to investigate and predict the changes in the form of wheel and rail profiles. As the tribological system behaviour changes with different weather and lubrication conditions, common wear laws shall be improved. By studying the surface of wheels and their roughness on a roller rig, a method to parametrize and adapt the wear laws according to the conditions used in experiments are aimed to be developed.

It is known that the status of the surface of wheel and rail changes continuously. Whereby investigations by Lundmark et al. [1] show that the surface roughness (Ra-values) amended slightly after a distance of 400 km [1], though the surface microstructure changes continuously depending on the actual situation. Investigations of Viereck [2] indicate a smoothing of the surface based on micro slip as well as slight macro slip. In the case of high macro slip is roughening expectable. [2]

To predict the wear of wheel and rail profiles, in common approaches multi-body simulations are used. For this wear laws are used which indicates a proportional correlation between the removed material and the frictional energy. Whereby, the proportionality changes non-linear and its function is defined with certain parameters. These parameters vary, among other things, depending on the particular authors presenting them.

The authors developed a method to improve the investigation of the parameters by implementing an innovative experimental approach of continuously measuring the surface status. The first investigations of Schneider et al. [3] show the ability to apply the scattered light technique on a single-wheel roller test rig. It is assumed, that the current dominant wear mechanism can be identified by continuously measuring the evolution of the wheel surface. In the following paragraphs are the scattered light technique, the calculation method, and the first results introduced.

2 STATE OF THE ART

For the investigations done in this work, models describing the wear in the wheel-rail contact were considered. The description of those models and approaches are the first part of this section followed by the description of the measurement and testing equipment used for the experiments done.

2.1 Wear modelling in the wheel-rail contact

The tribological interaction in the wheel-rail contact is a complex system. While the forces occurring from the relative movements and the loads in the contact are dependent on the state of the surface of the frictional partners and the intermediate medium between them, they are also attacking and therefore changing the surfaces. As this work focuses on the occurring damage processes in the wheel-rail contact, the influence on the adhesion is not further described.

The material removal on wheel and rail is dominated by multiple parallel acting mechanisms. *Schelle* [4] gathered the occurring mechanisms as adhesion, abrasion, surface breakdown and tribochemical reactions. The acting mechanisms in the contact depending on the loads attacking the frictional partners. As they act parallel, their dominance however changes and with it, the resulting wear on wheel and rail. Resulting from the said effects a continuous change in the state of the surface and its topography can be assumed.

The removal of material from the frictional partners of wheel and rail is considered in two commonly used models. The first one considers the removed material proportional to the energy transmitted between the frictional partners. The removed material Δm is calculated by the frictional work $E_{friction}$ multiplied with a coefficient of proportionality k_i:

$$\Delta m = k_i \cdot E_{friction} \tag{1}$$

The other common model, the model of *Archard* [5], considers a proportional dependency between the removed material Δm and the normal force N multiplied with the

sliding distance s between the friction partners divided by the hardness of the harder friction partner H.

$$\Delta m = k_i \cdot \frac{N \cdot s}{H} \tag{2}$$

Experiments have shown a nonlinear behaviour of the coefficient of proportionality for both models. With certain limits of the loads occurring, the material removal rate rises sharply. This effect results from different wear mechanisms acting in the contact patch. In general, the literature identifies two to three wear areas, mild, severe and catastrophic wear.

The resulting nonlinear behaviour has been described for both common models. For the model of *Archard* [5], the different coefficients depending on the relative velocity between the frictional partners and the contact pressure are shown in Fig. 1. It is assumed that depending on the relative velocity in the contact patch and the contact pressure, the dominant wear mechanisms change and therefore the amount of removed material changes.

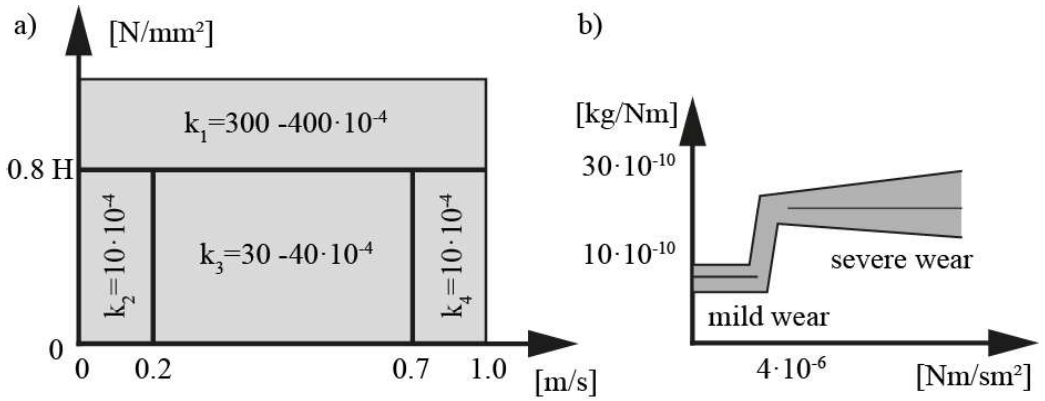

Fig. 1 a) he model of *Archard* [6] and b) the model of *Krause* and *Poll* [8]

For the model considering the removed material as proportional to the frictional energy, the coefficient is mostly determined according to the experiments of *Krause* and *Poll* [7] depending on the frictional power density in the contact patch $\Phi_{friction}$, which results as the frictional power divided by the size of the contact patch.

$$\Phi_{friction} = \frac{P_{friction}}{A_{contact}} \tag{3}$$

The behaviour of the proportionality coefficient depending on the frictional power density can be seen in Fig. 1. The wear is separated into mild and severe wear.

As both models show the nonlinear behavior resulting from different wear mechanisms, it is assumed that the change of the surface state shows similar changes in its evolution. For the following considerations, the model of proportionality between frictional energy and worn material is used.

As the behavior of the material is strongly influenced by the environmental conditions, the shown models resulting from experiments done in the laboratory cannot be seen as

applicable to every situation in the operation of a railway vehicle. Therefore, the coefficients and boundaries used in predictions of the wheel profile wear are often adapted. [4]

2.2 Scattered light technique

The VDA 2009 [9] describe the scattered light technique as a method to measure continuously the changes in the surface roughness of components. It can be used to monitor the surface status of produced components. Whereby in that area the technique has to deal with vibrations and impurities [10] which are also present at a single-wheel roller test rig. A known disadvantage of this method is that it is not possible to calculate the geometrical roughness (e.g. Ra) direct from the scattering angle distribution. [9]

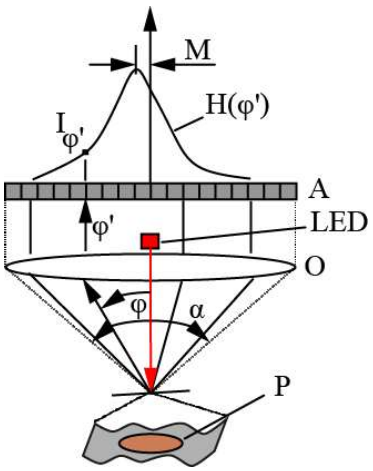

Fig. 2 Principle sketch of the scattered light technique (in accordance with [9])

Fig. 2 presents a principle sketch of the scattered light technique. The sensor detects the variation of scattered light distribution value (S_d) of a rough surface in the area of the microstructure (P). For this shines a LED through an objective (O) on the rough surface of the test component. The reflected light will be detected within the angle of α whereby the discrete angle φ correlate with the appropriate detected intensity ($I_{\varphi'}$). This results in the standard scattered light distribution ($H_{(\varphi')}$) which is necessary for the calculation of the scattering angle distribution A_q (see equation (4)). [9]

$$A_q = k \cdot \sum (\varphi' - m)^2 \cdot H_{(\varphi')} \qquad (4)$$

2.3 Measurement equipment and test rig

The tests were performed on a single-wheel roller test rig of the IFS. It consists of a wheel and a driven rail-wheel. The wheel can be broken with brakes or the rail-wheel can be broken using the motor. The pressure between wheel and rail-wheel can be increased by applying pressure to the air bellows. A detailed description can be found in [3].

To measure continuously the variation of the roughness is the scattered light sensor *OS500* of *OptoSurf GmbH* used. The contact point and the size of the contact area are determined by a system described in detail in chapter 3.2.

For carrying out the experiments is a defined positioning of the used sensor necessary. To guarantee that, the sensor is positioned in mounting support to prevent any movements due to vibrations of the test rig. The measured area is positioned in line with the contact point of the wheel (see Fig. 3) and the measuring direction of the *OS500* sensor is also marked in Fig. 3, which is of relevance to the results. Additionally is the distance between the sensor and the wheel surface defined and adjusted (in accordance with [11]).

Fig. 3 Measurement setup of the OS500 sensor

3 EXPERIMENTAL PROCEDURE AND CALCULATION BASIS

In the following chapter, the general experimental procedure, and the developed and used calculation methods are introduced.

3.1 The procedure of the experiments

During the execution of the experiments, the position of the wheel to the rail wheel has been kept constant. Whereas multiple other factors are varied which are:

- The breaking pressure
- The type of braking
- The wheel speed
- The wheel load (in the form of pressure in the air bellows about the wheel)

To investigate the influence of the above-mentioned points on the measurement data, the factors have been varied individually. Furthermore, to receive bases for the evaluation of the measurement are so-called “basis-measurements” performed. During these basis-measurements were the wheel speed set at 2 km/h, the brake type selected as motor-braking and there was no additional load applied. This configuration is selected to prevent any influence on the measurement by various loads, speeds, and braking pressure. The basis-measurements were performed before and after every measurement. In addition, was every experiment repeated three times to exclude the effects of previous experiments with different parameters. In Table 1 are performed experiments without the basis-measurements listed.

Table 1: List of experiment settings

Experiment number	Speed in km/h	Additional wheel load in bar	Breaking type and breaking pressure in bar
V1-V3	30	0	motor
V4-V6	30	2	3
V7-V9	30	4	3
V10-V12	30	6	3
V13-V15	30	8	3
V16-V18	30	1	3
V19-V21	30	0	1
V22-V24	30	2	1
V25-V27	30	4	1
V28-V30	30	6	1
V31-V33	30	8	1

After the repetition of the experiments is the geometry of the wheel measured to ensure the usage of the actual geometry for the calculation.

3.2 Calculation of the resulting contact area

The calculations of the area of contact require at first knowledge about the point of contact and second knowledge about the wheel and rail profile. In the case of a single-wheel roller test rig can be the profile measured by using the MiniProf BT system of Greenwood Engineering. Identifying the point of contact requires knowledge about the position of wheel and rail. Therefore the lateral displacement between wheel and rail as well as the angle between wheel and rail around the vertical and the longitudinal axis are measured with a sensor system. The parameters to be measured are shown in Fig. 4.

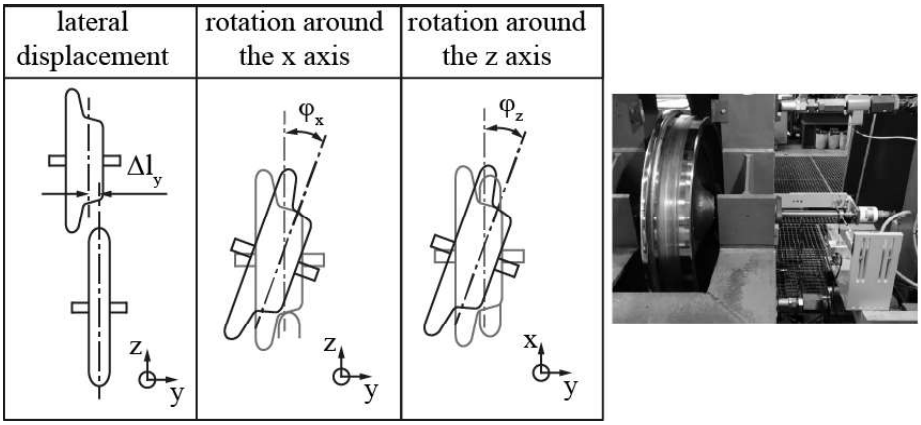

Fig. 4 Degrees of freedom to measure by the sensor system and the measurement system attached to the roller rig

To identify those parameters, a construction from cable potentiometers is applied. The first potentiometer is applied between the yoke of the roller rig and an implemented plate. Additionally to that, the axis of the wheel shaft is extended. Applied to this axis, further cable potentiometers are applied to measure the angles between the wheel and rail profiles. The complete construction can be seen in Fig. 4.

From the position of the profiles to each other, the contact points and patches can be calculated. To this end, a simplified calculation based on the penetration of the two measured profiles is applied. This proceeding is verified by measurements of the resulting contact area using pressure measurement film of type HHS (super high pressure) of Fujifilm.

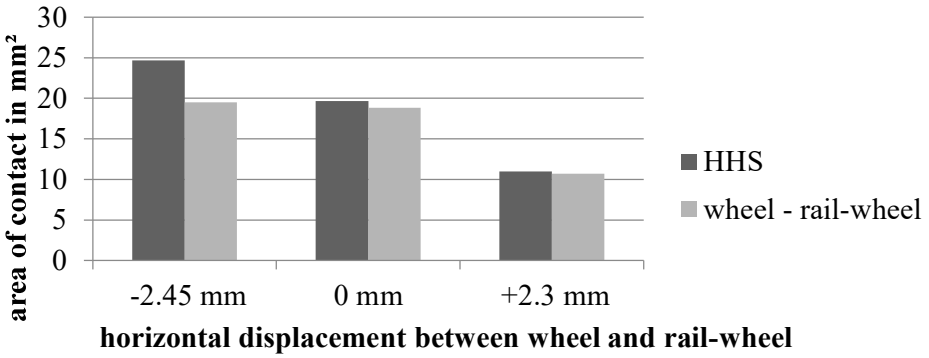

Fig. 5 Verification of the calculation method

Fig. 5 shows the results of an exemplary measurement of the contact area using pressure measurement film compared to the calculated results of the calculation method for the contact patch. A deviation in the case of a horizontal displacement of -2.45 mm can be identified. Whereby, the deviations are in general very low. The deviations can be caused by the roughness of the contact partners.

3.3 Parametrization of the wear models

As described in chapter 2.1, the wear and its dependency show a nonlinear behaviour. As the coefficient of proportionality shows the dependency on the frictional power density as shown in Fig. 1, the relationship can be set up as the following equation.

$$k_i\left(\Phi_{friction}\right) = k_m \cdot \left[1 + (X-1) \cdot \frac{1}{1 + e^{-C_1 \cdot (\Phi_{friction} - C_2)}}\right] \qquad (5)$$

With the parameters defining the nonlinear behaviour:

- k_m: The coefficient of proportionality for mild wear
- X: The increase of the material removal per frictional work as $X = \frac{k_s}{k_m}$
- C_1: The parameter describing the range of frictional power density over which the mild wear changes to severe wear
- C_2: The limit of frictional power density, when mild wear changes to severe wear

Krause and *Poll* determined $C_2 = 4\frac{W}{mm^2}$ in their experiments. However, it was stated, that many environmental factors could influence the wear of the materials. Therefore, the method developed in this works aims to simplify the identification of the described parameters while applying loads to the wheel-rail contact.

The function described by equation (5) is shown qualitatively in Fig. 6.

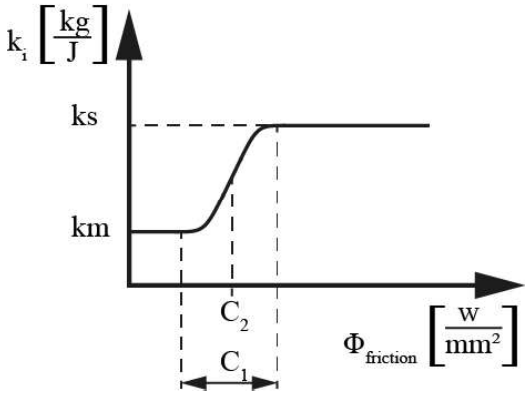

Fig. 6 The model of *Krause* and *Poll* is described as a mathematical function according to equation (5)

From the shown parameters, k_m and k_s need to be investigated by comparing the removed material either per weighting of the wheel or by comparing the surface geometry before and after the measurement. As the generated worn material in the experiments is very difficult to obtain this work focuses on determining the parameters C1 and C2 defining the transmission between mild and severe wear.

To this end, the aim is to identify the difference between the surface roughness of a segment before and after it passes the contact between both wheels by continuously characterizing the state of the wheel surface with the measurement system described in chapter 2.2. The input data from the experimental setup is saved as time-dependent vectors, therefore the incoming continuous data needs to be suitably processed to register the discrete states of the surfaces. In the first step, the measured velocity of the wheel is considered to specify the time slots to determine the rolled distance on the circumference of the wheel. The distance equals the integral of the measured velocity.

$$s(t) = \int v(t)dt \tag{6}$$

For the discrete measurement data given from the experiment, the travelled distance equals:

$$s_n = \sum_{i=1}^{n} v_i \cdot \Delta t \tag{7}$$

Depending on the length of one circle segment the number of investigating segments m, which have passed, can be calculated:

$$u_i = 2 \cdot \frac{\pi}{m \cdot r} \tag{8}$$

The same segment of the wheel passes the measurement with the scattered light sensor and the contact with the roller at different times. These events happen at different time slots, which can be calculated by the defined angular distance between the two points. By assigning the related state of the surface to the occurred contact forces and velocities, the correlation between those forces and velocities and the state of the surface can be investigated.

The loads in the contact are characterized by the longitudinal relative velocity w_x, the adhesion force T_x, and the resulting friction power $P_{friction}$.

Table 2: Calculation basis

Parameter	Input	Corresponding Characterization
Longitudinal relative velocity w_x	angular velocity wheel ω_w radius wheel r_w angular velocity drive wheel ω_D radius drive wheel r_D	$w_x = \omega_D \cdot r_D - \omega_w \cdot r_w$
Longitudinal adhesion Force T_x	Longitudinal force T_x	Directly measured
Frictional Power P		$P = T_x \cdot w_x$

To have a certain value to describe the occurred loads on the surface the parameters are taken on average over the preceded determined time slots. Additional to that, the resulting points are smoothed to improve the readability.

With the size of the contact patch determined as described in chapter 3.2 and the occurring frictional power, the power density in the contact can be determined. The correlation between the power density and the state of the surface characterized by the scattered light measurements is investigated by the described methodology. The occurring forces are sorted to the occurring states of the surface taking into account the angular distortion due to the roller rig.

4 RESULTS AND DISCUSSION

The development of the evolution of the surface was recorded. The results in comparison to the occurring frictional power density are shown in Fig. 7. The settings regarding the wheel load applied for every experiment can be found in Table 1.

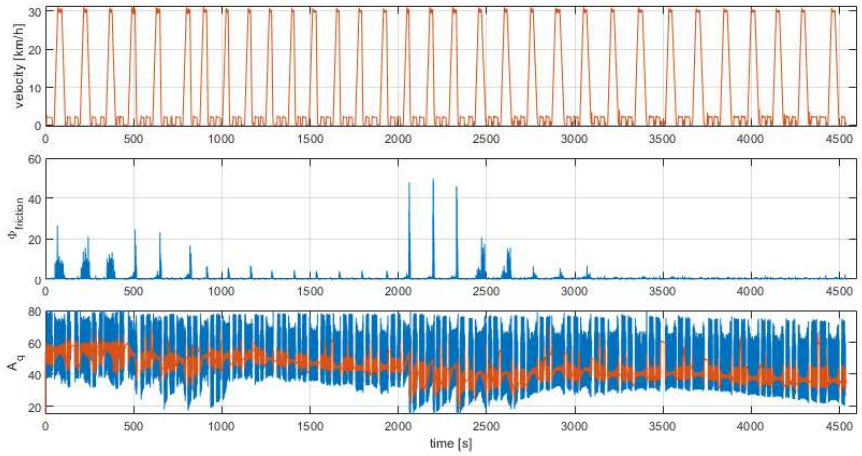

Fig. 7 The results of the driven velocity, the power density and the corresponding surface state for 32 of the 33 experiments

Visible is the mostly constant surface state during the experiments. However especially in braking processes with high power density in the contact patch the A_q value decreases. For further visualization, a breaking process with high power densities is shown in Fig. 8.

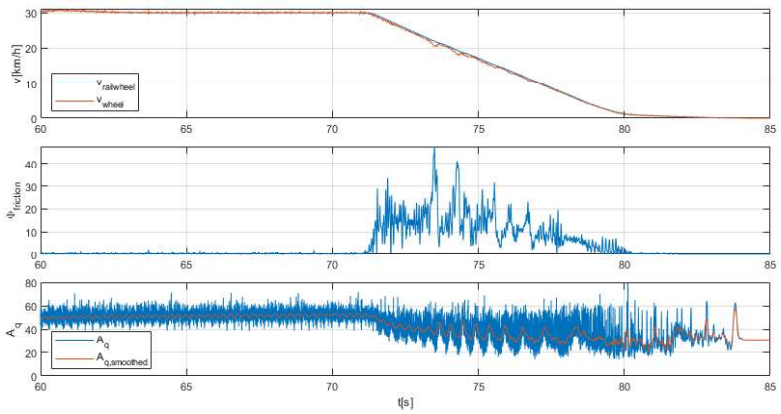

Fig. 8 Detailed view of a braking process with high power density

From the experimental approach, the change in the state of the surface can be compared before and after getting in contact with the rail wheel. Thereby the friction conditions are measured. Plotting the smoothed change of the surface state dA_q (in colors) depending on the surface state before the contact and the frictional power density, Fig. 9 can be generated.

In the range of a power density lower than approximately $5\ W/\ mm^2$, a relatively high A_q value is generated. With increasing power density, a certain range of power density between $\Phi_{friction} = 5 - 10\,W/mm^2$ is reached, in which the boundary between decreasing and increasing the surface roughness cannot be determined exactly. In this range, the boundary between increasing and decreasing surface roughness de-

creases sharply and then goes into an almost constant state for power densities above $10\,W/mm^2$. To investigate the effects on the boundary further, the boundary of the lowest and highest $A_{q,in}$ in red plus symbols and in green asterix, for which a decreasing or increasing A_q of the surface can be obtained, is plotted over the power density in Fig. 10.

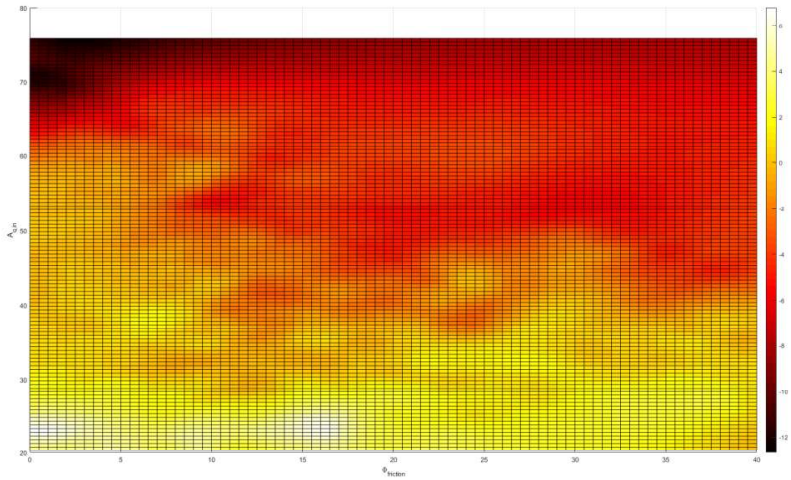

Fig. 9 The change of the surface depending on the frictional power density and the incoming surface state

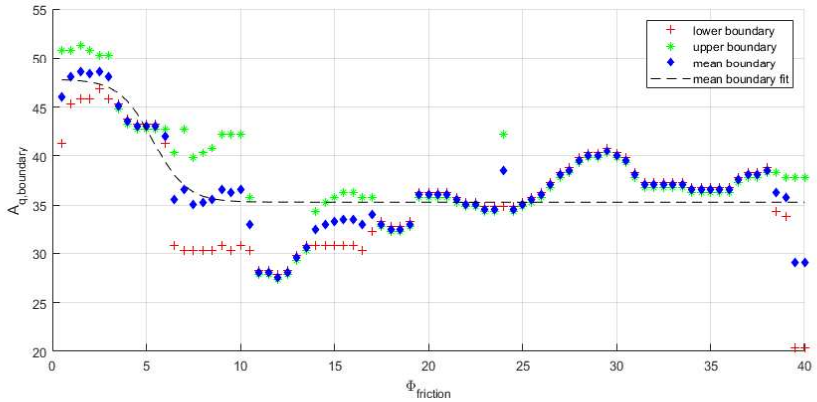

Fig. 10 The boundary values $A_q$over the frictional power density $\Phi_{friction}$

Already marked in figure 13, as a dashed line is a fit of a function similar to equation (5) of the mean of the boundary values, shown in blue diamonds. Assuming that the behaviour of the surface is dependent on the acting wear mechanisms in the contact, the nonlinear transmission from mild to severe wear can be parametrized. For the performed experiments the resulting values are listed in Table 3.

Table 3: Results for the parameters defining the assumed transmission between mild and severe wear

Parameter	Value
C_1	$1.13\ mm^2/W$
C_2	$5.37\ W/mm^2$

The value for C_2 is not the same as for the experiments of *Krause* and *Poll* but still in a very good range. The results are plausible; however, a wide range of surface behaviour can be obtained. As the accuracy and precision of the used measurement equipment for the forces and the velocities might have a lot of outliers, deviations in the values are possible. Nevertheless, a systematic change in the surface evolution can be determined and defined by the built measurement approach. Further investigations regarding the comparison of different environmental and lubrication conditions can clarify the needed precision and accuracy in measurements. Additional to that, investigations of the model of *Archard* as investigations regarding further parameters will follow.

5 CONCLUSION

- An experimental approach for the investigation of the surface evolution has been applied to a roller rig
- Additional to that, a measurement system to calculate contact patch and contact forces was implemented
- By comparing the surface before and after the contact the influence of the contact conditions is investigated; the occurring contact forces and velocities are measured
- A transmission between different systematic behaviours of the state of the surface could be seen, the validation of the results needs to follow
- Further optimization of the experimental equipment can improve the results
- Further investigations concerning the influence of the contact pressure and the relative velocities shall be done according to the model of *Archard*
- Comparing investigations of lubricants and materials can be done to further investigate the variation of wear behaviour

6 ACKNOWLEDGEMENT

The authors express their gratitude to the Deutsche Forschungsgemeinschaft (DFG) for providing financial support under Grant No. 441889189.

7 REFERENCES

[1] Lundmark J., Höglund E., and Prakash B., 2006,“Running-in behaviour of rail and wheel contacting surfaces,” *AITC-AIT 2006: 5th International Conference on Tribology; 20 - 22 September 2006, Parma, Italy*.

[2] Viereck U., 2008. *Dynamisches Kraftschlussmodell zur Optimierung von Gleitschutzsystemen*, Zugl.: Aachen, Techn. Hochsch., Diss., 2007, VDI-Verl., Düsseldorf.

[3] Schneider P., Stratmann I., Rakowitsch M., and Schindler C., 2022,“Untersuchung der Interaktion zwischen Reibleistung im Rad-Schiene-Kontakt und der durch

Streulichtmessungen charakterisierten Radoberflächentopographie," *IRSA 2021 Tagungsband, Proceedings 3rd International Railway Symposium Aachen, Aachen, Germany, 21-23 November 2021 / Herausgeber/Editors: De Doncker, Rik W; Nießen, Nils; Friesen, Nadine; Schindler, Christian*, RWTH Aachen University, Aachen, pp. 109–119.

[4] Schelle H., 2014. *Radverschleißreduzierung für eine Güterzuglokomotive durch optimierte Spurführung*, Technische Universität Berlin.

[5] Archard J. F., 1953,"Contact and Rubbing of Flat Surfaces," Journal of Applied Physics, **24**(8), pp. 981–988.

[6] Enbolm R., 2006,"On Simulation of Uniform Wear and Profile Evolution in the Wheel - Rail Contact," Doctoral thesis, Aeronautical and Vehicle Engineering, Railway Technology, KTH, School of Engineering Sciences (SCI).

[7] Krause H., and Poll G., 1986,"Wear of wheel-rail surfaces," Wear, **113**(1), pp. 103–122.

[8] Zobory I., 1997,"Prediction of Wheel/Rail Profile Wear," Vehicle System Dynamics, **28**(2-3), pp. 221–259.

[9] Verband der Automobilindustrie, 2010,"Geometrische Produtspezifikation - Oberflächenbeschaffenheit - Winkelaufgelöste Streulichtmesstechnik, Definition, Kenngrößen und Anwendung," VDA 2009:2010-07.

[10] Böhm J., Jech M., and Vellekoop M., 2010,"Analysis of NM-Scale Scratches on High-Gloss Tribological Surfaces by Using an Angle-Resolved Light Scattering Method," Tribol Lett, **37**(2), pp. 209–214.

[11] OptoSurf GmbH, 2009,"Oberflächenmesssystem OS 500: Bedienungsanleitung," 3rd ed.

ADVERTISEMENTS

NIPPON STEEL

< Rolling Stock Parts >

-Solid rolled wheels	-Wheels & axle	-Driving gear units
-Flexible couplings	-Couplers-Draft gears	-Air Springs
-Bogie	-Active suspensions	-Pneumatic spring tilting system

Steering Bogie

Excellent Curving Performance

◆Silent curving

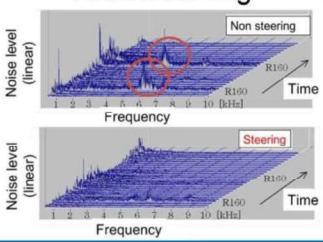

◆Improve Derailment Safety

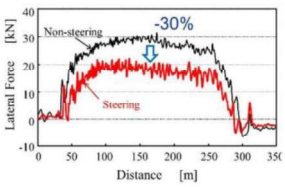

Active Suspensions

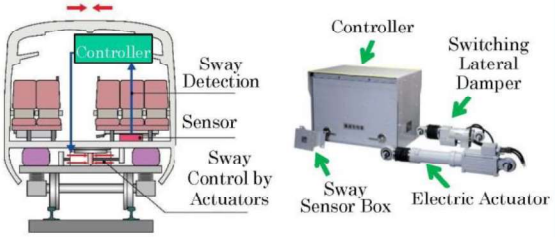

Comparison of Lateral Acceleration

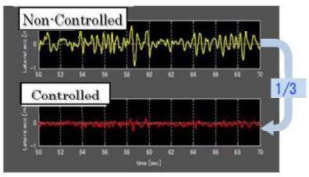

◆***Decrease Lateral Acceleration***

◆***Adopted to Shinkansen (High Speed Railway) in Japan***

Pneumatic Spring Tilting System

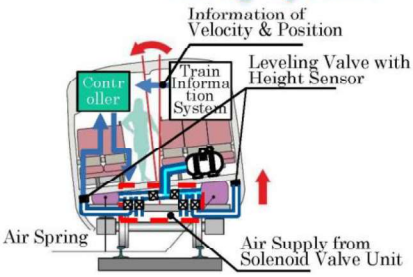

Comparison of Lateral Acceleration

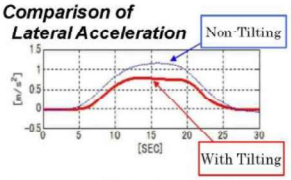

◆***Decrease Unbalanced Centrifugal Acceleration in Curve***

Head office 2-6-1 Marunouchi, Chiyoda-ku, Tokyo 100-8071, Japan
Phone +81-3-6867-6902
Fax +81-3-6867-4958
http://www.nipponsteel.com

NIPPON STEEL CORPORATION

OWNERSHIP STRUCTURE AND LINE NETWORK

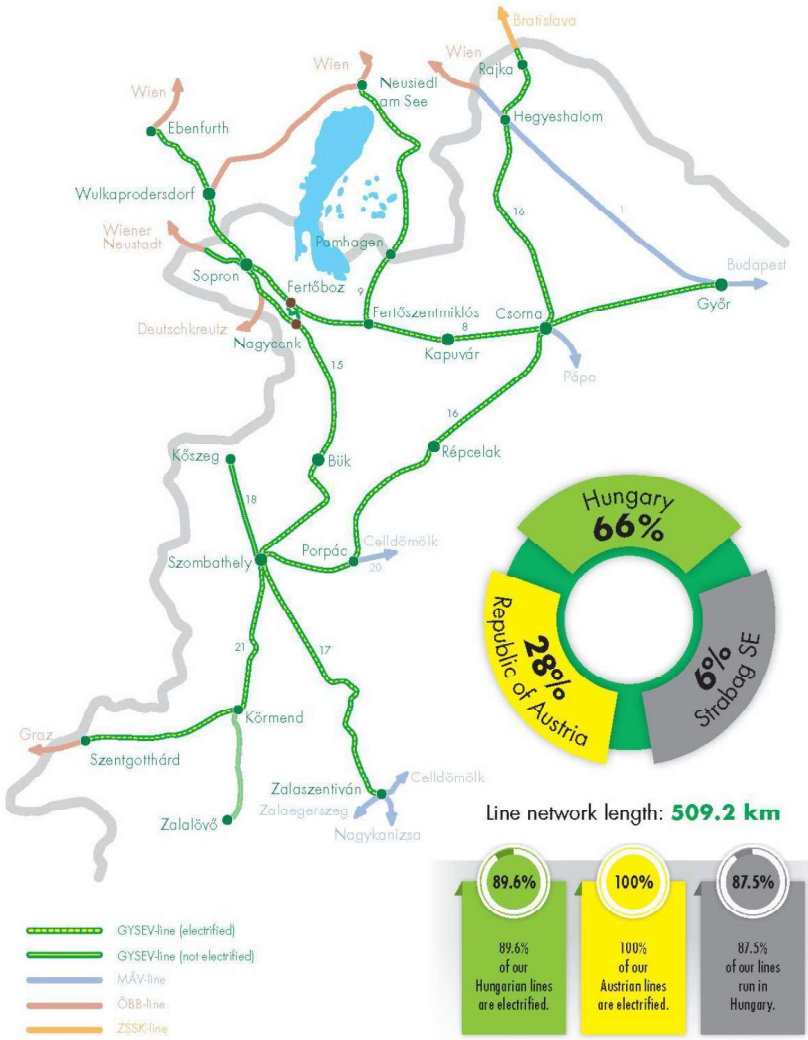

GYŐR-SOPRON-EBENFURTI RAILWAYS PRIVATE COMPANY LIMITED BY SHARES WWW.GYSEV.HU

MISSION AND VISION

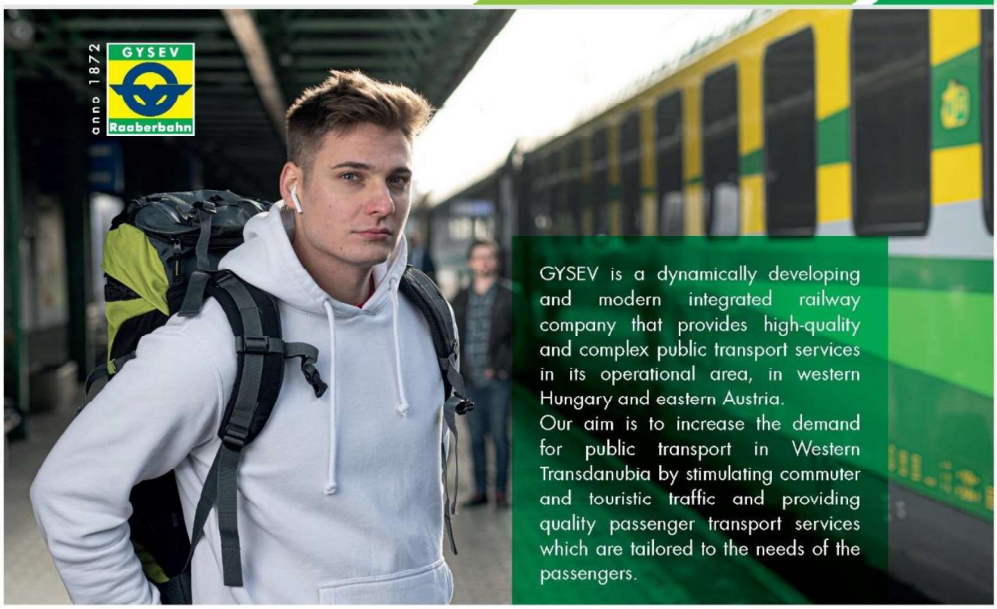

Number of passengers: **5.33 million**	• in Hungary: **4.062 million** • in Austria: **1.272 million**
Total travel distance of passengers: **274.29 million km**	• in Hungary: **168.019 million km** • in Austria: **106.270 million km**
Weight of transported goods: **6604 thousand tons**	• GYSEV CARGO: **3486 thousand tons** • RAABERBAHN CARGO: **3118 thousand tons**
Punctuality	• in Hungary: **96.49%** • in Austria: **96.4%**

GYŐR-SOPRON-EBENFURTI RAILWAYS PRIVATE COMPANY LIMITED BY SHARES WWW.GYSEV.HU

Knorr-Bremse Rail Systems Budapest

Braking systems produced at the railway development and production center of Knorr-Bremse Budapest are used in railway vehicles running in more than a hundred countries of the world: high-speed trains, passenger and freight trains, trams and metro trains. Here in Budapest, we are making the accelerating future safer.

One billion people around the world put their trust in systems developed by Knorr-Bremse every day. And we serve the trust placed in us with stability and continuous innovation. Every finished product, every development and innovation is backed by a high level of engineering and manufacturing expertise. Our portfolio has been continuously expanding since 1996 and Knorr-Bremse Budapest now performs group-wide tasks in the areas of product innovation, software-hardware research and development, warehouse service and purchasing.

Our continuous technological developments, investments and trainings allow us to always ensure the highest quality for our partners. Eco-design approach accompanies our product design processes, and the aim of our electronic developments is to operate autonomous systems on the railway as well. The innovative technology of 3D metal printing is already part of our everyday life, since we started to use it for the first time within the Knorr-Bremse group. With the development of our new digital automatic coupler we are part of one of the most important railway industry developments today: we contribute to the shift of freight traffic to an environmentally friendly track: from road to rail.

In our internship programs, future engineers can get familiar with the current technological trends and processes of the industry first-hand. We provide real knowledge to our colleagues at the beginning of their careers, involving them in real situations and presenting exciting challenges. The aim of our research cooperation with higher education is to deepen theoretical knowledge in practical experience, so that present and future passengers can entrust themselves to the most outstanding specialists on the railways.

We are improving indomitably! Will you join in?

careers.knorr-bremse.com

Knorr-Bremse Rail Systems Budapest

We have represented the five core values of Knorr-Bremse in Hungary for 26 years, that define our everyday life and contribute to our continuous improvement.

Technological excellence

Due to our innovative approach, we experiment with the latest technologies, such as metal printing, artificial intelligence or augmented reality. More than 250 people work in the field of product development, including mechanical and electronic development, who inspect products 24 hours a day on nearly 80 test benches to represent the highest possible quality.

Entrepreneurship

We are characterized by continuous expansion and development, we take ownership of the challenges of the company, and we see opportunities for development in new projects. Areas of development and production have developed together, in parallel, over the years, because we believe that the key to success is continuous renewal and improvement.

Reliability

We develop and manufacture complex products (brake mechanics, air supply units, brake control modules, safety-critical electronic systems, etc.) in accordance with the most diverse customer expectations. Our partners can count on us, our products meet individual needs, therefore accuracy and reliability are essential in all areas of our company.

Passion

Being present in the railway industry we are looking for opportunities to be represented in as many areas as possible. We work closely with higher education institutions in training, development and research: we support talented university students and teachers with a scholarship program, and high school students can gain relevant work experience in our equipped training center. We are active supporters and participants of professional conferences and forums in Hungary and abroad.

Responsibility

We take responsibility for our products, our activities cover the entire process of the product life cycle from design through production to product aftercare. In addition to professional responsibility, our social commitment can be experienced by our volunteer colleagues through our Local Care program.